The role of fire in the coevolution of vegetation, soil and landscapes in south eastern Australia

Assaf Inbar

(ORCID: 0000-0001-5861-963X)

Thesis submitted in total fulfilment of the requirements of the degree of
DOCTOR OF PHILOSOPHY

December 2017

School of Ecosystem and Forest Sciences

Faculty of Science

The University of Melbourne

Abstract

Fire is an important process in the earth system, with biological, ecological, hydrological and geomorphological consequences varying from negligible to severe. The short-term effect of fire on earth system processes had been studied in detail, however, its role in the coevolution of soil and vegetation within the *critical zone* has never been addressed. In South Eastern (SE) Australia, local studies have shown that post fire runoff and erosion rates increase with aridity (the ratio between potential evapotranspiration and precipitation). The systematic variation in forest type, fire frequency and post fire response make SE Australian uplands an excellent natural laboratory to study the role of fire in coevolution of the *critical zone*. The aim of this study was to explore the role of fire in coevolution and to identify the key mechanisms, processes and feedbacks involved. Observations in which drier forests burn more frequently and yield more post-fire runoff and erosion, were used to hypothesize that in SE Australian uplands, fire has a critical role in the coevolution of the critical zone, and that its contribution increases systematically with aridity.

Three different methods were used to address the presented aim. The first method focused on the long-term fingerprints of coevolution, soil depth and landform. By considering the observed climate-related differences in forest type, fire frequency and erosion rates, I hypothesised that soil depth and hillslope gradient are north-south asymmetric, and that the magnitude of that asymmetry varies systematically with climate. I addressed these hypotheses by analysing data from soil depth measurements and topographic analysis of digital elevation models. Results showed that soil depth decreased non-linearly with aridity, and that south facing hillslopes were on average steeper and their soils deeper than those facing north. Indices of asymmetry in soil depth (*SAI*) and hillslope gradient (*HAI*) expressed a humped-type relationship with aridity, with a peak close to the water-energy limit boundary, pointing to the key role of climate and possibly fire in controlling differential hillslope-scale coevolution across pedomorphic and geomorphic timescales.

In the second method, I used a new numerical model in order to: (i) test the hypothesis that fire related processes and feedbacks are critical to explain observed patterns and magnitude of differences in system states across the landscape, and that their effect increases with aridity; and (if the hypothesis was supported), (ii) evaluate the role of fire related mechanisms in the coevolution process. The model was formulated and parameterised to express

processes typical to SE Australian systems, and was evaluated with literature and empirical data. Simulations with stochastic fire controlled by soil moisture deficit replicated the observed pattern and magnitude of difference in system states. The net effect of fire on soil depth increased non-linearly with aridity when results from these simulations were compared to those without fire (i.e., coevolution only controlled by climate). Analysis of simulations designed to isolate the key processes affected by fire indicated that model outputs are sensitive to fire frequency and the effect of individual fires on infiltration capacity (*Ic*), and less so to the effect of fire on forest cover. Using model simulations, a fire-related eco-hydro-geomorphic feedback was identified in which a long-term increase in post-fire erosion might contribute to more frequent fires and more erosion.

The aim of the third approach was to evaluate and quantify, using intensive field measurements, the way in which contemporary vegetation and soil depth affect the partitioning of rainfall and solar radiation, and to estimate the implications of this on processes in the coevolution of the critical zone. Sub-canopy microclimate (and open reference sites) was measured at sites across an aridity gradient, and the effect of partitioning of rainfall and solar radiation on coevolution was addressed by analysing soil moisture and temperature data, which are central to several processes in coevolution: productivity, flammability and weathering. Results showed that throughfall decrease and net shortwave radiation under the canopy increase with aridity due to the lower rainfall and higher canopy openness (respectively). On wet (dry) sites, the closed (open) canopy and the deep (shallow) soils partition water and energy in a way that resulted in wetter (drier) soils throughout the year, pointing to lower (higher) flammability and higher (lower) productivity. Mean annual soil water stores decreased non-linearly with aridity, and were more than 5 times higher on wet sites, despite annual rainfall only differing by a factor of ~2. Soil weathering is affected by soil moisture, and the results indicates that the differences between the system states may be amplified by weathering rate differences. The results points to a coevolutionary feedback between weathering, productivity, erosion and fire, which is controlled by the partitioning of water and energy across the vegetation and soil.

Overall, results show that fire can play a significant role in the coevolution of soil, vegetation and landscapes in SE Australia. This work is the first to show the importance of fire related eco-hydro-geomorphic feedbacks in coevolution, controlled by soil moisture. Fire was found to operate within feedback loops between its effects on system properties and consequential

changes in fire frequency. Two feedback loops were identified: between fire frequency and erosion, and between soil development and fire frequency. By its effect on infiltration capacity and the corresponding reduction in soil depth in direr forests, fire was found to exaggerate the effect of climate on coevolution, and helps to explain the extreme differences in observed system states across an aridity gradient.

Declaration

This is to certify that:

The thesis comprises only my original work towards the PhD except were otherwise indicated in the acknowledgment section.

Due acknowledgment has been made in the text to all other material used. The thesis is fewer than 100,000 words in length, exclusive of tables, maps, bibliographies, and appendices.

Signature

Assaf Inbar

Acknowledgements

I want to thank my supervisors, Associate Professor Gary Sheridan, Professor Patrick Lane and Dr. Petter Nyman for their inspiration, motivation, help and support throughout this process, and for keeping their door open. Gary's passion and enthusiasm to this difficult topic forced me to always see the big picture and has been an anchor back to reality every time that I got lost in those little details. Petter's brilliant and creative advice were always priceless, especially when one needs to be focused and productive. Thank you, Pat, for keeping an eye open on my progress throughout the candidature, and making sure everything is timely and in order. Thank you, all. I hope I have made you proud.

I want to thank the University of Melbourne, the Faculty of Science and the School of Ecosystems and Forest Sciences for their support, and to the Department of Environment Land Water and Planning (DELWP) for the top-up scholarship (funded by the Integrated Forest Ecosystem Research project). I also want to acknowledge two special people: Philip Noske for his amazing professional support in the field and in keeping me together during tough times. Craig Baillie for his priceless help in the field and the lab, and a great deal of laughter during field work in the Aussie bush. Special thanks to Dr Christoph Langhans for his advice, ideas and friendship. Many thanks also to: Dr Francis Rangers of the USGS for his collaboration, inspirations and ideas, Dr Rene van Der Sant, Daniel Metzen and Walter Box.

Last but not least, to my little family. I wouldn't have been able to make this without the support of my wonderful wife Kika and my amazing son Omer. I hope that this period will be memorable despite some difficult times and me being absent more often than not. I am so very proud of you both, and I'm looking forward to spending the rest of my life with you.

Table of contents

List of Figures

List of tables

Notations

aET	Actual evapotranspiration	L/T
AFC	Average fire cycle	T
AI	Aridity index	-
bRF	Structural biomass removed as response to fire.	-
B	Biomass	M DM/L^2
B_l	Total biomass	M DM/L^2
B_l	Leaf biomass	M DM/L^2
B_{lmax}	Maximum leaf biomass	M DM/L^2
B_{smax}	Maximum structural biomass	M DM/L^2
B_{max}	Biomass holding capacity	M DM/L^2
B_s	Structural biomass	M DM/L^2
b_{ret}	Water retention parameter	-
C_F	Cover fraction	-
C_{P-air}	Specific heat of air at constant pressure	MJ/kg/^{o}c
d_r	Inverse relative distance between earth and sun	-
D	Rate of deep drainage	L/T
D_c	Detachment capacity	L/T
D_l	Diffusivity	L/T
D_{nc}	Depth of the non-cohesive layer	L
D_{nl}	Diffusivity of the non-linear diffusion	L^2/T
e	Canopy water content ratio	-
e_a	Actual vapour pressure	kPa
e_E	Available volume in the canopy	L/T
e_s	Saturated vapour pressure	kPa
E_d	Soil diffusive erosion rate	L/T
E_f	Soil fluvial erosion rate	L/T
E_p	Potential evapotranspiration	L/T
E_s	Factor reducing E_p to achieve maximum soil evaporation	-
E_{net}	Net erosion rate	L/T
E_{imax}	Maximum evaporation of intercepted water from the canopy	L/T
$E_{\max}$	Maximum evaporation	L/T

$E_{p-daily}$	Mean annual daily E_p	L/T
ET_{max}	Maximum evaporative demand	L/T
E_w	Evaporation from soil under wilting point	L/T
f_c	Boolean fire coefficient	-
G	Soil heat flux	MJ/m^2/day
G_N	Mean gradient of north (equatorial) facing hillslope	L/L
G_S	Mean gradient of polar (south) facing hillslope	L/L
G_{sc}	Solar constant	MJ/m^2/min
h	Soil depth normal to slope	L
H	Soil depth	L
$\overline{H}$	Mean soil depth	L
$\overline{H_S}$	Mean soil depth at polar (south) facing hillslope	L
$\overline{H_N}$	Mean soil depth at equatorial (north) facing hillslope	L
H^*	Exponential folding depth of the soil production rate	L
HAI	Hillslope asymmetry index	-
i_{inf}	Proportion of throughfall that infiltrates the soil	-
i_{int}	Proportion of rainfall stored in canopy	-
i_{thr}	Proportion of rainfall becomes throughfall	-
i_{ro}	Proportion of rainfall that does not infiltrate (and becomes runoff)	-
I_a	Actual infiltration rate	L/T
I_c	Infiltration capacity rate	L/T
I_P	Potential infiltration rate	L/T
j_{dh}	Proportion of flux falling directly over canopy that “hits” canopy.	-
j_{dm}	Proportion of flux falling directly over canopy that “misses” canopy.	-
J	Total flux	-
J_L	Flux of water/energy passing through leaves	-
J_S	Flux of water/energy passing to soil	-
k_{lp}	Leaf production rate	1/T
k_{ss}	Structural biomass senescence coefficient	1/T
kss_{max}	Maximum biomass senescence coefficient	1/T
kss_{min}	Minimum biomass senescence coefficient	1/T
K_B	Biomass decay coefficient	1/T
K_e	Erosivity	T/L

K_s	Saturated hydraulic conductivity	L/T
L_T	Lag between peak E_p and peak solar forcing	T
LAI	Leaf area index	-
LAI_{gmax}	Highest possible "global" LAI of native vegetation	-
LAI_l	Modelled leaf area index	-
LAI_{lmax}	Highest possible "local" LAI value per site	-
LAI_r	Ratio between modelled to maximum LAI	-
LW_{net}	Net longwave radiation	MJ/m^2/Day
LW_{net-bc}	Net longwave radiation below the canopy	MJ/m^2/Day
MAP	Mean annual precipitation	L/T
MW_{wv}	Ratio of molecular weight of water to dry air	-
n	Porosity	-
N_d	Number of days in a year	-
n_T	Manning's roughness coefficient for cohesive material	T/L$^{1/3}$
NPP	Net primary productivity	M DM/L^2/T
p	Hourly rainfall	L/T
p_{nc}	Proportion of non-cohesive material transported by peak stream power	-
p_t	Hourly throughfall	L/T
p_{thr}	Total throughfall	L
p_{int}	Intercepted rainfall	L
p_x	Sub hourly rainfall intensity	L/T
p_L	Portion of hourly rainfall "hitting" the leaves	L
$\overline{\mathrm{P}}$	Mean annual precipitation	L/T
P_a	Atomic pressure	kPa
P_f	Probability of ignition	-
P_{wd}	Annual probability of water deficit	-
$\overline{P_{wd}}$	Mean annual probability of water deficit	-
q_d	Sediment flux	L/T^2
$q_{d_{net}}$	Net diffusive flux out of the modelled pixel	L/T^2
Q_0	Runoff	L/T
Q_{15}	Peak runoff rate	L/T
$r_{P_{wd}}$	Ratio between the $\overline{P_{wd}}$ of the sites at the two climatic extremes (driest and wettest)	-
r_{RI}	ratio between average fire cycle of the driest to that of the wettest	-

R_a	Extra-terrestrial radiation	MJ/m^2/Day
RH	Relative humidity	%
R_{net}	Net radiation	MJ/m^2/Day
R_{net-bc}	Net radiation below the canopy	MJ/m^2/Day
s	Degree of saturation	-
$\bar{s}$	Number of days soil moisture was below cutoff	-
s_{cut}	Degree of saturation at water deficit cutoff	-
s_h	Degree of saturation at hygroscopic capacity	-
$s_{w,}$	Degree of saturation at wilting point	-
s^*	Degree of saturation at incipient stomata closure	-
s_{fc}	Degree of saturation at field capacity	-
s_E	Actual pore volume remaining in soil	L
S_{cap}	Canopy water storage	L
S	Gradient	-
Sc	Critical gradient above which hillslope diffusion becomes infinite	-
S_{LAI}	Volume of water that can be stored by a unit *LAI*	L/L/L
SAI	Soil asymmetry index	-
SW_{in-bc}	Incoming shortwave radiation below the canopy	MJ/m^2/Day
SW_{in-o}	Incoming shortwave radiation at the open	MJ/m^2/Day
SW_{net}	Net shortwave radiation	MJ/m^2/Day
SW_{net-c}	Net shortwave radiation at the canopy	MJ/m^2/Day
SW_{net-bc}	Net shortwave radiation below the canopy	MJ/m^2/Day
SW_{net-o}	Net shortwave radiation in the open	-
T_a	Actual transpiration	L/T
s_{svp}	Slope of the saturation vapour pressure versus temperature curve	kPa/^{o}C
T_s	Mean daily temperature	^{o}C
T_{air}	Temperature under the canopy	K
T_{sky}	Temperature measured in the open	K
T_{surf}	Surface temperature	K
T_{max}	Maximum transpiration	L/T
TLE	Transport limited erosion rate	L/T
VWC	Volumetric water content	cm^3/cm^3
VWC_{SBI}	Volumetric water content at soil-bedrock interface	cm^3/cm^3

VWC_{surf}	Volumetric water content at the surface	cm^3/cm^3
VWC_{wp}	Volumetric water content at theoretical wilting point	cm^3/cm^3
VWC_{fc}	Volumetric water content at theoretical field capacity	cm^3/cm^3
VWC_{int}	Integrated volumetric water content	cm^3/cm^3
$\overline{VWC_{int}}$	Mean annual integrated volumetric water content	cm^3/cm^3
V_f	Sky view fraction	-
V_s	Mean annual soil water stores	L
VPD	Vapour pressure deficit	kPa
VPD_{bc}	Vapour pressure deficit below the canopy	kPa
VPD_c	Vapour pressure deficit at the canopy	kPa
WUE	Water use efficiency	M_{CO2}/ M_{H2O}
Z	Elevation	L
α_{PT}	Coefficient for the Priestley-Taylor equation	-
α_f	Albedo of forests	-
β	Evaporation efficiency	-
β_r	Root density exponential decay term	1/M
γ	Psychrometric constant	kPa/^{o}C
δ	Solar angle	rad
Δ	Gradient of saturated vapour pressure	-
Δd	Difference between maximum and minimum values of daily E_p	L/T
ε	Rate of soil production from below	L/T
ε_{canopy}	Canopy emissivity	-
ε_{sky}	Sky emissivity	-
ε_{surf}	Surface emissivity	-
$\in$	Soil production rate	L/T
$\in_o$	Maximum soil production (at H=0)	-
θ_m	Soil moisture modifier	-
λ_v	Latent heat of vaporisation	MJ/kg
μ	Ratio of night-time to daytime CO_2 exchange	-
η	Maximum transport coefficient (for depth dependent diffusive sediment transport)	L^2/T
ρ_r	Rock density	M/L^3
ρ_s	Soil density	M/L^3
ρ_w	Density of water	M/L^3

σ	Ignition probability	-
σ_{SB}	Stephan-Boltzmann constant	$MJ/K^4/m^2/day$
τ	Shear stress of overland flow	Pa
τ_{crit}	Critical shear stress	Pa
φ	Interception evaporation efficiency	-
φ_L	Latitude	rad
Φ	Resource allocation coefficient	-
ω_s	Sunset hour angle	rad
ω	Conversion factor of CO_2 to dry biomass	kg DM/kg CO_2
Ω	Stream power	Pa/s
Ω_{nc}	Critical stream power ($\Omega = 0$)	Pa/s
∇	Divergence operator	-

1 Introduction

1.1 What is coevolution

Landscapes are constantly changing. Tectonics and climate drive soil production and erosion which act simultaneously on the lithosphere to shape the landscape (Dietrich et al., 2003). The legacy of these processes and their rates, determine the current "state" of the landscape, in which landform, soil and life interact and coevolve (Dietrich & Perron, 2006). The critical zone is defined as the boundary layer in which rock, soil, water, air, and living organisms interact. Coevolution of soil and vegetation within the critical zone is a complex, interdisciplinary, non-linear process that is constantly occurring across earth systems at multiple scales in all environments (Troch et al., 2015).

In biology, coevolution usually refers to the combined evolution of two or more species, in which the evolution of one affects the evolution of the other and vice versa (eg., Lawlor & Smith, 1976; Thompson & Cunningham, 2002). In earth (Corenblit et al., 2007; Pelletier et al., 2013) and hydrological (Berry et al., 2005; Troch et al., 2013, 2015; Yoshida & Troch, 2016a) sciences coevolution is defined as the interactions and feedbacks between life and its surroundings (Corenblit et al., 2011; Corenblit & Steiger, 2009; Dietrich & Perron, 2006; Phillips, 2016; Porder, 2014). In the past, research was focused on processes within each individual discipline, however more recently the importance of interdisciplinarity in understanding and predicting complex behaviors of systems has been acknowledged (Troch et al., 2015; Wagener et al., 2010).

In the hydrological literature, the term coevolution usually describes the coevolution of vegetation, soil and landform within catchments, or *catchment coevolution* (Troch et al., 2015; Yoshida & Troch, 2016b). Budyko (1974) found that hydrological partitioning of catchments can be well predicted by the ratio of net radiation to the energy required to evaporate the mean annual precipitation, defined as the 'evaporative index of dryness' or the *aridity index*. Hydrologists note that *Budyko*'s somewhat surprising result raises the question of whether this simple hydrological response of catchments regardless of inter-annual variations in climate properties and catchment characteristics points to coevolution of catchments with climate forcings (Troch et al., 2013). In other words, have catchment properties that might alter the relationship between climate and rainfall partitioning developed "in-sync" with the climate, therefore strengthening the climate vs rainfall

partitioning relationship. The *catchment coevolution* bottom-up approach has been proposed as a tool that can assist hydrologists in addressing this question, which may also help scientisits to predict the hydrological response of catchments (i.e., stream flow quantity and quality) under a changing climate (Troch et al., 2015). The main idea behind this framework lies with the notion that better predictions of hydrological response under possible climatic changes could be achieved by better understanding how catchments have evolved into their current state (Troch et al., 2015; Tromp-van Meerveld & McDonnell, 2006; Wagener et al., 2010)

Studies in coevolution can be divided into *observational* (or top-down) studies, which use coevolution theory in order to explain observed behavior or geomorphic signatures (Troch et al., 2013; Yoshida & Troch, 2016b; a), and *modelling studies* (bottom-up), that try to understand the processes and feedbacks involved in coevolution by using models that predict observed behavior or patterns in nature (eg., Pelletier et al., 2013). Surprisingly, probably due to the complexity and interdisciplinarity of coevolution processes and feedbacks, there are a relatively small number of studies that consider coevolution together from both perspectives (Pelletier et al., 2013). Models are often constrained to a subset of the interactions within systems, such as the effect of: climate-vegetation interactions (Zhou et al., 2013); climate-soil-vegetation interactions (Brolsma & Bierkens, 2007; Gao et al., 2014; Montaldo et al., 2005); climate-vegetation-landform interactions (eg., Istanbulluoglu & Bras, 2006; Yetemen et al., 2015b); vegetation-landform interactions (eg., Istanbulluoglu et al., 2004; Istanbulluoglu & Bras, 2005; Saco & Moreno-De Las Heras, 2013; Tucker et al., 1999) and more.

1.1.1 Coevolution – conceptual model

Evolution is defined here as the change in the internal state of a system with time due to ongoing external forcing. In order for evolution to occur, the system needs to have the ability to change and to be "pushed" between different system states (Figure 1-1). The term "system" in this definition could be replaced by: molecule, organism, critical zone unit, ridge or any other biotic, abiotic or a combination entity. Theoretically, even in simple settings, evolution may not be a linear process, and it has the potential to reach a steady state, where the net change in the state of the system is *zero*. Coevolution occurs when a system is made of several internal components that have the ability to change, and by that affect the evolution

of the other components in the system (Figure 1-1). Since systems are usually internally complex, studying coevolution could then be conceptualized to be a more detailed understanding of the evolution trajectory of a specific system.

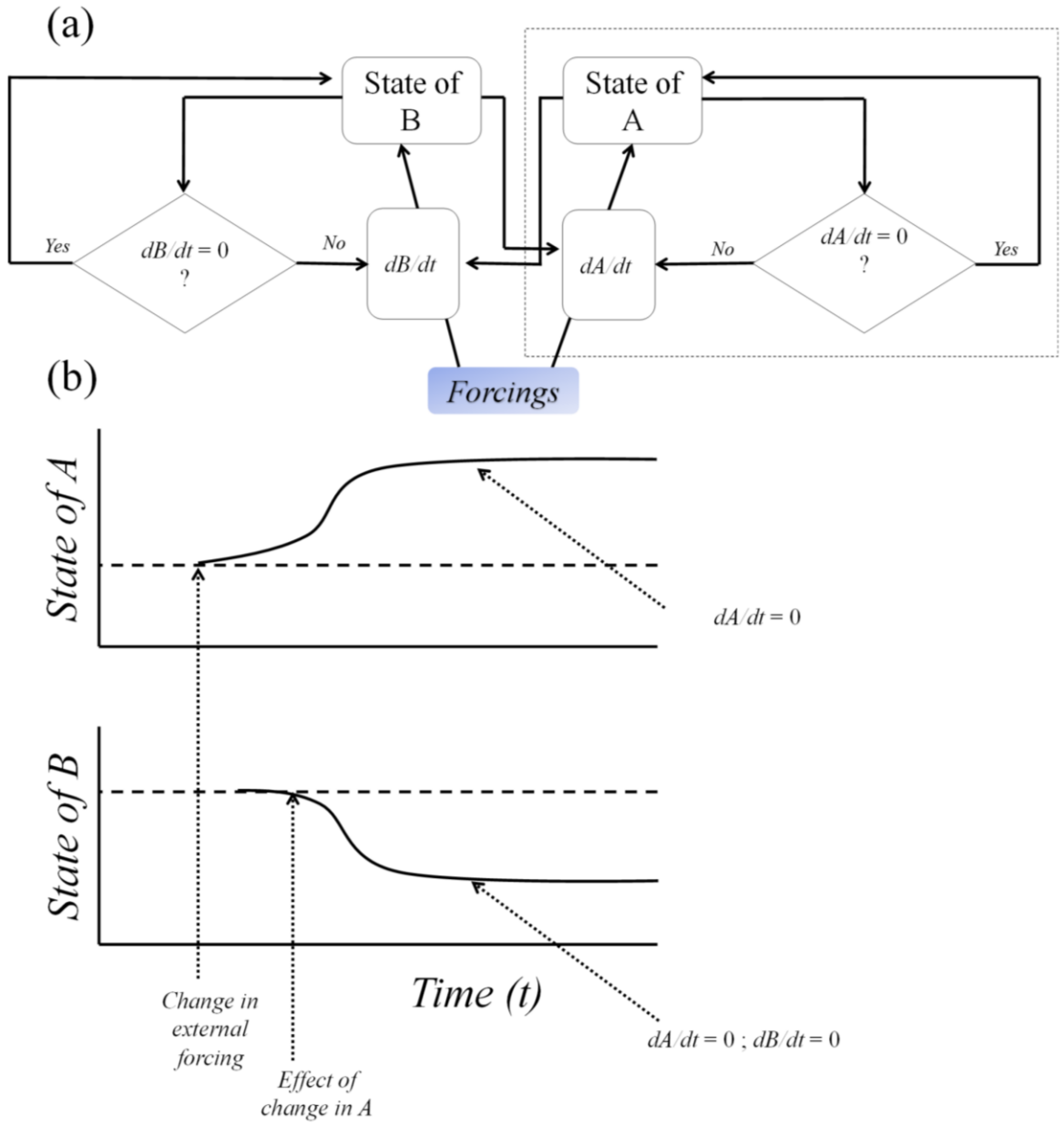

Figure 1-1 - (a) A simple description of a non-specific coevolution process. The contents of the rectangle that is surrounded by the dashed line describes a "simple" evolution process of entity *A* with time, under external forcings. Changes in *A* will continue until it will not respond to the continuous forcings, and the net change in A will be *zero*. When the system is made of two (or more) components, changes in the state of *A* affects and affected by the state of *B*, and vice versa. In this case, the system will undergo change until both *A* and *B* will stop

responding to external perturbations, and the net change in both will be *zero*; (b) a simple graph that explains the trajectories of coevolution.

The coevolution of the critical zone with time is consistent with an emerging Darwinian approach, in which change in a the system occurs in both directions, that is, vegetation is affected by the soil (by its ability to store water, for example), but also has the ability to modify the soil properties in a way to maintain its existence and proliferation (Corenblit et al., 2007; Eagleson, 1982; Verboom & Pate, 2013). The effect of these coevolution processes across geological timescales may ultimately affect landscape evolution, generating distinct system "fingerprints" that can sometimes be observed or quantified.

1.2 Literature review and knowledge gaps

1.2.1 Drivers and timescales

The coevolution of life, soil and landscapes are intimately linked, and represent the interplay between erosion, weathering, hydrology and ecology (Dietrich & Perron, 2006). In a recent review paper, Troch et al. (2015) reviewed the recent progress in catchment coevolution. The authors used Jenny's approach to soil forming factors (Jenny, 1941) and described four catchment forming factors, all of which affect the coevolution of catchments and its properties across all scales: Climate, Tectonics, Geology and Time. Theoretically, all these factors, operating across different timescales, determine the coevolved state of a catchments and its *hydrological age*, as they describe it, and its hydrological response. With respect to time, Troch et al. (2015) divided the continuous coevolution processes into useful, discrete, categorical timescales; ecosystem-, climate- and geological-, in which catchments develop. The authors, among others (eg., Lin, 2011; Rodriguez-Iturbe et al., 1999; Sivapalan, 2003; Wagener et al., 2010), suggested that interdisciplinary and holistic approaches are necessary in the understanding coevolution across temporal and spatial scales.

Coevolution is made of small processes which are constantly affecting the system properties. For example, across *ecosystem timescales*, vegetation properties could change due to short–term changes in climatic forcing. These changes could be due to the actual changes in climate (eg., Cramer et al., 2001; Davis & Shaw, 2001; Fletcher et al., 2014a) or due to smaller scale

adjustments to landscape form (eg., Yetemen et al., 2015b) that could affect the distribution of climatic forcing across the landscape (Yetemen et al., 2015b; Zhou et al., 2013).

1.2.2 Effect water availability on vegetation

The distribution on vegetation across the landscape into niches that are driven by variations in (landscape-affected) microclimate is a frequently observed example of responses of vegetation at *ecosystem timescales*. Microclimate and water availability are important drivers of the distribution of vegetation across the landscape (eg., Berry et al., 2005; Budyko, 1974; Givnish et al., 2014; Nyman et al., 2014b; Specht & Wood, 1972), and vegetation is quick to respond to changes in climatic forcing, in comparison to soils and landscapes. By downscaling climate information across Victoria, Nyman et al. (2014b) found that tree height decreased systematically with a decrease in water availability at very small scales, which depended on both regional climate but also small-scale variability in elevation and solar exposure (i.e., hillslope orientation). Pelletier et al. (2013) reported a non-linear increase in biomass with elevations at the Sky Islands in Southern Arizona. The authors also found that north facing hillslope host thicker biomass than south facing ones. Biomass was found to increase non-linearly with a metric that expresses the location specific effective energy and mass transfer (EEMT) to the system, which represent local microclimatic conditions (Chorover et al., 2011; Rasmussen et al., 2011, 2015), and was shown to be related to soil development (Lybrand & Rasmussen, 2015; Rasmussen & Tabor, 2007). These results give an example of the interactions between topographic-affected microclimate, soil and vegetation that point to coevolution processes in the small and intermediate timescales (Pelletier et al., 2013; Rasmussen et al., 2015).

Soil moisture mediates the effect of climate on the distribution of vegetation across the landscape at different scales (eg., Brolsma & Bierkens, 2007; Ivanov et al., 2008; Rodriguez-Iturbe et al., 1999; Zhou et al., 2013). By using a cellular automata model combined with an ecohydrology model, Zhou et al. (2013) found that the effect of topographic-driven variations in potential evapotranspiration , soil moisture and water stress, affect plant distribution at an annual scale, similar to observed patterns of vegetation in a catchment in Central New Mexico. In an ecohydrological monitoring study at a smaller catchment in Central New Mexico, Gutierrez-Jurado et al (2013) reported that solar radiation exerted a first order control on the dynamics of evapotranspiration (ET) and soil moisture residence time across

the north and south facing hillslopes. Vegetation across the catchment varied markedly depending on hillslope aspect, where north facing hillslope hosted a juniper savanna, and the south a creosote scrubland. The authors found that the two hillslopes expressed distinct soil water pools for evaporation demand throughout the year, where the north facing aspect was wetter for longer comparted to its south facing counterpart, possibly affecting the observed differences in the distribution of vegetation across the catchment. Lastly, the two hillslopes showed different runoff dynamics pointing to possible differences in erosion processes (Gutiérrez-Jurado et al., 2007) with geomorphic implications at *geological timescales* (eg., Istanbulluoglu et al., 2008; Yetemen et al., 2010).

1.2.3 The importance of soil depth in coevolution

In geomorphological literature, the word *soil* is often replaced by *regolith*, which essentially represent the transportable parts of the weathered bedrock. Herein I will refer to regolith as soil, mainly due to its importance in terms of water-holding and hydrological properties. With a direct or indirect influence of climate, vegetation also affects the soil it is supported by (Amundson et al., 2007) either assisting its creation from the parent material (eg., Corenblit et al., 2011; Jenny, 1941; Pawlik et al., 2016; Roering et al., 2010), by controlling its transport through fluvial or colluvial processes (Gabet et al., 2003; Pelletier et al., 2013; Roering et al., 2010; Wilkinson et al., 2009), or by altering its physicochemical (eg., Lado et al., 2004; Saiz et al., 2012) and hydraulic properties (Archer et al., 2016; Lohse & Dietrich, 2005; Thompson et al., 2010).

One of the most comprehensive works in coevolution was undertaken by (Pelletier et al., 2013) who constructed a coupled-system model that included eco-pedo-geomorphic feedbacks across a climate and elevation gradient. In their model, soil production and colluvial sediment transport rates were coupled to EEMT and biomass, both of which increased with elevation. The modelling results by Pelletier et al. (2013) replicated trends and magnitudes quantified for the Sky Islands in southern Arizona, (USA), in the distribution of soil depth, biomass, relief and mean distance to valley when running the model for geological timescales. The authors found a feedback in which the soil depths was controlled by its own depth (as proven imperically by Heimsath et al., 1997) and by vegetation density and its effect on geomorphic processes. The authors underscored the importance of incorporating soil depths in landscape evolution modelling framework, a factor which had

often been neglected (Pelletier et al., 2013). In their model, biomass was considered a function of EEMT, and was not limited by soil depth or any of the soil properties that control plant available water. Development of a soil mantle is essential for ecohydrologic dynamics, and soil depth is an important property that can set up an limit to biomass production due to its water holding characteristics (Meyer et al., 2007) and consequential geomorphic transport processes (Dietrich et al., 2003) that themselves control soil depth.

1.2.4 Eco-geomorphology and eco-hydro-geomorphology

Vegetation protects the soil, providing cover via the canopy and leaf litter (eg., Dunkerley, 2015), and by increasing the mechanical strength of the soil via plant roots (eg., Reubens et al., 2007) . Vegetation-related increases in soil organic matter and macroporosity have also been shown to increase infiltration rates (Thompson et al., 2010) and reduce overland flow (eg., Lane et al., 2004; Lohse & Dietrich, 2005). Thus, an increase in vegetation is often associated with a reduction in runoff and sediment yield (eg., Collins et al., 2008; Istanbulluoglu & Bras, 2006; Langbein & Schumm, 1958). By studying the relationship between climate (effective precipitation) and erosion rates across small watersheds in western United States Langbein and Schumm (1958) showed that sediment yield peaks when effective precipitation is around 300mm/yr (approximately at semi-arid climate) and attributed this to increase (decrease) in vegetation density above (below) that point. In a landscape morphology analysis of a semi-arid basin, Yetemen et al. (2010) found that landscapes under forest vegetation are steeper and have lower erodibility compared to landscapes vegetated with grass or shrubland. The effect of roots in reducing critical shear stress for grass vegetation on topographic steepening under uniform uplift regime was reproduced by a modelling frameworks by Collins et al. (2004), and by *Istanbulluoglu et al.* (2005) for static forest vegetation. In the latter study, stochastic fire regime caused a flattening of the landscape. These changes in landform can potentially affect the distribution of climatic forcing (mainly solar radiation) and cause variable changes in vegetation structure (eg., Zhou et al., 2013) and erosion processes that in turn affect asymmetric landform changes (eg., Yetemen et al., 2015b).

The development of a vegetation community at a point can have implications on long term development of landscapes (Istanbulluoglu & Bras, 2005; Saco et al., 2007; Yetemen et al., 2010, 2015b). For example, Yetemen et al. (2015b) added an eco-hydro-geomorphic

component influenced by soil moisture and landscape position on top of an existing landscape evolution model, mimicking a semi-arid catchment in Central New Mexico, USA. In response to the spatially explicit representation of solar radiation, the modelled landscape developed an asymmetric shape, in which north (equatorial) facing hillslopes were steeper than their south (polar) facing counterparts under uniform uplift conditions. The authors attributed this result to the effect of solar radiation on soil moisture and vegetation (grass) patterns and the latter's effect on fluvial erosion processes. This eco-hydro-geomorphic phenomenon, also known as *hillslope asymmetry* has been observed worldwide (eg., Ben-Asher et al., 2017; Dohrenwend, 1978; Istanbulluoglu et al., 2008; McGuire et al., 2014; Parsons, 1988; Poulos et al., 2012; Yetemen et al., 2010) and is attributed to different microclimatic conditions and erosion efficiency due to solar exposure (eg., Istanbulluoglu et al., 2008; Richardson, 2015). Using the same model, Yetemen et al. (2015a) succeeded in replicating a trend in this landscape-scale phenotype found by Poulos et al. (2012) across the whole length of the American cordillera. The observed pattern shifted between both hemispheres, and became more prominent in mid-latitudes, due to the incident angle of the sun (Poulos et al., 2012). Other interesting contributions modelled the development of asymmetric hillslopes only by different hillslope diffusivity (Ben-Asher et al., 2017) or erosion efficiency (Richardson, 2015). The contribution of Yetemen et al. (2015b) was in the integration of a ecohydrology-vegetation-erosion-landscape feedback, in which changes in landform affected the distribution of solar radiation across the landscape, which in turn affected vegetation density and geomorphic processes, feeding back to changes in landform.

1.2.5 Fire and coevolution

Records of wildfire date as early as the Silurian (~420 million years ago), after the appearance of carbon-rich terrestrial plants, fluctuating back and forth throughout this time, mainly due to different concentrations of atmospheric O_2 (Scott & Glasspool, 2006), affecting the development of different fire tolerance traits (Bowman, 2000; Bowman et al., 2009). In Australia, for example, fire tolerant species replaced rainforest taxa since the drying out during the Tertiary, reinforced by the availability of fuel and the subdued topography of the arid continent (Bowman, 2000). It has been shown that different fire regimes can explain the presence and boundaries of different ecosystem states across the landscape (Bowman, 2000). Thus, it is plausible that long-lasting, long-term and steady fire regime can push a system

towards a steady-state with the fire frequency (Bowman, 2000), that is, when the net change in vegetation and soil is zero as long as fire frequency stays the same. However, since fire regime tend to change with climate (eg., Lynch et al., 2007; Power et al., 2008), consequential changes in vegetation are inevitable, as paleo-fire records show (Fletcher et al., 2014a), in turn causing a change in erosion processes and magnitudes (eg., Meyer et al., 1992; Pierce et al., 2004).

The geomorphic consequence of wildfire varies between low (Lane et al., 2004, 2006) to very high (eg., Moody & Martin, 2001a; Nyman et al., 2011; Prosser & Williams, 1998; Shakesby & Doerr, 2006) and includes several types of geomorphic processes (eg., Benda & Dunne, 1997; Gabet & Dunne, 2003; Roering & Gerber, 2005; Shakesby et al., 2006). In many cases, the immense heat during fire can cause significant changes in soil hydrological properties close to the soil surface (Cawson et al., 2016; Certini, 2005; Inbar et al., 2014), despite the good insolation properties of the soil (Hillel, 1982). These effects often cause severe water repellency (eg., DeBano, 2000a; Larsen et al., 2009) or soil sealing (Inbar et al., 2014; Larsen et al., 2009), which result in lower infiltration rates and higher overland flow response (Doerr et al., 2006). By burning the vegetation cover, fire opens the opportunity for rainfall drops to detach soil particles by direct impact and by the shear stress of overland or concentrated (rill) flow (Shakesby & Doerr, 2006).

While the majority of the studies concentrate on the short term geomorphic consequences of fire, only a handful of studies look at its effect on longer timescales. These studies concentrate on varying possible effects of fire on long term sediment budgets and landscape development (Benda & Dunne, 1997; Istanbulluoglu et al., 2004; Istanbulluoglu & Bras, 2005; Roering & Gerber, 2005). For example, Istanbulluoglu et al. (2004) looked at the effect of fires on frequency and magnitude of sediment delivery in the Idaho batholith using a numerical model that simulated the development of soil mantle. In their model, forests supplied root cohesion and surface resistance, which were altered when stochastic fire went through and burned the forest cover. By using model simulations, the authors found that wildfire controlled the timing and magnitude of episodic erosion processes when compared to undisturbed forests, and as a consequence, caused an increases drainage density at geological timescales (Istanbulluoglu et al., 2004). Gabet and Dunne (2003) used a modelling framework to investigate the effect of vegetation changes (i.e., shrubland to grassland) and fire on long term sediment yield from a steep hillslopes in California. The model predicted that different vegetation types would result in different fire severities and overall rates of

sediment yield in response to fire and intensive rainfall. The authors predicted that the expected changes in vegetation due to climate change will have higher effect on long term sediment yield than changes in the magnitude and frequency of meteorological events.

1.3 Key knowledge gaps, research aims and research questions

The above studies provide useful information on fire-driven processes that change the landscape, however the contribution of fire to the long term structure and function of the critical zone remain unclear. Coevolution of the critical zone includes biological, ecological, geomorphological and hydrological processes that operate simultaneously together in long timescales and evolve systems in different trajectories under the influence of climate (when holding geology and tectonics constant; Troch et al. (2015)). Fire clearly plays part in these interacting processes, however, its role in the coevolution of the critical zone has never been studied. For example, it is clear that the fire regime can change due to fluctuations in climate (Bowman et al., 2009), making it a dynamic process, rather than a disturbance with a fixed return interval. However, shifts in fire regime can cause irreversible changes to vegetation patterns and soil mantle (Bowman, 2000; Fletcher et al., 2014a). Here it is suggested that the changes in fire regime can significantly alter coevolution trajectories either by affecting patterns in vegetation and in turn altering erosion rates (Fletcher et al., 2014a) and soil depth, or by affecting erosion processes and soil depth, and in turn affecting patterns in vegetation (Milodowski et al., 2015). The aim of this study is to explore the role of fire in the coevolution of soil and vegetation within the critical zone. This thesis will answer these two high-level research questions:

(i) What is the role of fire in the coevolution process?

(ii) If it does play a role, what are the mechanisms involved?

In order to address these questions, several processes related to the effect of fire needs to be identified. Here I suggest that the effect of fire on coevolution involves feedbacks between its hydro-geomorphic consequences (Shakesby & Doerr, 2006) on soil depth and biomass, and their ecohydrological control on flammability.

1.3.1 SE Australia as a natural laboratory

It is suggested that SE Australia uplands is an ideal location to study the effect of fire on coevolution for the following reasons: (i) the area is tectonically stable since late Cainozoic (Wellman, 1987); (ii) mid-intermediate elevation across the uplands (up to 1200m) were not glaciated during late Pleistocene (Barrows et al., 2001) narrowing down the possible geomorphic processes; (iii) similar to the rest of Australia, the area experiences variations in fire regime since mid-tertiary with severe vegetation changes from fire-sensitive to fire-tolerant species (Bowman, 2000). (iv) the dissected and steep nature of the landscape creates variations in climatic niches within relatively small spatial scales. A more detailed description on the SE Australian uplands can be found in Chapter 2.

In the forested SE Australia uplands, vegetation and soil properties vary markedly depending on elevation and landscape position (Cheal, 2010; Costermans, 2006; Specht & Wood, 1972). For example, hillslopes on high elevation (i.e., ~1000m asl) are often covered by closed, thick forests with tall trees that grow on top of deep and well-developed soil (Figure 1-2a and Figure 1-2c), whereas hillslopes on north facing slopes in lower elevation are often covered by open forests with short trees that grow on top of an undeveloped and thin soil mantle (Figure 1-2b and Figure 1-2d). These variations in vegetation also brings variations in fire regime, in which wet forestss have significantly lower fire frequency than dry ones, which can vary between 120 to 20 years between fires events, respectively (Cheal, 2010). In this area, surface runoff (i.e. hillslope scale overland flow) and erosion rates from unburnt forests are relatively low (Cawson et al., 2013; Lane et al., 2004). The effect of fire on erosion rates has been found to be highly variable, ranging from almost no effect (Lane et al., 2006) to increases of several orders of magnitude (Nyman et al., 2011; Sheridan et al., 2016). Similar to forest type and fire frequency, post fire hydro-geomorphic response in the area was also suggested to be controlled by climate (Sheridan et al., 2016), with high runoff and erosion rates across more arid sites, and low runoff and erosion rates across less arid ones. For example, on a recent study of post-fire runoff rates across an aridity gradient, Van der Sant (2016) showed that dry sites produce significantly more runoff than wetter ones for a given cumulative rainfall, and that runoff ratio (i.e., the ratio between runoff and rainfall) increases nonlinearly with aridity.

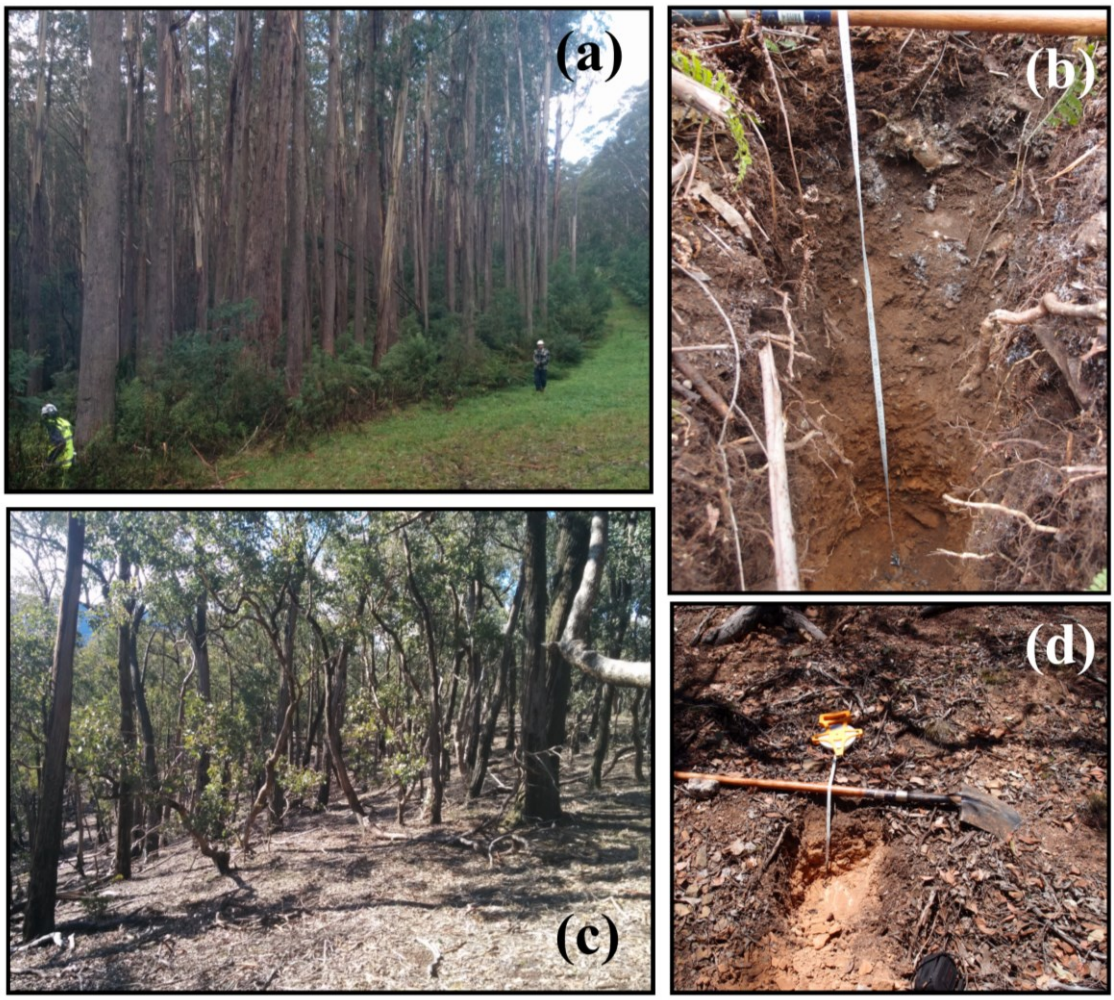

Figure 1-2 – Pictures of two of the sites used in this study that illustrate the range of differences in system states in across the aridity domain. The thick and tall forest at a The Triangle (a) that covers a very deep (1.2m) soil (b) are compared with the sparse and open forest (c) on top of a very thin (0.2m) soil (d) near lake Eildon, Victoria. Details of The Triangle and Eildon sites scould be found in chapter 5 and 2, respectively.

In SE Australia, other than variations across elevation gradients, differences in vegetation, soil (Nyman et al., 2014b; Rees, 1982) and erosion processes (Noske et al., 2016) can also occur on smaller spatial scales, such as between north (equatorial) and south (polar) facing aspects, presumably linked to differences in solar radiation. For example, Noske et al. (2016) reported that runoff and erosion rates from a burnt north facing catchment were substantially higher than from an adjacent catchment facing south. Nyman et al. (2011) reported a large number of debris flow events, all originating from burnt dry, north facing catchments that

were covered by heathy, grassy and shrubby dry eucalyptus forest types which were burnt at high or very high severity. An example of differences in hydro-geomorphic response after a severe fire between north and south facing hillslopes is presented in Figure 1-3.

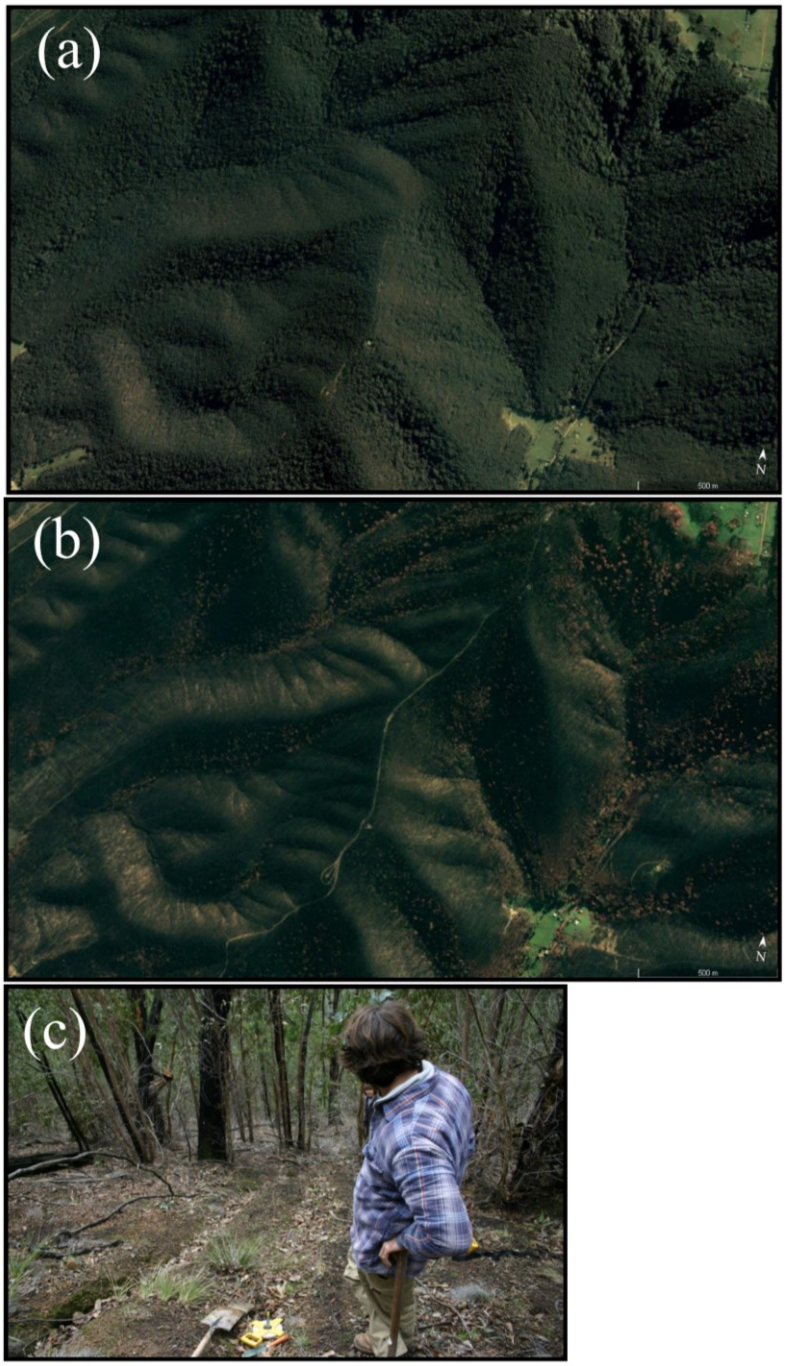

Figure 1-3– Google earth image of small catchment near King Lake (Elevation: 541; MAP 1199mm/yr), Victoria, which were severely burnt during a wildfire in February 2009 (infamously known as the Black Saturday fires). Image (a) was taken from Google earth historical imagery on August 2001, while Image (b) was taken on May 2009, three months

after the fire. Hillslope erosion processes could be seen on the north facing hillslopes (hosting drier forest) and none on the south facing ones (hosting wetter forest). Figure (c) shows an example of rills on north facing hillslopes after the 2009 Black Saturday fire at Sunday Creek, Victoria. Image 2017© DigitalGlobe using Google earth.

1.4 Hypothesis and methodology

Considering the above, I hypothesise that in SE Australia, fire has a critical role in coevolution, and can explain the observed patterns and magnitude of differences in system states of soils, vegetation and fire regimes, and that its relative role in coevolution increases with aridity. In order to test the hypothesis, and to explore mechanisms, processes and feedbacks related to coevolution of the critical zone in SE Australia I use three independent methods that vary in focus and timescale, and are divided into four chapters as follows (Figure 1-4):

- **Chapter 2**: The first approach focuses on the long-term fingerprints of coevolution. Here I argue that the long-term variations in erosion processes driven by climate and fire should have distinct fingerprint across soil depths and landforms. I use the observed differences in vegetation and erosion rates across different topographic positions (i.e., elevation and hillslope aspect) and hypothesise that these conditions: (i) result in asymmetry in soil depth and hillslope gradient as seen elsewhere (eg., Ben-Asher et al., 2017; McGuire et al., 2014; Poulos et al., 2012), where south facing hillslopes will have deeper soils and will be steeper than north facing ones; and that (ii) the magnitude of this asymmetry will vary with climate in a way that is consistent with the way the magnitude of post-fire erosion varies with climate. I use soil depth measurements and topographic analysis of Digital Elevation Models, in order to test these hypotheses.

- **Chapter 3 and 4**: In the second approach, I use a newly developed numerical model (Chapter 3), in order to: (i) to test the hypothesis that fire related processes and feedbacks are critical to explain observed patterns and magnitude in system states across the landscape, and that their effect of on coevolution increases with aridity; then, given the hypothesis is true, (ii) to evaluate the role of fire related mechanisms in coevolution (Chapter 4). Here, the effects of fire related processes on coevolution are expected to increase across an increasing aridity gradient due to the lower vegetation cover (Nyman et al., 2015a), higher fire

frequency (Cheal, 2010) and higher post-fire runoff and erosion rates observed as aridity increases (Sheridan et al., 2016). In order to test the hypothesis, I developed a numerical model that simulates the coupled ecohydrological, hydrological and geomorphological processes typical to SE Australian systems with stochastic fire driven by soil moisture deficit. The model is then used to decouple the effect of fire from that of climate on the coevolution of the critical zone by running simulations with and without a fire regime across a climatic gradient. Next, other model simulations are used in order to examine the mechanisms which control the effect of fire on coevolution, specifically: fire frequency, the effect of fire on post-fire soil hydraulic properties and on vegetation cover; and to evaluate processes and feedbacks which link ecohydrological and geomorphological processes with fire that control coevolution trajectories.

Chapter 5: The third approach focuses on short term processes and feedbacks related to coevolution under contemporary conditions. At small scales the partitioning of energy and water by vegetation and soil influence important processes in the coevolution of the critical zone. The aim of this study was to evaluate and quantify, using intensive field measurements, the way in which vegetation and soil depth affect the partitioning of rainfall and solar radiation, and to estimate what are the implications of this partitioning on processes in coevolution of the critical zone. I address the aim by measuring the sub-canopy microclimate (and open reference sites) across a climatic gradient for one year. The effect of partitioning of water and energy on coevolution is then addressed by analysing soil moisture and temperature data. This chapter gives a unique snapshot of processes and feedbacks that both affected by and contribute to the coevolution of the critical zone.

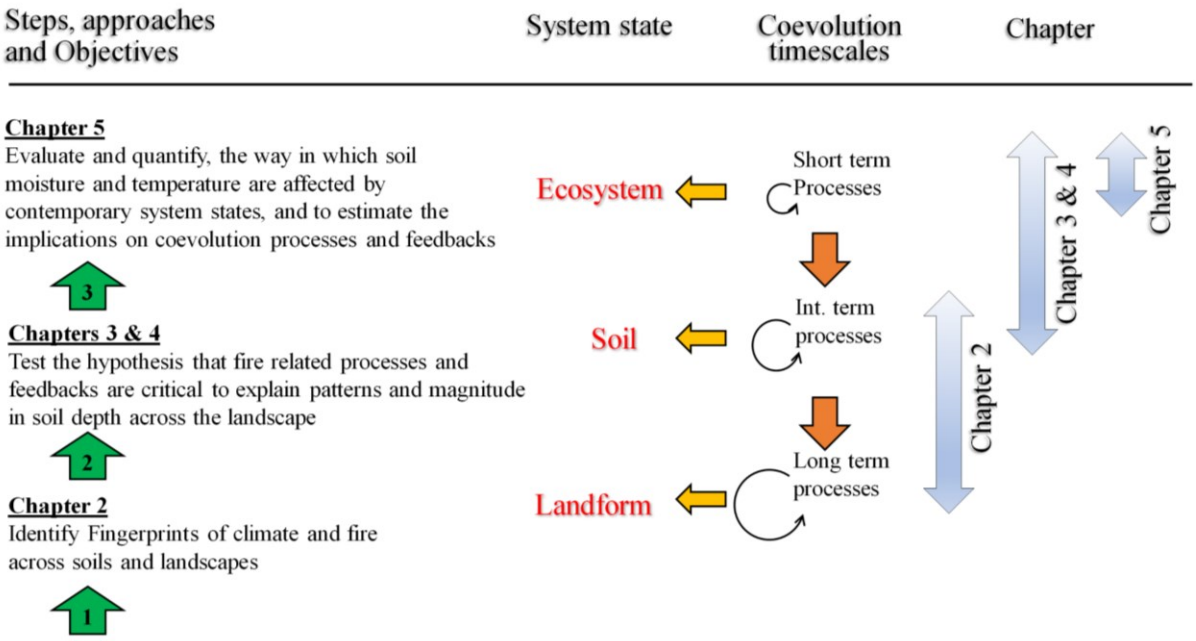

Figure 1-4– An illustration of the structure and logic of the thesis ordered by steps that focus on different timescales in the coevolution process.

2 Climate dictates patterns of hillslope asymmetry in fire-prone landscapes of South Eastern Australia

2.1 Abstract

Hillslope asymmetry is often attributed to differential soil production and erosion resulting from aspect-related differences in insolation. At global scales, the magnitude of these differences vary systematically with latitude. However, it is proposed that at regional scales, these variations are climate controlled. Here landscapes in SE Australia are investigated to evaluate the hypotheses that soil depth and hillslope gradient are north-south asymmetric, and that the magnitude of this asymmetry varies systematically with climate. Patterns of asymmetry in soil depth and landform were quantified using soil depth measurements and topographic analysis across a contemporary rainfall gradient. Results show that south (polar) facing hillslopes are persistently steeper, and have greater soil depth, than north (equatorial) facing slopes. Both soil depth and landform asymmetry trend non-linearly with climate, with a maximum near the water-limited boundary, where vegetation cover varies most rapidly with aridity, suggesting a possible long-term role for vegetation in hillslope development.

2.2 Introduction

The effect of hillslope aspect on vegetation (eg., Bale et al., 1998), soil (Anderson et al., 2013; Lybrand et al., 2011) and landform morphology (Gutiérrez-Jurado & Vivoni, 2013; Istanbulluoglu et al., 2008) is well recognised. In mid-latitudes under stable uniform tectonic settings, hillslope asymmetry is attributed to differential erosion processes across aspects due to radiative forcing (Pelletier & Swetnam, 2017; Yetemen et al., 2015b) and associated vegetation patterns (eg., McGuire et al., 2014; Yetemen et al., 2015b).

Hillslope asymmetry emerges across many scales. For example, in a study across the whole of American cordillera, Poulos et al. (2012) found a systematic distribution of hillslope asymmetry with latitude in both hemispheres. This pattern was successfully replicated in a landscape evolution modelling experiment by Yetemen et al. (2015a), only by varying daily incoming net radiation patterns with latitude. At smaller scales, microclimatic-driven hillslope asymmetry has been studied in semi-arid to sub-humid basins (Istanbulluoglu et al., 2008; Yetemen et al., 2010), in cinder cone fields (eg., McGuire et al., 2014), and across

mountain ranges (eg., Dohrenwend, 1978). Asymmetry in temperate forested regions has been largely unexplored.

Landform and vegetation can be tightly coupled (eg., Dietrich & Perron, 2006). Vegetation reflects climatic conditions at large (eg., Tesemma et al., 2014), intermediate and small (eg., Nyman et al., 2014b) scales. Since vegetation cover has a strong effect on soil erosion (Istanbulluoglu et al., 2004; Istanbulluoglu & Bras, 2005) and soil development (eg., Amundson et al., 2015), local variations in microclimatic conditions often result in differential erosion processes and soil depths (eg., West et al., 2014). At the scale of a single ridgeline, these differences can result in soil depth asymmetry on opposing slopes (eg., Lybrand & Rasmussen, 2015; West et al., 2014), which leads to asymmetric slopes over geological timescales.

Here it is argued that in complex mountainous regions where precipitation and insolation vary dramatically at short spatial scales in response to aspect and elevation, the magnitude of asymmetry in both soil depth and hillslope gradient will also vary. The Eastern Uplands in south eastern Australia offer an outstanding opportunity to study the effect of climate on the development of hillslope asymmetry within a relatively uniform latitude. This fire-prone, forested, post-orogenic landscape, is unaffected by glaciation, had limited anthropogenic interference, and hosts relatively large climatic gradients across relative small spatial scales where lithology and orogeny are non-variable. The area currently hosts a wide range of Eucalyptus dominated forest types, ranging from temperate rainforests to open woodlands, which vary dramatically in structure largely as a function of climate, topography and fire regime. Studies in this region have shown that geomorphic processes, and in particular post-fire erosion, are highly sensitive to the local moisture regime, with regional variation in rainfall and local variation in solar radiation both acting to produce contrasting erosion responses to wildfire (Noske et al., 2016; Nyman et al., 2015b; Sheridan et al., 2016). In addition the large differences in vegetation that emerge from variable radiation and rainfall has large implications for fuel moisture and fire regimes (Bradstock, 2010; Nyman et al., 2015a). While topographic-related variation in these processes are likely to promote asymmetric hillslopes, it is unclear if the current landscape shows any evidence of asymmetry that corresponds with observed contemporary processes.

In this chapter, I test the hypothesis that (1) north-south asymmetry in SE Australia develops in response to radiative forcing in accordance with what has been documented elsewhere, and

(2) the magnitude of asymmetry depends on climate. These hypotheses are tested by quantifying patterns of asymmetry in both soil depth and landform in the dissected landscape of the Eastern Uplands across an aridity gradient.

2.3 Materials and Methods

2.3.1 Regional description

The Eastern Uplands (Figure 1-1*a*) are a part of the Great Dividing Range, a belt of ridges, plateaus and corridors in south eastern Australia, with elevations varying from 200 to 2000 m ASL. The range consists mainly of Palaeozoic marine sedimentary (mudstone, shale and sandstone), fluvial sedimentary and metamorphic rocks, and some acid plutonic outcrops (granite and granodiorite) which appear in patches throughout the region. The peak in uplift was in late Cainozoic, and currently occurs at very low rates (Wellman, 1987). Annual variability in temperature and rainfall are large due to Southern Annular Mode (SAM), ENSO (El Niño-Southern Oscillation) and positive Indian Ocean Dipole (pIOD) events. Victoria has a temperate climate with mild summers, and cool, wet winters (Stern et al., 2000). Mean annual precipitation (MAP) range from 600 to 2500 mm and mean annual temperatures range from 25.8 to 17.6 in summer and 13.4 and -1.1 in winter, for low and high elevations, respectively. There is no evidence for glaciation during last glacial maxima (LGM; 17-13.5ka BP) in the study area. During LGM, most of the Uplands was treeless and limited to herbal alpine communities. This was slowly replaced by rainforest and tall and open forest taxa as climate became warmer and effective precipitation increased (~6ka BP; (McKenzie, 1997, 2002)). Fire activity was found to increase with temperature and biomass, with fire-tolerant sclerophyll species increasingly replacing fire intolerant rainforests (Lynch et al., 2007).

Current vegetation in the region is classified based on Specht and Wood, (1972): Under higher rainfall conditions (MAP > 1200 mm), vegetation is dominated by tall closed forest combined with dense understory, often occupying sheltered valleys and/or on the south facing aspects. On higher elevations (>2000 m ASL), vegetation shifts towards alpine open type forest. Under drier conditions, (MAP of 600-800 mm) and moderate elevations (500-600 m ASL) vegetation is dominated by dry open forests consisting of various mixed-species Eucalyptus communities with sparse understory.

The moisture regime across the region has been mapped using annual Aridity Index (AI), which can be regarded as a proxy for water availability using: $AI = {}^{E_P}/_{\overline{P}}$, where E_P [mm/yr] is potential evapotranspiration; and $\overline{P}$ is mean annual precipitation [mm/yr]. Asymmetry was first investigated with respect to AI using three focus-sites located in the Early-Devonian Norton Gully Sandstone (NGS) formation, which consists of variable (although mostly vertical) bedded strata of marine sedimentary rocks, that mainly include relatively thick strata of sandstone (with some siltstone and claystone layers). The three focus sites, referred to here as "Wet" (MAP~1660 mm), "Damp" (MAP~1288 mm) and "Dry" (MAP~942 mm) were chosen for in-depth analysis of asymmetry (Table 2-1). A regional analysis of hillslope asymmetry was carried out using elevation data from the entire Eastern Upland domain. Mean AI values ($\overline{AI}$) for each of the focus sites were calculated from a downscaled (i.e., 20 m) raster based on regional extrapolated climatic data (see Nyman et al., 2014b for details and sources), and are detailed in Table 2-1.

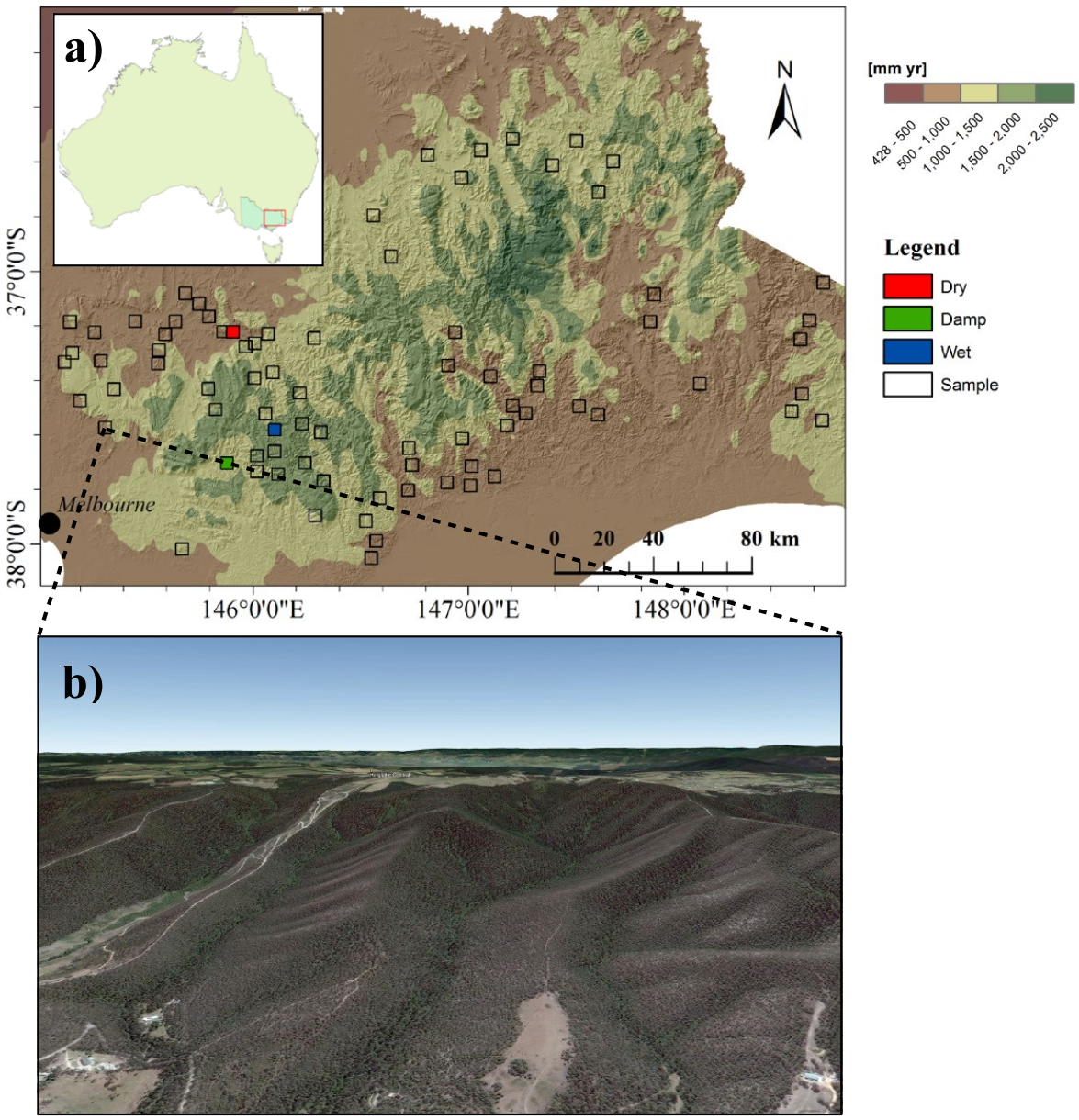

Figure 2-1 - Mean Annual Precipitation covering a Hillshade of the Eastern Uplands (a) with the 81 5x5 km sample areas within the domain; Coloured polygons designate locations where S-A curves were compiled for Figure 2-2; and (b) an example of hillslope asymmetry at a catchment near King Lake, Victoria (MAP 1000-1400 mm/yr; 37°31'48.39"S 145°18'51.30"E). Image by © DigitalGlobe, 2017, obtained from © Google Earth™.

Table 2-1 - Site Characteristics.

	Aspect	Mean MAP	Mean Elevation	Mean Daily Net Radiation [a]	$\overline{AI}$	Mean gradient	mean soil depth	HAI	SAI
		mm	m	MJ/m^2/day			m		
Wet	S	1660	811	11.5	0.71	0.57	1.17	1.03	1.32
	N			16.9	0.96	0.56	0.88		
Damp	S	1288	449	11.2	1.30	0.45	1.14	1.13	2.2
	N			16.5	1.01	0.40	0.52		
Dry	S	942	390	10.5	1.43	0.35	0.50	1.16[b]	1.77
	N			16.0	1.76	0.30	0.28		

[a] Data from downscaled net radiation layer (Nyman et al., 2014b)

[b] Adjusted according to LiDAR values (Appendix I , section I.2)

2.3.2 Asymmetry Calculations

Slope-Area curves

Slope area (S-A) curves are landscape descriptors that describe how gradient changes with the increase in contributing area (eg., Willgoose et al., 1991b). By analyzing such plots one can observe distinct hydrologically functional drainage components, which sheds light on the governing processes in catchment evolution (Istanbulluoglu et al., 2008; Yetemen et al., 2010). The peak of the S-A plots (inflection point) represent the average area in which convex hillslopes transition into concave channels and valleys and indicates a transition between diffusive hillslope processes and convective fluvial ones (Chadwick et al., 2013; Istanbulluoglu et al., 2008; Willgoose et al., 1991b; Yetemen et al., 2010). Using this distinction, the areas below the inflection point can be regarded as the proxy for average hillslope length in the area (Grieve et al., 2016). Using a 5x5 km 10m digital elevation model (DEM) from each of the three focus areas, S-A plots were generated using D8 'gradient' and 'contributing area' products of Topotoolbox2 package (Schwanghart & Scherler, 2014) for MATLAB (MathWorks®, USA). Median of gradient values for all the pixels within evenly spaced contributing area bins, are plotted within a log-linear space. For each area hillslope asymmetry was derived by binning slope and area pixels into north and south aspects, with north and south facing hillslope bins including aspects from 270^o-90^o and 90^o-270^o, respectively.

Quantifying soil depth asymmetry

Asymmetry in soil depth was quantified by field measurements along contour lines on representative south and north facing hillslopes at each of the three focus sites. Depth measurements were obtained by hand auger, motorized auger, and rod penetration apparatus (until refusal point); road cutting surveys (when available) and soil pits. Altogether, total of 212 depth measurements were used, split per site and aspect and averaged for contributing areas < 0.01 km^2, thus ensuring that data was obtained within the hillslope and not in convergent or channelized domain. This cut-off area was roughly estimated by the mean area at the inflection point according to the S-A plots (eg., Chadwick et al., 2013).

Mean of measured soil depth from each aspect (Table 2-1) were used to calculate the soil depth asymmetry index (SAI) by: $\mathrm{SAI} = \overline{\mathrm{H_S}}/\overline{\mathrm{H_N}}$, where $\overline{\mathrm{H_S}}$ and $\overline{\mathrm{H_N}}$ are mean soil depth [m] of the south and north facing hillslopes, respectively. SAI represents the direction and magnitude of the asymmetry in soil depth, where $\mathrm{SAI} = 1$ indicates no soil depth asymmetry, SAI >1 when mean depth on the south facing slopes are deeper than the north facing ones, and vice versa.

A continuous metric of expected SAI across the climatic domain were obtained by fitting a function describing the change in observed soil depth with AI:

$$\overline{\mathrm{H}} = \frac{1}{1 + \exp^{-4.77\,(\mathrm{AI}-1.14)}} + 0.29 \qquad (2.1)$$

where $\overline{\mathrm{H}}$ is mean soil depth [m]. A sigmoid model represented the best fit to measured data with $R^2 = 0.93$ (compared to $R^2 = 0.88$ for linear fit). The continuous metric of expected SAI was calculated using Eqn. 2.1 and simple functions that reflects the change in AI of south and north facing aspects with change in mean AI of sampled 5x5 km areas across the domain (details in section Appendix I I.2).

Quantifying hillslope asymmetry

Hillslope asymmetry index (HAI) was quantified using the same approach as the SAI, for the purpose of quantifying the direction and magnitude of hillslope asymmetry (i.e., how steeper

is one hillslope compered to its counterpart). I define $HAI = G_S/G_N$, where (G_N) and (G_S) are median gradient of north and south facing hillslopes, respectively. As for the soil metric, $HAI > 1$ indicates that the south facing hillslopes are steeper than the north facing ones, and vice versa. The index resembles a metric suggested by *Poulos et al.* (2012), who used a logarithm of the HAI, in that it captures the direction of the asymmetry. The authors used the metric to visualize hillslope asymmetry reversal with latitude by changing its sign.

HAI was calculated for 81 sampled 5x5 km areas across the Eastern Uplands varying in geology and mean AI (Figure 1-1a). For each sampled area, median gradient was calculated for south and north facing hillslopes bins using a 10m DEM. The quality of the DEM used for this analysis is discussed in Appendix I . Due to the complex terrain of the Uplands, locations were hand-picked using ArcGIS 10.3 and Google EarthTM, sampled from AI categories. The selected sites were tested under the following criteria: (i) mostly forested; (ii) dissected and relatively steep (iii) contains similar proportion of hillslope facing all aspects (in 45^o bins); (iv) include most east-west facing ridges; and (v) not containing any escarpment-type geological structures. For each location, mean AI was calculated using a 20m downscaled AI raster (Nyman et al., 2014b) using MATLAB (MathWorks®, USA). To constrain the analysis to hillslopes close to the ridgeline, all pixels with slopes lower than 5^o and with areas higher than 0.1 km2 were removed from the calculation.

2.4 Results

In general, median gradient decreases with MAP (Figure 2-2), with maximum of 0.4 and 0.6 for south facing hillslopes at the dry and wet sites, respectively. Judging from the area at the inflection point, hillslopes are the longest on the wet and damp sites (Figure 2-2). South facing hillslopes are consistently steeper for a given contributing area than north facing ones, however the difference between the aspects is the lowest in the wet site (Figure 2-2). Note that the form of the S-A plot of the north (south) facing pixels in the damp site, resembles both aspects of the dry (wet) site, which might indicate a process shift between the two aspects at the damp site. Here the effect of climate on landform is highlighted, as sites share similar lithology and only vary with MAP.

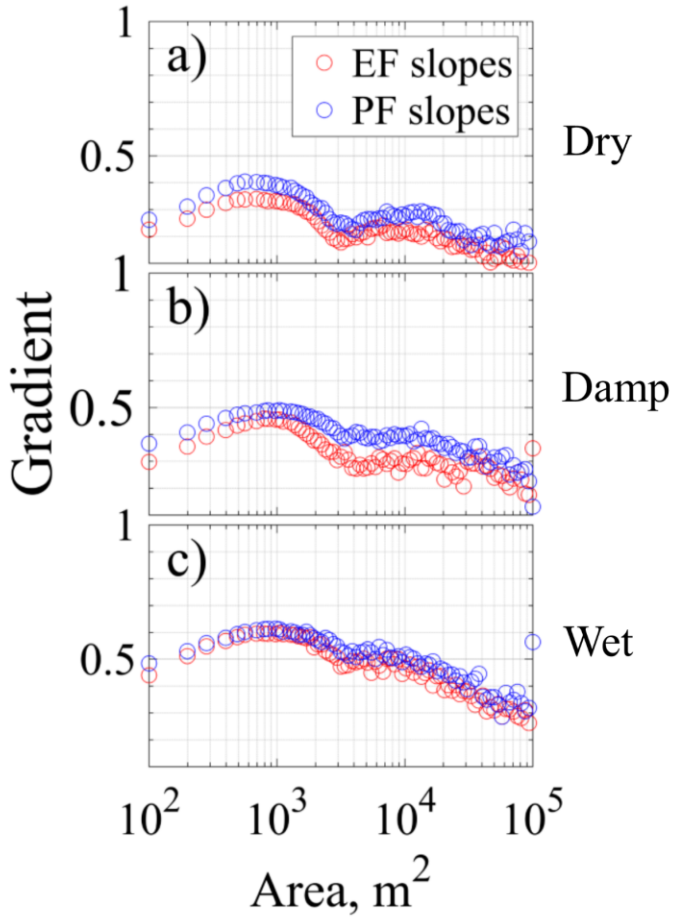

Figure 2-2 - S-A curves for the dry (a), damp (b), and wet (c) focus sites. Note that in this analysis two types of DEM sources were used (Appendix I).

Mean soil depth have range from 1.17-0.28 m. There is a nonlinear decrease with AI, with the highest rate of change in soil depth occurring between an AI of 0.9-1.5 (Figure 2-3*a*). The measured asymmetry in soil depth is highest at the damp site and lowest at the wet (Figure 2-3b). Expected and observed SAI values (based on Eqn. 2.1) peak at mid-AI values (Figure 2-3b). Despite the natural variations in HAI, south facing hillslopes are persistently steeper across the domain, crossing geological configuration and lithology type (Figure 2-3c). Interestingly, the magnitude of HAI increases with AI, peaks at between values of 1.5-2, after which it decreases to lower values.

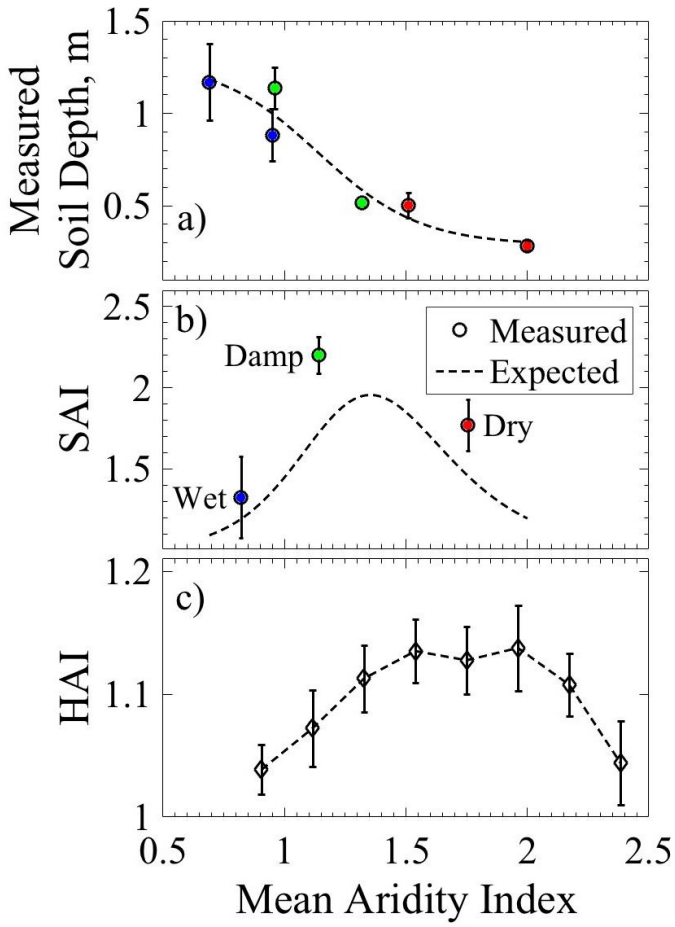

Figure 2-3 - (a) means of measured soil depths at the wet (blue) damp (green) and dry (red) sites as a function of mean AI (Table 2-1); (b) Soil depth asymmetry index (SAI) plotted on the AI scale. Dashed line indicate the "expected" SAI across the domain (Appendix I); and (c) Means of Hillslope asymmetry Index (HAI) values binned by AI classes. Original data ranged across 81 5x5 km polygons in various locations in the Victorian highlands. In all plots, error bars represent standard error.

2.5 Discussion

Several studies have shown that whether due to higher MAP with increasing elevation or lower insolation due to aspect, wetter hillslopes were steeper than drier ones. This was ascribed to lower erodibility, possibly due to denser vegetation (Istanbulluoglu et al., 2008; Yetemen et al., 2010). Our results show that in the Eastern Uplands south facing hillslopes are consistently steeper than the north facing ones, both on top of similar (Figure 1-2) and

different parent material (eg., HAI>1 across the AI gradient; Figure 2-3c). The fact that this pattern persists across a variety of geological structures, points to climate, and solar radiation in particular, as being the highest probable driver on hillslope asymmetry (Pelletier & Swetnam, 2017; Poulos et al., 2012; Yetemen et al., 2015b). The southernmost part of SE Australia lies close to the lower latitude where Poulos et al., (2012) found a reversal in hillslope asymmetry in the southern hemisphere. This implies that hillslope asymmetry might be influenced by local factors and less so as global phenomenon. Across the areas covered by this study, south facing hillslopes were on average 8.6% steeper than north facing ones, with a maximum of 15% difference in mid-AI values. The variability of HAI values in our data shows that the magnitude of hillslope asymmetry is not equal across the domain. Figure 2-2 shows a pattern in the difference between the gradient of south and north facing hillslopes with MAP. Across all geological structures a "hump" pattern emerges with contemporary climatic conditions (Figure 2-3c), emphasizing the long-term role of climate on landscape evolution.

Hillslope evolution is driven by the balance between processes that convert bedrock to transportable material and those that transport it downslope. Thus, current soil depth patterns show a snapshot in hillslope evolution and the governing processes that shape it. The decrease in mean soil depth with AI (Figure 2-3a) supports findings by Lybrand et al. (2011) who reported an increase in soil depth measurements with elevation, a proxy for rainfall and temperature (and thus AI), at the Sky Islands, Arizona. The general decrease in soil depth with AI (Figure 2-3a) despite the overall reduction in median slope (Figure 2-2) emphasizes the role of climate as a primary driver in the evolution of soil depth and landform across the domain. Although logical, to our knowledge, a sigmoidal relationship between soil depth and AI has not previously been identified. However, similar pattern have been found for forest LAI at the study area (Figure 4i in Tesemma et al., 2014) which might suggest a connection between the ecohydrology to the geomorphology in the coevolution of catchments in the studied area.

On the ridge scale, where geology is similar across aspects, differences in soil depth highlight the effect of microclimate (eg., Anderson et al., 2013) and vegetation (Amundson et al., 2015) in recent pedo-morphic timescales. It is postulated that the thinner soils on equatorial (north) facing hillslopes as reported in this study (Figure 2-3b), and consistent to others (eg. Dohrenwend, 1978; West et al., 2014), are more erodible and have lower residence time then polar (south) facing slope. Using an exponential soil production function (see Heimsath et al.,

1997) with mean measured soil depths (Table 2-1), and assuming that the current soil depth is in steady state (i.e., soil production equals erosion), the difference in the rate of soil production between aspects is the highest in the damp site, where soil is produced 3.46 times faster on the north facing hillslope.

A possible explanation for the SAI differences across our domain (Figure 2-3b) is that differences in water availability affect forest cover (see Figure 4i in Tesemma et al., 2014), which in turn causes differences in geomorphic processes between the aspects. Despite the steep slopes (Figure 2-2c), the forest on both aspects of the wet site is not limited by water (Table 2-1), which results in a uniformly high forest cover (Figure A- I-3a). At the dry, both aspects are water limited, and although some differences in vegetation density are seen, forest is mostly sparse (Figure A- I-3c). In contrast, ridges at the mid-AI value (damp) site are close to the *Budyko's* water-limited energy-limited boundary (Table 2-1; (Budyko, 1974)), resulting in a substantial contrast in forest cover between the aspects (Figure A- I-3b). Forest cover influences the relative importance of fluvial and diffusive erosion processes (eg., Istanbulluoglu et al., 2004), so it is possible that at these mid AI-value (damp) sites the opposing aspects are dominated by very different erosion processes, operating at different rates, resulting in large differences in soil depth, which in long timescales may affect hillslope asymmetry (Figure 2-2).

Fire may also play a role in asymmetry. In SE Australia, current fire frequency-severity combination vary across the landscape as a function of climatic conditions, controlled by weather patterns (Mariani et al., 2016; Mariani & Fletcher, 2016), and fuel load and moisture (Bradstock, 2010; Nyman et al., 2015a). Recent studies in the Eastern Uplands had shown a strong positive relationship between AI and post-fire runoff rates (Sheridan et al., 2016), soil erosion (Noske et al., 2016) and debris-flows (Nyman et al., 2015b). These climate driven variations in fire regime and post-fire hydro-geomorphic processes have the potential to influence soil depth and hillslope asymmetry by differential erosion rates across the landscape.

Overall, the documented patterns of asymmetry point to a strong effect of climate on soil development and landscape evolution. Asymmetry in both landform and soil is most pronounced near the water-limited boundary, where vegetation cover changes most rapidly with aridity (Tesemma et al., 2014). This result, whereby soil depth and hillslope asymmetry peak at similar AI (Figure 2-3b and 3c), is somewhat surprising considering the oscillation of

climate during the Quaternary (eg., Petit et al., 1999) and the different timescales at which soil profiles and hillslopes are shaped. From these results (Figure 2-3b and 3c), is it plausible to postulate that the short-term erosion rates are a good approximation of the long-term ones? Or are the similar AI values for these asymmetry peaks for soil and landform just a coincidence? Vegetation patterns were vastly different to the current (McKenzie, 1997, 2002) during the LGM, thus it is unlikely that vegetation contrasts across north-south hillslopes were associated with the distinct fire and/or erosion responses that have been observed across AI gradients in the current climate. The reasons for the observed similarity in the peaks in SAI and HAI at similar AI (Figure 2-3b and 2-3c) are the subject of further investigation.

Clearly, more work is needed to determine the exact mechanism underlying the asymmetry in this SE Australian landscape. With cosmogenic and radio-nuclides there may be opportunities to obtain the long and short term rates of hillslope erosion (Dosseto & Schaller, 2016) and how this varies with aspect across the domain. This would provide some insights into whether current patterns of asymmetry correspond with differences in denudation that one would expect to see. In the contemporary climate the role of fire and vegetation on the development of asymmetry can be explored with coupled eco-geomorphic models (eg., Yetemen et al., 2015b). The large body of research on erosion processes in this region (eg., Lane et al., 2006; Noske et al., 2016; Nyman et al., 2011; Sheridan et al., 2007) would facilitate the development of such models.

2.6 Conclusions

This study investigated the hypotheses that a) soil depth and hillslope gradient are north-south asymmetric, and b) that the magnitude of this asymmetry varies systematically with climate. The results supported the hypotheses; soils were deeper, and hillslopes steeper on the south facing slopes compared to the north facing ones. The magnitude of asymmetry both in soil depth and gradient peaked at the water-limitation boundary. This highlights the effect of climate on the magnitude of asymmetry in both soil and landform, and the possible role of vegetation in controlling geomorphic processes.

The observed patterns in this chapter provides evidence of climatic-driven long-term coevolution process, printed across soils and landscapes. The exact mechanisms and

importance of coevolution to the emergence of patterns of soil depth and landform across the landscape is unclear. However, based on contemporary research, it seems that climate, fire and ecohydrological feedbacks may be important. The role of fire in particular may be dominant due to its effect on erosion processes. Using theoretical models of coevolution may provide a useful avenue for evaluating in more detail how ecohydrology, geomorphology and fire interacts in the coevolution of the critical zone, and how they contribute to the development of current patterns of soil and landform.

3 A model for evaluating the role of fire on coevolution of the critical zone in SE Australia

3.1 Abstract

The interactions between patterns of asymmetry and climate suggest that the landscape in SE AU is product of coevolution of vegetation, soil and topography. Coevolution is a complex non-linear process that spans over multiple temporal and spatial scales. Progress in understanding of such a complex process can be achieved by a combination of observations, measurements and biophysical models that bridge multiple short-term processes and simulate them over longer timescales. The objective of this chapter is to describe a newly developed numerical model that was developed in order: (i) to test the hypothesis that fire related processes and feedbacks are critical to explain observed patterns and magnitude in system states across the landscape, and that their effect of on coevolution increases with aridity; then, given the hypothesis is true, (ii) to evaluate the role of fire related mechanisms in coevolution. The model was designed and formulated to simulate processes typical to SE Australian systems. The one-dimensional model tracks the evolution of soil depth, standing biomass and water availability under continuous rainfall and energy fluxes typical to SE Australia. Ecohydrological processes that maintain the forest structure and net primary productivity are modelled, together with stochastic fire that depend soil moisture deficit. Soil depth is controlled by soil production and erosion, which depend on forest cover and soil surface properties that vary depending on fire and climate. The model was parameterised with data from literature, field experiments and from site attributes at specific points in the landscape that represent different climate regimes. Evaluation of model output showed strong correspondence with predictions of hydrological partitioning based on the Budyko framework (Budyko, 1974). Furthermore, the partitioning of rainfall into evapotranspiration (ET), interception loss, soil evaporation and transpiration is consistent with values measured locally in previous studies. Fire regimes, modelled as a function of soil moisture deficit, yield a Weibull type distribution, similar to other fire frequency models. Modelled vegetation recovery trajectories predict reasonable time-to-recovery of leaf area index (*LAI*) and structural biomass across different forest types and recovery strategy compared to literature values. The model predicts similar trends in runoff ratio and peak discharge after fire across an aridity gradient, however, possibly underestimates runoff ratio values at wetter sites compared to literature values. Finally, post fire and background erosion rates compared

reasonably well with the limited literature values, especially in dry sites. Based on the success of the model at replicating the observed hydrologic, geomorphic, and fire frequency patterns, it is concluded that the model provides a robust, transparent, and defendable method to evaluate the role of fire in the coevolution of the critical zone.

3.2 Introduction

3.2.1 Previous work on modelling Coevolution of the critical zone.

Coevolution is often explored using models due to its complexity, crossing spatio-temporal scales and disciplines. Studies that use models explicitly designed to answer questions in the coevolution of vegetation, soils and landscapes are rare (Pelletier et al., 2013). However, many studies used models that had been designed to examine different aspects of coevolution, and can be regarded as such. Some examples are cellular automata (Caracciolo et al., 2014; Dunkerley, 1997; van Wijk & Rodriguez-Iturbe, 2002; Zhou et al., 2013), landscape evolution (Istanbulluoglu et al., 2004; Istanbulluoglu & Bras, 2005; Tucker et al., 2001; Willgoose et al., 1991b), and soil-profile development (Cohen et al., 2010; Temme & Vanwalleghem, 2016) models. Furthermore, these models are used to look at unique processes and interaction in coevolution, such as the effect of vegetation-erosion interactions on landscape evolution (Collins et al., 2004; Istanbulluoglu et al., 2004; Istanbulluoglu & Bras, 2005; Tucker et al., 1999), effect of climate-topography interactions on vegetation structure (Brolsma & Bierkens, 2007; Zhou et al., 2013) and landscape development (Yetemen et al., 2015b), effects of climate on soil development (Cohen et al., 2013), and many more.

Most landscape evolution models can be considered as coevolution models. However, in most cases, the effect of climate on vegetation, and the effect of vegetation on geomorphic processes are lumped inside empirically-calibrated coefficients (Dietrich et al., 2003). In some cases, simulating components such as vegetation and soil might be unnecessary for the main purpose of studying landscape development. Vegetation and soil are incorporated into landscape evolution models whenever a model's purpose is to looks into specific effects of vegetation on soil or landscape development. For example, Pelletier et al. (2013) developed a coupled-system landscape evolution model in order to study the observed patterns in soil, vegetation and landform across the sky islands of southern Arizona, USA. The model

simulated eco-pedo-geomorphic feedbacks across a climate and elevation gradient. Their results showed that the model *self organized* into observed trends only by coupling soil production and topographic development, which depend on vegetation density, and without explicitly modelling ecohydrological processes driving the development of the vegetation itself. In their exercise, the effect of vegetation is implicitly modelled by relating a semi-empirical climatic index, Effective-Energy and Mass Transfer (EEMT) to coefficients responsible for soil production and landscape development. The authors underscored the importance of including soil depth balance to landscape evolution models as it mediates the feedbacks among vegetation, soils and topography.

In another study, Tucker and bras (1999) looked into the effect of the dynamic of vegetation on erosion in the long-term geomorphic processes and landscape morphology. In this case the authors incorporated the relationship between vegetation cover and critical shear stress and the effect of runoff on the vegetation dynamics in their landscape evolution model. Collins et al. (2004) studied the feedback between of riparian vegetation and geomorphic dynamics on landscape evolution on a semi-arid hypothetical landscape. Here, other than the resistance to erosion, plant growth and decay is incorporated in order to model vegetation colonisation. The authors found that plants steepen the landscape and reduced drainage density (Collins et al., 2004). Plant growth in this model was achieved by a simple mathematical growth model, without modelling ecohydrology and productivity. Moreover, the model did not include soil depth and its possible effect on plant available water (PAW) and vegetation carrying capacity (Meyer et al., 2007).

Recent work show that incorporating ecohydrology and dynamic vegetation contribute to studying the effects of climatic conditions on geomorphic processes and landscape evolution (Istanbulluoglu & Bras, 2006; Yetemen et al., 2015b), and even global landscape morphology patterns (Yetemen et al., 2015a). Yetemen et al. (2015b) studied the effect of solar radiation on landscape evolution. The authors added a combination of ecohydrological and biomass balance components on an existing landscape evolution model (Tucker et al., 2001), both directly affected by the uneven distribution of daily solar radiation across the landscape. Their model emphasised the effect of solar radiation on controlling water availability, vegetation patterns, erosion processes and landform in semi-arid ecosystems. Their model uses grass for simplicity. By using grass, effective soil depth was considered to be the depth of the root zone (i.e., 10-20cm deep), and soil depth was not assumed as a limit for water holding capacity (Istanbulluoglu & Bras, 2006; Yetemen et al., 2015b), in contrast to forest

ecosystems. Temperate forests, are more complex, and models including coupled ecohydrological-geomorphological processes in the coevolution of these type of systems are absent from the relevant literature.

A key feature of the forest ecosystem is wildfire, which has been considered to be a significant geomorphological agent (Shakesby & Doerr, 2006). As such, the different effects of fire on short term hydro-geomorphic response have been widely studied (eg., Moody & Martin, 2001b; Nyman et al., 2011; Prosser & Williams, 1998; Sheridan et al., 2007), however, only a handful looked at its long term effects, either on sediment yield from burnt hillslopes and channels (Benda & Dunne, 1997; Gabet & Dunne, 2003) or on landscape evolution (Istanbulluoglu et al., 2004; Istanbulluoglu & Bras, 2005). In these studies, fire was designed to be a decoupled stochastic event, which eliminated the vegetation and changed soil properties, with potential to trigger geomorphic events. Fire depends both on large-scale climatic drivers (eg., Mariani et al., 2016), but also on the hydrological states of systems (Nyman et al., 2015a; Taufik et al., 2017), making it a dynamic process rather than a decoupled stochastic disturbance. Despite the fact that fire affects biological, ecological, hydrological and geomorphological processes, its role within the coevolution of the critical zone has been largely unexplored.

The SE Australian uplands are home to various types of forest, ranging from open dry sclerophyll woodlands to temperate rainforests. These forests vary in their flammability, fire frequency and post fire hydrologic response, making the SE Australian uplands an excellent natural laboratory to study the role of fire in coevolution. The aim of this chapter is: (i) to test the hypotheses that fire related processes and feedbacks are critical to explain observed patterns and magnitude in system states across the landscape, and that their effect of on coevolution increases with aridity; then, given the hypothesis is true, (ii) to evaluate the role of fire related mechanisms in coevolution. The chapter will include a conceptual model definition, a detailed model description and a model evaluation.

3.2.2 Model design criteria

Unique set of criteria are required in order to model SE Australian systems:

- The different coupled soil-vegetation systems coevolve under different climatic forcings. A model representing those systems would need to be able to simulate the coevolution of

these coupled systems under different forcings (without fire). The model should include ecohydrological driven biomass production and processes that control soil depth.

- Since forest types are characterised by distinct fire regimes (Cheal, 2010), and flammability is highly dependent on fuel load (Pausas & Paula, 2012) and moisture status of the system (Keetch & Byram, 1968; Nyman et al., 2015a; Walsh et al., 2017), the modelled system should be able to simulate flammability depending on its hydrological state.

- For the model to simulate these systems, it should be able to express fire-related ecological and geomorphological processes typical to SE Australian systems. Typically, the model should be able to simulate different fire adaptation and recovery strategies of the local forests, and the local nature of post fire hydro-geomorphic response, which tend to vary with aridity (Noske et al., 2016; Sheridan et al., 2016).

- Before being used, specific model outputs should be evaluated using data, literature and expert knowledge in order to make sure it appropriately simulates local systems and thus to be able to represent critical zone units typical to SE Australia.

3.2.3 General conceptual model of coevolution

Figure 3-1 illustrates the general high level conceptual model that describes how the critical zone system evolves across different timescales. The coupled system consists of soil and vegetation, both of which have the ability to change under different conditions. Fluxes of water, energy and carbon are partitioned and flow through the system, forcing small changes to each of the system components. For example, rainfall, energy and soil depth determine the water availability, controlling establishment of vegetation physiologically adapted to cope with available resources. Vegetation, in turn, can directly and indirectly influence its surroundings through biotic processes that changes soil properties (eg. water retention, infiltration etc.), and ultimately its ability to store water. Such biotic processes vary and can be as simple as an addition of soil organic matter and can accumulate to bio-geomorphic effects on soil depth. Processes such as fire makes changes across all systems components and, if repeated in a faster frequency than its "normal" capacity, can push the system into different coevolution trajectory through feedbacks that affect its frequency.

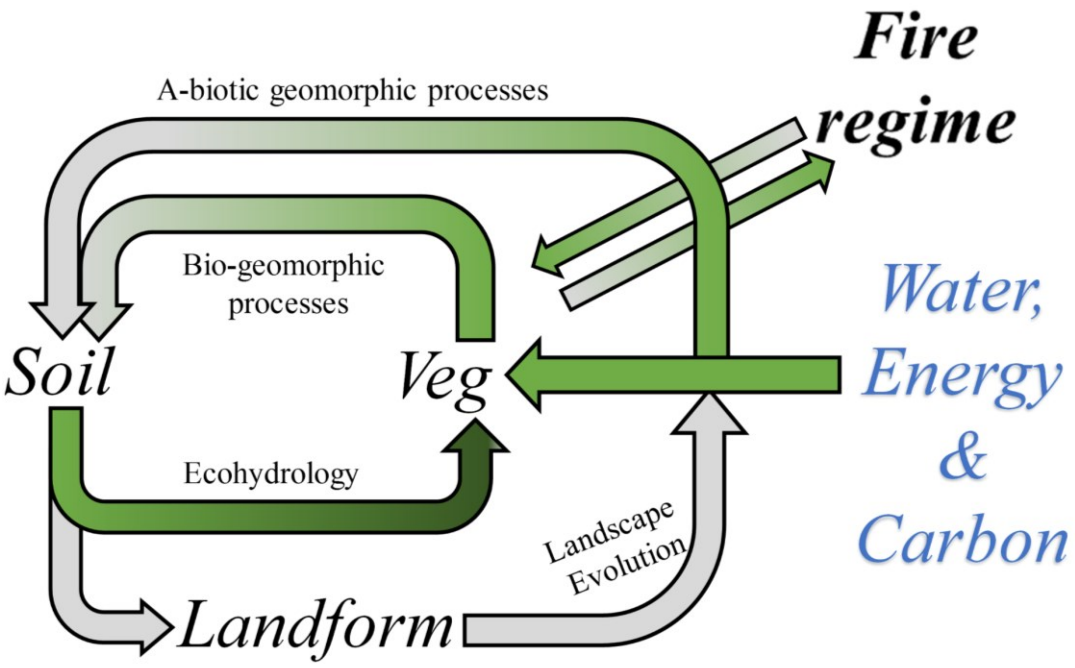

Figure 3-1 - Schematic representation of a conceptual model that describes the coevolution of the coupled soil-vegetation system.

3.2.4 Time and Space - Conceptual 1D point model

A 1D model was developed, which incorporates the important processes in the coevolution of the critical zone in forested uplands in SE Australia, and which explicitly includes fire as a process. Since coevolution spans over long timescales, the model runs in daily time-steps up to several hundreds of thousand years, assuming changes in slope are negligible, allowing vegetation and soil to coevolve and drainage position to stay constant. The short timescales and the fact that Australia is regarded tectonically stable (Bishop, 1985), it is assumed that change in elevation (dZ/dt, where Z is elevation [L] and t is time [T]) is negligible and is disregarded by this model.

The 1D model simulates the evolution of a hypothetical point in space with soil and vegetation, located 50 m from the ridgetop. This drainage position was chosen in order to avoid more complex erosion-deposition balance and substantial water subsidies further down in the convergent zone, while still maintaining the potential effect of topographic aspect on the energy balance. For simplicity, inflow of subsurface water from the ridge-top is assumed negligible.

3.2.5 General modelling approach

A schematic description of the inputs and outputs of energy and matter, and the processes that control their partitioning across reservoirs through the modelled system is presented in Figure 3-2. The model runs on daily time-steps between rainstorms, and on an hourly basis within rainstorm cells, and track changes in soil depth and biomass. It uses stochastically generated rainfall that fills water reservoirs in the modelled system, erodes soil and play a role in net primary productivity (i.e., conversion of radiative energy into biomass), which in turn controls the partitioning of rainfall and energy fluxes as they pass through the system. The model includes a stochastic wildfire component linked to soil moisture deficit. Stochastic wildfire burns the vegetation, temporarily changing soil hydrological and physical properties, and the partitioning of rainfall and energy. Furthermore, the model simulates the hydrological response of the system to fire (i.e., change in vegetation cover, infiltration capacity, soil erodibility etc.) which had been shown to depend on climate (Langhans et al., 2016a; Nyman et al., 2014a; Sheridan et al., 2016).

The model was inspired by eco-hydro-geomorphic models such as that presented in Yetemen et al. (2015b) (and the models that were used and inspired their work), and others (eg., Istanbulluoglu & Bras, 2006; Pelletier et al., 2013; Zhou et al., 2013), and uses interlinked Ecohydrological, Geomorphic and Biomass balance processes under climatic forcing to drive coevolution, by numerically solving continuity equations for the four state variables that tracks changes in soil depth, soil moisture, biomass and canopy water stores in every time-step.

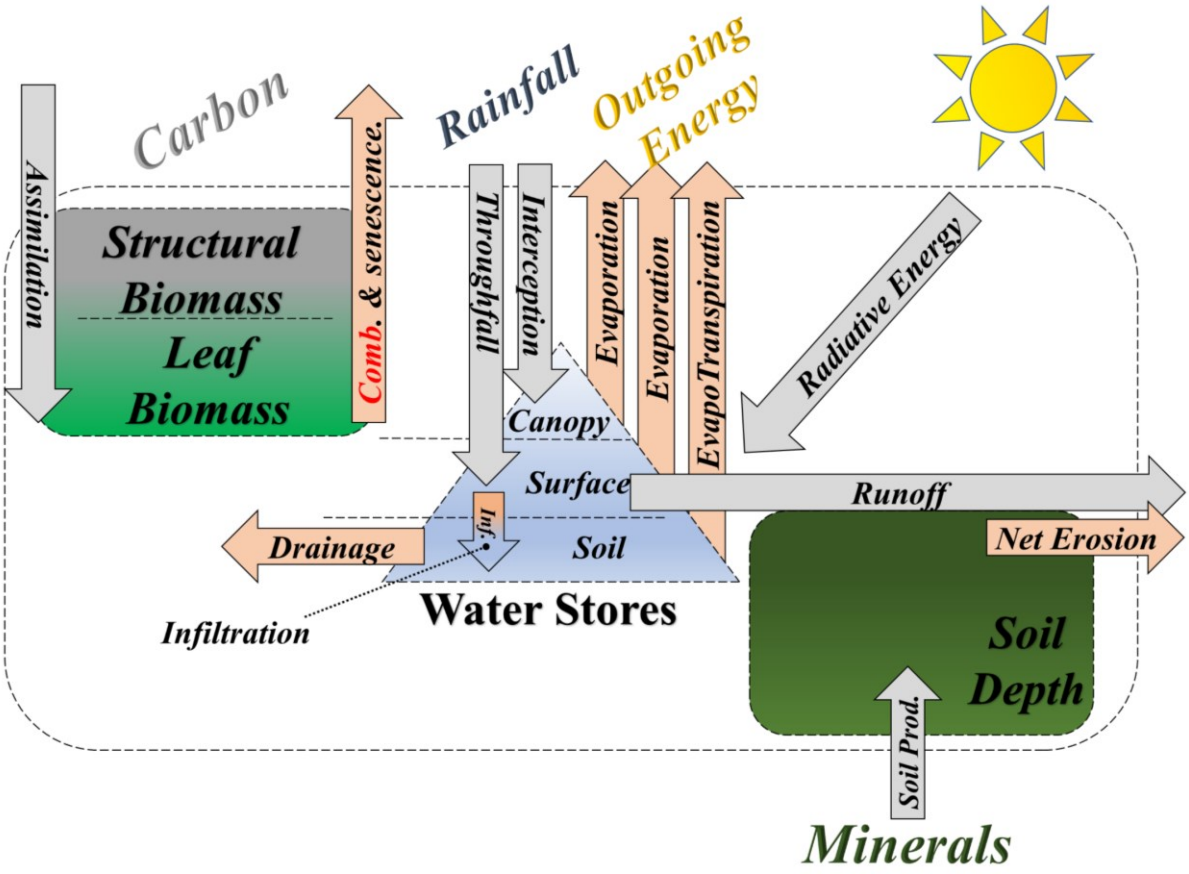

Figure 3-2 –Schematic description of the inputs and outputs of energy and mass, and the processes that control their partitioning across reservoirs through the modelled system. Rainfall enters the system and fills water reservoirs in the soil and canopy. Net radiation evaporates some of that water and drive the assimilation of carbon through photosynthesis. Carbon exit the system by decomposition and combustion (fire), which also releases stored energy. Soil can be eroded by gravity and by the shear power of water that doesn't infiltrate.

3.2.6 State Variables in the model

Soil Depth

Soil depth, clay and organic matter content and porosity affect the water holding capacity of the soil (Klute et al., 1986), which control plant available water and the amount of biomass it can hold (Meyer et al., 2007; Milodowski et al., 2015). For simplicity, soil is represented in this model by a single state variable – depth. The model allows soil depth to change, while keeping other variables that affect plant available water constant. Furthermore, for simplicity, the whole soil profile is considered to be uniform, mobile and readily accessible to plant roots

for the water balance. A similar approach was used by others for simplifying complex eco-hydrological processes (Zhou et al., 2013). The fact that soils in different hydrological ages might have different water holding capacity properties (Jenny, 1941) due to differential weathering and erosion rates (Lybrand et al., 2011; Lybrand & Rasmussen, 2015) is acknowledged, and will be discussed.

The model tracks soil depth in the middle of a hypothetical pixel as a state variable, which updates daily. During the simulation, soil moisture changes as a response to input and output of water from rainfall and deep drainage, respectively, and control net primary productivity and biomass production.

Soil depth at a point (H) is assumed to equal the balance between the production of new soil from the bedrock below, and the loss of soil by erosion processes. The rate of change in soil depth with time is therefore expressed as:

$$\rho_s \frac{\partial H}{\partial t} = \rho_r \in [f(H)] + \rho_s E_{net}[f(H, LAI, K_e)] \quad (3.1)$$

where $\in$ is the rate of soil production [L/T] which is an exponential function of soil depth (Heimsath et al., 1997); E_{net} is net erosion rate [L/T], which happens in an event based advective (fluvial) processes, and in background gravity driven diffusive) processes; and ρ_r and ρ_s are rock and soil densities [M/L^3], respectively. Erosion rates depend on soil depth (H), vegetation cover (LAI) and erosivity (K_e). Aeolian deposition is assumed negligible, and input of organic matter and nutrients, and chemical loss by the leaching water are not considered in the model.

Downslope transport of sediment is split into two categories: diffusive- and advective- fluvial processes (Dietrich et al., 2003; Tucker & Hancock, 2010). Diffusive processes are mainly gravity-driven, and controlled by processes such as soil creep, wetting-drying cycles, bioturbation, dry ravel etc. (Dietrich et al., 2003; Gabet et al., 2003; Roering et al., 1999, 2010). Fluvial processes, on the other hand, are driven by the shear stress of water running on a surface, and include (with increasing significance): sheet flow (inter-rill) erosion, rill erosion and debris flows (Dietrich et al., 2003; Tucker & Hancock, 2010). The model herein considers both types of sediment transport mechanisms (diffusive and fluvial), and highlight the type of processes that are most likely to dominate on hillslopes in the SE Australian landscape, based on empirical evidence and expert opinion.

Soil Moisture

The soil moisture mass balance equation is:

$$nH\frac{\partial s}{\partial t} = I_a[f(\overline{AI}, s, K_s)] - D[f(s, K_s)] - aET[f(LAI, s)] \quad (3.2)$$

where s is degree of soil saturation (i.e., the proportion of pore space occupied by water); n is porosity; I_a is actual infiltration [L/T]; D is rate of deep drainage [L/T], which is a function of s and saturated hydraulic conductivity (K_s) [L/T]; and aET is actual evapotranspiration [L/T], which depends on leaf area index (*LAI)* and s.

Vegetation

The biomass (B) [M DM/L^2] mass balance equation (Montaldo et al., 2005) is given by:

$$\frac{dB}{dt} = NPP[f(T_a, s, LAI)] - K_B B \quad (3.3)$$

where NPP is net primary productivity [M DM/L^2/T], which depend on actual transpiration (T_a) [L/T], soil moisture (s) and LAI; and K_B is the biomass decay coefficient [-], which encapsulates plant mortality and forest self-thinning processes (Trouvé et al., 2017). The original model by Montaldo et al. (2005), and adopted by others (e.g., Yetemen et al., 2015b; Zhou et al., 2013), uses a dought factor to limit productivity in water stress conditions. These conditions are not within the scope of this study and thus ommitted from the modeling framework. The efficiency of plants in this energy conversion, as expressed by water use efficiency (WUE), depend mainly on species; for simplicity, all plant functional types throughout the domain are assumed to comprise *Eucalyptus* forest, and are assumed to share the same capabilities for this energy conversion.

Canopy water stores

Rainfall that reaches the canopy is either stored in the canopy, or reaches the forest floor as throughfall. The balance in the canopy storage is expressed by:

$$S_{cap}\frac{de}{dt} = p\, i_{int}[f(LAI)] - aET[LAI]e \quad (3.4)$$

where, e is canopy water content ratio; p is rainfall intensity; i_{int} is the proportion of the rainfall that is stored in the canopy, which depend on LAI; and S_{cap} is canopy water storage [L].

3.2.7 Wildfire

Wildfire plays a big role in the evolution of the Australian vegetation (Pausas & Keeley, 2014), and has been present in the SE Australian landscape since mid-Tertiary (Mooney, 2012). In general, fire frequency depends on climatic conditions, fuel availability and moisture. Bradstock et al. (2010) suggested the theory that in dry climates, fire is limited by fuel availability, while in wetter climates such as in temperate SE Australia, where fuel is abundant, fire is controlled by fire weather and fuel moisture state (Bradstock, 2010).

A fire model was developed by linking fire probabilities to soil moisture deficit, allowing fire regimes to evolve with changes in climate as well as water holding capacity (Appendix II). Fire frequency in the model was calibrated using forest Average Fire Cycle (*AFC*) of different vegetation types across the domain (Cheal, 2010). Using this approach allows the model to calculate annual flammability using water deficit status, which depends on the eco-hydrology during the previous year. The model only considers major high severity wildfires since evidence shows that the effect of low severity fires on the woody vegetation and soil are relatively minor (Prosser & Williams, 1998).

3.2.8 Wildfire impacts

Major high severity wildfires removes the vegetation and litter cover and causes a change in the soil hydraulic and physical properties (Certini, 2005; DeBano et al., 1998; Inbar et al., 2014), which increases the chance of high magnitude erosive events in case of high intensity rainfall (Langhans et al., 2017; Nyman et al., 2011, 2014a, 2015b). In SE Australian forests, the effect of fire on hydrology is variable, but has been shown to increase erosion by up to several orders of magnitude compared to pre-fire conditions (Noske et al., 2016; Sheridan et al., 2007; Smith et al., 2011b). A major cause of this erosion is the significant reduction in infiltration capacity as a result of a cohesive, water repellent layer residing several centimetres below a loose non-cohesive mixture of ash, gravel and sediment at the surface (Nyman et al., 2013; Smith et al., 2012). Nyman et al. (2013) had shown that rainfall needs to exceed an intensity-duration threshold in order to remove most of the non-cohesive layer on these steep hillslopes. A significant erosion event results when these post-fire conditions on

steep dry hillslopes are present when highly erosive rainfall that exceeds this threshold occurs (Nyman et al., 2011). In other cases, only a portion of the non-cohesive layer is removed, while the remainder is incorporated back to the soil during recovery (Nyman et al., 2013).

Recent studies have shown that aridity index (Budyko, 1974) is highly correlated with the effect of fire on soil hydraulic properties (Noske et al., 2016; Sheridan et al., 2016), with high erosion events occurring mostly on more arid hillslopes (Nyman et al., 2011). Forests in SE Australia seldom yield significant runoff when unburnt (Bren & Turner, 1979; Cawson et al., 2013; Prosser & Williams, 1998) due to the high volume of macro-pores and high infiltration capacity (Lane et al., 2004; Sheridan et al., 2007) typical of forest soils, and despite water repellent condition that may naturally occur during dry months (Burch et al., 1989). However, other evidence show that drier forests yield some runoff, which still has the potential to erode some soil, despite it being cohesive in the unburnt state (Burch et al., 1989). In order to stay true to the erosion processes observed across local systems as described by Nyman et al. (2013), the soil was conceptually divided into two states. When unburnt, the soil is considered cohesive, and is eroded in a *detachment limited* fashion. After fire, the soil surface becomes non-cohesive, which is eroded in a *transport limited* fashion. More specifically, the model adopts these two type of fluvial erosion processes, depending on a two-layer soil state : (i) *Detachment Limited Erosion* occurs when overland flow erodes top of the cohesive layer. This type of erosion occurs as long as it is not covered by a non-cohesive layer, and depends on shear stress; and (ii*) Transport Limited Erosion* which occurs only within the first year after fire, as long as the non-cohesive layer is still present, and depends on stream power during a 15 minute high-intensity rainfall event (*I15*). The erosion model was parameterised with an extensive dataset on runoff and erosion processes in the SE Australian forested landscape (Langhans et al., 2016b; Noske et al., 2016; Nyman et al., 2013; Van der Sant, 2016). A detailed description of how erosion was modelled is presented in section 3.3.6.

Post fire vegetation recovery is very important to the scale and magnitude of hydro-geomorphic response to fire (Langhans et al., 2016a; Shakesby et al., 2007). Vegetation recovery in SE Australia is relatively rapid, and the window of disturbance usually lasts between 2-5 years after the fire, when runoff and erosion response return to pre-fire conditions (Brown, 1972; Lane et al., 2006; Nyman et al., 2011). The response of SE Australian temperate forest vegetation to fire can be divided into two main strategies: (i) *"Fire Sensitive" Species* (FSS), or "Obligate seeders", that die and open the space for

competition to their decedents and other opportunists, which dominates forests under damp-wet rainfall regime; and (ii) *"Fire Tolerant" Species* (FTS), or "resprouters" that regenerate through resprouting of epicormics shoots, and dominate forests under lower-intermediate rainfall regime (eg., Clarke et al., 2015; Fairman et al., 2016). The two recovery strategies in these forests control the effect of fire and the rate of recovery. Applying a simple approach, it is assumed that the proportion of tree species that are hosted in a given location varies non-linearly with aridity. Using this assumption, every modelled site, depending on its aridity, has different proportions of these two types strategies, which determines the vegetation response to fire (Clarke et al., 2015). For example, in low aridity index (<1), which host high proportion of FSS, a modelled fire kills most of the vegetation and the recovery of biomass starts from *zero*. Conversely, in more arid forests, which host increasingly higher proportions of FTS, fire only kills a smaller proportion of the vegetation, and recovery of biomass starts from a higher value, significantly reducing the time to full recovery (Clarke et al., 2015). A detailed description on how post-fire recovery was modelled is presented in section 3.3.6.

A well-established theory in disturbance ecology suggest that repeated fires can cause a shift in vegetation communities, recovery from which can be irreversible or a long-term process (Bradstock, 2010; Fletcher et al., 2014a; Thomas et al., 2014). In a recent meta-analysis paper, (Fairman et al., 2016) put forward a theory that describes recovery processes of SE Australian vegetation communities from repeated wildfires. The authors suggested that a change in vegetation community is plausible if a wildfire occurs before the forest floor seedbank could recover from a severe wildfire. Even though vegetation community changes are an important process, it was not included it in the current modelling framework, because it is not the focus of the study and because vegetation community properties are not modelled. Future developments of the model have the potential to implement the hypothetical model suggested by Fairman et al. (2016).

3.3 Algorithms & Equations

3.3.1 experimental sites

The following section will provide specific details and formulations that were used in order to solve the four conservation equations described above (Eqn 3.1-3.4). In order to constrain the model performance to the climo-spatial domain, some of its essential components were

parameterised using observations and data from representative sites. Details of these sites are presented in Table 3-1, and essentially represent the conditions at 50m down from the ridge-line. Mean annual precipitation (MAP) were obtained from gridded source (Australian Bureau of Meteorology, 2017), based on interpolations between rainfall measurements. Sites were: Eildon (MAP = 942 mm/yr); *Christmas Hills* (*CH*, MAP = 870mm/yr); *Reefton* (*RT*, MAP = 1311 mm/yr), Frenchman's spur (*FS*, MAP = 1660 mm/yr) and *The Triangle* (*TT*, MAP = 1748 mm/yr). In each location a north and a south facing hillslope was chosen in order to vary short wave radiation, as expressed with different calculated daily potential evapotranspiration ($\overline{Ep}$; Table 3-1). Soil depth was measured at each location using soil pits and/or auger holes approximately 50m down the slope, depending on accessibility (Table 3-1). Field assessments of forest type were used in order to constrain biomass to local estimations (Grierson et al., 1992; Volkova et al., 2015) and calibrate the fire model (see Appendix II). Detailed descriptions of the model and governing equations are presented in the next section. Parameter values that are used in the model simulations are presented in Table 3-2.

Table 3-1 - Characteristics and site attributes of the parameterisation sites.

Site	Aspect	Elev.	MAP[*1]	Mean Annual Ep[*2]	Aridity[*3]	Slope	Soil Depth[*4]	PAI[*5]	Ecological Vegetation Class	Estimated biomass	Source[*6]
		m	mm/yr	mm/yr		deg	[m]			kg DM/m^2	
Eildon	North	455	942	1895	2.49	32.24	0.20	1.73	Grassy Dry Forest	11.5	(Volkova et al., 2015)
	South	455	942	1263	1.77	29.31	0.48	2.08	Grassy Dry Forest	16	(Volkova et al., 2015)
Christmas hills	North	272.5	870	1767	2.31	14.80	0.48	1.73	Grassy Dry Forest	11.50	(Volkova et al., 2015)
	South	272.5	870	1356	1.78	16.70	0.48	2.08	Grassy Dry Forest	16	(Volkova et al., 2015)
Reefton	North	614	1311	1892	1.5	29.76	0.45	1.97	Shrubby foothill forest	22.50	(Volkova et al., 2015)
	South	614	1311	1310	1.04	22.12	1.15	4.22	wet forest	42.37	(Grierson et al., 1992)
Frenchman's spur	North	1085	1660	1844	1.07	25.74	1.26	3.35	Montane Dry woodland	45	(Grierson et al., 1992)
	South	1085	1660	1290	0.75	26.02	1.08	3.78	Montane Damp Forest	39.48	(Grierson et al., 1992)
The triangle	North	1065	1748	1726	1	10.60	1.73	3.35	Montane Damp Forest	39.48	(Grierson et al., 1992)
	South	1065	1748	1525	0.88	7.60	1.29	3.78	Montane wet forest & Cool Temperate rainforest	41.7	(Grierson et al., 1992)

[*1] interpolated long-term data from Bureau Of Meteorology

[*2] calculated using Eqn 3.6 with mean daily net radiation (R_{net}) and mean daily temperature (T_s) values from the downscaling gridded data (Nyman et al., 2014b) for each of the sites.

[*3] calculated using Ep/P;

[*4] Normal to slope, measured approx. 50 m downslope

[*5] Values taken from (Walsh et al., 2017). Plant Area Index for Eildon and Frenchman's spur were estimated to be similar to the ones at Christmas Hills and The Triangle, respectively.

[*6] Source for estimated biomass - Table 2 in (Volkova et al., 2015); Table 4 in (Grierson et al., 1992)

3.3.2 Climatic forcings

Evaporation demand (E_p)

Energy from shortwave radiation is introduced at daily time-steps as evaporative demand (or Potential evapotranspiration, E_p [L/T]) and was calculated using a cosine function (Yetemen et al., 2015b; Zhou et al., 2013):

$$E_p(DOY) = \frac{\Delta d}{2} cos\left[2\pi\left(\frac{DOY - L_T - {N_d}/{2}}{N_d}\right)\right] + E_{p-daily} \quad (3.5)$$

Where DOY id day of the year; Δd (L/T) is the difference between maximum and minimum values of daily E_p; L_T is the lag between peak E_p and peak solar forcing (set to 30 days); N_d is number of days in a year; and $E_{p-daily}$ is mean annual daily E_p. Daily PET value sets the upper boundary of energy input to the system. The data for Δd and $E_{p-daily}$ was obtained using the Priestly-Taylor equation (Priestley & Taylor, 1972):

$$E_p = \alpha_{PT} \frac{\Delta R_{net}}{\Delta + \gamma} \frac{1}{\rho_w \lambda_v} \quad (3.6)$$

where R_{net} is net radiation [MJ day]; Δ is the slope of the saturation vapor pressure versus temperature curve [kPa/^{o}C]; α_{PT} is a constant (Table 3-2); γ is psychrometric constant [kPa/^{o}C] calculated using $\gamma = (C_{P-air} P_a)/(MW_{wv}\, \lambda_v)$, where C_{P-air} is specific heat of air at constant pressure [MJ/kg/^{o}c], P_a is atmospheric pressure [kPa], MW_{wv} is ratio of the molecular weight of water to dry air [-]; ρ_w is mass density of water [1000 kg m3]; and λ_v is latent heat of vaporisation [MJ/kg], calculated using: $\lambda_v = 2.501 - 0.002361\, T_s$, where T_s is mean daily temperature (in celsius). Data for R_{net}, and T_s were abtained using available gridded downscaled values (Nyman et al., 2014b), which take into account slope and aspect, and include both direct and diffuse shortwave and net long wave radiation, based on long term data from Australian Bureau of Meteorology. The Priestley-Taylor equation calculates evaporation demand from wet surface in the absence of the advection component found in the, more complex, *Penman-Montieth* equation (Monteith, 1965). The equation assumes that the land surface is sufficiently wet and is in equilibrium with the atmosphere. These assumptions might cause overestimation of E_p, especially on the dry end of the aridity domain. While acknowledging this possible room for error, Priestley-Taylor equation was

chosen for its lower number of parameters (eg. as compared with the Penman-Montieth equation) and its relatively simple applicability in such theoretical 1D model.

Rainfall

The model simulations run on daily time-steps between storm events and on hourly time-steps within rain cells. Using hourly rainfall (p, [L/T]) allows the model to better represent inter-storm hourly variations in intensity which cannot be captured by using daily rainfall, and is critical for fluvial erosion processes (eg. Kean et al., 2011). A description of how sub-hourly rainfall intensity is derived from hourly rainfall is described in the next section. Poisson shaped rainfall was generated by single-site Neyman-Scott Rectangular Pulse (NSRP) model (Camici et al., 2011; Cowpertwait et al., 1996; Tarpanelli et al., 2012) calibrated using hourly rainfall measured in several sites across the domain. Details of the calibration of the NSRP model, and the creation of simulated rainfall for sites across an aridity gradient are presented in Appendix III . To reduce simulation times, the NSRP model was set to run only for 1000 years and the same rainfall is repeated if simulations run for longer times, building on the assumption that 1000 years of hourly rainfall is sufficiently long to capture temporal rainfall variability.

3.3.3 Ecohydrology

Partitioning of rainfall and solar radiation

Partitioning of rainfall and solar radiation by local vegetation is an important component in coevolution by its control on the water balance under the canopy (Eagleson, 1982). A generalized concept was adopted in which rainfall and energy fluxes can be partitioned between the leaves the trees and the bare soil. In order to apply this simple concept, a dynamic variable cover fraction (C_F) was adopted, which represents the projection of surface area occupied by trees:

$$C_F = \frac{LAI_l}{LAI_{gmax}} \tag{3.7}$$

where LAI_l is modelled Leaf Area Index (LAI); and LAI_{gmax} is the highest "global" possible LAI of native vegetation in the area (Table 3-2), calibrated with measured PAI data using hemispherical photography analysis (Table 3-1), as described in Section 3.5. Rainfall and

energy fluxes over the area of the covered fraction C_F can be partitioned further into fluxes that pass through the leaves and onto the soil surface, and those that land directly on them (LAI_r):

$$LAI_r = \frac{LAI_l}{LAI_{lmax}} \tag{3.8}$$

where LAI_{lmax} is highest possible "local" LAI value per site (Section 3.5). Using this general assumption, total flux (J) of either rainfall or solar radiation, could be partitioned between the leaves (J_L) and the soil (J_S):

$$J_L = J\, j_{dh} = JC_F LAI_r \tag{3.9}$$

$$J_S = J\, j_m + J\, j_{dm} = J(1 - C_F) + JC_F(1 - LAI_r) \tag{3.10}$$

where j_{dh} is the proportion of the flux directly over the canopy that "hit" the leaves, ($j_{dh} = c_F\ LAI_r$); j_{dm} is the proportion of the flux directly over the canopy that "missed"/goes between the leaves ($j_{dm} = c_F\ (1 - LAI_r)$); and j_m is the proportion of flux that misses the trees and reached the soil directly ($j_m = (1 - c_F)$).

The model uses a simple way for the partitioning of both rainfall (p; L/T]) and potential evapotranspiration (E_p; [L/T]) in the canopy. When referred to, hourly rainfall (p, [L/T]) or potential evapotranspiration (E_p, L/T]), can be substitute J in Eqn 3.9 and Eqn 3.10.

Interception, infiltration and overland flow

High intensity sub-hourly rainfall (<30min) had been shown to drive post-fire high magnitude erosion events (eg. Kean et al., 2011), therefore a method that uses sub hourly rainfall to simulate erosion processes is proposed. The NSRP model builds on the assumption that rainfall events are made of several storm cells (Cowpertwait et al., 1996). To obtain sub-hourly rainfall the intensity within hourly rainfall is assumed to be exponentially distributed (Istanbulluoglu & Bras, 2006) with a Probability Density function (PDF) and cumulative Density Function (CDF), shown here in their generic forms:

$$f(x \le p_x) = \lambda\ exp^{-\lambda_p p_x} \tag{3.11}$$

$$F(x \le p_x) = 1 - exp^{-\lambda_p p_x} \tag{3.12}$$

where $\lambda_p = 1/p$; and p_x is sub hourly rainfall intensity. Here a method similar to the one proposed by Kandel et al. (2005) is applied, in which hourly rainfall (p, [L/T]) is scaled down to sub-hourly rainfall using its CDF. Available canopy space (e_E,[L/T]) can then be used as a cutoff value to partition the rainfall into throughfall and intercepted water, and then potential infiltration (I_P, [L/T]) as a cutoff value to partition the throughfall into runoff and percolating water.

Interception

The model tracks canopy storage e (Eqn 3.4), defined as the proportion of the canopy carrying capacity that is occupied by water ($1 > e > 0$). Available volume in the canopy (e_E) is calculated using $e_E = (1 - e)S_{cap}$, where S_{cap} is canopy water storage capacity [L]. e_E can be later used as a cutoff value for calculating the proportion of rainfall to be stored in the canopy (i_{int}) and the throughfall (i_{thr}) using the cumulative distribution function of the portion of the hourly rainfall "hitting" the leaves p_L [L]:

$$i_{int} = F(p_L \leq e_E) = 1 - exp^{-\lambda_{p_L} e_E} \quad (3.13)$$

$$i_{thr} = F(p_L > e_E) = 1 - i_{int} \quad (3.14)$$

where $\lambda_{p_L} = \frac{1}{p_L}$, and $p_L = p\ (c_F\ LAI_r)$, using Eqns 3.7 and 3.9. Total throughfall (p_{thr} ; [L]) can be calculated by adding the rainfall that went through the canopy using $p_{thr} = i_{thr}\ p_L + p\ c_F\ (1 - LAI_r) + p(1 - c_F)$, and the addition to the intercepted water [L] with $p_{int} = i_{int}\ P_L$.

Canopy water storage capacity is calculated using:

$$\mathrm{S_{cap}} = S_{LAI}\ LAI \quad (3.15)$$

where S_{LAI} is the amount of water that the can be stored per unit LAI [L/L/L]. S_{LAI} in the model is used to calibrate the interception in the water balance evaluation.

Infiltration and runoff

A similar approach was used to partition throughfall into runoff and infiltrating water. Conceptually, soil hydraulic properties were split into infiltration capacity (*Ic,* [L/T]) and hydraulic conductivity (*Ks* [L/T]). *Ic* is defined as the boundary layer between the atmosphere and the soil profile, which sets the capacity of the soil to allow infiltration,

whereas soil's ability to conduct water within its profile is defined as *Ks*. The distinctions between the two properties is important for the conceptual model of infiltration and runoff generation. While both of the soil properties depend on texture, soil aggregation and macro porosity, *Ic* is also highly dependent on water repellency (Nyman et al., 2010) and as a result its value changes over time. The potential infiltration rate (I_P) [L/T] is defined as:

$$I_P = \min(I_c, k_s) \tag{3.16}$$

Both variables serve as a limit for actual infiltration (I_a, [L/T]) of the throughfall, combined with a volume limit that is defined as the actual pore volume that is left in the soil profile to accommodate the infiltrating water, which is calculated using: $s_E = (1 - s)nH$. Generally, forest soils within this climatic domain (where 700<MAP<1800 mm/yr) have relatively high k_s due to relatively large concentration of macropores (Rees, 1982). Furthermore, infiltration excess overland flow, occurring mainly after fire, dominates runoff generation across the domain, while saturation excess overland flow was hardly recoded, especially in the divergent upper part of the hillslope (Lane et al., 2004). For this reason, one value was chosen to represent $k_s$across the domain (Table 3-2), while *Ic* was allowed to vary. Forested catchments in SE Australia have low runoff coefficients when unburnt, as a result of relatively high infiltration capacities (Cawson et al., 2013), however fire often changes soil hydrological properties (Ebel, 2013; Inbar et al., 2014). Here, *Ic* was set to depend on time since fire and aridity:

$$\ln(I_c) = r_{a_{y=i}} \overline{AI} + r_{b_{y=i}} \tag{3.17}$$

Where $\overline{AI}$ is mean aridity index ($\overline{AI} = \overline{E_p}/\bar{P}$ where $\overline{E_p}$ and $\bar{P}$ are mean potential evapotranspiration and precipitation, respectively) calculated for a 100 year period; and $r_{a_{y=i}}$ and $r_{b_{y=i}}$ are constants which depend on the number of years (y=i) since the last fire (i.e., 1st year, 2nd year and unburnt). During model simulations $\overline{AI}$ is calculated annually (starting from year 101) and combined with time since fire (Table A- IV-1) to calculate *Ic* (Eqn. 3.17). Mean aridity index for 100 years is considered here assuming an estimated 100 lag between changes in climate to changes in soil hydraulic properties. Values for $r_{a_{y=i}}$ and $r_{b_{y=i}}$ parameters were calibrated using a published data from the area for burnt forest (Table 2 in Langhans et al., 2016b) and from other sources for unburnt forests. Details on parametrization of Eqn 3.17 can be found in Appendix IV .

The proportion of throughfall that does not infiltrate (i_{ro}), and the proportion that does (i_{inf}) was calculated using the CDF of the hourly throughfall (p_{thr}, [L/T]) and I_P as a cutoff:

$$i_{inf} = F(p_{thr} \leq I_P) = 1 - exp^{-\lambda_{P_{thr}} I_P} \tag{3.18}$$

$$i_{ro} = F(p_{thr} > I_P) = 1 - i_{inf} \tag{3.19}$$

where $\lambda_t = {}^{1}/_{p_{thr}}$. Actual infiltration ($I_a$, [L/T]) and runoff ($Q_0$, [L/T]) are then calculated using:

$$I_a = \min(i_{inf} p_{thr}, s_E) \tag{3.20}$$

$$Q_0 = \begin{cases} p_{thr} - I_a, & p_{thr} \geq I_a \\ 0, & p_{thr} < I_a \end{cases} \tag{3.21}$$

High erosion events are often triggered by high intensity rainfall that falls within 10-15 minutes (eg., Langhans et al., 2016b). Peak runoff rate (Q_{15}, [L/T]) is defined as the significant part of the runoff during 15 minutes of rainfall, assuming that every hourly rainfall has 15 minutes that hold the highest intensity. In order to make this generalization, intensities are assumed to be exponentially distributed, with one dominant peak of high intensity rainfall within every hour of rainfall. Q_{15} is calculated by solving the CDF of the hourly runoff for the third quartile $\{Qt_3 = F(Q_0 > Q_{15}) = 1 - [1 - exp^{-\lambda_{Q_0} Q_{15}}]\}$.

$$Q_{15} = -\frac{\ln(1 - Qt_3)}{\lambda_{Q_0}} = -\frac{\ln(0.25)}{\lambda_{Q_0}} \tag{3.22}$$

where $\lambda_{Q_0} = 1/Q_0$; $Qt_3 = 0.75$. Q_{15} is used in the model for transport limited erosion purposes.

Deep drainage

The approach proposed by Istanbulluoglu et al. (2006) and Zhou et al. (2013) was adopted for calculating deep drainage (D, [L/T]):

$$D(s) = K_s \, s^{(2b_{ret}+3)} \tag{3.23}$$

where b_{ret} is a water retention parameter (Table 3-2) (Zhou et al., 2013). The following assumptions are made regarding deep drainage (i) there are no subsurface inflows; (ii) soil properties (i.e., k_s and n) are homogenous throughout the soil depth; (iii) the soil is only

drained when soil moisture is above field capacity (s_{fc}): $s_{fc} < s < 1$; and (iv) the excess soil water drains vertically and is lost via deep drainage (DD).

Evapotranspiration

Similar to Zhou et al. (2013), Maximum evaporative demand (or maximum potential evapotranspiration; ET_{max}; [L/T]) was defined as the maximum daily ET of the system, and was calculated using:

$$ET_{max} = T_{max} + E_{\max} \tag{3.24}$$

where T_{max} and $E_{\max}$ are maximum transpiration and evaporation [L/T], respectively. Here, ET_{max} was assumed to be partitioned between the canopy to evaporate intercepted rainfall and drive the transpiration process, and the soil to drive soil evaporation. The method proposed above is used in order to partition daily E_p between the soil and the vegetation (by substituting J with E_p; J_L with T_{max} and J_S with $E_{\max}$in Eqn 3.13 *and* 3.14, as follows:

$$T_{max} = E_p[E_p - E_{ia}]\ c_F\ LAI_r \tag{3.25}$$

$$E_{max} = E_s[E_p - E_{imax}]\ [c_F(1 - LAI_r) + (1 - c_F)] \tag{3.26}$$

$$E_{max} = E_s[E_p - E_{imax}][1 - c_F\ LAI_r] \tag{3.27}$$

where E_s is a factor reducing E_p to achieve maximum soil evaporation, with the value of 0.7 (Istanbulluoglu et al., 2012; Zhou et al., 2013); and E_{imax} is maximum evaporation of intercepted water from the canopy, assumed to be the first to satisfy the evaporative demand, and defined to be the minimum of the total daily evaporative demand and the actual canopy water storage [L/T] :

$$E_{imax} = \min\ (\ E_p\ ,e\ S_c\ ) \tag{3.28}$$

Assuming homogeneous evaporation from the canopy (i.e., regardless on the location on the canopy), actual evaporation from the canopy water storage is calculated using:

$$E_{ia} = E_{imax}\ \varphi(e) \tag{3.29}$$

Where φ is interception evaporation efficiency term based on canopy water storage (e) and d defined here for simplicity as:

$$\varphi(e) = \begin{cases} 0, & e = 0 \\ 1, & e > 0 \end{cases} \quad (3.30)$$

Similar to (eg., Istanbulluoglu & Bras, 2006; Laio et al., 2006; Yetemen et al., 2015b; Zhou et al., 2013), actual evapotranspiration (ET_a;[L/T]) is calculated using:

$$ET_a = ET_{max}\, \beta(s) \quad (3.31)$$

where β is evaporation efficiency, which depends on soil moisture (s), and calculated using:

$$\beta(s) = \begin{cases} 0, & s \le s_h \\ E_w \dfrac{s - s_h}{s_w - s_h} & s_h < s \le s_w \\ \dfrac{s - s_w}{s^* - s_w} & s_w < s \le s^* \\ 1 & s > s^* \end{cases} \quad (3.32)$$

where $s_h, s_{w,} s_{fc,}$ and s^* are saturation degree at hygroscopic capacity, wilting point, field capacity and incipient stomata closure, respectively. E_w is evaporation from soil under wilting point has the value of 0.1 mm/h (Laio et al., 2006). Values for $s_h, s_{w,} s_{fc,}$ and s^* are presented in Table 3-2, and represent values for clay loam soil (Clapp & Hornberger, 1978), which is a common soil type at the domain (Rees, 1982).

3.3.4 Biomass balance

Net primary productivity (*NPP*; [M DM/L^2/T]) was calculated using:

$$NPP = 0.75\,(1 - \mu) T_a\, WUE\ \ \rho_w\ \ \omega \quad (3.33)$$

where WUE is water use efficiency [M $_{CO2}$/ M $_{H2O}$]; ω converts CO_2 to dry matter; ρ_w is density of water [M/L^3] (Table 3-2); and T_a is actual transpiration [L/T]. This followed a simple conceptual model used by Zhou (2013) (see section 2.2 and Eqns. 8 and 9 in their paper) in which transpiration drives *NPP*, which corresponds to the difference between gross primary productivity and autotrophic respiration. Actual transpiration (T_a) was calculated using:

$$T_a = ET_a \left({}^{T_{max}}/_{ET_{max}} \right) \quad (3.34)$$

In the model, *NPP* is partitioned into two structures: leaf biomass (B_l,[M DM/L^2]) and structural biomass (B_s, [M DM/L^2]), using a simple resource allocation coefficient: $\Phi = (1 - LAI_l/LAI_{lmax})$ similar to Williams and Albertson (2005) (Appendix B in their paper). B_s consists of both root and above ground woody biomass. B_l is calculated using:

$$\frac{dB_l}{dt} = \Phi NPP + f_c \Phi\, k_{lp} \theta_m B_{lmax} - k_{sl} B_l, \qquad (3.35)$$

where k_{sl} is leaf senescence coefficient; f_c is fire coefficient (a Boolean variable that gets the value of 1 only in a year after a fire to activate leaf recovery from seeds or resprout), k_{lp} is leaf production rate [1/T] which is a calibration parameter; θ_m is a modifier that depends on soil moisture; and B_{lmax} is maximum leaf biomass. The left term in the right side of Eqn 3.35 represent the rate of leaf biomass addition, which depend on *NPP* (Eqn 3.33) and on the allocation of resources towards producing leaves (Φ); The second (middle) term represents the recovery rate of leaf biomass after a severe crown fire; and the right term represent leaf senescence rate. It is assumed leaves are the first to regenerate and do so with energy source stored in the structural biomass (in case of resprouter species) or in the seeds (in case of obligate seeder species). The leaf regeneration itself occurs only on the first year after fire ($f = 1$), and depend both on the rate of regeneration (k_{lp}) and on soil moisture (s) to drive the carbon sequestration process for building leaf biomass. After the first year of recovery is over ($f = 0$), recovery follows a regular path of biomass accumulation ($f\Phi\, k_{lp} \theta_m B_{lmax} = 0$). θ_m is calculated using:

$$\theta_m = \begin{cases} 1 & s \geq s^* \\ \left\{\frac{s - s_w}{s^* - s_w}\right\}^M & s^* > s \geq s_w, \\ 0 & s < s_w \end{cases} \qquad (3.36)$$

where M is a calibration coefficient ($M = 4$). Using θ_m in Eqn 3.35 allows the leaf biomass regeneration to occur maximum rates when there is sufficient soil moisture, and in lower rates when soil moisture is limited. Actual leaf area index (*LAIl*) values are calculated from the B_l daily using $LAIl = B_l\, SLA$, where SLA is specific leaf area [unit-LAI/M] (Table 3-2), parameterized using literature values for eucalypt forests (Whitehead & Beadle, 2004).

Change in structural biomass with time is expressed by:

$$\frac{dB_s}{dt} = (1 - \Phi)\, NPP - \; k_{ss} B_s, \tag{3.37}$$

where k_{ss} [1/T] is the structural biomass senescence coefficient which limits biomass accumulation. Here, a conceptual theory is proposed, in which biomass accumulation depend mainly on available water and soil depth, as will be described below. In practice, this means that during the coevolution process, multiple potential maximum biomass values could develop, depending on water availability and water holding capacity of the soil. The following constraints are given in order to limit biomass accumulation: (i) under growing conditions (i.e., during recovery after fire), addition to structural biomass should be higher than biomass senescence, which can be achieved by low kss (eqn 3.37) values during vegetation recovery, and higher when enough structural biomass had been accumulated; and (ii) senescence of structural biomass reaches a maximum value (kss_{max}) only after around 80% of the vegetation has recovered. A logistic function for kss as a function of the proportion of structural biomass from its maximum is proposed:

$$kss = kss_{min} + \left(\frac{kss_{max} - kss_{min}}{1 + exp^{-a_{kss}\left(\frac{B_s}{B_{smax}} - c_{kss}\right)}} \right) \tag{3.38}$$

where Bs_{max} [M DM/L^2/T] is maximum structural biomass; a_{kss} and c_{kss} are calibrated constants; and kss_{min} is a minimum senescence rate constant, calibrated to reproduce reasonable post fire vegetation recovery (Table 3-2). kss_{max} is calculated using Eqn 3.37, and assuming that: (i) maximum senescence is reached when structural biomass had reached steady-state conditions (i.e., $B_s = B_{smax}$); and that (ii) under these conditions $LAIl$ had almost fully recovered $\Phi \approx 0$ (Eqns. 3.35 and 3.37):

$$kss_{max} = \frac{NPP(1 - \Phi)}{B_{smax}} \tag{3.39}$$

For simplicity reasons, the model does not explicitly track the density of dead biomass.

The maximum-biomass concept

Vegetation in the model partitions water and energy, which is an essential part of the coevolution process. It is assumed that biomass does not accumulate endlessly, and is constrained by several factors that limit productivity (Eamus, 2003). Primary productivity is maintained by supply of water, nutrients and sunlight (Eamus, 2003; Eamus et al., 2006).

Because the model is designed to simulate variety of forest types across the climatic domain, for simplicity, limitations on bioavailability of nutrients are assumed negligible. It is argued that this is a reasonable assumption considering possible nutrient recycling processes across the domain (Adams, 1995):

(i) the combination of relatively frequent fires with fast regeneration in dry sites which provides a flush of essential nutrients;

(ii) large quantities of wood residues and litter mass and relatively rapid decomposition rates maintain steady supply of nutrient in wet sites.

This means that the system will be in a state of either water or energy limitation depending on the climatic conditions during the simulation. Soil depth is another constraint on biomass, as it serves as the primary water store for the vegetation (Kosmas et al., 2000; Milodowski et al., 2015). By adopting Eagleson's optimality theory (Eagleson, 1982; Eagleson & Tellers, 1982), in which a coupled soil-vegetation system will always tend towards an optimized state (Hatton et al., 1997), biomass holding capacity (B_{max}, [M DM/L^2]) is introduced and represent an upper bound to net primary productivity for a given soil depth at a given climate regime. This limitation holds within it several other limitations (such as: space limitation) and means that biomass at any certain point in time will always be limited to the available water and soil depth. Once soil depth changes due to soil erosion of formation, maximum biomass holding capacity will change accordingly, and the actual vegetation will respond.

Here, an empirical model for maximum biomass B_{max} is proposed:

$$B_{max} = \alpha_b \, exp^{-m_1 \overline{AI}} \, (1 - \, exp^{-m_2 H}), \tag{3.40}$$

where α_b, m_1 and m_2 are empirical parameters (Table 3-2) calibrated using measured soil depths and literature biomass values (Further details are given in section 3.5); H is the mean measured soil depth at 50m downslope (based on a combination of measurements). The timeframe for calculating $\overline{AI}$ was chosen to overcome annual fluctuations in climate, which in any case not expected to produce drastic changes in maximum biomass values. Maximum biomass is then used to set an upper-bound for biomass growth, and is a sum of maximum leaf (B_{lmax}) and structural (B_{smax}) biomass.

Leaf biomass is calculated using $B_{lmax} = LAI_{lmax}/SLA$; where LAI_{lmax} is defined as the maximum Leaf Area Index value for the "optimal" vegetation/biomass (B_{max}), and is calculated using:

$$LAI_{lmax} = LAI_{gmax}(1 - exp^{-m_3 B_{max}}), \quad (3.41)$$

where α_{LAI} and m_3 are calibrated empirical parameters (See section 3.5).

3.3.5 Fire frequency and effect on vegetation and soil

In the model, fire regime is stochastically driven and based on probability of ignition (P_f), which depends on soil moisture and calculated once every summer on an annual basis:

$$P_f = \kappa_f \, P_{wd} + \delta \quad (3.42)$$

where P_{wd} is the probability of annual soil moisture to be below a certain water deficit cutoff (s_{cut}); and κ_f and δ are calibration parameters (See Appendix II for more details on the calibration process). P_{wd} is calculated using:

$$\overline{s} = \sum_{365}^{DOY=1} (s \leq s_{cut}) \quad (3.43a)$$

$$P_{wd} = \frac{\overline{s}}{365} \quad (3.43b)$$

where the numerator sums the number of days that soil moisture is under s_{cut} value within one year. s_{cut} was calibrated using Average Fire Cycle (AFC) estimates of typical SE Australian forests based on previous work (Cheal, 2010; Kennedy & Jamieson, 2007) that were compared to similar forests used to parameterize the model (See Appendix II). Once a year, a random number is generated (σ) and compared to P_f calculated for the previous year, and fire will occur when $\sigma < P_f$.

Fire Effects on Vegetation

The response of the vegetation to fire depend on the strategies acquired during evolution to cope with repeated fires (Bowman, 2000) (more details in section 3.2.8). After the fire

occurs, the model uses a factor (bRF) which determines how much of the structural biomass is removed as a response to fire (Figure 3-3):

$$bRF = \begin{cases} 1 & \overline{AI}, < 1 \\ a_{mort}\ \overline{AI}^{\ -b_{mort}} & \overline{AI}, \geq 1 \end{cases} \quad (3.44)$$

where bRF is proportion of trees that die due to fire from the total biomass; a_{mort} and b_{mort} are parameters based on estimates of post-fire tree mortality across an aridity gradient. Due to lack of literature data, the function was parameterised based on local observations and expert opinion depending on estimates of the proportion of FTS and FSS across the parameterisation sites, depending on their Ecological Vegetation Classes (Table 3-1).

After every fire, structural biomass is reduced using $B_{s_{post\_fire}} = B_s(1 - bRF)$. Practically, the complete burning of the leaves causes a temporary reduction in vegetation cover, as $c_F = 0$ and $LAI_r = 0$ (Eqns 3.7 and 3.8), which affects both canopy interception and evapotranspiration, while the proportion of tree mortality affects the recovery rate, as it sets a starting point to the structural biomass to regenerate from. For example, a wet forest will take longer time to regenerate its structural biomass compared to a mixed specie forest on a drier site.

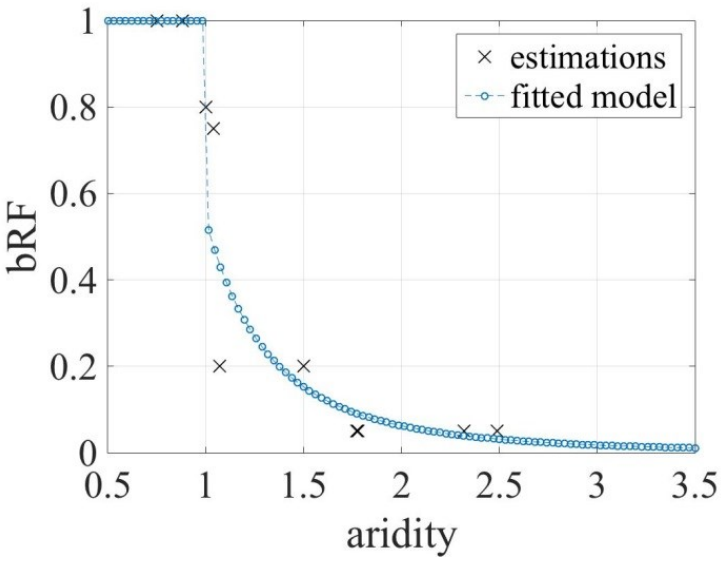

Figure 3-3 - Biomass reduction function as a function of aridity (Eqn 3.44). Values for this function were estimated using expert opinion.

3.3.6 Soil depth balance

Soil depth is modelled on daily time steps for long term processes (i.e., diffusive sediment movement and soil production from bedrock), and on hourly basis for short-term fluvial erosive response to rainfall. Soil depth balance is calculated by:

$$\frac{\partial H}{\partial t} = \frac{\rho_r}{\rho_s} \in -(E_f + E_d) \tag{3.45}$$

where ρ_r and ρ_s are rock and soil density, respectively, $\in$ is soil production rate [L T], E_f and E_d are soil fluvial and diffusive erosion rates [L T], respectively.

Soil Production

Soil production ($\in$*;* [L T]) is calculated using the commonly-used exponential function (Heimsath et al., 1997):

$$\in = \in_o \ exp^{-H\cos\theta / H^*} \tag{3.46}$$

where $H\cos\theta$ is soil depth normal to slope (θ), H^* is the *e*-folding depth of the soil production rate (usually 0.5); and $\in_o$ is maximum soil production when H=0. Soil production is also likely to be affected by climate (eg., Amundson et al., 2015; Norton et al., 2014; Perron, 2017; Stockmann et al., 2014), which influences plant establishment that in turn chemically and physically breaks the bedrock into transportable material (eg., Amundson et al., 2015; Gabet & Mudd, 2010), and controls the rate at which chemical reactions that weather the parent material operate (Dixon et al., 2009a; b; Dixon & von Blanckenburg, 2012; Egli et al., 2008; White & Blum, 1995). It seems, however, that other factors (eg., rate of uplift, variability in bedrock type and density etc.) that also play a role in determining the rate in which consolidated bedrock turns into non-consolidated transportable material, make a relationship between soil production and climate weaker. Due to the lack of defendable parameters that relate soil production rate to climate, a fixed value for $\in_o$ (67.5 m/Myr; Table 3-2) from Australia was chosen to represent the range in climates in the area (Heimsath et al., 2001).

Fluvial Erosion

The soil in the model is treated as one uniform functional unit with the capability to store water and support vegetation. The ability of the soil column (or regolith) to be transportable

depends on its erodibility, which in an unburnt state is assumed to be uniform with depth. However, local evidence show that after a severe wildfire the top part of the soil loses its cohesiveness and immediately becomes highly erodible (Nyman et al., 2011; Smith et al., 2011b). A work conducted on the Victorian highlands, Nyman et al. (2013) found that the depth of this non cohesive layer declines exponentially until it almost vanishes 3 years after the fire, with the steepest decline happening over the first year.

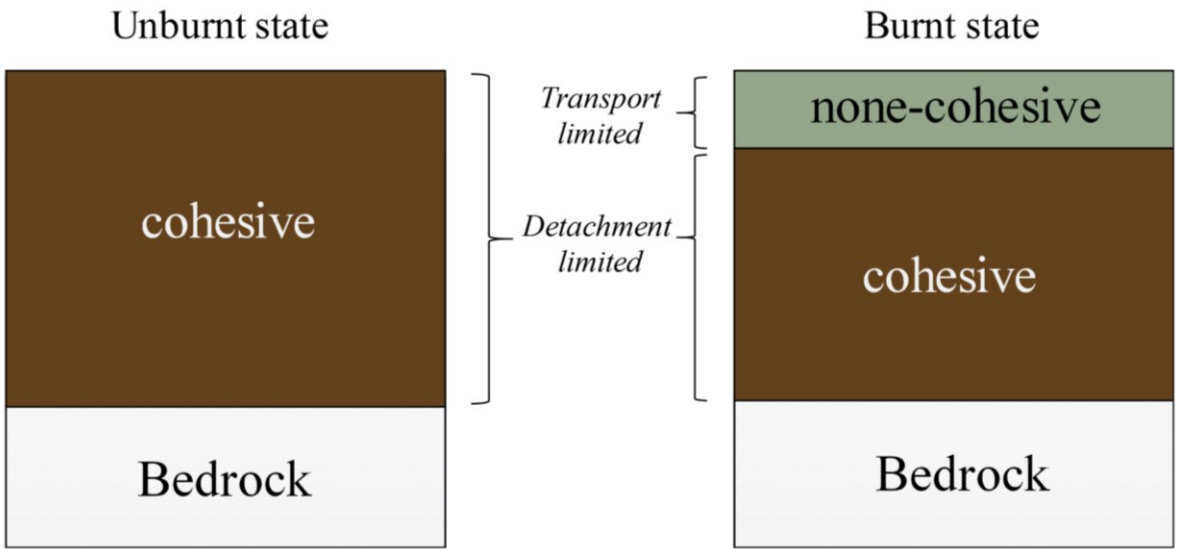

Figure 3-4 –Conceptual representation of erodibility across the soil profile. Soil profile in the model is defined to have two states: Left box represent a soil that is cohesive throughout the profile. Erosion in this case is considered detachment-limited. The right box represent a soil directly after fire, where the top layer is non cohesive. Erosion of this non-cohesive layer is treated as transport-limited.

The model treats erosion from cohesive and transient non-cohesive soil layers, differently. Erosion from the cohesive layer is assumed to be detachment-limited (DLE), as it is limited by the erodibility of the soil. Erosion of the erodible non-cohesive top layer is assumed to be mostly transport limited, as it is limited by the capacity of overland flow to transport (as opposed to detach) sediment (Nyman et al., 2013).

Transport limited erosion (TLE, [L/T]) is calculated using:

$$TLE = d_{nc(t)}\, p_{nc} \tag{3.47}$$

where $d_{nc(t)}$ is the depth of the NC layer at time t; and p_{nc} is the proportion of the NC layer that is eroded per unit time, since the erosion happens on an hourly basis.

Evidence show that the erosion of the NC layer occurs by high intensity rainfall, with the potential to turn into a highly erosive overland flow event (Nyman et al., 2011; Smith et al., 2012). The proportion of NC material that is removed per unit stream power is based on an empirical relationship found by Nyman et al. (2013) (Fig. 10 in their paper).

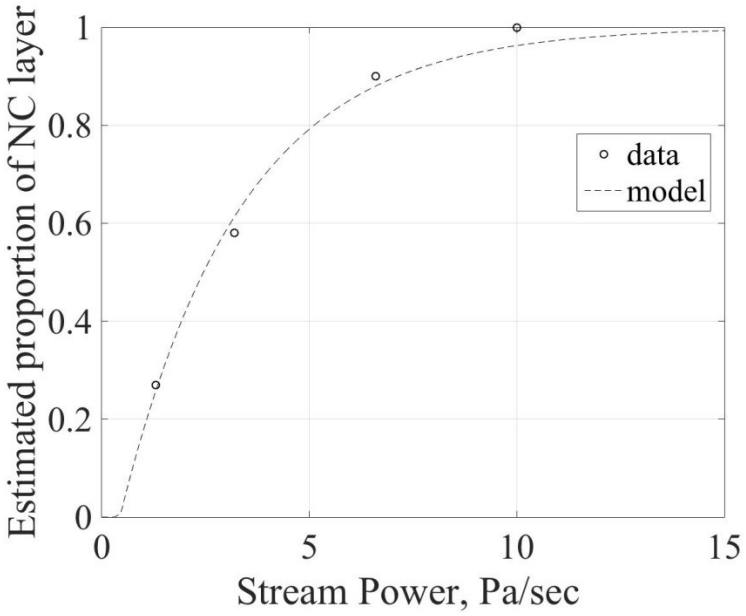

Figure 3-5 – Measured (Nyman et al., 2013) and modelled (Eqn. 3.47) proportion of NC meterial eroded as a function of stream power (Ω).

The proportion of NC material (p_{nc}) transported by peak stream power Ω [Pa/sec] (Figure 3-5) is expressed by:

$$p_{nc} = 1 - a_{nc}\, e^{-b_{nc}\,\Omega} \tag{3.48}$$

where a_{nc} and b_{nc} are calibrated constants (Table 3-2) . Critical stream power Ω_{nc} (when $p_{nc} = 0$) using the data from Nyman et al. (2013) is 0.46 Pa/sec (Table 3-2) Stream power calculated from peak 15 minute runoff values Q_{15} (Eqn.3.22) by:

$$\Omega = \rho_w\, g\, Q_{15} \sin S \tag{3.49}$$

where ρ_w is density of water [M/L^3]; and g is gravity acceleration constant [9.8 m/sec^2]. Note that Q_{15} is calculated for every rainfall event (Eqn. 3.22). This assumes that every rainfall event has a peak 15 minutes intensity (I15). Low I15 will result in low Q15, which can potentially erode a very small portion of the NC layer.

The model generalizes the initial depth of the NC layer, d_{nc_max}, to be 9mm, which translates to 2.7mm of cohesive material, assuming only 30% of the weight to be mineral soil and gravel (as opposed to organic carbon) (Nyman et al., 2013). After the first year following wildfire, the model incorporates the *NC* layer back to the soil mantle as a cohesive medium, which turns "off" transport limited erosion until the next fire. It is assumed that the initial depth of the NC layer, $d_{nc(t_{sf}=0)}$ (t_{sf} is years since last fire), also takes time to recover, which means that a post fire NC layer will be thinner if a fire reoccurs before the system had fully recovered. The initial depth of NC layer is calculated using $d_{nc(t_{sf}=0)} = d_{nc\_max}\, P_{nc\_rec}$, where P_{nc_rec} is the proportion NC depth of the potential maximum, which is calculated using the assumption that it takes 10 years for the post fire *NC* layer to regain maximum depth:

$$P_{nc\_rec}(t_{sf}) = \begin{cases} 0, & t_{sf} \le 1 \\ 0.11\, t_{sf} - 0.11 & 1 < t_{sf} \le 10 \\ 1, & t_{sf} > 10 \end{cases} \quad (3.50)$$

Detachment capacity (D_c,[L/T]) in the model is calculated using:

$$D_c = \frac{K_e(\tau - \tau_{crit})}{\rho_s} \quad (3.51)$$

where τ is shear stress of the overland flow [Pa]; τ_{crit} is critical shear stress, or shear strength [Pa]; and K_e is soil erodibility [T/L]. Values of both parameters were taken from *Wagenbrenner et al.* (2010) for unburnt forests (Table 3-2). Shear stress is calculated using Manning's equation:

$$\tau = \rho_w\, g\, {n_T}^{n_{st}}\, \mathrm{Q}^{n_{st}}\, (\sin S)^{m_{st}} \quad (3.52)$$

where Q is discharge at 50 m down the slope [L^3/T/L]; n_{st} and m_{st} are 0.6 and 0.7, respectively; and n_T is sum of manning's roughness, estimated here as 0.1 (Table 3-2).

Diffusive processes

Diffusive processes include all non-fluvial gravity driven sediment transport down the slope. These processes have been studied for almost a century, but their rates are very hard to quantify due to their slow nature. The basic equation expresses a linear relationship between the flux of sediment (q_d, [L/T]) down a hillslope and the hillslopes gradient:

$$q_d = -D_l \nabla Z \tag{3.53}$$

where D_l is the diffusivity [L/T] coefficient, Z is the elevation, and ∇ is the divergence operator. Evidence of nonlinearity in the diffusive process was reported by Roering et al. (1999) who formulated the following:

$$q_d = -\frac{D_{nl} \nabla Z}{1 - (\frac{\nabla Z}{Sc})^2} \tag{3.54}$$

where q_d is in [L^2/T]; D_{nl} is diffusivity of the non-linear diffusion [L^2/T]; and Sc is a critical slope that when passed ($\nabla Z > Sc$), diffusive flux will become infinite (Roering et al., 1999). The nonlinear diffusive sediment transport has been found to be more appropriate to steeper terrain compared to its linear counterpart (Dietrich et al., 2003). In later work, by using a relatively simple landscape evolution model, Roering (2008) found that observable landform is predicted better when scaling the diffusive process with soil depth. The Author changed the non-linear diffusion equation by:

$$q_d = -\frac{K_c(h) \nabla Z}{1 - (\frac{\nabla Z}{Sc})^2} \tag{3.55}$$

where K_c [L^2/T] is a constant that scales non-linearly with soil depth (h), expressed as $K_c(h) = \eta(1 - exp^{-\beta_r h})$, and η and β_r are calibrated constants (Roering, 2008). This concept is based on the idea that diffusive processes usually occur closer to the soil surface and that there is a finite soil depth below which the diffusive processes are minimal.

The logic behind the soil depth dependency is to capture the effect of vegetation on background erosion processes (Roering et al., 2010). This means that deeper soils can hold more vegetation. More soil means that the soil can hold more water and will be heavier. More vegetation means more tree throw events and more burrowing animals, which, when compared to a thinner soil environment, transport more soil in diffusive-like processes.

Furthermore, using a non-depth dependent diffusive equation (Eqns 3.53 and 3.54), means that rate of diffusive processes will be equal on hillslopes with similar gradient but different ecosystem, for example, open woodland and closed rainforest, which is logically improbable.

Unlike the event-based fluvial representation in the model which assumes that there is no deposition of sediments from upslope, diffusive sediment movement is slower and more incremental and also represent sediment deposition. In order to calculate diffusive flux at a point (i.e., 50 m down the hillslope), it was necessary to account for flux into and out of the model unit. To keep things simple, the model calculates the difference between a flux going out of a hypothetical pixel which center is at 30m down slope with a given gradient, and the flux out of the center of the modelled pixel at 50m with its gradient. The net diffusive flux out of the modelled pixel ($q_{d_{net}}$) is calculated using:

$$q_{d_{net}} = -\left[q_{d_{out}} - q_{d_{in}}\right] = -\left[\frac{K_c(h_{50m})\mathrm{S}_{50}}{1-(\frac{\mathrm{S}_{50}}{Sc})^2} - \frac{K_c(h_{30m})\mathrm{S}_{30}}{1-(\frac{\mathrm{S}_{30}}{Sc})^2}\right] \qquad (3.56)$$

where h_{50m} and $h_{30m}$are soil depths at 50m and 30m downslope, respectively, which for simplicity assumed to be equal; and S_{50} and S_{30} are gradient at 50 m and 30 m down the slope, where $\mathrm{S}_{50} > \mathrm{S}_{30}$, which makes the left term on the right side of the equation with a higher value than the one on the right, in a way that there is always a net loss of sediment at the 50m point.

Table 3-2 - List of parameter descriptions, values with their source.

Para.	Description	Value	Source
S	Slope	26.62	Mean of all the slopes of the steep sites
L_T	lag between peak E_p and peak solar forcing [Days]	30	Estimated
α_{PT}	coefficient	1.26	(Priestley & Taylor, 1972)
S_{LAI}	Volume storage per unit LAI.	1	Calibrated
k_s	Saturation hydraulic conductivity, [mm/h]	200	Estimated
b_{ret}	Water retention parameter	4.9	(Zhou et al., 2013)
p_{nc_max}	Maximum proportion of the *NC* layer that is eroded at time t, [Pa/sec]	1.33	Calibrated
Ω_{nc}	Critical stream power, [Pa/sec]	0.46	Calibrated

a_{nc}	Constant	1.16	Calibrated
b_{nc}	Rate of increase in the proportion of NC layer eroded	0.34	Calibrated
E_w	evaporation rate form soil under wilting point	0.1	(Laio et al., 2006)
n	Porosity (clay loam)	0.5	(Clapp & Hornberger, 1978)
s_h	Soil saturation ratio at hygroscopic capacity	0.1	(Clapp & Hornberger, 1978)
s_w	Soil saturation ratio at wilting point	0.36	(Clapp & Hornberger, 1978)
s^*	Soil saturation ratio at incipient stomata closure	0.5	estimated
s_{fc}	Soil saturation ratio field capacity	0.64	(Clapp & Hornberger, 1978)
k_{lp}	leaf production rate [1/T]	0.001	Calibrated
k_{sl}	leaf senescence coefficient	$5e^{-5}$	Calibrated
M	exponent	4	Calibrated
kss_{min}	Minimum senescence coefficient (structural biomass)	$4e^{-5}$	Calibrated
a_{kss}	Calibration constant	100	Calibrated
c_{kss}	Calibration constant	.95	Calibrated
α_B	System "global" maximum biomass [Kg DM/m^2]	69.11	Calibrated
m_1	exponents	0.43	Calibrated
m_2	exponents	1.79	calibrated
m_3	Exponent	$4.42e^{-5}$	calibrated
LAI_{gmax}	Maximum LAI for the domain	4.17	Calibrated
SLA	specific leaf area [unit LAI/gr]	$4e^{-3}$	(Whitehead & Beadle, 2004)
κ_f	Slope of probability reduction	$14.7e^{-2}$	Calibrated
δ	Maximum fire probability	$1.5e^{-3}$	Calibrated
s_{cut}	Soil Moisture Deficit cutoff value	0.39	Calibrated
a_{mort}	Minimum tree mortality (caused by fire)	0.54	Calibrated (from estimated values)
b_{mort}	Decay of tree mortality function	3.11	Calibrated (from estimated values)
ρ_r	Density of bedrock, [kg/m^3]	2650	
ρ_s	Density of soil, [kg/m^3]	1325	Calculated
ρ_{NC}	Density of non-cohesive (*NC*) material, [kg/m^3]	1325	Assumed
$\in_o$	Maximum soil production rate, [m/Myr]	67.5	(Amundson et al., 2015; Minasny et al., 2015)
H^*	Exponential folding depth of the soil production rate	0.5	(Amundson et al., 2015)
K_e	Detachment limited erosivity [sec/m]	$1.5e^{-6}$	(Wagenbrenner et al., 2010)
τ_{crit}	Critical shear stress, [Pa]	0	(Wagenbrenner et al., 2010)

n_T	Manning's roughness for cohesive material	0.02	Estimated as cohesive river bed (Table 3 in Coon, 1997)
n_{st}	Empirical constants	0.6	(Istanbulluoglu & Bras, 2005; Willgoose et al., 1991a)
m_{st}	Empirical constants	0.7	(Istanbulluoglu & Bras, 2005; Willgoose et al., 1991a)
Sc	Critical gradient above which hillslope diffusion becomes infinite	1.25	(Roering, 2008)
η	Maximum transport coefficient, [L^2/T]; (calibrated by (Roering, 2008))	$4.5e^{-3}$	(Roering, 2008)
β_r	Root density exponential decay term [m^{-1}]	2.6	(Roering, 2008)

3.4 Model implementation

The purpose of the model is to evaluate the role of fire in coevolution within the Victorian forested uplands and simulates a hypothetical point located 50 m down the ridgeline, with a specific aspect and rainfall regime to vary the climatic forcings. A flow chart that described daily model simulations is presented in Figure 3-6. Simulations run on a daily basis inter-storms, and hourly basis intra-storms for a selected number of years and tracks changes in soil depth, biomass, soil moisture and canopy water storage, while the critical zone evolves. Every daily cycle, evapotranspiration rate is calculated, depending on the moisture status across the system's reservoirs and on the partitioning of the evaporative demand between the canopy and the soil. Furthermore, *NPP* is calculated daily, and its products are allocated between the structural and leaf biomass, depending on the recovery state of the forest and on transpiration rates. Once a year (on the 1st of January) the flammability status is calculated depending on antecedent moisture conditions in the system, and a stochastic fire occurs occasionally, burning the leaves and a proportion of the structural vegetation, depending on the vegetation type.

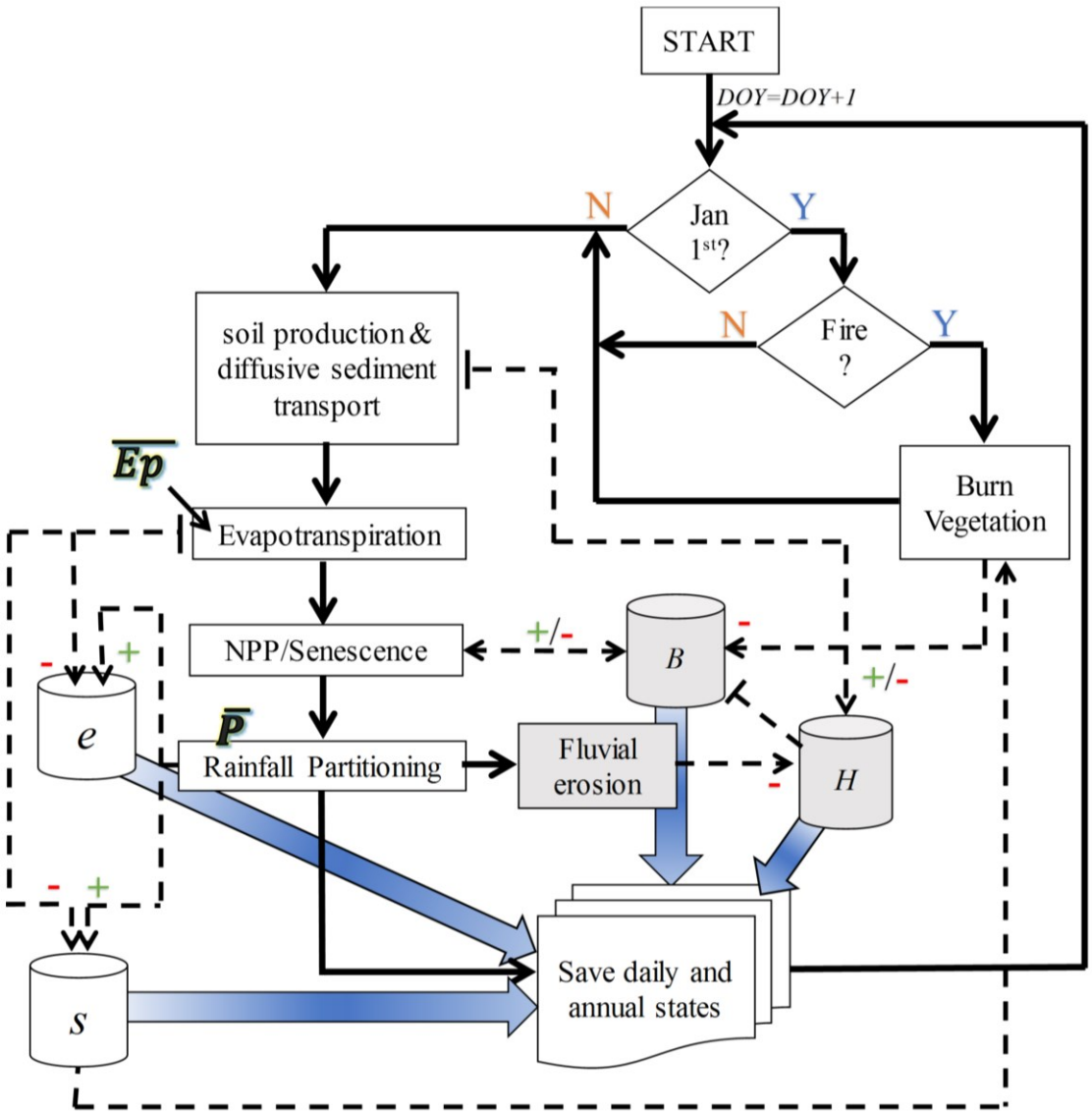

Figure 3-6 – A flow chart that describe the model cycle, processes and the change in the state variables. In this flow chart: a box represent a process; a diamond represent a decision; full line arrows represent progress order; dashed arrows represent changes in state variables (cylinders); arrows with blunt end represent control of the state variable on the process it is pointing at. DOY is day of year (1/365).

3.4.1 Climatic forcings during simulations

The amount of incoming solar radiation a hillslope receives is determined by the latitude and its slope and aspect orientation (eg., Yetemen et al., 2015b; a; Zhou et al., 2013). In order to obtain uniformity and to isolate climatically driven echo-hydro-geomorphic processes, slope across all simulations was kept constant (Table 3-2) while aspect was predefined before each

simulation as either north or south orientation. To obtain variations in climatic scenarios, the model was designed to simulate 5 different rainfall regimes, ranging from ~542 mm/yr to ~1610 mm/yr (more details in Appendix III), and potential evapotranspiration (E_p; Eqn 3.5) typical to either north or south facing aspects. These conditions enabled the usage 10 different climatic scenarios using pairs of rainfall and E_p.

During simulations daily E_p for north and south facing hillslopes were calculated using Eqn 3.5 with $E_{p-daily}$ and Δd typical to each aspect. For simplicity, typical aspect-specific values for $E_{p-daily}$ and Δd were calculated by averaging their values from the three steepest parameterisation sites (Eildon, Reefton and Frenchman's Spur; Table 3-1). This approach assumes that values for $E_{p-daily}$ and Δd do not vary significantly within each aspect, as long the slope is similar. This approach neglects the possible higher proportion of diffuse short-wave radiation and might cause overestimation of E_p, especially in higher rainfall/elevation sites. It is argued that this simplification is sufficient for the purpose of the model, however, it is considered to be a model limitation. Mean values used for $E_{p-daily}$ were 5.15 mm/day and 3.62 mm/day; and for Δd 5.78 mm/day and 6.48 mm/day for north and south facing slopes, respectively.

3.5 Model Parameterisation and calibration

3.5.1 Parameterisation and Calibration processes

The model was parameterised and calibrated using local data wherever possible. Figure 3.7 shows some of the key components in the model and what type of data used for parameterisation.

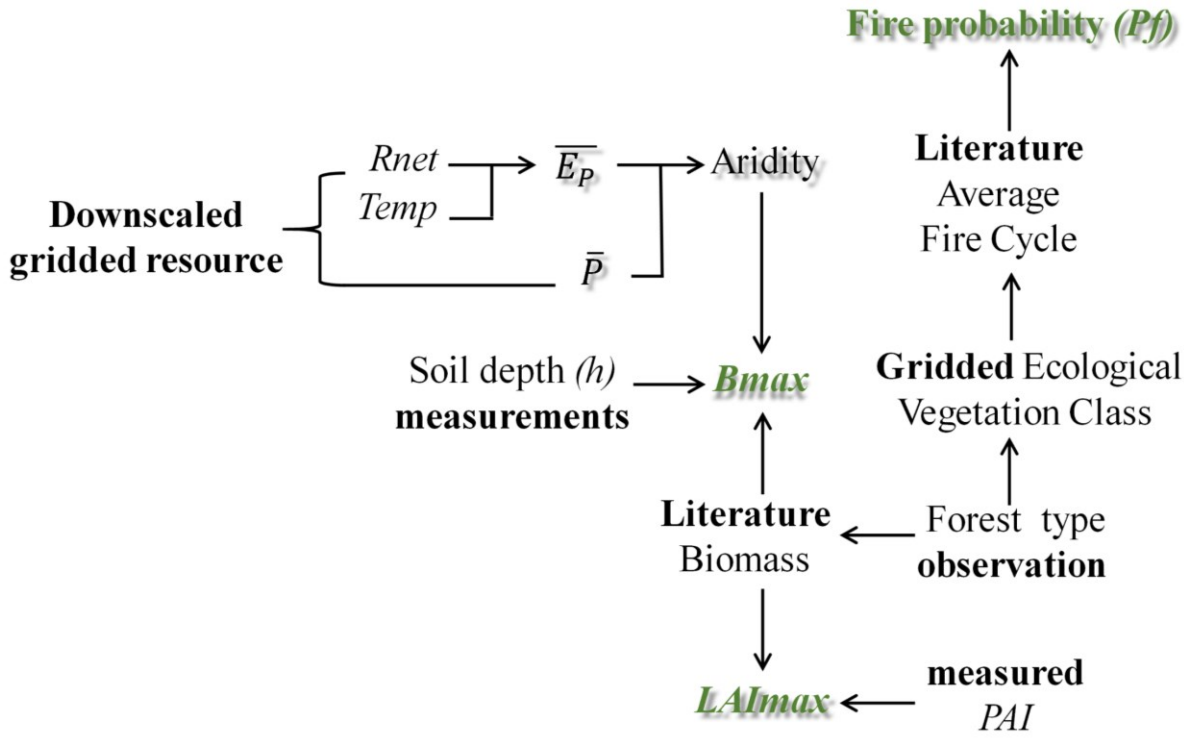

Figure 3-7 - Parameterization of some key model component and their sources. Function that calculate the variables in green were obtained for the parametrisation sites (Table 3-1) using various sources: measurements, observations, gridded resources (Australian Bureau of Meteorology, 2017) and literature values.

Aridity

Aridity for the parametrisation sites (Table 3-1) was calculated by dividing potential evapotranspiration ($\overline{E_P}$) by mean annual precipitation ($\bar{P}$), both in [mm/yr]. $\overline{E_P}$ was calculated using Eqn 3.6 (Priestley & Taylor, 1972) with downscaled gridded net radiation (*Rnet*) and temperature data for each parameterisation site (Nyman et al., 2014b), and $\bar{P}$ was sampled from a gridded data for mean annual precipitation [mm/yr] (Australian Bureau of Meteorology, 2017)

Maximum biomass B_{max} ***)***

Maximum biomass (B_{max}) is necessary to constrain site productivity, which was assumed to be limited by soil depth and aridity. Parameters for Eqn 3.40 (Table 3-2) were obtained by plotting biomass values with measured soil depth (H [m]) and calculated aridity values for each of the 10 parameterisation sites. Since biomass was not explicitly measured, estimated

literature biomass values (Table 3-1) combined with several anchoring points (i.e., assuming that *zero* soil depth holds *zero* biomass, regardless of aridity) were used to calculate B_{max}, as presented in Figure 3-8. Estimated biomass values were determined by comparing observations of vegetation structure, forest type and data from gridded Ecological Vegetation Classes (EVCs) across the sites, with estimated biomass value for similar forests taken from Volkova et al., (2015) and Greirson et al. (1992), for vegetation in Victoria (Table 3-1).

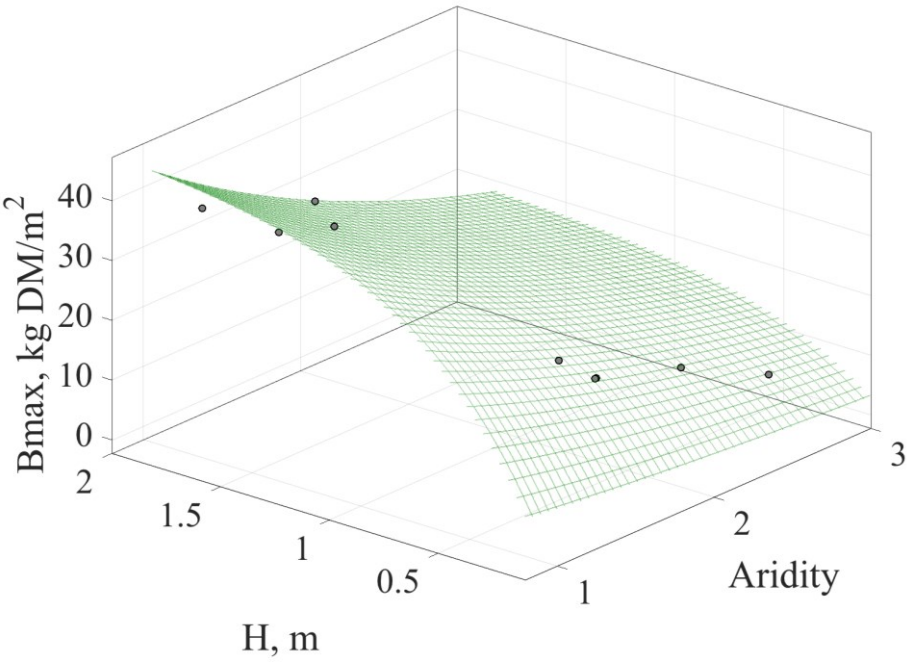

Figure 3-8 Maximum biomass conceptual model fitted to measured soil depth data (H), aridity and biomass values from the literature (R^2=0.97; RMSE=3.34 kg DM/m^2) for the 10 sites. Note that the model was forced to have zero biomass when soil depth is zero, regardless of the aridity.

Maximum LAI (LAI_{lmax})

Maximum *LAI* (LAI_{lmax}; Eqn 3.41) limits *LAI* accumulation and is essential to the partitioning of rainfall and energy by the vegetation (Eqns 3.7 and 3.8). In the model, LAI_{lmax} is constrained by relating it to specific literature biomass values (Table 3-1). This component was calibrated using measured plant are index (PAI) obtained by hemispherical photography analysis (Table 3-1), plotted against the estimated literature values of biomass each at the parameterisation sites (Figure 3-9).

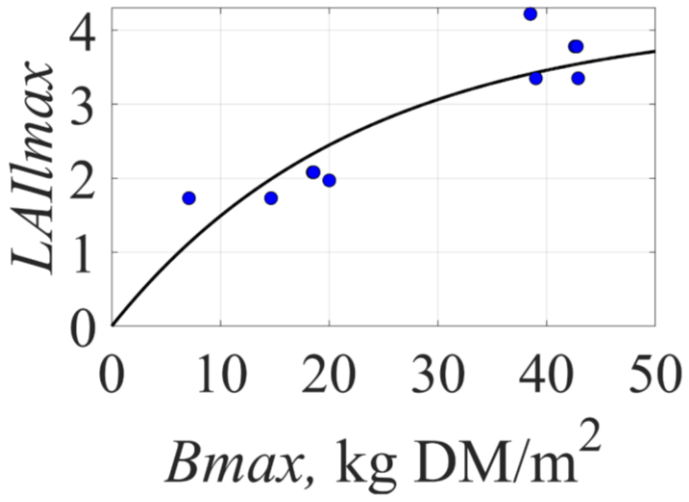

Figure 3-9 - The function calculating the maximum LAI (LAI_{lmax}) fitted to literature values for biomass across the 10 parameterisation sites. Note that the LAI_{gmax} (Table 3-1) can be calculated using the maximum value that the LAIlmax asymptotes towards (Eqn 3.41).

Calibration of canopy water holding capacity (S_{LAI})

Preliminary sensitivity analysis of the ecohydrological partitioning was done by simulating 1000-year simulations without fire for 10 different climate scenarios (varying in rainfall and solar exposure). Results showed that interception loss is very sensitive to small changes in canopy water storage capacity parameter S_{LAI} (water depth per unit LAI, [L/L/L]), compared to transpiration, soil evaporation and stream flow. It was then assumed that the capacity S_{LAI} is similar at all the sites, as all are occupied mainly by eucalypt type forest. Thus, S_{LAI} was calibrated by achieving around 20% interception loss in the wettest site, assuming it resembles a mature mountain ash forest (60-120 years old) (Vertessy et al., 2001). Although the calibrated S_{LAI} seems high (i.e., for 1 unit of LAI to hold 1mm of water), it may be that the calibration compensates for other processes that are not explicitly modelled, for example, interception of throughfall by leaf litter (Dunkerley, 2015) (which increase as vegetation becomes denser, (Nyman et al., 2015a)), and by tree bark. Other possibilities include: (i) underestimation of evaporation during rainfall, which has been shown to have a significant effect on interception capacity (eg., Dunkerley, 2008); (ii) underestimation of the effect of canopy in intercepting rainfall by the current model (Eqns 3.13 and 3.14); (iii) improper representation of the NSRP model in simulating rainfall.

3.6 Model evaluation and discussion

3.6.1 Ecohydrology

Predictions of ET were plotted within the *Budyko* framework (Figure 3-10) in order to evaluate how the model reproduces some existing theoretical relationship between climate and transpiration. The Budyko framework estimates the evaporative index (proportion of ET from the long term rainfall), using an index of long term climatic forcing balance (or aridity), which is calculated by the proportion of evapotranspiration from the long term mean annual rainfall (Budyko, 1974). Results show a relatively high agreement between the two models (RMSE=0.07 units; Figure 3-10) indicating that the model reasonably predicts the partitioning of rainfall in agreement with expectations. The Budyko framework generally predicts the effect of aridity on water balance at large spatial scales, so deviations in ET/P at this scale are expected (Troch et al., 2013; Zhang et al., 2004), and explained by various point-scale differences, such as soil water holding capacity, soil/rooting depth, average storm depth (eg., Donohue et al., 2012).

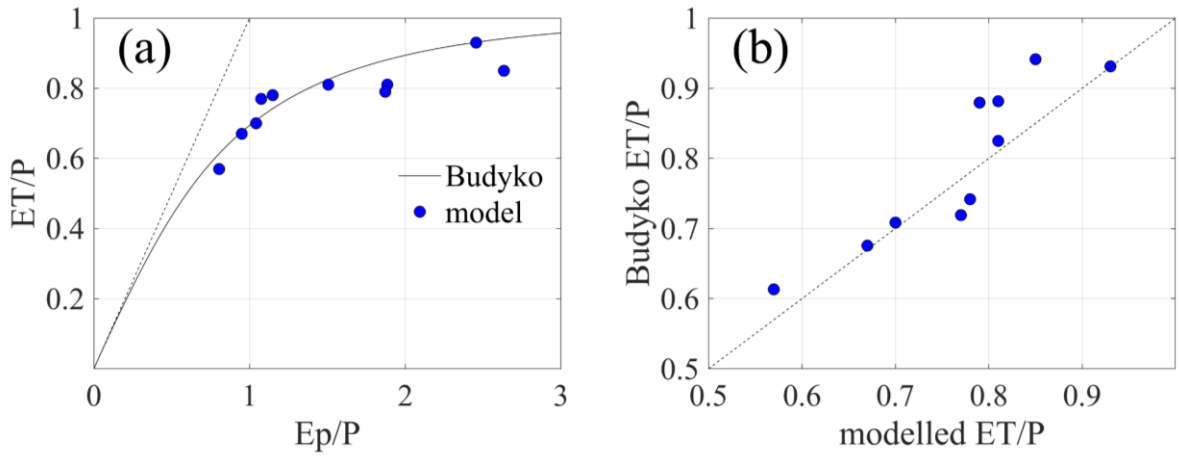

Figure 3-10–Long term modelled ET/P from 10 simulations with varying climatic scenarios (section 3.4.1) plotted on top of the Budyko framework, (a); and the comparison of ET/P between the two models (b). RMSE = 0.07. Dashed line in (a) is plotted using Budyko's original equation (Budyko, 1974):

$$ET = \left[E_o P \tanh(P/E_o)\left(1 - \cosh(E_o/P) + \sin(E_o/P)\right)\right]^{0.5}.$$

The next step was to evaluate how the model partitioning of ET into transpiration, soil evaporation and interception loss compared with observations. Due to scarcity of studies that quantify the partitioning of rainfall across a variety of climatic conditions across the eastern uplands, modelled values for typical Wet, Damp and Dry sites were compared with three studies from available literature with corresponding rainfall-forest type combinations. Modelled values were obtained from 1000 year-long simulations running with three different climatic scenarios typical to wet, damp and dry sites (with aridity of 0.75, 1 and 1.5), without fire and with fixed soil depths. Observations were taken from three studies from local literature with corresponding rainfall-forest type combinations. Sites in Vertessy et al. (1998, 2001) are described to be a pure mountain ash (*Eucalyptus regnans*) stand, which typically occupy intermediate elevations (200-1000m) with a mean annual rainfall of 1200-1800mm (Vertessy et al., 1998). The intermediate aridity site (Nolan et al., 2014) is described as a mixed species stand with measured 1155 mm/yr annual precipitation on the year of measurements. The more arid site (Mitchell et al., 2012) is described as a Dry sclerophyll forest with mean annual precipitation <1200 mm/yr. Modelled predictions of partitioning were found to correspond well to the published data (Figure 3-11). This result is an independent evaluation and provides strong case for the validity of the eco-hydrology component of the model. Furthermore, these results provide support to the simplification assumptions that were made in calculating daily E_p (See section 3.4.1).

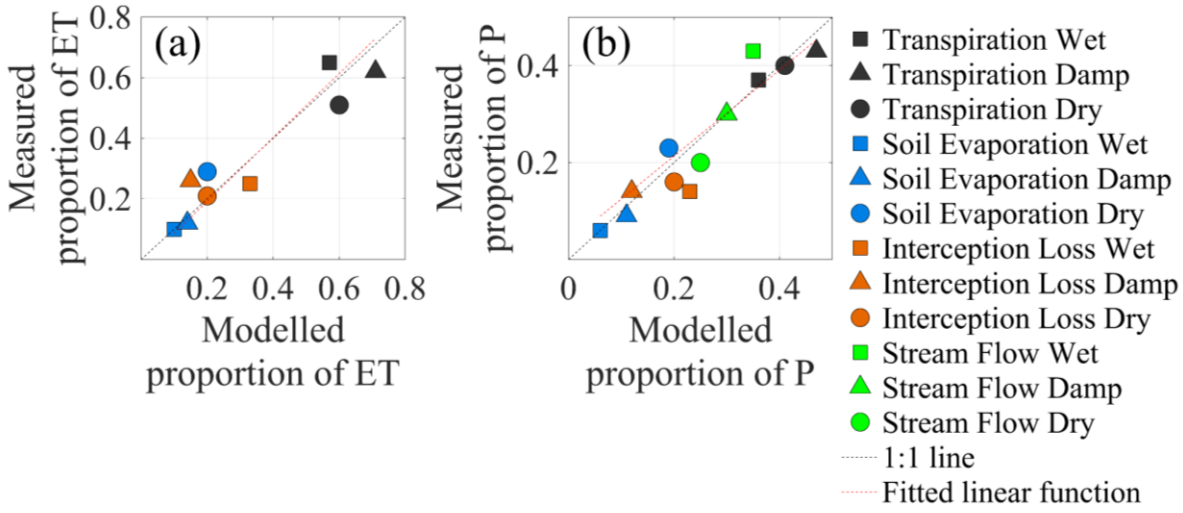

Figure 3-11 – Modelled vs literature values for transpiration, soil evaporation and interception loss as a proportion of ET (RMSE=0.03; (a)) ; and transpiration, soil evaporation, interception loss and stream flow as a proportion of P (RMSE=0.03; (b)) for sites with three estimated aridity values. Modelled hypothetical sites were compared with

measurements from Vertessy et al. (1998, 2001), Nolan et al. (2014) and Mitchell et al. (2012), for wet, damp and dry forests.

Hydrological partitioning in the model was examined further for a larger range of climatic scenarios by running 1000 year-long simulations for ten different climatic scenarios similar to the parameterisation sites (Table 3-1). The purpose of this analysis was to evaluate if the systematic change in rainfall partitioning along an aridity gradient was reasonable for the model domain. Results show that the proportion of soil evaporation increases and that of stream flow decreases with increasing aridity (Figure 3-12). The increase in soil evaporation with aridity is caused by higher evaporative demand at the soil surface due to lower PAI values (Table 3-1) as aridity becomes higher and vegetation becomes sparser and more water limited. The large increase in soil evaporation occurs between aridity 1.15 to 1.5, possibly due to the fact that soil becomes significantly shallower in sites between these aridities (Table 3-1). As soil evaporation becomes higher, transpiration becomes lower. This can be explained by the reduction in soil depth and LAI with increase in aridity. The modelled proportion of interception loss was relatively constant throughout the climatic domain (Figure 3-12), similar to other local studies (Mitchell et al., 2012; Nolan et al., 2014; Vertessy et al., 2001).

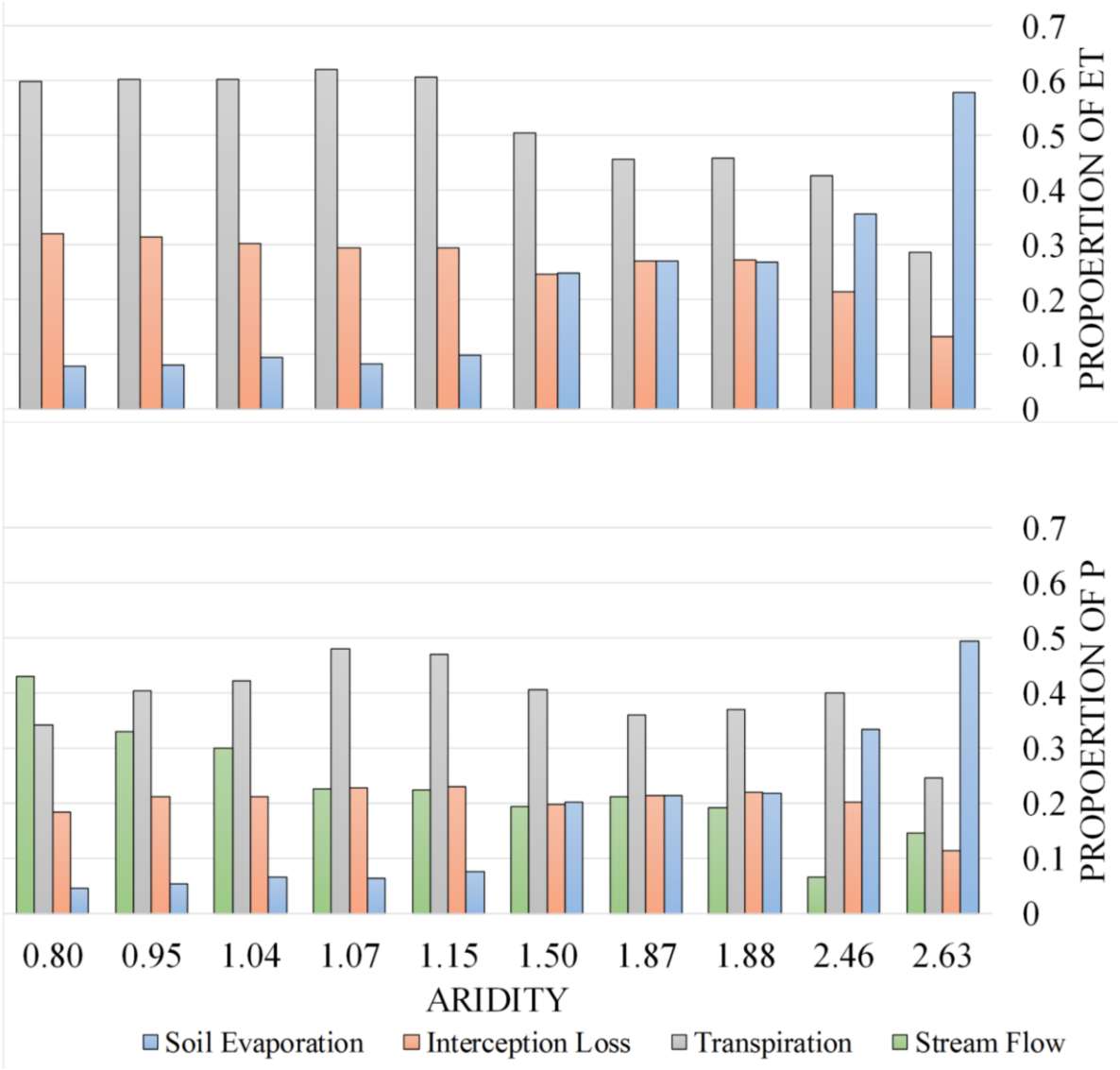

Figure 3-12– Partitioning of ET into soil evaporation, interception loss and transpiration (a) and of P to soil evaporation, interception loss, transpiration and stream flow (b), ordered in increasing aridity. Plots produced by running 1000 year simulations with 10 different climatic scenarios (section 3.4.1) without fire.

3.6.2 Fire

Fire regime

The fire regime was calibrated using Average Fire Cycle estimations (Appendix II). In order to evaluate how the modelled fire regime corresponds with real fire regimes, the output distributions of fire frequency were compared with published theoretical distributions. A

Weibull distribution was the best fitted distribution for fire frequency for a 10000 year simulation (Figure 3-13), which is a commonly observed fire distribution (Johnson & Wagner, 1985; McCarthy et al., 2001). Weibull distribution means that the flammability of a site is a power function of time since fire (McCarthy et al., 2001). According to the way that the fire model was calibrated, flammability should not change with time since fire, as it was not restricted by fuel availability, but only to soil moisture thresholds (Appendix II). Thus, it appears that that soil moisture dynamics, which is controlled by ecohydrology and rainfall, can be a major control on the return interval distributions in a widely used common distribution model (Gill & McCarthy, 1998; McCarthy et al., 2001).

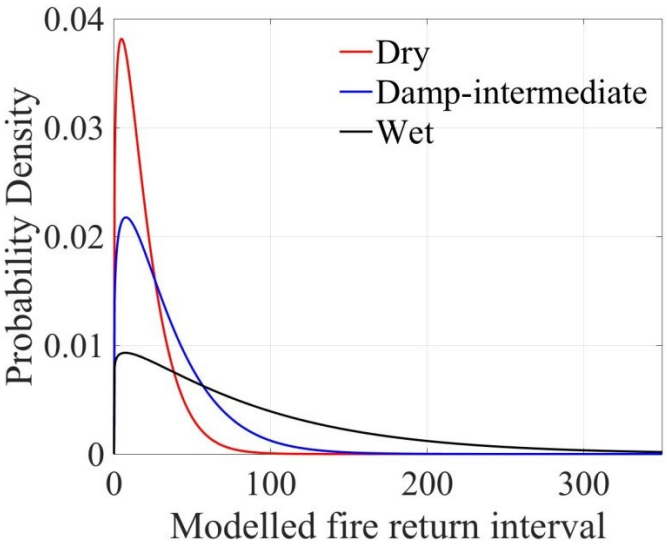

Figure 3-13 – Weibull probability density functions fitted to modelled fire return interval for 3 sites: dry (aridity=2.61), Damp (aridity=1.49) and wet (aridity=0.82). Mean fire return interval for the sites were 18.3, 32.6 and 87.3 years, for dry damp and wet sites, respectively. Results were analysing 10000 year simulations with wet, damp and dry climatic scenarios.

Evaluation of post fire recovery trends

Vegetation and ecohydrology showed realistic time to recovery based on literature (Gharun et al., 2013a; Nolan et al., 2015) and expert opinion. The model was designed to allocate productivity into producing leaves on the first years after fire, in order to drive transpiration and photosynthesis and generate recovery. Then, when recovery of LAI increases bigger proportion of primary productivity is allocated into the recovery the structural biomass (Eqn 3.35 and 3.37). Figure 3-14 shows the recovery of the LAI and structural biomass (*Bs*) with

time since fire for simulations expressing dry (Figure 3-14a and b), damp (Figure 3-14d and e) and wet (Figure 3-14g and h) climatic scenarios across a 10,000 year simulation. Modelled results showed that, on average, it takes between 10 to 15 years for LAI to recover to pre-fire values when the model was forced with wet (Figure 3-14g and g), damp (Figure 3-14d and e) and dry climatic conditions (Figure 3-14a and b), which is reasonable according to expert opinion.

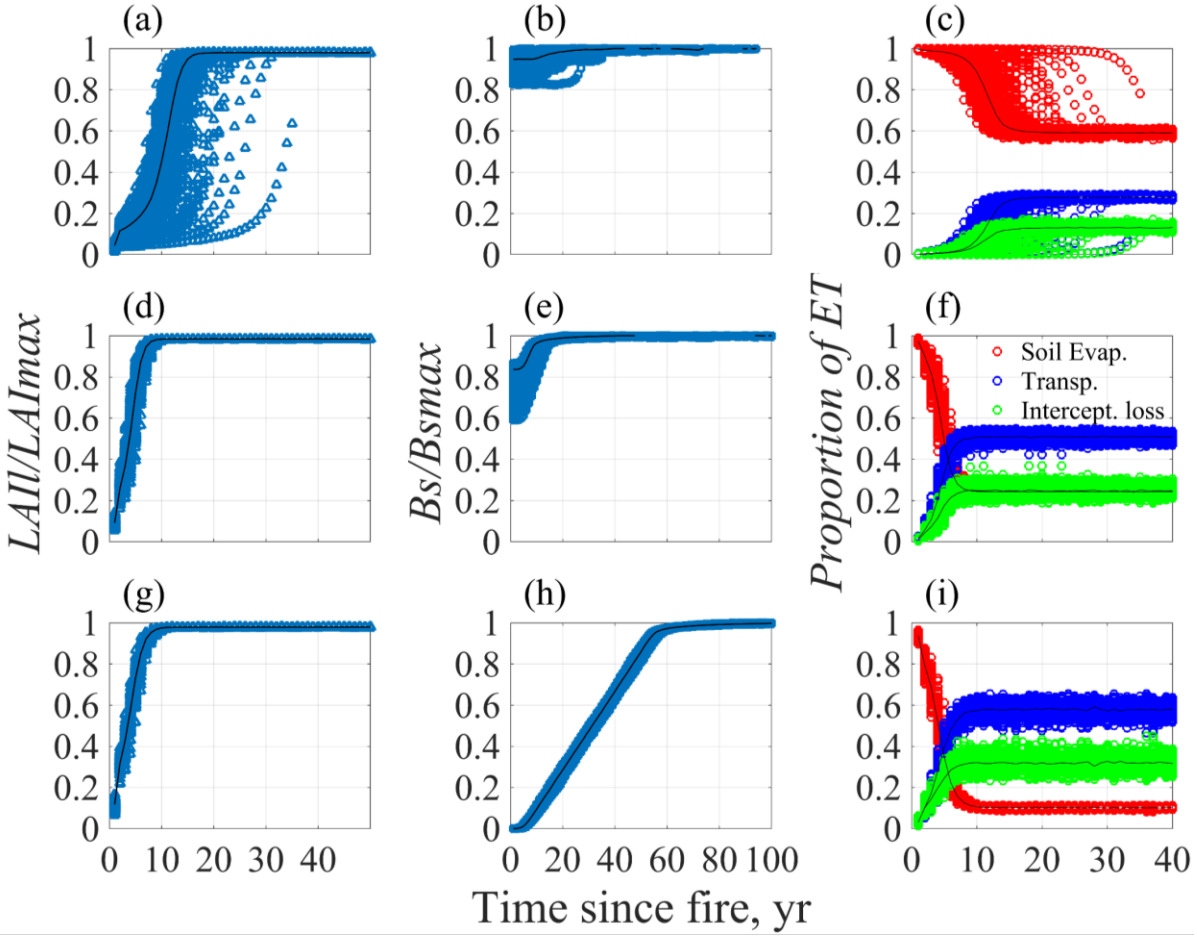

Figure 3-14 – Modelled recovery of LAI (a, d and g), structural biomass (b, e and h) and proportion of ET (c, f and i), for hypothetical dry (top row), intermediate/damp (middle row) and wet (bottom row) climate simulations. Aridity values were 2.61, 1.49 and 0.82 for dry, damp and wet sites, respectively. Black line indicate median of the modelled values for a given time since fire. Red, purple and green dots (on c, f and i) represent soil evaporation, transpiration and interception loss (as proportion of ET), repectively.

On drier mixed species forests, which are colonized by various combinations of fire "tolerant" species, considerable proportions of the structural biomass survive after a fire, while leaves regenerate from epicormic shoots (Bowman, 2000). Modelling results showed that the recovery period of *LAI* vary considerably across the simulation that was forced by dry climatic conditions (Figure 3-14a). It was suggested that in these conditions, the variations in rainfall and thin soils were the main factors limiting the recovery rates (Eqn 3.35 and 3.36). On the other hand, the modelled fire only burnt a small proportion of structural biomass (Figure 3-14b and e). This sets a higher starting point for the recovery of structural biomass (Bs), which recovers relatively quickly.

Forest on wetter climates (aridity<1) are characterised by single-species stands (mainly mountain or alpine ash stands) with thick understory. In these forests, a severe fire not only burns the leaves, but also kill the trees, and the recovery of the biomass starts from the large seed bank in the soil (Benyon & Lane, 2013; Clarke et al., 2015; Fairman et al., 2016). This type of recovery strategy was roughly replicated by the model (Figure 3-14h). Despite the fact that the fire killed all the structural biomass, LAI recovered within 10 years of the fire, possibly due to the relatively high soil moisture content. In these type of forests, the recovered LAI is compensated by seedlings that regenerate after the fire (Benyon & Lane, 2013), which results in a considerable reduction in stream flow in these type of forests within 20-30 years after the fire (Kuczera, 1987; Vertessy et al., 2001). With time, the density of the trees is reduced and the individual trees grow in the expense of others and biomass accumulation reaches a plateau. Results from the model showed that recovery of the structural biomass plateaus at around 60 years. It is postulated that even though forest structure might change after that period, by self-thinning for example, overall biomass (both understory and overstory) doesn't change much beyond the 60 year mark.

Post fire recovery of vegetation is important for catchment hydrology. The right column on Figure 3-14 shows the recovery of the partitioning of ET into soil evaporation, transpiration and interception loss, across the dry (Figure 3-14c), damp (Figure 3-14f) and wet (Figure 3-14i) simulated scenarios. Results show that the rate of recovery of the ecohydrology depended on the recovery of the *LAI* since the partitioning in the model depend on the recovery of the canopy (Eqns 3.13-3.14 and 3.25-3.26). Once the $LAIl/LAI_{lmax}$ reached 1 (Eqn 3.8), canopy cover is at its maximum according to biomass holding capacity of the soil (Eqn 3.41 and 3.40).

In a vegetation recovery study, Gharun et al. (2013a) found that resprouting eucalypt forest exhibit a slower recovery of LAI after fire, as compared to ash forests. The authors claim that in these type of forests, it is very unlikely that foliage cover in regrowth stands would exceed pre-fire cover within the first decade after fire. Nolan et al. (2015) found that the overall length of recovery for evapotranspiration and streamflow of a damp mixed-specie forest was 8-12 years, much less than for a wet-eucalypt forest recovering from seedlings only. Most of the studies on post-fire recovery of ecohydrology are based on limited number of forest stands, while the long term effect of fire on ecohydrological partitioning is scarce, and rely mostly on short-intermediate term stream flow observations (Kuczera, 1987). It seems that the modelled recovery time of both biomass and ecohydrology sit within reasonable range, considering the model's objectives.

3.6.3 Runoff and peak discharge

Overall it seems that the model predicts the right trend in runoff ratio (RR; the proportion of runoff from rainfall) across the aridity domain, possibly underestimating runoff for wetter sites (low aridity). In a recent field experiment, Van der Sant (2016) measured runoff on 5 sites across an aridity gradient using 8 m and 16 m paired plots. The author found a strong relationship between RR and aridity and concluded that aridity can be a good predictor for runoff production across the eastern uplands. Figure 3-15 shows a comparison between post-fire modelled and a function fitted to measured event-based runoff ratios as a function of aridity, as reported in Figure 4-40 in Van der Sant (2016). Modelled runoff ratios were calculated for 8 difference climate model conditions (4 different rainfall regimes across north and south facing aspects) over 10000-year simulations, only for the first year post-fire. These were compared with a function fitted from measured runoff ratio values.

Overall, modelled RR show similar pattern with aridity as the measured values, as it fits between the function fitted for 8m and 16m plots on high aridity values (Figure 3-15). Unlike the model presented here, measured RR values were obtained across storms that are longer than one hour, possibly missing rainstorms that weren't long or intense enough to be recorded on the tipping bucket on the runoff troughs. By excluding small rainstorms (lower than 10mm/h), modelled RR increased to higher levels and showed similar patterns with the measured data from the 8m long plots (Figure 3-15). Modelled RR underestimated measured values when simulated under wet conditions. It is plausible, that compared to drier sites,

there are higher chances that the high non-water repellent patches somewhere along the hillslope (Nyman et al., 2014a) will cause run-on from the upper part of the hillslope to infiltrate on low aridity sites, which would potentially reduce the RR to near zero. For example, Sheridan et al. (2007) suggested that that on very wet sites, post-fire runoff and erosion were generated from several meters from the stream rather than the hillslopes themselves.

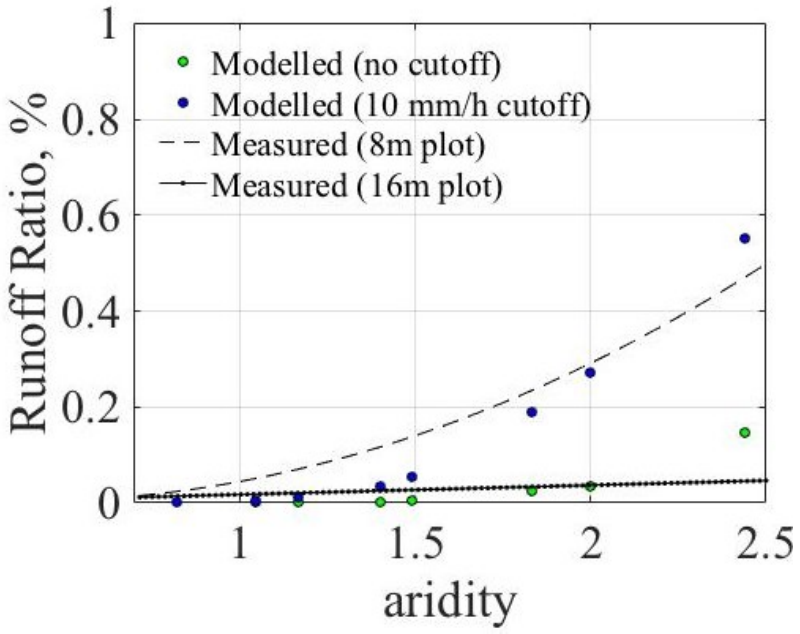

Figure 3-15 – Modelled and measured event-scale runoff ratio for first year after fire. Modelled values represent event-scale runoff ratio with a 10mm/h hourly rainfall intensity threshold (i.e., excluding all relatively "small" rainfall events), and event-scaled runoff ratio for all the rainstorms. Lines are functions fitted to measured event-based runoff ratio from 8 meter and 16 meter plots (Van der Sant, 2016), The two plot lengths are presented to illustrate the effect of scale on possible results. Modelled data represent values for 50 m hillslope stretch.

Within high intensity rainstorms, extreme short duration-high intensity bursts of rainfall have been shown to be the most erosive, and could possibly trigger extreme post-fire erosion events such as debris flows, when soils are less permeable (Nyman et al., 2011, 2015b). The performance of the model in predicting peak flows (Q15) was evaluated by comparing modelled peak runoff for a set of simulations varying in rainfall and solar radiation (which creates variations in aridity) with a surface fitted to runoff data from Van der Sant (2016)

(Figure 3-16). Results show that the modelled values follow similar trend in Q15 compared to the measured function. It is argued that in a way that it is sufficient for the model's purpose (Figure 3-16).

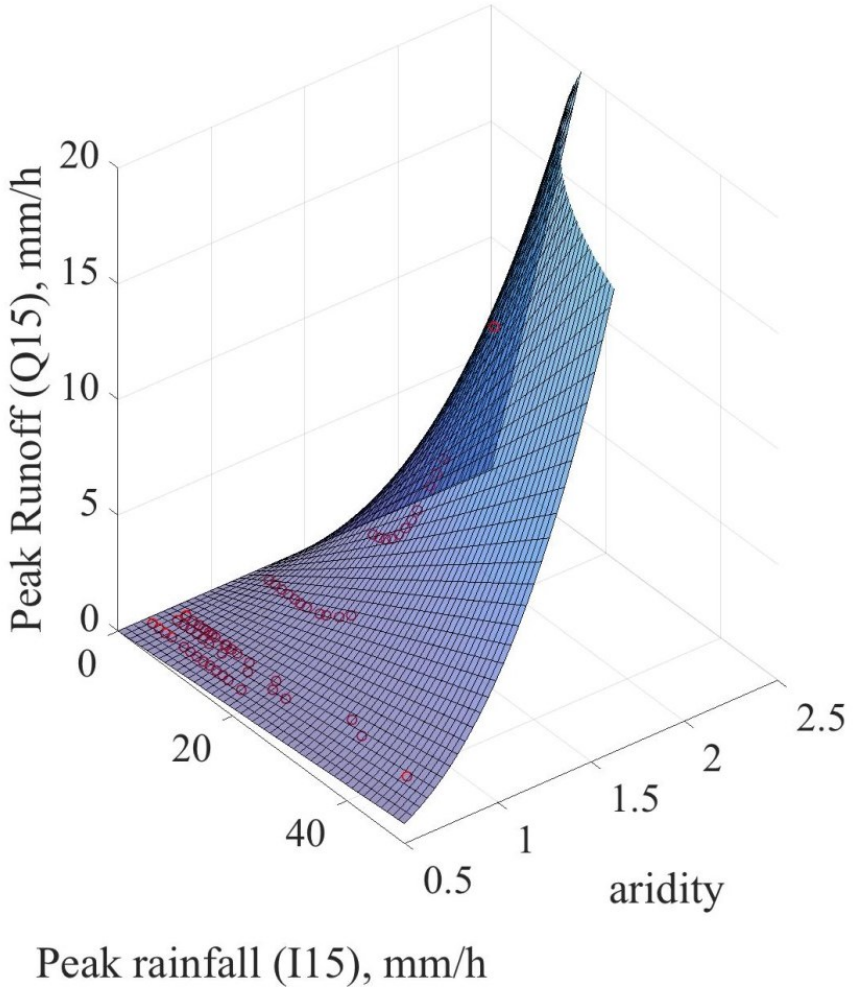

Figure 3-16 – Peak runoff rate (Q15, [mm/h]) as a function of peak rainfall (I15) and aridity for first year after fire. Surface represent a function fitted to measured data from Van der Sant (2016) (Figure 4-41). The function had the form of $Q15 = 2e^{-4}\ I15\ AI^{3.76}$, respectively. Modelled *Q15* for each pair of *I15* and aridity was calculated by using Eqn 3.12 with post-fire infiltration capacity (*Ic*) values (Eqn 3.17) as cutoff for several aridity values.

Modelled peak discharge showed similar trend with rainfall intensity as measured values on a dry site (Figure 3-17). Measured discharge data was obtained from a study that monitored two small (0.29 ha) and relatively dry (mean aridity of 2.2) north and south facing headwater catchments at Stoney Gully Catchment, Victoria, starting approximately six months after it

was severely burnt on February 2009 (as known as the Black Saturday fires) (Noske et al., 2016). Modelled values were produced by running the model under dry climatic forcings (MAP of 760mm/yr) and using infiltration capacity (*Ic*) for one year after the fire at similar aridity (Eqn 3.17; see Appendix IV for more detail). Modelled predictions slightly underestimate (overestimate) peak discharge at low (high) values (Figure 3-17b). However, overall, despite differences in spatial scale and slope, results show that modelled discharge per unit area follow similar trends as the measured data (RMSE = 32 m^3/ha/hr).

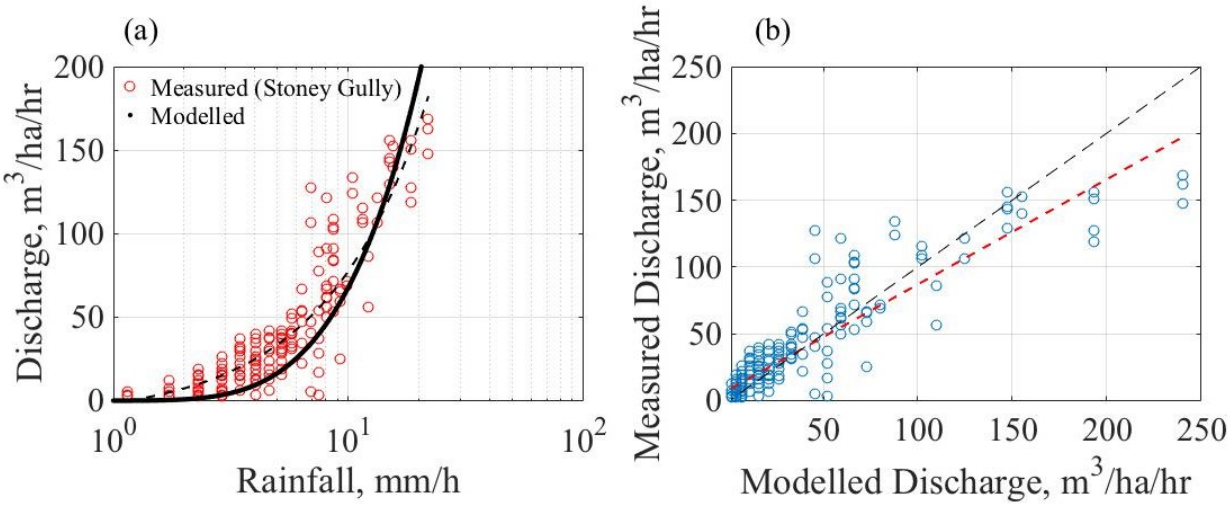

Figure 3-17 - Measured and modelled discharge for the first year after a fire, as a function of rainfall depth (a); and a comparison between modelled and measured discharge values (RMSE = 32 m^3/ha/hr) (b). Dashed line in (a) is a linear function fitted to the measured data. Red and Black dashed lines in (b) represent fitted linear function and 1:1 line, respectively.

3.6.4 Erosion rates

Mean sediment yield from four studies are summarized in Table 3-3, while modelled values from sites of similar rainfall are presented on Table 3-4 and summaries and compared with modelled values in the following paragraphs. The purpose of the analysis was to determine if the model produces erosion rates that are reasonable in terms of overall magnitude and variation across the domain. In addition, erosion rates are paired with approximated fire return intervals to determine if denudation rates are reasonable given the limited data on these rates in the region.

Table 3-3 - Sources of measured sediment yield, and estimated fire return interval and long-term erosion rates

Location	Source	MAP	Type	Time since fire	mean sediment yield	Estimated fire interval*1	Estimated long-term erosion rate*2
		[mm]			[t/ha/yr]	[yr]	[mm/ky]
Stoney Gully	*Noske et al* (2016)	954	small headwater	1 5	10.05 0.12	20	47
Upper Yarra Catchment	*Cawson et al* (2013)	1200	hillslope/ unbound plot	1 unburnt	0.19 $1.3e^{-4}$	30	0.49
Ella creek	*Smith et al* (2011a)	1400	catchment	2 unburnt	0.11 0.01	60	0.9
East Kiewa	*Lane et al* (2006)	1800	catchments	1 unburnt	2.96 0.23	80	20.32

*1 – estimated by using site description and choosing similar fire interval of a similar site (Kennedy & Jamieson, 2007).

*2 – estimated using simple calculation of measured post fire and unburnt erosion rates and fire frequency, and converted to mm/kyr by using soil bulk density of 1300 kg/m^3.

Literature values show the highest sediment yield in dry sites, compared to wet ones, with a minimum of one order of magnitude difference between the burnt and unburnt states (Table 3-3). This is consistent with reports of higher overland flow values at sites with higher aridity (Sheridan et al., 2016; Van der Sant, 2016).

Measuring erosion rates from a pair of severely burnt headwater catchments in north eastern Victoria, Noske et al. (2016) reported a mean sediment yield of 10.05 T/ha/yr during the first year after the fire, about two orders of magnitude higher than that measured five years after the fire. The authors link the increased erosion to the reduction in infiltration rates (due to hydrophobic conditions on the soil surface), which resulted in higher runoff ratio, reaching average values of 0.46 first year after the fire. Modelled values for similarly dry sites (modelled using MAP of 722mm/yr and 943mm/yr) show comparable sediment yields (eg., 3.2-8.57 t/ha/yr and 0.15-0.65 t/ha/yr from hypothetical sites on north and south facing hillslopes, respectively; Table 3-4). Under dry conditions, modelled values reach up to one order of magnitude above mean sediment yield levels in an unburnt state (Table 3-4). Both literature and modelled values show an overall decreasing trend of post-fire sediment yield levels as climate becomes wetter (Table 3-3 and Table 3-4), with an exception of East Kiewa

(Lane et al., 2006), where measured values that were reported were one order of magnitude higher than modelled values. The authors reported 2.96 t/ha/yr of sediments (both as suspended and bedload) exported from a burnt catchment, over 100ha in size. The source of the high increase in sediment yield after fire was ascribed to be colluvium originated from close to the channel rather than from upper parts of the burnt hillslopes (Lane et al., 2006; Smith et al., 2011b), as these did not show any sign of rill erosion, and measured infiltration rates on these hillslopes were very high (Sheridan et al., 2007). On a rainfall simulation study conducted on a similarly wet forest, (Lane et al., 2004) did not record any runoff from the burnt hillslope, even when simulating a rainfall event exceeding 100 year interval. It is argued that the low runoff and erosion rates simulated by the model are consistent with observations at very wet forests across Victoria.

Recently, evidence of high intensity debris-flows had been reported in south eastern Australia, and Victoria (Nyman et al., 2011). These events were estimated to export sediment 2-3 orders of magnitude more (113-294 t/ha/event) than annual background erosion rates (Nyman et al., 2015b). These events were shown to originate from hillslopes covered by burnt dry eucalyptus forests (Nyman et al., 2011; Smith et al., 2012). Although debris flows are processes that are out of the scope of this model, the initiation process as described in Langhans et al. (2017) is related to the effect of fire on the physical and hydrological properties of the surface soil layer at the hillslopes level, and depends on the storage of non-cohesive material on these hillslopes (Nyman et al., 2014a).

Although very diverse, the effects of fire on surface processes are generally captured by this model and can explain the large differences between simulations of dry and wet hypothetical sites in long term erosion rates (Table 3-4). The variability in reported values across different climatic domains, forest types, fire severity and scales make it difficult for the ability of a model to reproduce accurate runoff and sediment outputs that are comparable. Furthermore, most studies only measure hydrological response after one fire event, and possibly a few years after (Lane et al., 2006; Noske et al., 2016; Smith et al., 2011b; Van der Sant, 2016). The model presented here runs stochastically tens to hundreds of fires during one simulation, each different rainfall regime, which, naturally, has the potential to vary the type of response. Overall it seems as if the trends in runoff and erosion that are reproduced by the model are in at the right order, and values are at the right order of magnitude to measured values (see Table 2 in Smith et al. (2011c) for more values from Victoria), and between different modelled sites and burn states.

Table 3-4 - Mean sediment yield after fire and in unburnt state for hypothetical sites under four different rainfall regimes. Values for were based on one 20,000 year simulation for each of the sites. Note that values can change according to the stochasticity of the fire and rainfall regime. Better results might be achived by running the model for several simulations with different stochastic rainfall and fire regimes.

Mean rainfall depth	Aspect	Time since fire	mean sediment yield	Modelled fire interval	Years between debris flow events*	Denudation rate
[mm]			[t/ha/yr]	[yr]		[mm/kyr]
722	North	1	8.57	19	540	95.8
		Unburnt	0.65			
	South	1	1.86	29	4,000	14.1
		unburnt	0.14			
943	North	1	3.2	25	2,500	18.2
		Unburnt	0.15			
	South	1	0.48	38	∞	10.2
		Unburnt	0.13			
1261	North	1	0.67	28	10000	10.9
		unburnt	0.13			
	South	1	0.2	69	∞	12.7
		Unburnt	0.17			
1611	North	1	0.42	60	∞	13.1
		Unburnt	0.17			
	South	1	0.21	95	∞	12.8
		Unburnt	0.17			

*Calculated by the evacuation of more than 50% of the non-cohesive layer by one rainfall event.

3.6.5 Denudation rates

It has been suggested that Australia has been fluvially denuding over the last 200 Myr due to the lack of major mountain building activity (Kennet & Blewett, 2012). This lead to the assumption that erosion rates had been relatively low compared to tectonically active landscapes (Bishop, 1985). Similar to runoff and erosion rates, measured and estimated

values of denudation rates in Australia are highly variable. For example, Bishop (1985) suggested denudation rates in south eastern Australia during the last 15-20 Myr to be 10 mm/kyr. The author ascribed the low rates to forest cover and low tectonic stability. Fifield et al. (2010) estimated denudation rates of 3-7mm/kyr and 1-5 mm/kyr from two forested catchments in south eastern Australia. At these locations, the authors estimated soil production to have similar values, with a 10-fold increase in erosion rates with more disturbed hillslopes. In the East Kimberly, however, the authors estimated that 20kyr erosion rates were 10-24 mm/kyr, with modern erosion rates of 200mm/kyr. Heimsath et al. (2009) estimated denudation rate from a basin at a retreating escarpment in Northern Territory to be 10-40 mm/kyr, while Smith et al. [2012] estimated these rates to be 27 mm/ky from a first order catchment in Victoria. In a recent study, Hancock et al. (2017) summarised a long term monitoring experiment of several steep catchments in New South Wales. The authors estimated denudation rates from two of undisturbed forested catchments to be around 70mm/kyr. The steepness of the catchments (mean slope of ~22 degrees) was suggested as a plausible reason for the relatively high denudation values compared to background values in the literature (such as in Fifield et al. (2010) and Bishop (1985)).

Even when considering the variability in literature estimates of denudation rates and the steepness of the modelled hillslopes, modelled denudation rates across the simulated sites are high, especially at the drier sites (Table 3-4). In most cases, denudation rates are estimated by using uranium isotopes and cosmogenic nuclides (Dosseto & Schaller, 2016), which average hundreds of thousands to millions of years, and might miss contemporary erosion processes which might be considerably different than the longer term average (Dosseto et al., 2010; Suresh et al., 2014). The fact that this model is based on observed contemporary processes (Langhans et al., 2016b; Noske et al., 2016; Nyman et al., 2013; Sheridan et al., 2016), its overestimation of denudation rates might actually be reasonable considering the fact that the climate in the region became warmer and wetter since the last deglaciation (McKenzie, 1997, 2002).

3.7 Conclusions

The chapter describes a numerical model developed with the objective to evaluate the role of fire on coevolution. The model was designed to simulate the coevolution of soil and vegetation of under steady climatic conditions and including a stochastic fire regime which

depends on the system's moisture status. Potential feedbacks between the soil, vegetation and fire are fundamental processes of coevolution and important to the model design. By utilizing a unique set of ecohydrological and geomorphological components, the model tracks the evolution of soil depth, vegetation and fire regime, by efficiently running hourly rainfall and daily solar radiation across thousands of years. The model was parametrised and calibrated using a combination of data sources including a very large dataset on hydrological processes in fire-prone forest of SE Australia. The concept of optimality (Eagleson, 1982) was combined with literature values to develop a general relationship between B_{max}, soil depth and aridity. The model was found to perform remarkably well in hydrological partitioning across a relatively wide range of aridities. The distribution of fire return intervals under the influence of soil moisture are consistent with observed fire regimes. Surface runoff and erosion also showed good correspondence with observation available from literature values. With strong overall performance of the model in predicting observable trends in ecohydrological partitioning, fire frequency distributions, vegetation recovery and rainfall-runoff-erosion response across an aridity gradient, it is reasonable to assume the model to serve as a robust tool for studying the effect of fire on the coevolution in the SE Australian forested systems.

4 Determining the role of fire in the coevolution of soil and vegetation using a modelling approach

4.1 Abstract

It had been shown that coupled soil-vegetation systems coevolve with climate, and that their current state represents the legacy of this coevolution process. Fire disturbs key processes across forest systems, however, its relative role in the coevolution of soil and vegetation remains unexplored. In SE Australian uplands, forest type, fire frequency, and soil depth vary systematically with aridity. The aims of this chapter were to: (i) test the hypothesis that fire related processes and feedbacks are critical to explain observed patterns and magnitude of differences in system states across the landscape, and that their effect increases with aridity; and (if the hypothesis was supported), (ii) evaluate the role of fire related mechanisms in the coevolution process. This chapter focused on the following mechanisms: (a) the effect of individual fires on the forest cover and infiltration capacity; (b) the effect of fire frequency; and (c) ecohydrological and geomorphological processes and feedbacks that control fire frequency. In order to achieve those aims, several numerical simulations were developed using 1D model designed to simulate a SE Australia systems, in which soil depth and biomass are output variables. Results showed that model simulations replicated the observed trend and magnitude of difference in soil depths with aridity when simulations were designed to include stochastic fire regimes, and that the net effect of fire on soil depth increased non-linearly with climate. Analysis of numerical simulations indicated that both the magnitude of differences in soil depth and the location of the threshold with respect to aridity depend on fire frequency, and on the effect of fire on infiltration capacity (*Ic*). Calculation of time to steady state (s-s) soil depth showed that building of the soil profile on dry (wet) sites were shorter (longer) than interglacial fluctuations in climate, leading to the hypothesis that only contemporary soil depths at these two climatic extremes are close to steady state. The dependency of fire frequency on soil depth and climate highlights an important feedback loop in which increased erosion due to higher fire frequency might actually reinforce it, contributing to higher fire frequency and more erosion. This fire related eco-hydro-geomorphic feedback eventually stops when there is no soil left or when climate, vegetation, soil and fire regime reach a new steady state.

4.2 Introduction

In his classical work, Budyko (1974) showed that the ratio between long term mean annual rainfall and solar radiation can predict catchment hydrological partitioning, and also can explain global distribution of vegetation and soil types (Berry et al., 2005). On the catchment scale, Donohue et al. (2012) explored the importance of smaller scale landscape (i.e., soil water holding capacity and rooting depth) and climatic (i.e., rainfall depth) attributes on the distributions of stream flows around Budyko's framework. On small spatial scales, topographic complexity affect (and in some cases is affected by) the distribution of rainfall and solar radiation, which creates differences in water availability across the landscape (Nyman et al., 2014b; Rasmussen et al., 2015). These topographically-driven variations in water availability can force the coevolution of soil and vegetation in different trajectories which can result in very different systems, sometimes in very small proximity (Lybrand et al., 2011; Rasmussen et al., 2015).

The variations in the coupled soil-vegetation systems (eg., different critical zone units) across the landscape implies that the coevolution process operates differently under different climatic and microclimate drivers. The assumption is that given similar starting conditions (i.e., slope, soil depth, topographic condition, bedrock type etc), the critical zone will evolve similar to others when subjected to similar climatic forcing. The development of topographic asymmetry is a good example of the long term end-product of a coevolution process (Istanbulluoglu et al., 2008). It was shown that this morphologic signature is driven by the differential spatial and temporal distribution of solar radiation across hillslopes that share similar lithology and rainfall regime (Anderson et al., 2013; Gutiérrez-Jurado & Vivoni, 2013a; b; Yetemen et al., 2015b). The different vegetation structure across these hillslopes affects the hydrological response to rainfall (Gutiérrez-Jurado et al., 2007), and dictates the type and rates of erosion processes in which one slope is eroding in different rate than its opposing counterpart (Istanbulluoglu et al., 2008; Yetemen et al., 2015b).

The partitioning of water and solar radiation by the vegetation determines the microclimatic conditions under the canopy. Eagleson (1982) suggested that under steady climatic drivers, canopy structure is optimized in order to maximize soil moisture and primary productivity, and minimize water stress, by affecting the microclimatic conditions, the hydrological cycle and possibly the coevolution of the system. Canopy structure and function not only dictates evapotranspiration, but also affects the wetting and drying of the sub-canopy dead biomass,

which have a major influence on fire ignition and propagation (Nyman et al., 2015a). Under the framework defined by Eagleson (1982), an interesting question emerges: *does the canopy structure optimise to also generate an optimal fire regime?*

The water storage capacity of the soil dictates the potential water availability of a system and determine its potential primary productivity (Eamus, 2003; Shepard et al., 2015). The ability of the soil to store water is affected by the soil properties (Clapp & Hornberger, 1978; Saxton & Rawls, 2006), and also depends on the soil depth and developmental status (Jenny, 1941; Lohse & Dietrich, 2005; Young et al., 2004). The main soil properties that determine plant available water are texture, organic matter, and soil depth. Thus in losing soil by erosion processes, the water holding capacity of the soil decreases, potentially affecting the biomass holding capacity (Meyer et al., 2007; Milodowski et al., 2015).

Fire burns the vegetation cover, and exposes the soil to direct rainfall impact. The hydro-geomorphic significance of fire has been attributed to its effect on soil properties and infiltration capacity (DeBano, 2000a; Inbar et al., 2014; Shakesby & Doerr, 2006). Fire usually reduces infiltration capacity of the soil by imposing an increase in the proportion of soil affected by water repellency (DeBano, 2000a; Noske et al., 2016; Nyman et al., 2010). These changes in the hydrological properties of the system can result in elevated overland flow rates which in turn can lead to minor or major erosion increases (Lane et al., 2006; Moody & Martin, 2001b; Nyman et al., 2011; Prosser & Williams, 1998), with potential effects on soil depth and its water holding capacity in longer timescales. The effect of fire on landform has been investigated using landscape evolution models (Istanbulluoglu et al., 2004), however, its potential to effect the coevolution of the critical zone has never been studied.

The south eastern Australian forested uplands provide an ideal natural laboratory to investigate the role of fire in coevolution for several reasons: (i) the Australian vegetation is very flammable, and fire has been an important part of its system long enough to potentially have a significant effect on the coevolution process; (ii) forest and soil type vary significantly even in very close spatial scales, depending on landscape position and water availability (Nyman et al., 2014b). These different microclimatic conditions creates variations in fire regimes typical to the different forest types (Cheal, 2010; Kennedy & Jamieson, 2007); (iii) while fire causes an increase overland flow and erosion processes (Lane et al., 2006; Prosser & Williams, 1998; Sheridan et al., 2007), the abundance and severity of these events varies

systematically in this landscape, creating a gradient in terms of geomorphic sensitivity to fire (Noske et al., 2016; Nyman et al., 2011; Sheridan et al., 2016).

The aims of this chapter are to (Figure 4-1):

(i) test the hypothesis that fire related processes and feedbacks are critical to explain observed patterns and magnitude in system states across the landscape, and that their effect of on coevolution increases with aridity.

Then, given the hypothesis is supported,

(ii) to evaluate the role of fire related mechanisms in coevolution. This chapter focuses on the following mechanisms: (a) the effect of individual fires on the forest cover and infiltration capacity; (b) the effect of fire frequency; and (c) ecohydrological and geomorphological processes and feedbacks that control fire frequency.

In order to achieve those aims, several numerical experiments were designed using a 1D model designed to simulate a SE Australia systems, in which soil depth and biomass are output variables. Details about the model are presented in Chapter 3.

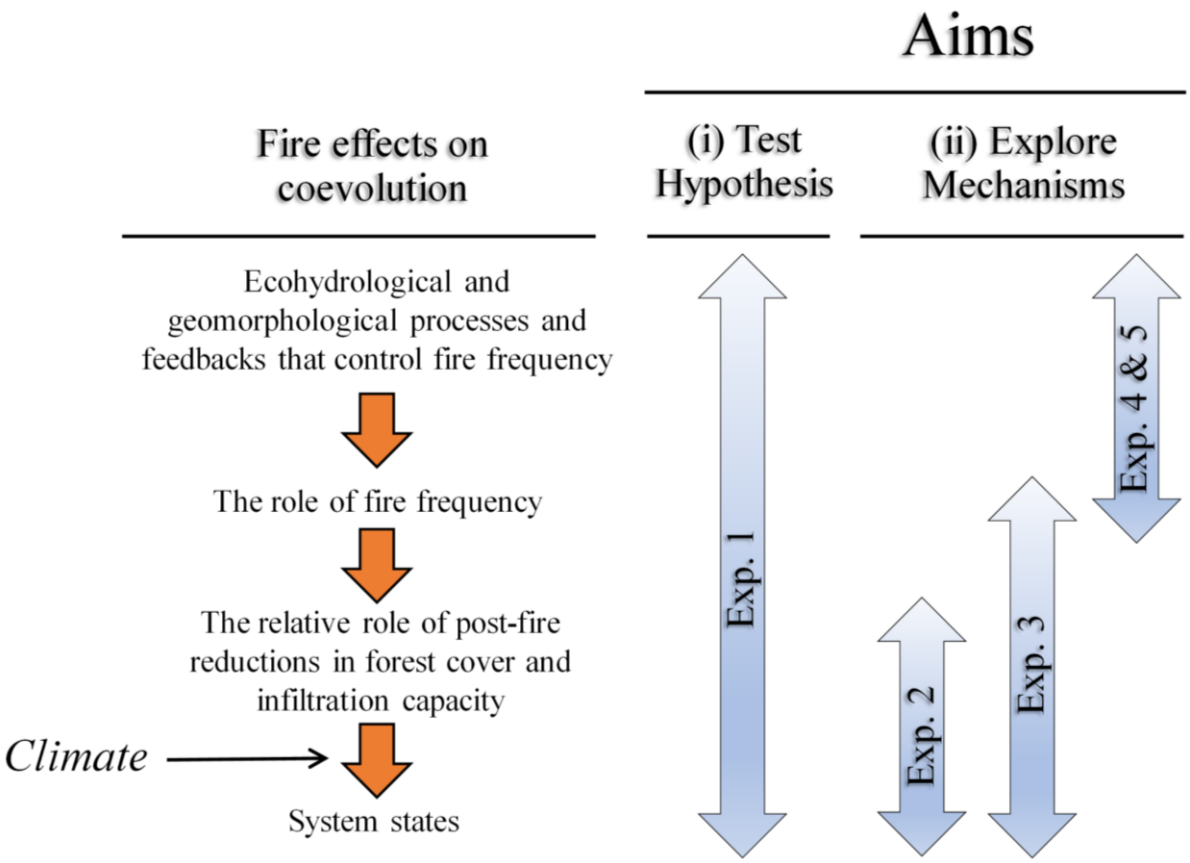

Figure 4-1 - Visual representation of possible fire related effects on coevolution, and how they are adressed in the chapter aims, and later in simulation experiments (Table 4-1).

4.3 Methods

Five different numerical experiments were designed in order to test the hypothesis and address the aims. Simulation details are presented in Table 4-1. In the simulations, different parameters were held constant either to observe model outputs or to perform sensitivity analyses for the model results that could untangle the coevolution process as it is modelled. Simulations were designed to run ten hypothetical systems across a climate gradient, varying in rainfall (See Table A- III-1 in Appendix III for information about the five different rainfall scenarios). Variations in energy were obtained by running the model for north and south facing solar exposure.

Table 4-1 - Experiment description and details.

Exp.	Purpose	Description	Climate scenarios		Fire	Soil depth	Duration [kyr]	Simulation sets
			MAP [mm/yr]	Aspect				
1	To test the hypothesis	In this experiment, simulations for different climatic conditions were set to run *with* and *without fire*. Simulations of hypothetical systems were allowed to coevolve from an initial soil depth of 0.5m under steady climatic conditions. The hypothesis was tested by examining simulation outputs of s-s soil depth and biomass. The predicted patterns in system states with respect to aridity where compared with observations from chapter 2.	542 721 942 1261 1610	N S	On Off	Variable	300[*b]	•*With fire* •*Without fire*
2	To evaluate how coevolution of the critical zone is sensitive to post fire reduction in forest cover and infiltration capacity	Sensitivity of s-s soil depth and biomass to the effect of fire on forest cover and *Ic* was evaluated by running independent simulations while bypassing (i.e., using unburnt values) the effect of fire on each of these system properties. This allowed the effect of fire on each of these system properties to be isolated from other factors. Results were analysed by comparing soil depth and biomass outputs lacking either the effect of fire on forest cover or the effect of fire on *Ic*, with those from simulations that included all these effects (simulation *With fire,* Exp. 1).	542 721 942 1261 1610	N S	On	Variable	300	•*Effect of fire on forest cover* •*Effect of fire on infiltration capacity*
3	To evaluate how coevolution of the critical zone is sensitive to variations in fire frequency	Sensitivity of soil depth and biomass to fire frequency was determined by setting fixed fire return intervals (FRI) in the model that override the moisture-driven fire regime module. This allowed the effect of fire frequency on the coevolved state to be isolated from other factors. Results were analysed by comparing soil depth and biomass from all simulations across an aridity gradient.	542 721 942 1261 1610	N S	On	Variable	300	•*20yr FRI* •*40yr FRI* •*60yr FRI* •*100yr FRI*
4	To evaluate the ecohydrological and geomorphological processes and feedbacks that control fire frequency	The effect of soil depth on FRI was examined by analysing changes in mean FRI as soil depth developed or eroded across different climatic scenarios. Mean FRI as a function of mean soil depth calculated for 1000-year bins for each simulation was plotted, and analysed with respect to aridity and aspect. The analysis provided insights on the effect of climate, soil depth and biomass on fire frequency.	542 721 942 1261 1610	N S	On	Variable[*a]	300[*b]	•*Effect of soil depth on FRI*
5		The effect of climate, forest cover and soil depth on FRI was determined by running long-term simulations with different combinations of soil depths, forest cover and climate scenarios. Results were analysed with respect to changes in FRI as a function of changes in LAI for different soil depths, rainfall and aspect.	542 721 1261 1610	N S	On	1 0.5 0.2	400	•*Effect of forest cover on fire frequency*

[*a] initial soil depths started were set to 0.2m for wet sites and 1.2m for dry sites in order to get the variability in soil depth and relate them to fire frequency.
[*b] durations were set to 300kyr for all simulations except for sites under low rainfall (MAP 541mm), that were sensitive to soil depth fluctuations. In this case simulations ran for 60kry.

4.3.1 Calculating time to steady state

Simulations were designed to run long enough until s-s (s-s) soil depth is reached. For efficiency in running simulations this meant that in some cases, an a-priori estimate of time-to-steady state had to be obtained. Special simulations were conducted in order to estimate the maximum time to s-s soil depth across the aridity gradient. These simulations were used only to solve the continuity of mass equation of the change in soil depth with time (Eqn 3.45). The simulations were designed to run on an annual basis using mean annual erosion rates (E_f) obtained from the long term (300kyr) model simulations at steady state conditions and using soil depth dependent geomorphic transport laws for $\in$ and E_d, as used in the model (see chapter 3 for more details). Soil depth temporal trajectories and s-s soil depths from these simulations were found to be very similar (not shown) to long term simulations of the model (which runs on a daily/hourly basis). A simple method to identify steady-state soil depth was developed in order to have a common way (i.e., across all simulations) of calculating the time it takes to reach that point. Time to s-s soil depth was determined by finding the simulated year range (within 1000 years) where the coefficient of variance [%] of soil depths (i.e., for the whole 1000-year range) was lower than 0.01%. Minimum time to s-s soil depth was found to vary between 37kyr to 112kyr, for the driest and wettest sites at aridities of 3.47 and 0.82, respectively. These results assisted in planning simulation times for the experiments (Table 4-1) but were also key to discuss modelled and observed patterns in soil depth.

4.3.2 Experiment 1: Testing the hypothesis

In this experiment simulations for different climatic conditions were set to run *with* and *without fire* (Table 4-1). The hypothesis was tested by examining simulation outputs of s-s soil depth and biomass. The predicted patterns in system states with respect to aridity where then compared with observations from chapter 2.

Simulations of hypothetical systems were allowed to coevolve from an initial soil depth of 0.5m under steady climatic conditions (Table 4-1). By analysing time to s-s soil depth (Section 4.2.1), simulations with fire and without were set to run for 300kyr, with the exception of the driest sites (MAP of 521mm) which had very thin steady state soil (~0.13m). In this case, with a 300kyr simulation, periods in which fire was more frequent than the site's tolerable frequency ended up depleting the soil completely and causing a system collapse. Thus, simulations for these sites were set to run for 60kyr (only when stochastic fire was

turned *on*), which is above the minimum time to steady state (estimated to be around 35kyr by using method described in section 4.3.1). Lastly, s-s soil depth and biomass values from each simulation were obtained by averaging of last 10kyr. This timeframe was assumed to be long enough to avoid the effect of higher-than-average fire frequency on mean s-s soil depth and biomass. Analysis of diffusive and fluvial soil erosion processes from model outputs was conducted in order to identify possible mechanisms in which fire effects coevolution. Lastly, time to s-s soil depth across the aridity gradient (section 4.3.1) was analysed in order to estimate whether contemporary soils are in steady state conditions which gives insights on the comparison between measured and modelled values.

4.3.3 Experiment 2: The relative role of post fire reductions in forest cover and infiltration capacity

Sensitivity of steady-state soil depth and biomass to the effect of fire on forest cover and infiltration capacity was determined by running independent simulations without the effect of fire on each of these system properties across 10 climatic scenarios. This allowed each effect to be isolated from the others. Results were analysed by comparing soil depth and biomass outputs from simulations in which either the effect of fire on forest cover or the effect of fire on infiltration capacity were turned "off", with those from simulations that included all these effects (from Treatment With Fire, Exp 1). steady state soil depth and biomass for these state variables were calculated in a similar manner to what is described in Section 4.3.2.

4.3.4 Experiment 3: Sensitivity of soil depth and biomass to fire frequency

Sensitivity of soil depth and biomass to fire frequency was determined by setting fixed Fire Return Intervals (FRI) in the model that override the moisture-driven fire regime module. This allowed the effect of fire frequency on the coevolved state to be isolated from other factors. Results were analysed by comparing s-s soil depth and biomass from all simulations across the aridity gradient.

Here, model simulations were designed to run under four different fire return intervals: 20yr-; 40yr-, 60yr, and 100yr FRI. Simulations started with soil depth of 0.5m, and ran for 300kyr under steady climatic regime (rainfall and aspect), allowing the development of soil and biomass with the new imposed fire regime. Steady-state soil depth and biomass for these state variables were calculated in a similar manner to what is described in Section 4.3.2.

4.3.5 Experiment 4: Effect of soil depth on fire frequency

On steep forested systems, depth is one of the soil properties that controls its water holding and biomass carrying capacity. Thus, changes in soil depth and biomass in these systems are expected to induce changes in soil moisture and fire frequency. The effect of soil depth on FRI was examined by analysis of changes in mean FRI as soil depth developed or eroded across different climatic scenarios. The analysis provided insights on the effect of climate, soil depth and biomass on fire frequency.

Here, simulations were designed to run 10 climate scenarios. Modelled systems were allowed to coevolve from shallow (deep) soil at wet (dry) systems in order to record variations fire frequency as soil depth increased (decreased). Mean FRI as a function of mean soil depth calculated for 1000-year bins for each simulation was plotted and analysed with respect to aridity and aspect.

4.3.6 Experiment 5: Effect of canopy cover and soil depth on fire frequency

Soil moisture at a point is controlled by climatic conditions, soil hydraulic properties and the partitioning and use of rainfall and solar radiation by the vegetation. Thus, fire frequency, which depend on soil moisture deficit, can be affected by changes in either one of those factors. The effect of climate, forest cover and soil depth on fire frequency was determined by running long-term simulations with different combinations of soil depths, forest cover (LAI) and climate scenarios. Results were analysed with respect to changes in FRI as a function of changes in LAI for different soil depths, rainfall and solar exposure (aspect).

In this experiment, leaf area index (LAI) was allowed to change, while soil depth (bucket "size"), and climate (rainfall and solar exposure) were kept constant. Each simulation started with $LAI = 1$, which increased in one unit every 100kyr. Simulations were set to run for 400kyr with 3 soil depths (0.2m, 0.5m and 1m), 4 rainfall regimes and with a north and a south facing aspect orientation, which summed up to a total of 24 simulations. Model output was analysed for the 4 LAI units (1-4) for each of the soil depth-rainfall-aspect combinations.

4.4 Results

4.4.1 Experiment 1: Testing the hypothesis

Both experiments *with fire* and *without fire* shows similar logistic relationship with aridity with respect to s-s soil depth, however, values from simulation *with fire* becomes lower beyond aridity 1.5 (Figure 4-2a). Soil depth at the two extreme cases (very wet and very dry) show similar values compared to measured values (Table 3-1). Similar to s-s soil depth, s-s biomass for simulations *with fire* shows a decreasing logistic pattern with aridity, however there is a reduction in biomass values at the lowest aridities to lower levels as compared to simulation *without fire* (Figure 4-2b). In the simulations *without fire,* s-s biomass decrease linearly and plateau in high aridity values. Overall, a consistent fire regime seems to reduce s-s biomass values with the highest effect at the high and low aridity (Figure 4-2b).

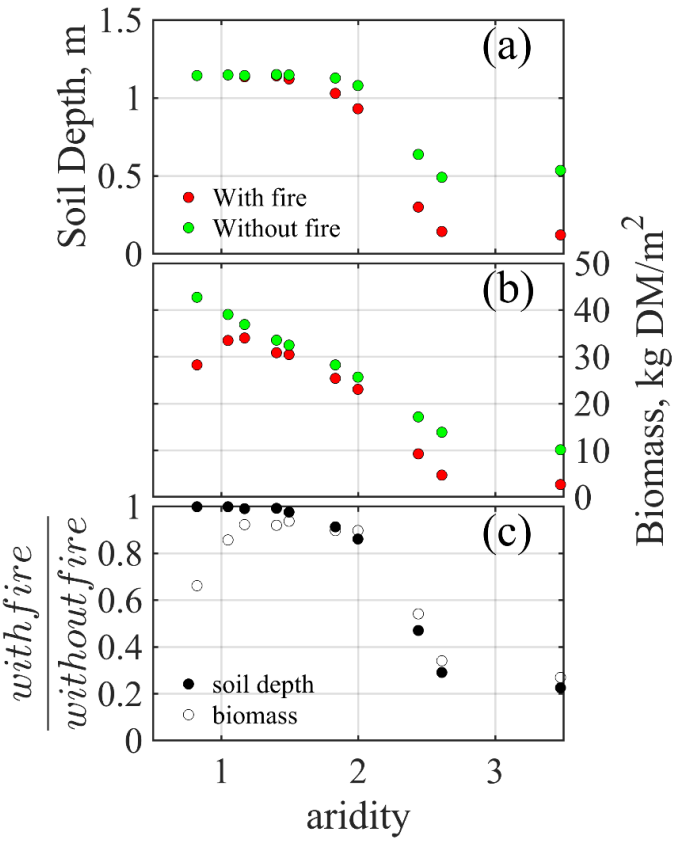

Figure 4-2 – Steady state soil depth (a) and biomass (b) for simulations *with* and *without fire*, and their ratio (*with fire*/*without fire*) (c) as function of aridity. 300kyr simulation were used in order to produce these results, except in the site with highest aridity, where soil depth was very sensitive to fire frequency and consequential erosion processes. In the latter case, model

simulated lasted 60kyr.Each marker accounts for steady-state soil depth or biomass from one simulation, which were calculated by an average of annual values in the last 10kyr.

The ratio between s-s soil depth (H_r) and biomass (B_r) of the two treatments were calculated using $H_r = H_{with\ fire}/H_{without\ fire}$, and $B_r = B_{with\ fire}/B_{without\ fire}$, where *H* and *S* are steady state soil depth and biomass, respectively (Figure 4-2c). This metric represents the strength of the fire effect and provides a basis for evaluating the contribution of fire to coevolution across a climate gradient. The results reveal that fire-effects were strongest in high aridity values on s-s soil depths and both in high and low aridity values in the case of s-s biomass (Figure 4-2c).

Effect of fire on fluvial and diffusive processes

Results show that fluvial erosion rates for simulations *with* and *without fire* start diverging beyond aridity 1.5, similar to the divergence in s-s soil depth seen in Figure 4-2a. However, the rates of fluvial processes only become dominant beyond aridity ~2 (Figure 4-3c). Beyond this threshold, simulations *with fire* show significantly higher fluvial erosion rates than those *without* (Figure 4-2a). This is suggested to be caused by the increase in the effect of fire on infiltration capacity (*Ic*; Eqn 3.17) and/or by higher fire frequency as aridity increases. Rates of diffusive processes are affected by the non-linear depth-dependent diffusive sediment flux equation used in the model (Eqn 3.55; (Roering, 2008)). These rates are higher in simulations without fire beyond aridity ~2 and similar below (Figure 4-3b), which could be explained by the deep s-s soil across wetter sites (Figure 4-2a).

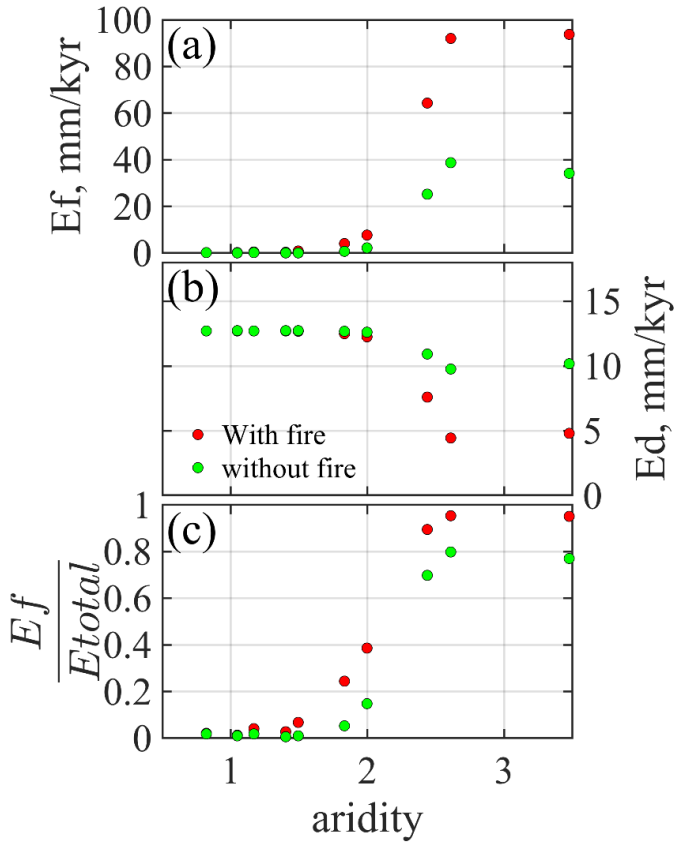

Figure 4-3 – Modelled fluvial (a) and diffusive (b) erosion rates and the proportion of fluvial from the erosion loss (Etotal) (c) as a function of aridity, calculated from long-term simulation with and without fire.

Time to Steady state

Time to s-s soil depths under different climatic conditions were evaluated using model simulations which only solved the continuity of mass equations for soil depth on an annual basis (see section 4.3.1). For a given set of climatic conditions (i.e., different rainfall and *Ep*), 100 independent simulations were conducted with a different initial soil depth (varying between 0.13m to 1.13m). Figure 4-4a shows the time it took to reach s-s soil depth in each simulation under different climatic conditions (displayed as aridity index). The purpose for using different initial soil depth was to include the effect of initial conditions on time to reach s-s. Median time to s-s for a given climatic conditions are plotted as a function of aridity index in Figure 4-4b. Each point in Figure 4-4b is the median of the 100 different simulations (i.e., which is practically the median time to s-s of each line in Figure 4-4a) plotted with the aridity index. Results show that the median time to s-s soil depth varies between 37kyr to

112kyr, for simulation forced by the driest and wettest climatic conditions , respectively, and that time it takes the model to get to s-s soil depth is decreasing with an increase in aridity, with a threshold/logistic shape similar to that of s-s soil depth (Figure 4-4a).

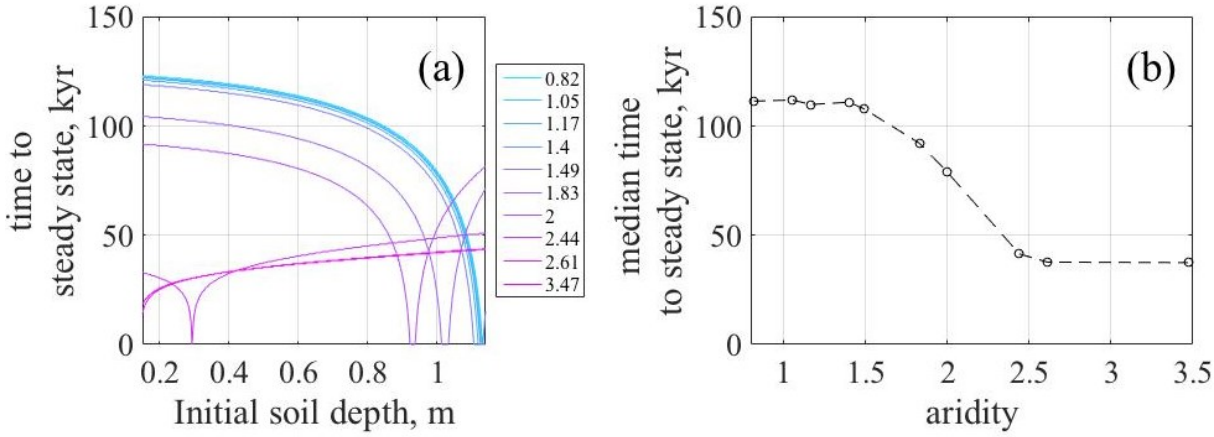

Figure 4-4 – Median time to steady state soil depth as a function of initial soil depth (a); and the time to steady state as function of aridity (b), calculated by the median time to steady state soil depth from 500 simulations forced by 10 different climate scenarios and with initial soil depth ranging from (0.13m to 1.13m).

4.4.2 Experiment 2: The relative role of post fire reductions in forest cover and infiltration capacity

Two simulation sets were evaluated with the aim to decipher the mechanisms in which fire controls soil depth and biomass in the coevolution process (Table 4-1). In the first set of simulations, *the effect of fire on forest cover* was turned "off" by forcing the model to bypass post-fire reduction of leaf biomass and LAI, and by that keeping forest cover at its unburnt value. In the second set of simulations, *the effect of fire on Ic* was turned "off" by forcing the model to bypass post-fire reduction of *Ic*, and by that keeping *Ic* at its unburnt value. Steady state soil depth and biomass from simulations *without fire* together with these two simulation sets were then compared to those *with fire*, which expresses conditions in which all fire effects are active (Experiment 1; Table 4-1), as presented in Figure 4-5.

Table 4-3 shows a comparison of the root-square-mean error (RSME) calculated for s-s soil depth and biomass (respectively) from simulations above (from experiment 1 and 2). Results show that s-s soil depth values from simulations in which *the effect of fire on Ic* was turned

"off" are closer to simulations *without fire* compared to simulations *with fire* (Table 4-2), and that the divergence increases as s-s soil depth become smaller (Figure 4-5a). This suggests that the effect of fire on *Ic* has an important role in explaining patterns of s-s soil depth showed in Figure 4-2a. Conversely, s-s soil depth values from simulations that the *effect of fire on forest cover* was turned "off" are closer to values from simulations *with fire*, indicating that the effect of fire on forest cover have lower impact on s-s soil depth, and cannot explain patterns in s-s soil depth shown on Figure 4-2a.

Similar to s-s soil depth, s-s biomass from simulations in which *the effect of fire on Ic* was turned "off" has higher impact on patterns seen in Figure 4-2b than simulations in which the *effect of fire on forest cover* was turned "off" (Figure 4-5b; Table 4-3). However, the difference is less obvious, probably due to the fact that s-s biomass values between all simulations only diverge on high and low aridity values (Figure 4-2b).

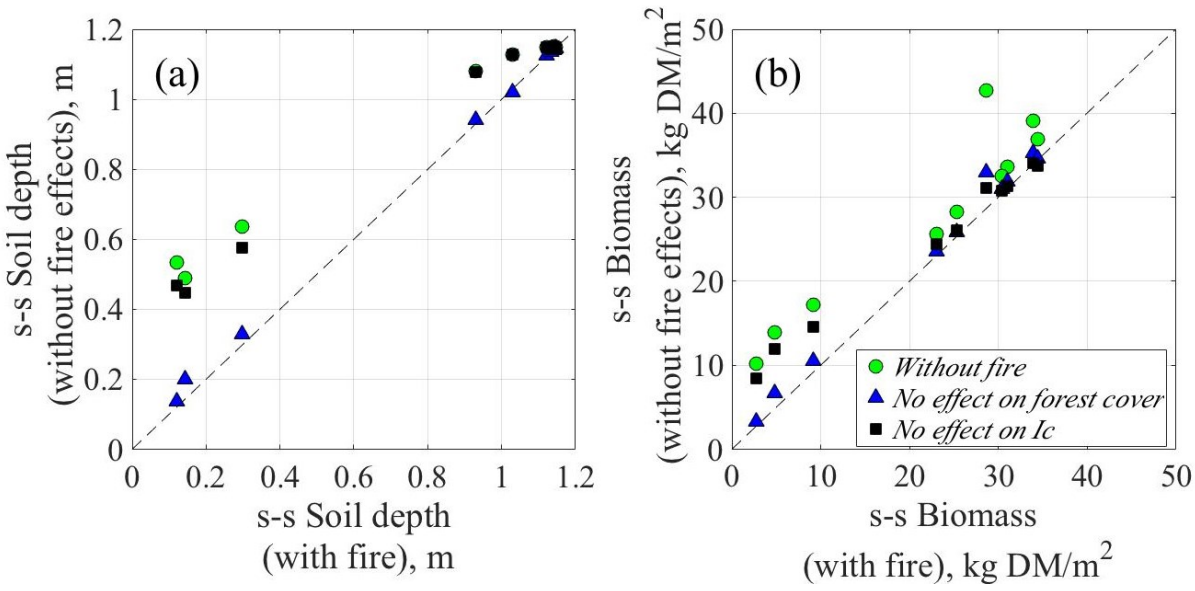

Figure 4-5 – Comparison of s-s soil depth (a) and biomass (b) between three simulations, where in each, some effect of fire was turned "off", with a simulation that had all the effects of fire turned "on". Simulations were: *witout fire*; *no effects of forest cover*; *no effects on Ic* (Table 4-1).

Table 4-2 – Comparison between the RSME calculated for s-s soil depth between simulations: *with fire*, *without fire*, *no effects of fire on forest cover* and *no effect of fire on Ic* (Table 4-1).

	Without fire	***no effects of forest cover***	***no effects on infiltration capacity***
With fire	0.44	**0.04**	0.39
	Without fire	0.41	**0.06**
		no effects of forest cover	0.35

Table 4-3 - Comparison between the RSME calculated for s-s biomass between simulations: *with fire*, *without fire*, *no effects of fire on forest cover* and *no effect of fire on Ic* (Table 4-1).

	Without fire	***no effects of forest cover***	***no effects on infiltration capacity***
With fire	17.83	**3.79**	7.23
	Without fire	14.04	10.61
		no effects of forest cover	**3.44**

4.4.3 Experiment 3: Sensitivity of soil depth and biomass to fire frequency

Results presented in Figure 4-6 show that fire frequency has the highest effect on soil depth in dry climates (higher aridity), and on biomass in wet climates. Similar to simulations *with fire* and *without fire* (Figure 4-2a), the relationship between s-s soil depth and aridity across the fire frequency treatments show a logistic/threshold relationship. The decreases in fire frequency (lower fire return interval) caused a shift in peak s-s biomass towards higher aridities, indicating a higher influence of fire frequency on s-s biomass

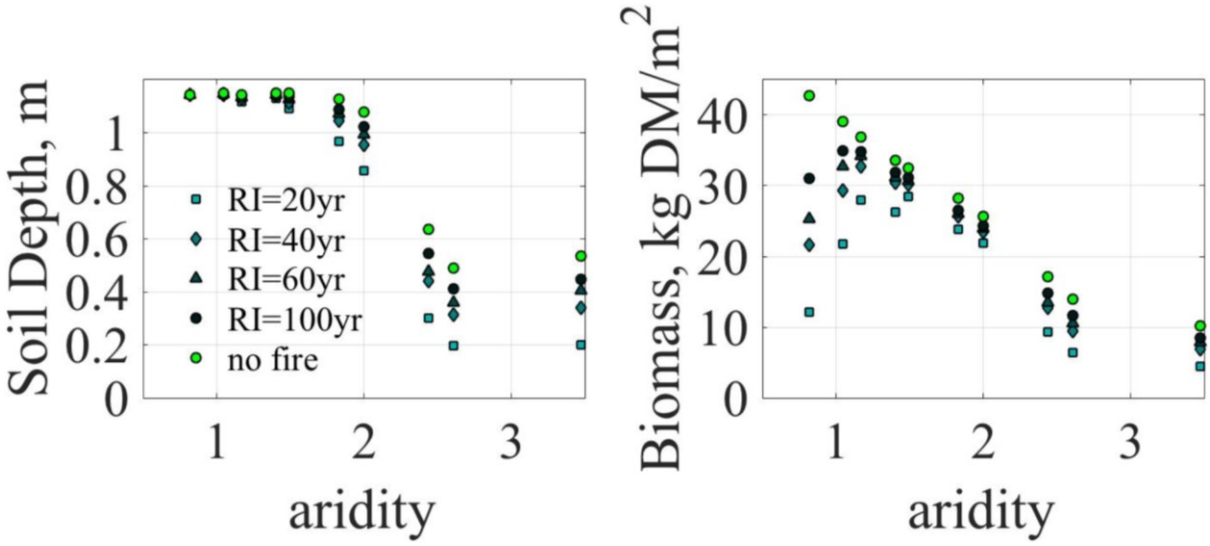

Figure 4-6– The effect of different fire return interval on s-s soil depth (a) and biomass (b) as a function aridity. Different fire regimes were "forced" on the model, replacing the fire frequency that depend on soil moisture deficit (Appendix II).

4.4.4 Experiment 4: Effect of soil depth on fire frequency

The results presented in Figure 4-7 show the effect of soil depth on fire return interval (FRI) across 10 climate scenarios. Fire return interval (which can also be regarded as typical forest age) at dry sites (i.e., with high aridity) and north facing systems are less sensitive to changes in soil depth (Figure 4-7). The sensitivity was further evaluated by plotting the slope of the linear function fitted to the data with aridity, as shown in Figure 4-7b. Indeed, results here show the decreasing sensitivity of fire return interval to soil depth as aridity increases, but also indicate a different magnitude across north and south facing hillslopes, where fire return interval on south facing hillslopes show higher sensitivity to soil depth compared to their north facing counterparts.

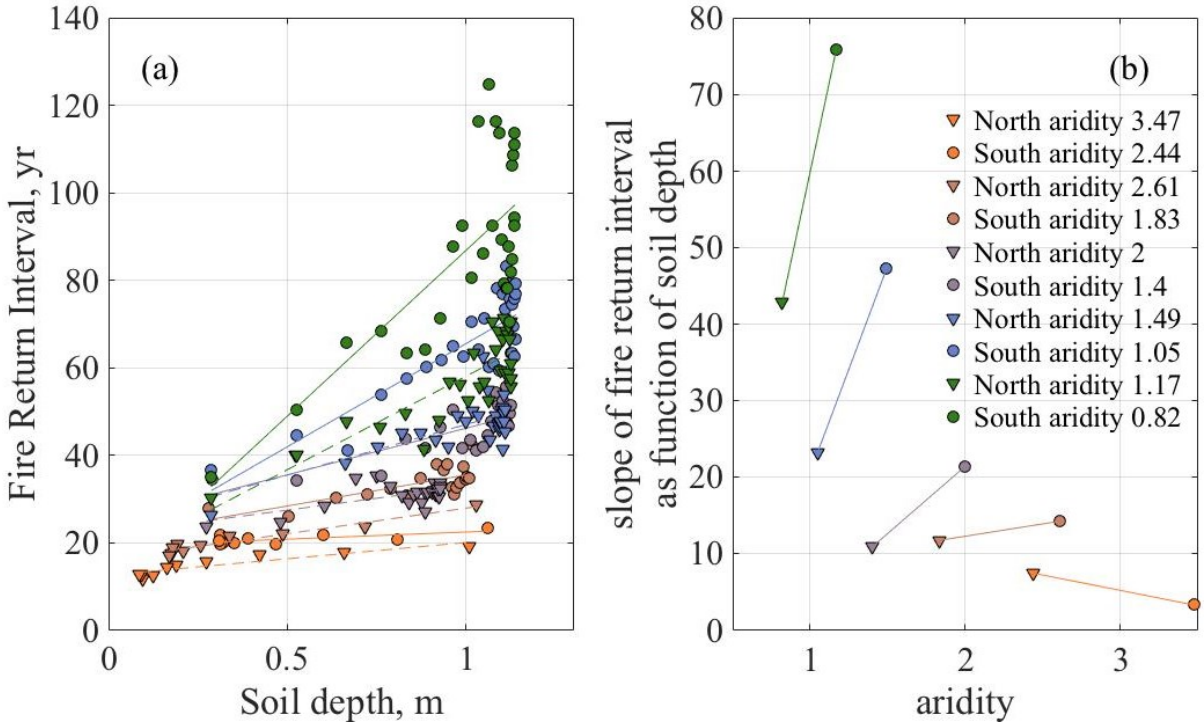

Figure 4-7 – The effect of soil depth on fire return interval across the aridity domain (a). Model simulations were designed to run for 300kyr (in the exception of for 60kyr on the driest pair) with 10 different climatic scenarios (i.e., north and south aspects with 5 different rainfall regimes). Simulations under wet and dry climatic conditions started with thin and thick soils, respectively, and allowed to reach s-s soil depth. Simulated timeseries data for Fire Return Interval and soil depth for each simulation were averaged into 5000-year bins to reduce clogging of the figure. The slopes of a linear fit from each of the 10 simulated timeseries data were plotted as a function of aridity in (b). Line connecting between north and south facing markers are for visual aid only.

4.4.5 Experiment 5: Effect of canopy cover and soil depth on fire frequency

The ecohydrological effect on fire frequency was assessed by running long term simulation with different LAI values which affects forest cover (Eqn 3.7-3.8), canopy water storage (Eqn 3.15) and transpiration (Eqn 3.24-3.26), all affecting soil moisture with a potential to influence fire in the model. The sensitivity of FRI to changes in LAI across a rainfall gradient and different topographic positions are presented in Figure 4-8.

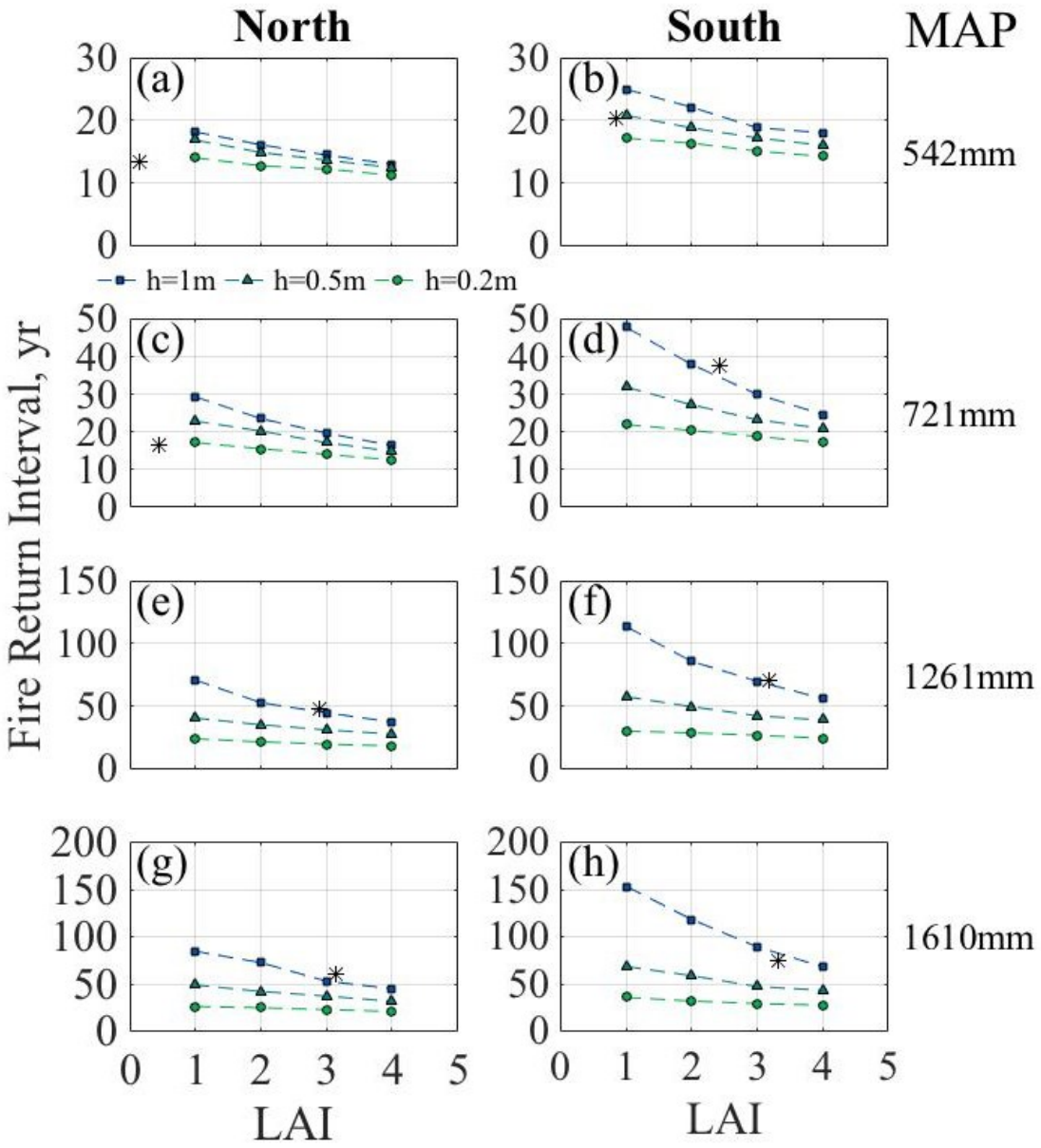

Figure 4-8– Sensitivity of fire return interval to changes in LAI and soil depth across a rainfall gradient and different topographic positions. Simulations for this experiment were designed to run for 400kyr, with steady soil depth and LAI changing from 1-4 in 1 unit LAI increments every 100kyr. Asterisks represent the LAI and fire return interval in steady state conditions (depending in s-s soil depth). Note that the scale of the y-axis increases with rainfall.

Asterisks in Figure 4-8 represent the steady state fire return interval for coevolved systems at each specific climatic condition (i.e., combination of rainfall and aspect). Assuming soil

depth doesn't change within several years' time, any point along the graph represent what would have been the FRI if there was any change in LAI, which could happen during drought conditions after dry years or immediately after fire, or after years that are above the mean annual precipitation. Overall, results show that FRI is higher (i.e., fires becomes less frequent) when soils are deeper soils and on south facing systems (Figure 4-8, right column) for a given combination of LAI and soil depth (Figure 4-8, left column). However, FRI increases with decrease in LAI, contrary to what one would expect (Figure 4-8). This phenomenon becomes stronger with increasing rainfall and soil depth and is stronger on south facing hillslopes (Figure 4-8, right column).

4.5 Discussion

4.5.1 Evaluating the hypothesis

Fire was found to have a substantial effect on s-s soil depth (Figure 4-2a), time to s-s (Figure 4-4) and fluvial processes (Figure 4-3a) especially above aridity 1.5. Results show that pattern of s-s soil depth with aridity that emerged when running model simulations *with* and *without fire* (Figure 4-2a and b) resembles the observed patterns of soil depth (Figure 2-3a), which highlights the effect of climate and possibly fire on the coevolution process and on development of soil depth in particular. Results show that fire increases the magnitude of difference in soil depth beyond aridity 1.5, to levels close to those that had been observed (Table 3-1). The increase in the effect of fire is related to fluvial erosion processes and feedbacks which dominate in coevolution on higher aridity values (Figure 4-3a). It was suggested that the difference in fluvial processes were related to either one or a combination of fire frequency, and the effect of individual fire in the reduction in forest cover and *Ic*.

Overall, s-s biomass density decreases with increasing aridity (Figure 4-2b). Steady state biomass from simulations follow the same pattern as s-s soil depth when aridity is higher than 1.5 and doesn't at lower aridities. This points to the fact that biomass is controlled by soil depth (and erosion rates) above that aridity threshold (i.e., as climate becomes drier) and by the effect of fire on vegetation below it. Similar to s-s soil depth, the sensitivity of s-s biomass to fire increases from mid- towards higher aridity values (Figure 4-2c). In lower aridities, on the other hand, while the sensitivity of s-s soil depth to fire is very low, s-s biomass show higher sensitivity, with a decreasing trend in values below aridity 1 (Figure

4-2b and c). The increasing sensitivity of s-s biomass to fire could be explained by the proportion of *obligate seeders* species, which was defined to be 100% below aridity 1 and in lower proportion on higher aridities (Figure 3-3). Because fire causes obligate seeder species to die and start regenerating from seeds, mean biomass under this aridity threshold are lower, on average, than what it would have been without the effect of fire (Figure 4-2b). Similar fire-related reduction in biomass was observed in high elevations across the Sky-Islands in Arizona (Pelletier et al., 2013).

The phenomenon that erosion controls vegetation patterns was observed by Milodowski et al. (2015) in the Northern-Californian Sierra Nevada, USA, where mean basin slope, a proxy of long term erosion rate, explained 32% of variance in above ground biomass, outweighing the effect of other factors, such as mean annual precipitation, temperature and lithology. The authors ascribed this effect to the reduction in water holding capacity due to limitation dictated by thinner saprolite. It should be stated that other factors such as seed or vegetation erosion (eg., Collins et al., 2004; Tucker et al., 1999; Yetemen et al., 2015b) were neither investigated in Milodowski and co-authors as in this contribution. It is recommended that these indirect effects of erosion should be addressed in more detail in future studies.

Similar threshold relationships of biomass with aridity was also found locally. Using remotely sensed data across some part of the eastern highlands in Victoria, Tesemma et al. (2014) found a decreasing sigmoidal pattern of forest LAI with aridity, with the threshold starting around aridity 1 (defined as: $P - PET = 0$, Figure 4i in the paper). Despite the fact that their results based on a short-term snapshot of the LAI condition, they highlight the effect of climate and possibly fire on vegetation patterns in the region.

Even though patterns and magnitude of difference in s-s soil depths are similar to what had been observed, (Figure 2-3a) modelled predictions overestimate the location of the threshold across the aridity axis (Figure 4-2a). The reasons for such discrepancy are suggested to be the following:

(i) Figure 4-2a shows predictions of s-s soil depth where it is in balance with climate, biomass and fire frequency. Due to lack of evidence from the literature, it is unclear whether contemporary soil depths (and thus biomass) are in such steady-state across SE Australian uplands. This can point to uncertainty in such a comparison between the observed and modelled values. For example, a recent study showed that soil in the snowy mountains in SE Australia had been getting deeper during the late Holocene (Stromsoe et al., 2016). The fact

that climate has been getting warmer and wetter since the LGM, and that forest are currently more abundant across the highlands (McKenzie, 1997, 2002) suggest that erosion and weathering regime might have changed, and that contemporary soils might not have had enough time to respond to these changes over the last 20kyr or so (Cohen et al., 2013). It is suggested that due to high erosion rates and frequent fires, the driest sites have the highest potential to be in steady state conditions (both in soils and biomass) within that period. And indeed, according to the analysis presented in Figure 4-4b, it takes dry sites ~37kyr to get to s-s soil depth, which is shorter than fluctuations in climate during the late Quaternary (Augustin et al., 2004; Petit et al., 1999). Wet sites, on the other hand, take 111 kyr which is longer or equal to fluctuations in climate during the late Quaternary (Augustin et al., 2004; Petit et al., 1999), which suggests that the soils at the wet end of the aridity spectrum might just stay relatively deep. On mid-aridities, the analysis suggest that soil might still be increasing in depth. In order to overcome this important knowledge gap, it is recommended to estimate contemporary and long term soil erosion and production rates, possibly using dating techniques for soil that do not require the assumptions of s-s soil depth (such as U-series)(eg., Dosseto & Schaller, 2016; Suresh et al., 2014), and compare them with short lived environmental radionuclides, such as ^{137}Cs or ^{210}Pb (Smith et al., 2011b; Walling & He, 1999).

(ii) Hillslopes with higher erodibility tend to become flatter, while those with lower erosion efficiency become steeper (Carson & Kirkby, 1972). This phenomenon was found to drive the evolution of hillslope asymmetry, where different microclimatic conditions control erosion rates on hillslopes facing different directions (Istanbulluoglu et al., 2008; McGuire et al., 2014; Richardson, 2015; Yetemen et al., 2015b), which was also found consistently across SE Australian uplands (Chapter 2). The discrepancy between the modelled and the measured soil depth values could also be explained by the fact that slope is kept constant throughout all model simulations. Moreover, changes in slope may result in different insolation (Yetemen et al., 2015b; a), which would indirectly alter its aridity. These conditions make the model underestimate soil depth on dry systems and overestimate soil depth on wet ones.

It is unlikely that a point scale model could accurately predict soil depth values across a complex landscape. The relatively simple formulation and parameterisation of the model impedes it from being able to give accurate predictions. For example, one model limitation is that it runs all its simulations with the same slope. This prevents the model from being able to

accurately simulate diffusive and fluvial erosion rates, which affects its ability to predict soil depth. However, it is argued that the current model design allows it to be able to give good predictions for the purpose of testing the hypothesis. Indeed, results show that the model successfully predicts both trends and magnitude of difference between systems states (Figure 4-2). The magnitude of difference in soil depth and forest type within the domain can be observed qualitatively (Figure 1-2), where forest type vary between open woodland with short and sparse trees to wet forest with trees that can be more than 70m tall, and that some consider to be *'the world's most carbon-dense forests'* (Keith et al., 2009). Overall, the findings support the posed hypothesis that fire related processes and feedbacks are critical to explain observed patterns and magnitude of difference in system states, and that their effect of on coevolution increases with aridity. This suggests that fire related processes and feedbacks push climate-driven dry systems to be even drier and exaggerates the difference in system states across the domain.

4.5.2 The relative role of post fire reductions in forest cover and infiltration capacity

Analysis of the different geomorphic processes across the aridity gradient suggests that the pattern and difference in s-s soil depth between simulations *with* and *without fire* might be caused by mechanisms which affect the consequence of individual fires and/or the rate in which these fires occur (i.e., fire frequency). The effect of individual fires was analysed by isolating *the effect of fire on forest cover* and *the effect of fire on Ic.*

Results show that values of s-s soil depth and s-s biomass are sensitive to the effect of fire on *Ic*, and that this sensitivity increases with aridity (Figure 4-5;Table 4-2;Table 4-3). It is suggested that post-fire reduction in *Ic* gradually increase the dominance of fluvial processes beyond aridity 1.5 (Figure 4-3c), which can explain the shallower soils from simulations *with fire* beyond that point (Figure 4-5a, Figure 4-2). On wetter sites (aridity<1.5), any increase in *Ic* does not have a significant difference on (the already low) runoff generation.

In a study of post fire infiltration and runoff measurements, *Sheridan et al* (2016) found that post-fire runoff generation was highly correlated with aridity, such that higher aridity areas were associated with higher post fire runoff ratios. These more arid locations appeared to be associated with younger and less developed soils, where high intensity rainfall events were more likely to induce high magnitude runoff and erosion events such as debris flows, as

observed across in south eastern Australia (Nyman et al., 2011, 2015b; Smith et al., 2012). Model results indicate that s-s soil depth (Figure 4-2a) and the time to reach steady state (Figure 4-4b) are determined mainly by erosion rates, especially in the drier portion of the aridity gradient, while it is less obvious in wetter climates were low soil production rates might be limiting soil depth.

Infiltration capacity values and the way they plot with aridity might point to another possible reason for the overestimation of the location of the threshold with respect to aridity axis. The model was parameterised using hundreds of hydraulic conductivity and rainfall simulation measurements that were roughly grouped together into three aridity values, which depended on forest type (Langhans et al., 2016b)(see Appendix IV). While the end members of the *Ic* values are at the right range, this model parameterisation might cause the location of *Ic* values to be misplaced cross the aridity axis. The development of soil hydraulic properties such as hydraulic conductivity and infiltration capacity, depend on geology, vegetation and climate (Lohse & Dietrich, 2005; Thompson et al., 2010). It is proposed that despite the empirical-based parameterisation, the model might benefit from decoupling of *Ic* from climatic forcing by including a model that captures the coevolution of these soil properties with time under the effect of vegetation and climate. It is suggested that such an addition to the model may help it to give more realistic predictions of soil depth.

The effects of fire on forest cover was found to have less effect on s-s soil depth, but more so on s-s biomass (Figure 4-5;Table 4-2;Table 4-3). These results indicate that the post-fire erosive damage after the burning of the canopy is not comparable to the that after the reduction of *Ic*. Similarly, Wilson et al. (1999) found that plots that were logged and not burnt yielded less runoff and sediment than plots that were logged and burnt or logged and disturbed.

4.5.3 Sensitivity of soil depth and biomass to fire frequency

The results show that an increase in fire frequency causes a reduction in s-s soil depth, but not under wet conditions (i.e., low aridity; Figure 4-6). The threshold in which s-s soil depth has the steepest slope as a function of aridity is slightly affected by the fire frequency, starting in aridity values higher than 1.5 when fire return interval is 20 years, and extends to aridity 1.8 as it decreases to 100 years (Figure 4-6). The most pronounced effect of fire

frequency on soil depth in dry climates can be explained by the low *Ic* values under these climatic conditions (Eqn 3.17; Appendix IV). On wetter climates, s-s soil depth is not sensitive to higher fire frequency, possibly due to the high post-fire *Ic* values (Langhans et al., 2016b).

Fire frequency changes with climate (eg., Fletcher et al., 2014b; Mariani & Fletcher, 2016; Petherick et al., 2013) and depend on fuel availability and moisture content (Bradstock, 2010). However, changes in fire regime occurs faster than changes in the soil hydrological properties which develop over millennia and more (Cohen et al., 2013). According to the modelling results, fluctuations in fire regimes, possibly due to changes climate, will mainly affect soil depth in sites under drier aridity, while in wetter sites, fire frequency will have less influence. This interpretation is based on the assumption that vegetation will always return to the same state after the fire, and ignores, for simplicity's sake, vegetation resilience and the irreversible effect of multiple fires on vegetation changes (Fairman et al., 2016; Gibson et al., 2015), which could potentially affect soil depth and start a new coevolution trajectory.

Lower fire frequency causes the peak in s-s biomass which was around aridity 1 to move towards aridity 1.5 (Figure 4-6b). Similar to the stochastic fire treatment (Figure 4-2b) the reduction in s-s biomass values under wet climate is attributed to the different proportions of the two types of regeneration strategies used by the model across the aridity gradient (Eqn 3.44 and Figure 3-3). The modelling results show (Figure 4-6) that in aridities where obligate seeders dominate (aridity<1), s-s biomass densities are substantially reduced when fire return interval (i.e., increase in fire frequency) becomes shorter than the time it takes vegetation to fully recover (typically 60-80 years; Figure 3-14h).

4.5.4 Effect of soil depth on fire frequency

Fire frequency is related to soil moisture and calibrated to reproduce observed mean fire interval (Appendix II). Figure 4-7 shows that when the soils are deep, for a given soil depth, fire return interval decreases dramatically with aridity. In this case, soil moisture and hence fire frequency are controlled mostly by climate (aridity) as are not limited by soil depth. Conversely, for thinner soils, aridity has a smaller effect on fire frequency because soil moisture is limited by soil depth (and storage of water) and less so by climate. This means that when soils are thin, fire frequency will be high and could drive post fire erosion

processes, even if climate will become wetter. Results show that FRI on wet sites is more sensitive to change in soil depth, than dry sites (Figure 4-7). It is suggested that on wet sites (with low aridity), rainfall supply is high, and the rate of change in moisture taken out of the soil by evapotranspiration is lower than the rate of the increase in moisture holding capacity as soil becomes deeper, which ends up with higher net soil moisture and lower FRI. Conversely, on dry sites, the rate of change in moisture holding capacity as soil becomes thicker is not high enough to overcome the low supply and high evaporative demand, which ends up with lower net soil moisture and consistently low FRI. These interpretations can also explain the higher FRI on the wetter, south facing systems compared to those facing north (Figure 4-7b).

These results point out to a feedback between erosion, (which control soil depth and water storage), climate (which controls supply and demand) and fire frequency. Furthermore, the synergistic effect of fire frequency (Figure 4-6) and the post-fire reduction in infiltration capacity (Figure 4-5), are responsible to the effect of this feedback on coevolution to be higher on dry sites, and less so on wet sites (Figure 4-2).

4.5.5 Effect of canopy cover and soil depth on fire frequency

The partitioning of rainfall and energy affect the microclimatic conditions across the landscape, which is important to the coevolution process. For example, in many places, a significant proportions of rainfall is lost by its capture and evaporation from the forest canopy (Carlyle-Moses & Gash, 2011; Muzylo et al., 2009; Van Dijk et al., 2015). This, in turn, affect the sub-canopy moisture that is held by the litter and in the soil (Hatton et al., 1988; Nyman et al., 2015a), affecting plant transpiration and primary productivity (Eamus et al., 2006). It was suggested that, in a long term process, canopy structure and density are optimized in a way to maximise soil moisture and plant productivity (Berry et al., 2005; Eagleson, 1982; Eagleson & Tellers, 1982). Here it is hypothesised that these canopy properties could potentially affect fire frequency, and that this is one of the ways that fire affects the coevolution process. The results presented here and in the previous section highlight the importance of the interplay between water supply, storage and demand. *However, how does all this control fire frequency?*

Similar to Figure 4-7 in the previous chapter, results in Figure 4-8 show that FRI increases (i.e., fire becomes less frequent) and becomes more sensitive to changes in LAI as soils become deeper. It is suggested that as soils become deeper, soil moisture is controlled by climatic forcing and their partitioned by the canopy. In shallow soils (i.e., 0.2m) on the other hand, soil moisture is less sensitive to climate because of the limited storage capacity. Figure 4-8 shows that FRI increases in lower LAI values, especially on deeper soils. It is suggested that, for a given soil depth, lower LAI translates to lower transpiration and higher throughfall, which results in higher soil moisture and to lower flammability. On south facing slopes (right column in Figure 4-8), the lower evaporative demand for given LAI and soil depth causes this phenomenon to be stronger compared to similar systems facing north (left column in Figure 4-8). Since the relationship between LAI, soil depth and climatic forcings affect flammability and fire frequency (Figure 4-6), it can potentially have a significant effect on the development of asymmetry in soil depth and biomass, however, these depend on the differential effect of individual fires on infiltration capacity as shown in section 4.5.2.

Theoretically, a reduction in LAI can be caused by either fire or under drought conditions. According to the model, any reduction in LAI will result, on average, in lower flammability, which might have some biological advantages in allowing the reestablishment of vegetation community. In practice, this is extremely advantageous in case of "obligate seeders" such as *eucalyptus regnans*, which grow on south facing slopes over deep soils in high-rainfall areas (Cheal, 2010; Costermans, 2006). In this case, the wetter conditions after fire, can assist in the regeneration of the new seedlings and give them advantage in allowing more rapid growth while they are competing for light. On dry mixed species forest, the wetter than normal conditions allow the resprouting of the existing fire-tolerant species through epicormic shoots (Burrows, 2013; Clarke et al., 2013). Theoretically, increase in LAI can occur after a year that was wetter than average, or when more biomass has spread onto the area, using the same water reservoirs as the native vegetation. According to the model, any increase in LAI will result, on average, in higher chance of fire. It is plausible that this phenomenon has biological advantages, such as removal of competitor species that are using the same water resources.

Here, the fire module is based on existing drought and fire danger indexes, which are supported by empirical evidence relating soil moisture to flammability (eg., Finkele et al., 2006; Keetch & Byram, 1968; Krueger et al., 2016). The implementation of this concept in this model has its limitations, as this theory does not consider the effect of canopy openness

on aerodynamic resistance (which reduces water pressure deficit and decrease evaporative demand) and fuel dryness, and the latter's potential effect on site flammability and fire probably (Nyman et al., 2015a, 2018; Walsh et al., 2017). Recent work has shown the spatial and temporal variability of litter moisture content between different forest types and topographic positions and their potential effect on site flammability (Nyman et al., 2015a). The model presented here does not track dead biomass, let alone it's moisture content. It is suggested that these combinations of approaches should be considered when modelling such fire prone systems in order to stay true to natural processes, depending on model aims.

4.5.6 Mechanisms controlling the effect of fire on coevolution

An example of the coevolution of systems across north and south facing hillslopes is presented and discussed in Appendix V for brevity's sake. In this example, two systems that differ only in solar radiation coevolve differently when they are forced by two changes in rainfall regime. These results enable the visualization of coevolution and the mechanisms that were discussed in this chapter and the rates in which they occur across the two aspects. The experiment presented on Figure A- V-1 and Figure A- V-2 highlights the patterns and rates in which systems coevolve from one state to the another due to fluctuation in climate. These changes take place as long as soil, biomass, climate and fire (regime and effects) are not in steady state. These different trajectories are suggested to cause asymmetry in vegetation, soil and possibly landscape (Chapter 2).

Results from the experiments presented above point to a feedback between erosion, soil moisture and fire frequency. In this feedback (Figure 4-9), long-lasting increase in fire frequency may cause more erosion which can lead to shallower soils, as long as erosion has higher rates than soil production. Shallower soils, in turn, have less water holding capacity, which can induce more water stress and cause more frequent fires. The effect of this feedback on soil depth depend on the developmental state of the soil, which controls the potential effect of individual fire infiltration capacity (*Ic*). The decrease in *Ic* with aridity (Sheridan et al., 2016) points to the fact that this feedback will be more active in the drier forests. It is argued that this feedback pushes dry sites to be drier than what they could have been without fire (Bond et al., 2005).

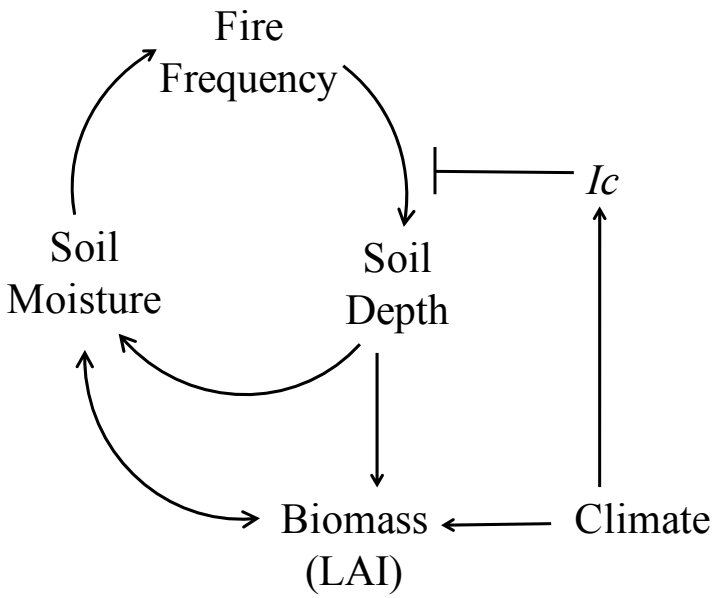

Figure 4-9– Schematic diagram illustrating feedback between soil depth (which is controlled by erosion or the lack therof) and fire frequency. In this feedback long-lasting increase in fire frequency may lead to more erosion and shallower soil, which by the reduction in soil water holding capacity, increase fire frequency. The effect of climate on observed post-fire reducrion in *Ic* keeps this feedback to be more active on drier end of the aridity spectrum.

Model simulations suggest that fire has a significant effect on the different trajectories in coevolution process, and in creating patterns of soil depth and vegetation across the landscape. By affecting rates of processes and feedbacks, fire exaggerates the differences in soil depth and vegetation on sites with higher aridity. Contradicting the regular definition of fire as an external "disturbance" to the system, results of this modelling exercise imply that fire is part of it, and that it evolves along with the soil and vegetation by affecting altering their properties. Moreover, it is suggested that fire may have even entered the way plants are hydrologically optimized to their surroundings, acting as a catalyst in the coevolution process.

4.6 Conclusions

Several numerical simulations were developed using a new 1D model designed to simulate coupled soil-vegetation systems typical to SE Australia systems, in which soil depth and biomass are output variables. Results show that:

- A decreasing logistic relationship emerged between s-s soil depth, biomass and climatic drivers (aridity) similar to measurements. The hypothesis that fire related processes and feedbacks are critical to explain observed patterns and magnitude in system states across the landscape, and that their effect of on coevolution increases with aridity was supported by the model results. Fire seemed to exaggerate the magnitude of difference in soil depth and biomass across the climatic gradient.

- The synergistic effect of Fire frequency and its effect on infiltration capacity was found to have the biggest influence on steady state soil depth and biomass above aridity 1.5. Below that aridity, fire frequency seemed to only affect biomass, mainly due to the type of fire recovery strategy. Infiltration capacity seems to an important system property which underscored soil development as a key process in coevolution.

- A long-term feedback between erosion and fire frequency was identified. By its effect on soil depth, fire induced erosion can increase fire frequency, which leads to more erosion and even more frequent fires.

- Results pointed to a possible feedback operating on shorter timescales between vegetation cover, soil moisture and fire frequency, in which fire frequency changes when forest cover is out of equilibrium with supply and demand of water and the available water stores.

It seems as if coevolution is the way in which the systems reorganize in order to achieve equilibrium between supply, storage and demand of water. In this process, soil moisture is centre in driving changes in the system through its affect productivity and fire frequency. Measurements of contemporary processes across the domain may help provide some insights into the way in which water and energy and partitioned and stored across the domain, and the potential implications on productivity, soil development, and flammability.

5 Water and energy partitioning across complex landscapes: potential implications for divergence in coevolutionary processes

5.1 Abstract

The partitioning of energy and water by vegetation and soil influence important processes in the coevolution of the critical zone. Models that examine theories of these processes can provide valuable insights and need to be backed up by empirical evidence. Actual measurements of water-energy partitioning are rare in context of coevolution. The aim of this study was to evaluate and quantify, using intensive field measurements, the way in which contemporary vegetation and soil depth affect the partitioning of rainfall and solar radiation, and to estimate the implications of this on processes in the coevolution of the critical zone. SE Australian uplands are a good natural laboratory to address the aims, as forest type and soil properties vary markedly across the landscape, due to the distribution of climate and fire. Partitioning of rainfall and energy was quantified by measuring microclimatic conditions inside and outside the forest for one year at three locations across a rainfall gradient: Christmas Hills (CH, 759mm/yr); Reefton (RT, 1314mm/yr) and The Triangle (TT, 1745 mm/yr). At each location plots were instrumented on north and south facing hillslopes to produce a total of 6 combinations of rainfall and insolation. The effect of the partitioning of water and energy on coevolution was then evaluated by analysing soil moisture and temperatures data, which affect key processes in the coevolution of the critical zone: (i) evapotranspiration and productivity; (ii) flammability; and (iii) weathering. Results show that throughfall decreases and net short-wave radiation under the canopy increases with aridity due to the lower rainfall and higher canopy openness (respectively). On wet sites, the closed canopy and the deep soil partitions water and energy in a way that resulted in wetter soils throughout the year, leading to lower flammability and higher productivity. On drier sites, the open canopy and shallow soil partitions water and energy in a way that resulted in drier soils, mainly in summer and autumn, leading to higher flammability and lower productivity. Mean annual soil water stores were found to decrease non-linearly with aridity, being more than 5-fold higher on wet sites compared to dry ones, despite annual rainfall only differing by a factor of ~2. Analysis of soil moisture and temperature suggest that soil temperatures are likely to control soil production at the drier sites, while variations in soil moisture are likely to control weathering of the soil profile and soil development on the wetter sites. The higher

weathering rates on the *wet* sites are suggested to increase the divergence between system states by keeping water holding capacity high, which feeds back to higher productivity, lower flammability and higher infiltration capacity. The lower weathering rates on the *dry* sites are suggested to increase the divergence in system states by keeping water holding capacity low, which feeds back to lower productivity, higher flammability and lower infiltration capacity. This points to a coevolutionary feedback between weathering, productivity, erosion and fire, which is controlled by the partitioning of water and energy through vegetation and soils. It is suggested that this feedback accelerates the rate of divergence in system states across the domain.

5.2 Introduction

5.2.1 Coevolution and climate

Coevolution of soil and vegetation occurs with the direct effect of climate (Berry et al., 2005; Pelletier et al., 2013; Troch et al., 2015). Basic optimality theories had suggested that vegetation communities develop in niches to optimize their water use efficiency and photosynthesis, with the available resources (Eagleson, 1982). Despite the fact that these theories may be too simplistic to represent real systems, they do build a foundation to the concept of coevolution (Berry et al., 2005).

The distribution of climatic forcing is not even across the landscape. This is especially the case in mid-latitude mountainous regions, where relatively small changes in elevation or aspect orientation results in significant differences in water and energy fluxes (Yetemen et al., 2015a), which in turn affect the coevolution processes that shape the critical zone in each location (Pelletier et al., 2013; Rasmussen et al., 2015). The SE Australian uplands are a good example of how complex terrain impacts on critical zone, as forest and soil hydraulic properties vary considerably in relatively small spatial scales. In this region, large variations in rainfall and small variations in the exposure to solar radiation have large effects on water availability (as expressed in the aridity index metric), which was hypothesised to drive the large differences in contemporary vegetation properties (Nyman et al., 2014b).

At small scales, vegetation determines how energy and water are partitioned between different components on the system. This in turn, has the potential to control processes and feedbacks that affect coevolution of the critical zone. For example, canopy partitions both

rainfall and shortwave radiation, controlling the distribution and storage of water in different components of the system: namely soil and litter. The amount of water that the soil can store had been shown to have a direct effect on net primary productivity (Eamus, 2003), canopy closure, and indirectly the system's flammability (eg., Finkele et al., 2006; Keetch & Byram, 1968; Krueger et al., 2016). The kinetic energy caused by short wave radiation at the forest floor is conducted down the soil profile (Hillel, 1982) which together with moisture and carbon, affects the rate of soil production by chemical weathering (Rasmussen & Tabor, 2007). While the general effect of climate on vegetation (Pelletier et al., 2013; Zhou et al., 2013), soils (Lybrand & Rasmussen, 2015; Pelletier et al., 2013; Rasmussen & Tabor, 2007), hydrology (e.g., Troch et al., 2015) and landform (Gutiérrez-Jurado & Vivoni, 2013a; Yetemen et al., 2015b) has been studied, the contribution of partitioning of water and energy by vegetation and soil in the context of feedback processes within coevolution hasn't been quantified (Gutiérrez-Jurado et al., 2013; Gutiérrez-Jurado & Vivoni, 2013b). It is argued that by creating different microclimatological conditions under the canopy, the partitioning of rainfall and solar radiation can affect the coevolution of the critical zone by differently allocating water and energy throughout the system. Therefore, the aim of this study was to evaluate and quantify, using intensive field measurements, the way in which vegetation and soil depth affect the partitioning of rainfall and energy in the critical zone, and to estimate what are the implications of this partitioning on coevolution processes.

5.3 Methods

5.3.1 Overview

Partitioning of rainfall and shortwave radiation was quantified by monitoring sub-canopy microclimate at six sites across an aridity gradient (varying in elevation and solar exposure) with different forest types for a duration of one year, and comparing the measurements to three nearby control sites situated outside the forest. The effect of partitioning on rainfall and solar radiation was assessed by monitoring soil moisture and temperature sensors at different depths in each of the six sub-canopy sites. The results were used to infer the potential effect of the partitioning of water and energy on three processes related to coevolution: evapotranspiration and productivity, flammability and soil weathering.

5.3.2 Site selection and description

Microclimate data was collected at three locations east-northeast of Melbourne, under an elevation/rainfall gradient (Figure 5-1). These sites were instrumented and provided data for several fuel moisture studies (Nyman et al., 2017, 2018; Walsh et al., 2017). For these studies, north and south facing hillslopes were selected at each location in order to vary solar exposure and to express variations in forest types typical of SE Australian landscapes. This study presents new data collected from the same plots (after their decommission), using a combination of pre-existing and new instrumentation that were installed in order to measure the partitioning of rainfall and solar radiation and other microclimatic conditions, as well as soil moisture and temperature. Site characteristics are presented in Table 5-1. A summary of sensor configuration at each site is presented in Figure 5-2 (more detailed information is provided in Appendix IV).

Rainfall varied significantly between the sites. Long term mean annual rainfall at Christmas Hills (CH) rainfall was 759 mm, at Reefton (RT) 1314 mm and at the Triangle (TT) 1745 mm (Table 5-1). In the SE Australian uplands, forest type and tree height is highly correlated to large and small scale variations in aridity index (Nyman et al., 2014b), which can be regarded as a surrogate for water availability (Budyko, 1974). Aridity index values for each site (Table 5-1) were acquired from a gridded resource calculated for Victoria (Nyman et al., 2014b). The aridity index resource was created by downscaling climate data (Australian Bureau of Meteorology, 2017) to a 20m pixel raster that includes the effect of topographic position (Nyman et al., 2014b). Aridity index was calculated by dividing downscaled mean annual potential evapotranspiration (calculated using the Priestly-Taylor equation; (Priestley & Taylor, 1972)) with mean annual precipitation.

Plant area index varied systematically with aridity across the sites, whereas the rate of change was most rapid at the close to the water-energy limitation boundary (Table 5-1). Net primary productivity in this part of Australia is relatively high, hosting forests that are considered to be extremely carbon-dense (Keith et al., 2009), which makes the fire activity in the region categorized as limited by fuel moisture rather than fuel availability (Boer et al., 2016). Thus, these conditions make a gradient in fire regime based on return interval across the experimental sites. For example, at CH, vegetation was characterised by Grassy dry forest (Table 5-1), which is estimated to have a fire return interval between 15-45 years, whereas

vegetation at the wet site (TT) was characterised as montane damp and wet forests (Table 5-1), where fire return interval is estimated to be between 80-300 years (Cheal, 2010).

Soil type and depth varied significantly between the sites (Table 5-1). At the dry sites (CH north and south and RT north), soils varied between 40-55 cm deep. Soil pits revealed a very thin (1-2cm) A horizon and poorly developed B and BC horizons with significant amount of gravel. At the wet sites (RT south, TT north and TT south), soil depth varied between 120-176cm. Mineral soils at these sites were covered by a relatively thick O horizon that varied between 5-15cm. Underneath, soils were highly developed with 24-40 cm thick A horizon, and very thick B horizon (92-126cm thick).

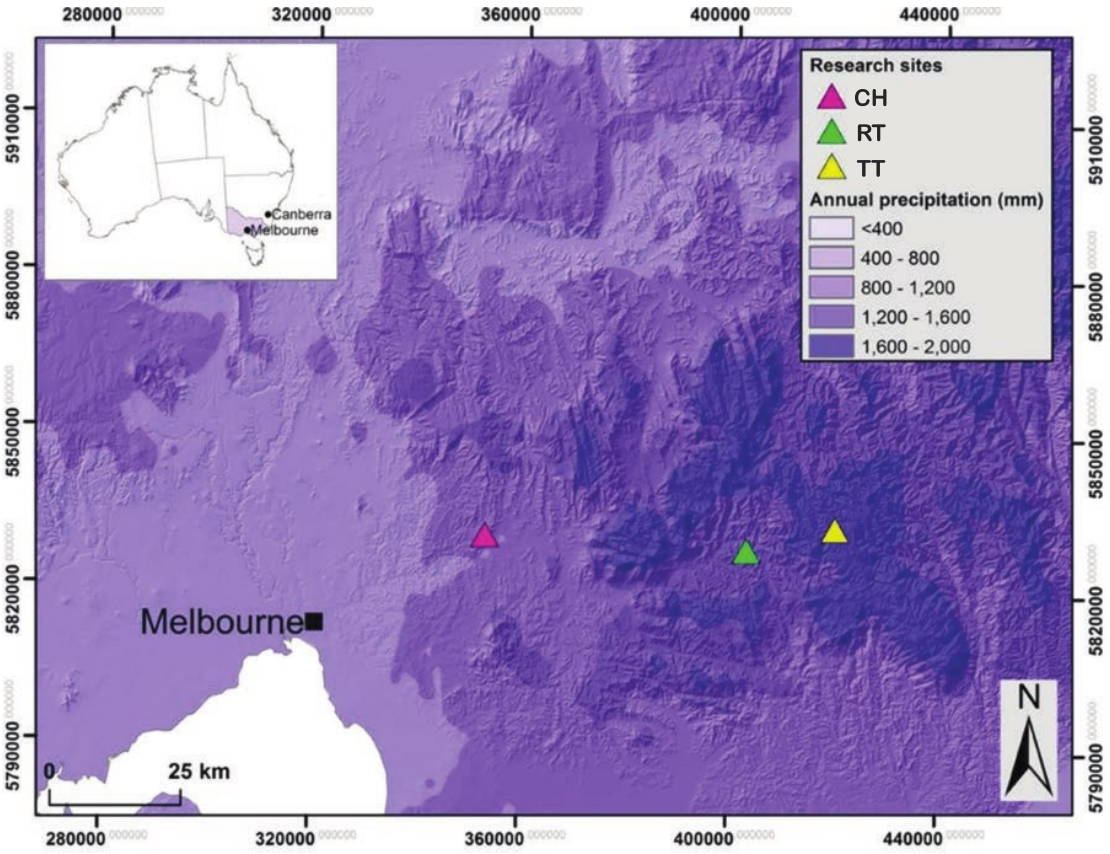

Figure 5-1 – Map of long term mean annual rainfall on top of a shaded digital elevation model of central Victoria. Selected sites are: Christmas Hills (CH), Reefton (RT) and The Triangle (TT).

Table 5-1 – Site characteristics

Site name	Aspect	Measured mean annual precipitation[*1]	Latitude	Longitude	*Ep*[*2]	Net short wave radiation[*3]	Slope	Elevation	Long term aridity[*4]	PAI[*5]	Soil Depth	Ecological vegetation class[*6]
		mm/yr	deg	deg	mm/yr	MJ/m^2/yr	deg	m			cm	
Christmas Hills (CH)	North	813.2	-37.6612	145.3368	1458.5	4304	15	285	2.32	1.74	55	Grassy dry forest
	South	(1.07)	-37.6584	145.3355			17	260	1.78	2.08	55	Grassy dry forest
Reefton (RT)	North	1193.4	-37.6983	145.8773	1338	4316	18	620	1.49	1.97	40	Wet forest
	South	(0.91)	-37.6986	145.8821			26	535	1.04	4.22	120	Shrubby foothill forest
The Triangle (TT)	North	1731.4	-37.6530	146.1028	1311.4	4080	11	1065	1	3.35	176	Montane wet forest
	South	(0.99)	-37.6536	146.1025			8	1064	0.88	3.78	105	Montane damp forest

[*1]Measured value. Values in parentheses are the deviation from the estimated mean annual precipitation data (Australian Bureau of Meteorology, 2017)

[*2]Potential evapotranspiration measured at the three open sites throughout the year of measurements. Calculated by using measured short wave radiation, temperature and relative humidity at the open sites, within the Priestley-Taylor equation (Priestley & Taylor, 1972).

[*3]Net short wave radiation calculated for the open site, using downscaled net radiation data (Nyman et al., 2014b) with the Priestley-Taylor equation for calculating potential evapotranspiration (Priestley & Taylor, 1972).

[*4]Calculated Aridity index (*Ep/P*) using gridded values from (Nyman et al., 2018) for the same sites.

[*5] From (Walsh et al., 2017) for the same sites.

[*6]Ecological Vegetation Class defined by (Cheal, 2010).

5.3.3 Measuring partitioning of rainfall and energy

The 20x20m microclimate sites at each elevation were located approximately 50 m down from the ridge under canopy cover on a north and south facing hillslope (Figure 5-2). After their re-configuration for this study, a time series of microclimate, soil moisture and temperature were recorded for a whole year, from 18/12/2015-17/12/2016 at each site. Microclimate measurements at each station were recorded using two Campbell scientific CX-1000 loggers, and included 3 pyronometers measuring short-wave radiation (SC300-L, Campbell Scientific Inc) and screen level temperature and relative humidity (CS215 probe, Campbell scientific). Throughfall was collected at each site using randomly distributed 2-3 rainfall troughs (1.2m long and 0.14 m wide) draining into 20L drums, which were weighed and emptied every download visit (2-4 week intervals) and converted to units of depth (i.e., mm).

For each paired north-south sites (i.e., for a given elevation), a reference (open) station measured rainfall (TB-3 tipping bucket rain gauge, Hydrological Services Pty Ltd, NSW, Australia), solar radiation (CS215 probe, Campbell scientific in 1 replicate) and screen level RH and air temperature using the same instruments, and wind speed using 3 cup anemometers (014A-L Campbell Scientific). Short wave radiation and wind speed were recorded in one minute intervals while air temperature and RH recoded in 30 minute intervals. All were then aggregated into a timeseries dataset of hourly and daily values.

Calculating net radiation and potential evapotranspiration

Energy input and evaporative demand were calculated in order to explore the partitioning of forcing between the open, sub-canopy and canopy levels. Net shortwave (SW_{net}, in [MJ/M^2/Day]), net longwave (SW_{net}, in [MJ/M^2/Day]) and net radiation ($R_{net} = SW_{net} + LW_{net}$; in [MJ/m^2/day]), potential evapotranspiration (E_p, in [mm/day]) and Vapour pressure deficit (VPD, kPa) were calculated using measured values from the sub-canopy microclimate sites and open reference sites in order to explore the balance between long and short wave radiation in controlling evaporative demand. Equations and methods for calculating net radiation are detailed in Appendix VII .

5.3.4 Measuring soil moisture and temperature

Soil moisture and temperatures were measured at each of the sub-canopy sites. Volumetric moisture content (VMC) was measured using ML2 and ML3 (delta T devices) at the surface of the soil using pre-installed sensors (Nyman et al., 2015a). Subsurface VMC was measured using EC-5 moisture sensors (Decagon Devices) that were installed for this study at several depths below the surface, down to soil-bedrock interface (SBI) (see Figure 5-2 and Appendix VI for sensor configuration). The subsurface moisture sensors were inserted in the soil by manually digging a soil pit, inserting the sensors horizontally at depths, and then covering the pit back up. Sensors were inserted into the wall facing upslope, that way avoiding the effects associated with digging and refilling the pit. Soil temperature was measured at the surface, in 20-30 cm below the surface and at the SBI. Details of sensor type and depths could be found in Appendix VI.

During installation, bulk density measurements were taken at each depth, close to the location of the sensor. In locations where bulk density couldn't be taken due to inadequate access, values were estimated to be at least as dense as the bulk density measurement above it (i.e., assuming soil could only become denser as it gets closer to the bedrock). Bulk density varied substantially between the sites and with depths, as with soil type (estimated using basic field texture).

Soil moisture estimation from sensors

The soil moisture sensors at the surface were calibrated per site for one of the previous studies, as described in Nyman et al. (2015a). Same calibration curves were used for this study. The sub-surface soil moisture sensors were calibrated in the lab (according the manufacturer's instructions) using soils sampled from around each sensor, and yielded individual calibration curves that convert the sensor output (in mV) to VWC (m^3/ m^3). Analysis of sensor outputs during calibration rejected the possibility to use single curve for all or for groups of sensors, as the sensors were sensitive to bulk density and soil type, both of which changed with depth. Some sensors failed during the measurements and were not included in the analysis unless it retuned to regular measurement values, and therefore considered an intermittent issue. Integrated VWC values for whole profile was calculated on a daily basis (using the VWC time series) by integrating between volumetric moisture at the different depths using a linear function.

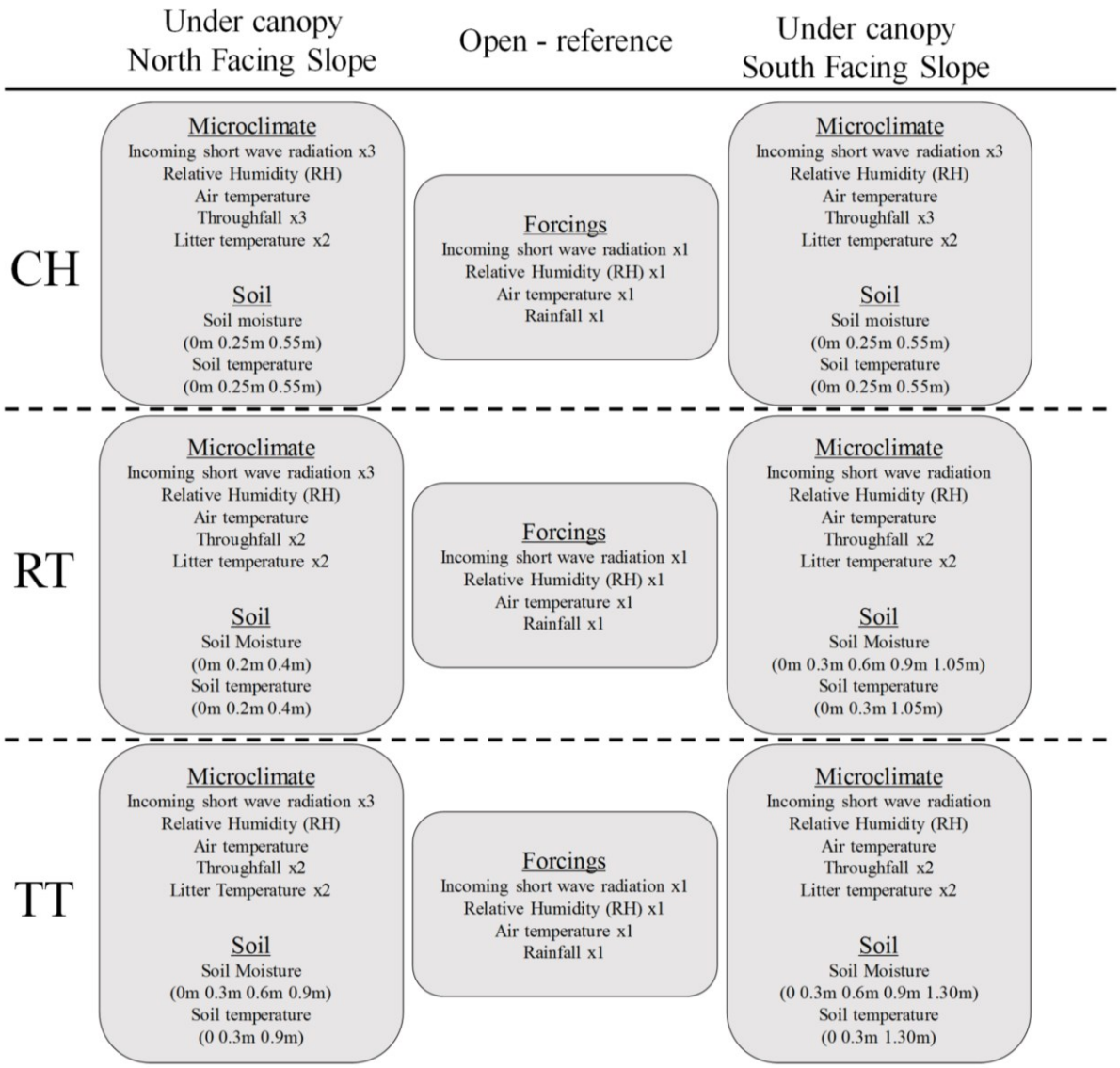

Figure 5-2 - Schematic representation of site configuration. Site details are presented on Table 5-1. Number of replicates (if above 1) is presented on the right hand side of each sensor. Depths of moisture and temperature sensors are written in parentheses.

5.4 Results

5.4.1 Partitioning of rainfall and solar radiation

Micrometeorological data measured at the sites is summarised in Table 5-2 (In order not to deviate from the main aim of the chapter, only some are presented, and other selected ones could be found in Appendix VIII). The sites yielded a relatively large amount of data from various sensors. Annual mean of daily air temperature decreased and mean daily RH

increased with elevation (Table 5-2), but did not vary much between the north and south facing sites. Potential evapotranspiration (E_p, mm) under the canopy was higher at north facing and drier sites (CH north and south and TT north), consistent with aspect and the amount of canopy cover (PAI, Table 5-1). The largest difference (480mm/yr) in E_p between the aspects was recorded at RT and smallest (120mm/yr) was recorded at TT. Consistent with soil depth (Table 5-1) mean temperatures at the SBI decreased with elevation. At TT south, mean temperatures at SBI was, on average, higher than at the surface and above the soil (i.e., air temperature).

Partitioning of rainfall

During the period of measurements, cumulative throughfall increased linearly with cumulative rainfall, and was very close across all the sites (Figure 5-3a), pointing to a similar throughfall ratio. Although total throughfall differed between the sites (Figure 5-3c), throughfall ratio showed only a slight increase with aridity, despite larger differences in PAI (Table 5-1). In general, throughfall was higher on the north facing aspects on CH and RT and showed an opposite trend in TT (Figure 5-3b). The latter reverse in the trend could be explained by the fact that one of the throughfall troughs on the south facing hillslope was positioned relatively close to a road where there is slight reduction in vegetation cover.

Table 5-2 – Microclimate measurements across the sites.

Site and aspect	Total throughfall depth*[1]	Daily air temperature*[2]	Mean RH*[3]	Sub canopy SW_{net} *[4]	Canopy SW_{net} *[5]	Sub canopy *Ep*[6]	Mean daily soil surface temp*[7]	Mean daily soil temp at SBI	Mean volumetric soil moisture	Mean of actual soil moisture*[8]
	mm	°c	%	MJ/m²/day	MJ/m²/day	mm/yr	°c	°c	cm^3/cm^3	mm
Christmas Hills - North	658 (0.81, 0.19)	14 (31, 4, 0.99)	75 (1.01)	1980 (0.46)	2001 (0.47)	671 (0.43)	20 (40)	18.9	0.22	261 (0.34)
Christmas Hills - South	616 (0.76, 0.24)	14 (32, 5, 1.02)	79 (1.06)	990 (0.23)	3127 (0.73)	425 (0.28)	20 (38)	14.1	0.15	180 (0.24)
Reefton - North	818 (0.69, 0.31)	13 (30, 2, 1.05)	79 (1)	1705 (0.4)	3254 (0.55)	753 (0.49)	14 (27)	13.84	0.19	192 (0.15)
Reefton - South	775 (0.65, 0.35)	13 (30, 3,1.03)	84 (1.06)	394 (0.09)	3862 (0.89)	272 (0.18)	12 (23)	11.54	0.30	598 (0.46)
The Triangle - North	1162 (0.67, 0.33)	8 (23, -1.4, 0.94)	89 (1.03)	956 (0.23)	3014.3 (0.74)	350 (0.24)	10 (21)	9.29	0.35	948 (0.54)
The Triangle - South	1262 (0.73, 0.27)	9 (24, -1.4, 1.01)	90 (1.04)	403 (0.1)	3659.2 (0.9)	229 (0.16)	9 (20)	9.77	0.37	808 (0.46)

*[1]In parenthesis: throughfall ratio and interception loss.

*[2]In parenthesis indicate (from left to right): daily maximum and minimum air temperatures and proportion of the mean from the mean at the open site.

*[3]Relative Humidity; Values in parenthesis indicate the proportion of the mean RH from the mean at the open site.

*[4]Net Short Wave Radiation below the canopy; Values in Parenthesis represent ratio between sub-canopy SW_{net} and at the open

*[5]Net Short Wave Radiation intercepted by the canopy; Values in Parenthesis represent ratio between canopy SW_{net} and at the open

*[6]Potential Evapotranspiration (Evaporative demand); Values in parentheses indicate proportion of the mean from the mean at the open site.

*[7]Values in parenthesis indicate daily maximum surface temperature.

*[8]In parentheses, proportion of long term mean annual rainfall (Australian Bureau of Meteorology, 2017).

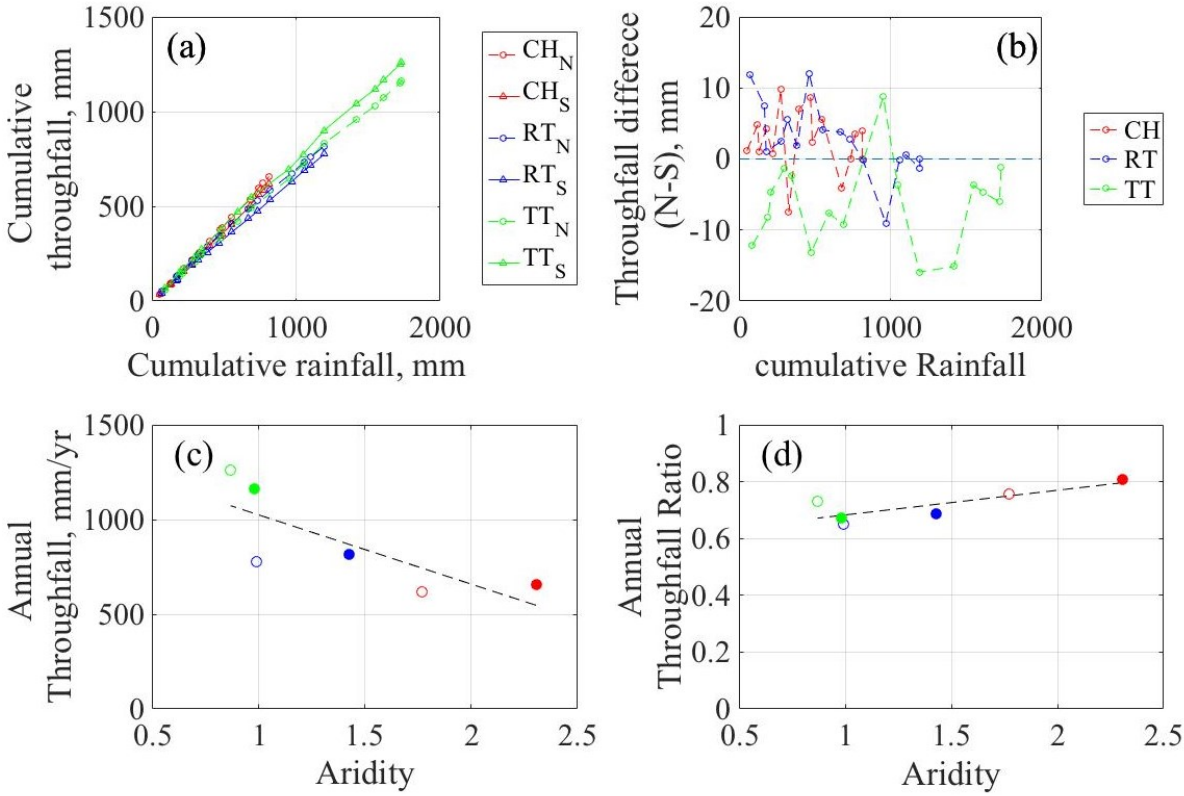

Figure 5-3 - Measured cumulative throughfall measured under the canopy (a), and the throughfall difference between the aspects (b) at CH, RT and TT, plotted as a function of cumulative rainfall measured at the adjacent open site at each location. Annual throughfall (c) and throughfall ratio (d) as a function of aridity for each of the sites (Table 5-1) Dashed line is a linear function fitted to the data.

Partitioning of solar radiation

The sub-canopy daily net radiation (R_{net-bc}) and its components, net short (SW_{net-bc}) and long wave radiation (LW_{net-bc}), are presented in Figure 5-4. Despite subtle differences, LW_{net-bc} oscillated around zero, depending the site and time of year (Figure 5-4, right column). For example, sub canopy values on south facing aspect at TT were positive year-round, whereas values on north facing aspect at CH were positive only 61% of the time, which is indicating that the soil is absorbing heat, probably as a direct response of short wave radiation (Figure 5-4a) and low PAI at this site (Table 5-1). Negative values were also calculated for all the open sites in summer (Figure 5-4, right column) for similar reasons. Despite the variations in LW_{net-bc}, it had little to no effect on R_{net-bc}, which is mainly

affected by net shortwave component (Figure 5-4, left column). SW_{net-bc} differed from one site to another. In general, north facing aspects had higher seasonal response (amplitude), and overall had higher values, compared to the south facing ones. The biggest difference between the aspects were on RT site, possibly due to highest difference in slope and PAI between the opposing aspects (Table 5-1). $SW_{net-bc}$was highest during summer and lowest during winter and showed very low values across the south facing aspects. This effect is assumed to be a combination of solar exposure, seasonal sun zenith angle, vegetation cover and sun path length through the canopy (Gutiérrez-Jurado & Vivoni, 2013b; Nyman et al., 2017; Yetemen et al., 2015b; Zhou et al., 2013).

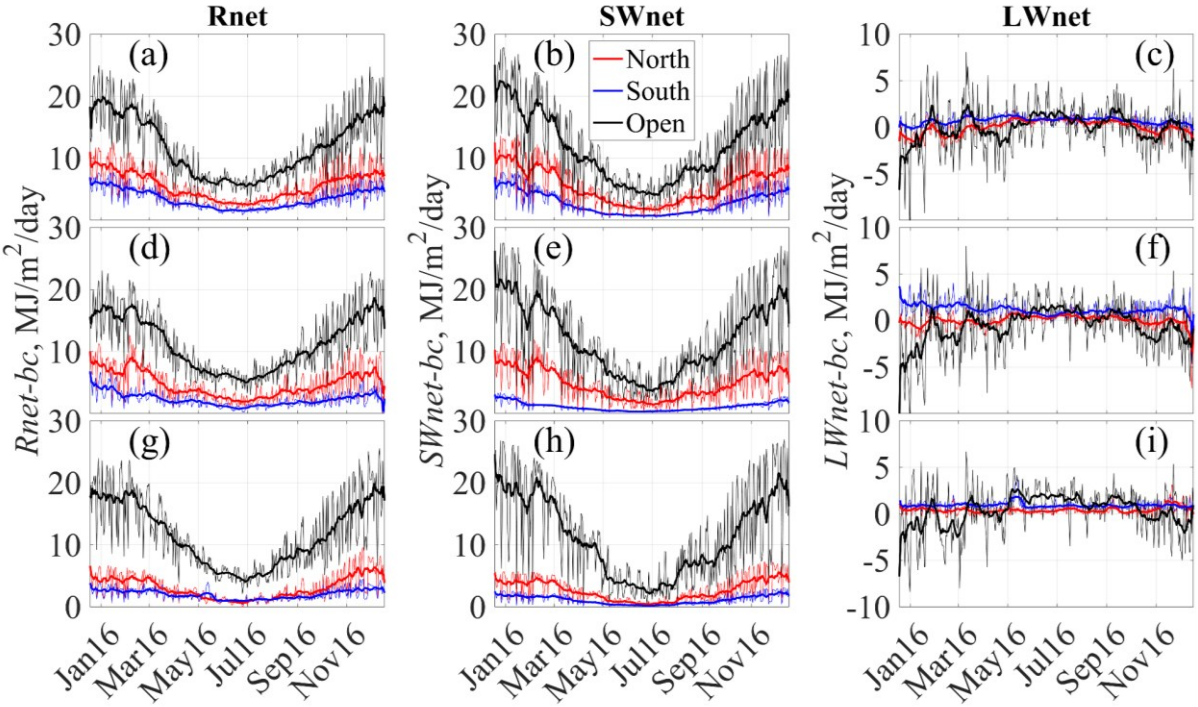

Figure 5-4 – Sum of daily sub-canopy net radation (*Rnet-bc*) and its components, net short- (SW_{net-bc}) and longwave radiation (LW_{net-bc}), in CH (a-c), RT (d-f) and TT (g-i), at the open and below the canopy on both aspects, across a year of measurements. For each plot, a 15-day moving average is plotted on top as a visual aid of trends.

Incoming shortwave radiation that was intercepted by the canopy (SW_{in-c}) was calculated by the difference between incoming shortwave radiation in the open and under the canopy ($SW_{in-c} = SW_{in-o} - SW_{in-bc}$). Net shortwave radiation at the canopy (SW_{net-c}) at each site was calculated by: $SW_{net-c} = SW_{in-c}(1 - \alpha_f)$, where α_f is albedo for dry, damp and wet

forests (0.15, 0.26 and 0.17, respectively; (Nyman et al., 2014b)). Figure 5-5 shows the calculated SW_{in-c} for all the sites throughout the year measurements.

As expected and similar to R_{net-bc} and SW_{net-bc}, the effect of seasonality (sun zenith angle) on SW_{net-c} is expressed more on south facing hillslope than on north facing ones. Generally, north facing hillslopes showed an increase in SW_{net-c} with increase in rainfall (Figure 5-5a, c and e), while this effect was smaller on south facing hillslopes (Figure 5-5b, d and f). This indicates that PAI has a bigger effect on interception of short wave radiation on the north facing hillslopes, while slope and aspect has a bigger effect on the south facing aspects. Canopies on the south facing hillslopes intercepted more short-wave radiation compared to the north facing ones (Figure 5-5, right column). The biggest difference between the intercepted and sub-canopy short wave radiation was at TT, where the PAI varies very little between the aspects (Table 5-1), and only a small proportion of the short-wave radiation is entering the canopy and reaching the forest floor. On north facing hillslopes at CH and RT, SW_{net-bc} and SW_{net-c} were similar, probably due to the lower PAI (Table 5-1) and the fact that north facing hillslopes are facing the sun and solar radiation has shorter canopy path-length before reaching the pyranometer (Nyman et al., 2017).

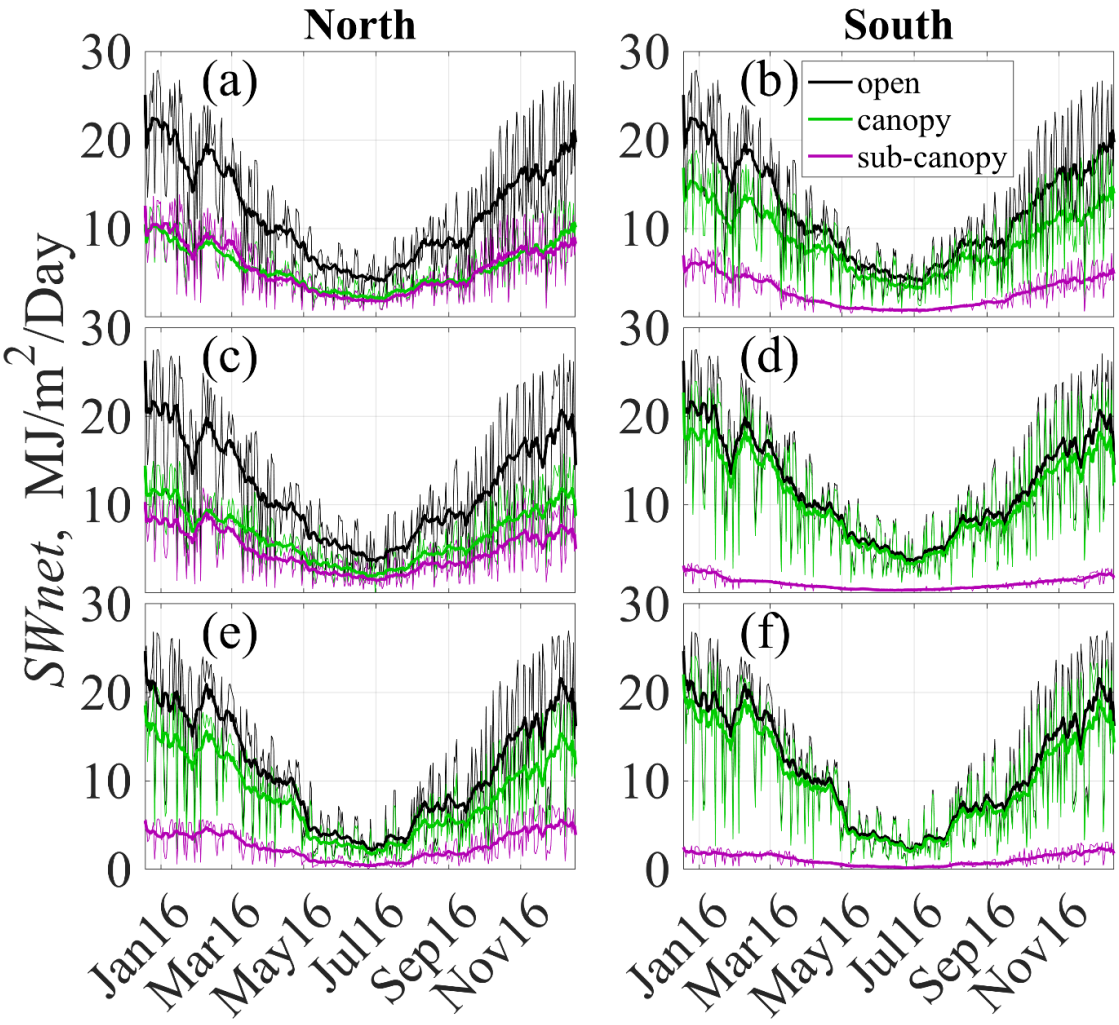

Figure 5-5– Net short wave radiation during the year of measurements, at the open, canopy and below the canopy at both aspects in CH (a-b), RT (c-d) and TT (e-f). bold lines are a 15-day moving average used to show tends.

Evaporative demand across the landscape

Evaporative demand (E_p) is often estimated by calculating potential evapotranspiration using the Penman-Monteith equation, which integrates the effect of net solar radiation, vapour pressure gradients, wind and aerodynamic resistance (Monteith, 1965), all of which affect the rate of evaporation of surface water from liquid to gas state. It is clear from the equation that the effect of solar radiation and vapour pressure deficit (VPD) on potential evapotranspiration is significant, but the effect of the latter is mediated by aerodynamic and surface resistance (Monteith, 1965). Here I use short wave radiation and VPD, based on measured values, to express the "potential" evaporative demand at the forest floor and the canopy, similar to the

approach taken by Nyman et al. (2018). Net shortwave radiation and VPD for below the canopy (SW_{net-bc}, and VPD_{bc}), at the open (SW_{net-o}, and VPD_o) and at the canopy (SW_{net-c}, and VPD_c) as a function of aridity are presented in Figure 5-6. Mean VPD_c was calculated using mean values of minimum, maximum temperatures and mean RH at each site and the corresponding value at the open site, assuming the values inside the canopy is somewhat between values inside and outside the forest. While SW_{net-o} did not vary considerably (Figure 5-6b), SW_{net-bc} increased with aridity, with higher values at the north facing hillslopes compared to the south ones (Figure 5-6a). Naturally, the trend reversed at the canopy level (Figure 5-6c). As expected, results show that short wave radiation at the forest floor and at the canopy depend on solar exposure and canopy cover and less so on elevation (Figure 5-6a-c), while VPD increases with elevation regardless of canopy cover (Figure 5-6).

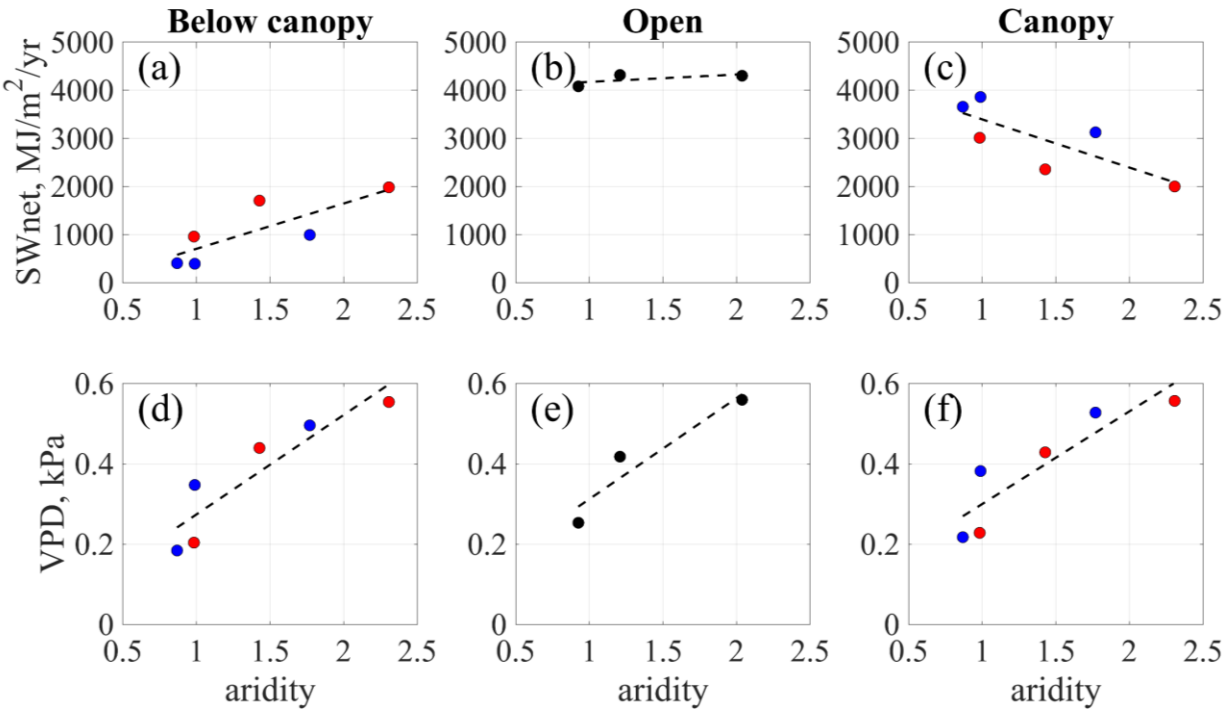

Figure 5-6– Annual sum of net short wave radiation (SW_{net}) and mean vapour pressure deficit (VPD) below the canopy (a and d, respectively), at the open (b and e, respectively), and at the canopy (c and f, respectively) as a function of aridity on north (red) and south (blue) facing aspects across an aridity domain. Net short wave at the canopy (SW_{net-c}) was calculated as a difference between incoming short wave radiation measured at the open and under the canopy, using different albedo values for each (see text). VPD at the canopy (VPD_c) at each site was calculated by using averages temperatures and RH from the open and

under the canopy. Note that the difference between the temperature and RH under the canopy and at the open were very small overall.

5.4.2 Soil moisture dynamics

Volumetric soil moisture measured at the surface (VWC_{surf}) and at the bedrock-soil interface (VWC_{SBI}) are presented in two left columns of Figure 5-7. The use of theoretical VWC values for wilting point (VWC_{wp}) and field capacity (VWC_{fc}) is approximated and used here to illustrate the difference in moisture state at each and between the sites rather than an exact value. Thus, VWC_{wp} can be regarded here as metric that points to theoretical water stress. Overall, it is possible to divide the six sites into two categories according to the response of the soil to rainfall, whereas CH north, CH south and RT north are considered *dry*; and RT south and both TT are categorised as *wet*. As expected, in all the sites, surface soil was more responsive to rainfall, and showed a seasonal response to increasing precipitation during winter. On the dry sites, VWC_{surf} was higher than VWC_{wp} only during winter (Figure 5-7a, b and d), while at the three "*wet*" sites, winter rainfall caused VWC_{surf} to raise above VWC_{fc} (Figure 5-7e, g and h).

Values of VWC_{SBI} at the three *wet* sties were less responsive to rainfall events (Figure 5-7g, h), which can be explained by the porous structure of the subsurface soil at that location as observed in the field. Furthermore, VWC_{SBI} at the three *wet* sites were close to or above VWC_{fc} (Figure 5-7e, g and h), which means that, theoretically, deep rooting vegetation could access moisture year-round, and that these sites were not limited by water. Conversely, VWC_{SBI} at the *dry* sites did not show an expected pattern, being close to VWC_{fc} at CH north, and below VWC_{wp} at the CH south (Figure 5-7a and b, respectively). Overall, both hillslopes at CH showed counterintuitive trends, where the north facing hillslope was wetter and the south facing hillslope was drier than expected. The fact the soil at the south facing hillslope is drier is somewhat surprising considering the lower shortwave radiation reaching the forest floor at that site (Figure 5-4b). Note that the drop in VWC_{SBI} signal in CH north on October 2016 (Figure 5-7a) is suspected to be due to a temporary malfunction of the sensor.

The integrated volumetric soil moisture (VWC_{int}; Figure 5-7c, f and i) was calculated using additional soil moisture sensors throughout the profile (see methods section). The three *wet*

sites (RT south and both aspects at TT) show expected patterns in VWC_{int} and are situated above VWC_{wp} year-round, and close to or above VWC_{fc} during winter (Figure 5-7f and i). Conditions on CH were different. On this location drier-north facing hillslope was above VWC_{wp} most of the year, whereas at the south facing hillslope was above it only in winter (since June 2016).

Figure 5-8a shows the mean annual integrated volumetric water content for the whole soil profile ($\overline{VWC_{int}}$) for each site, plotted as a function of aridity. Generally, $\overline{VWC_{int}}$ decrease as aridity increases, with CH north showing values higher than expected according to the overall trend (Figure 5-7a). Other than CH south, soils at rest of the sites were situated above VWC_{wp}.

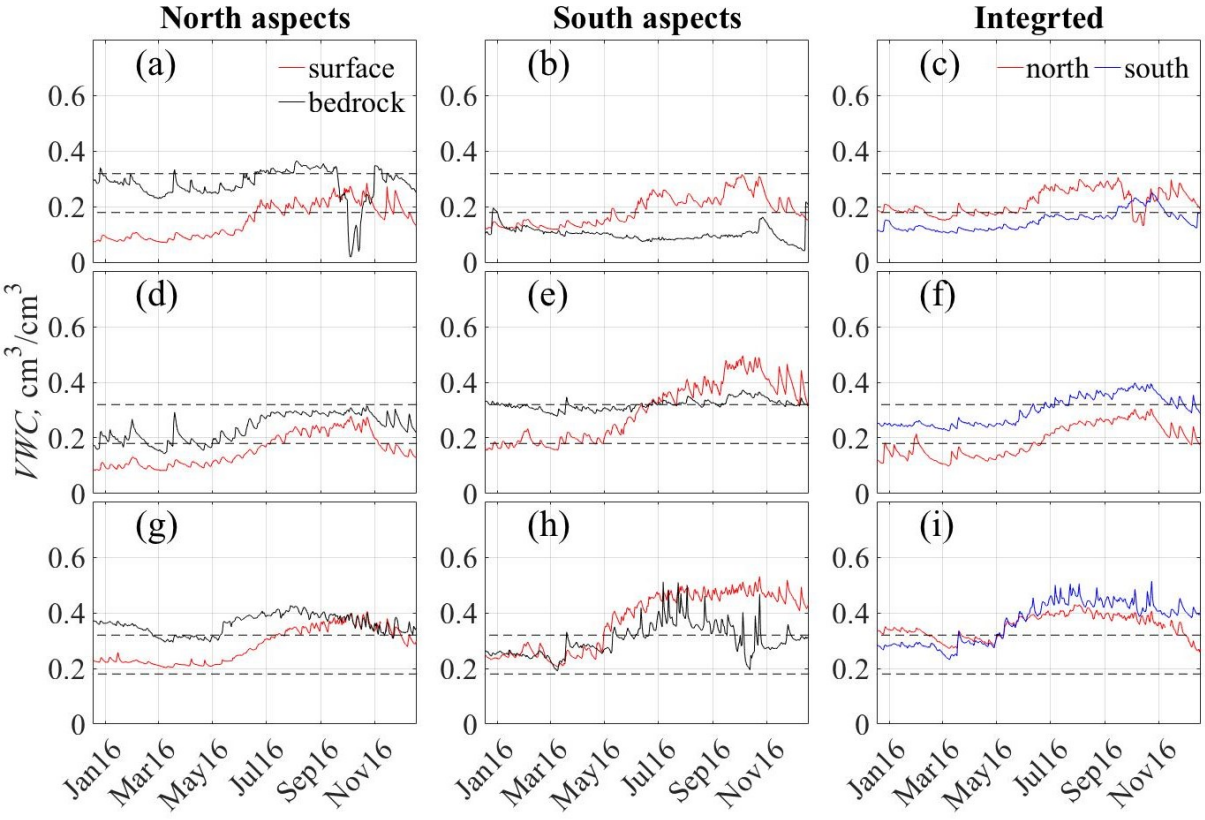

Figure 5-7 –Daily means of volumetric water content (VWC) measured at the surface and bedrock interface for north (left column) and south (middle column) facing hillslopes; and integrated volumetric water content (VWC_{int}) calculated from daily values from all the soil moisture sensors at each site (right column), for CH (a-c), RT (d-f) and TT (g-i) sites throughout the measurement period. Dashed black lines are the hypothetical values for VWC at wilting point (VWC_{wp}; lower line) and field capacity (VWC_{fc}; top line), and represent

theoretical plant available water capacity for clay loam (Clapp & Hornberger, 1978), typical to the area (Rees, 1982). The two left columns show only the VWC at the surface and at the bedrock interface, however the rest of depths are shown in Figure A- VIII-3 in Appendix VIII

The integration of soil moisture as presented in Figure 5-7c, 7f and 7i, does not represent the actual "bucket size" that takes into account soil depth. A rough estimate of the actual water moisture retained in the soil (V_s, [L]) was calculated using $V_s = h\ (\overline{VWC_{int}}/n)1000$ where h is soil depth [m], and n is porosity for clay loam, assuming that the mean texture between the surface and bedrock interface is that of a clay-loam, a typical soil found in forests in this region (Rees, 1982). Figure 5-8b displays the calculated V_s for each site plotted with aridity, while the mean values are displayed in Table 5-2. Results show that *Vs* exaggerates the differences in soil moisture across the domain (Figure 5-8b). Wetter sites contain more moisture compared to sites on the drier side of the spectrum (Figure 5-8b, Table 5-2). Soil on the *dry* sites held, on average, 15%-34% of long term annual rainfall per site, while the *wet* sites held 45%-52% (Table 5-2). In the aridity domain in this study, TT north contained more than 5 times as much water than CH south. The biggest difference in *Vs* between north and south facing hillslopes was observed on RT site, where the south held 3 times more water than its north facing counterpart.

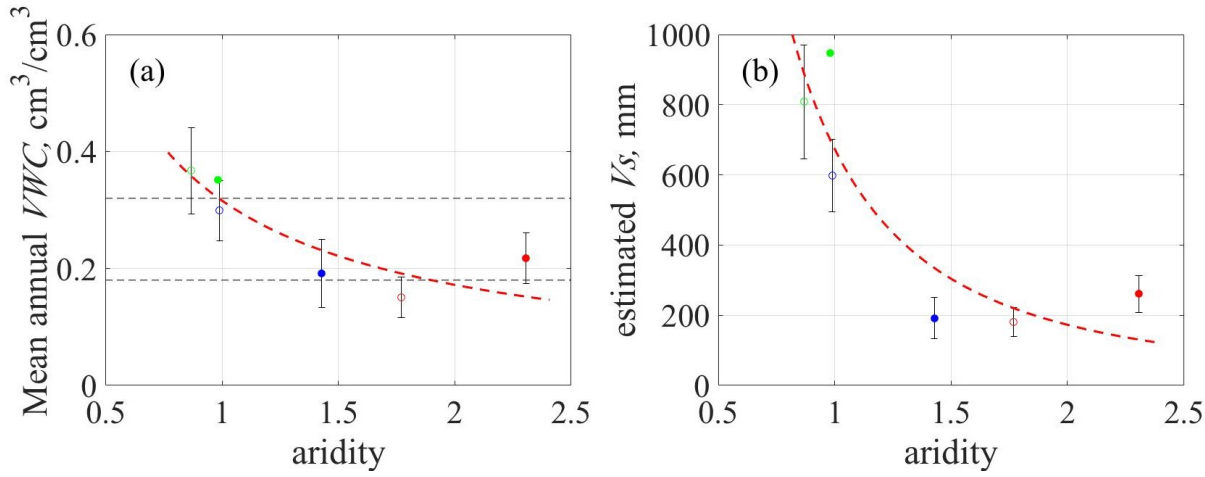

Figure 5-8 – (a) mean annual soil integrated volumetric water content ($\overline{VWC_{int}}$) and (b) mean annual water retained in soil (*Vs*) as a function of aridity for: CH (red) RT (blue) and TT (green); whereas markers representing north facing hillslopes are full. Power functions fitted for $\overline{VWC_{int}}$ (R^2=0.78; RMSE=0.05) and *Vs* (R^2=0.79; RMSE=170) are presented in dashed

red line. Horizontal dashed lines represent theoretical VWC at field capacity (top) and wilting point (bottom), based on clay loam soil. Bars represent standard deviation.

5.4.3 Soil temperature

Soil temperature varied with depths in all sites (Figure 5-9). Air temperature fluctuated on daily basis, while soil temperatures fluctuated less as the soil became deeper. Soil surface was warmer than the air in CH despite the drop in air temperatures in Autumn and winter (March-September), while in the two other sites air temperature was colder than soil temperature only in winter. In general, soil temperature showed an annual sinusoidal pattern, following trends in air temperature. As expected, the amplitude was smaller as the soil became deeper with an overall lower mean annual temperature at depths. On summer and spring, soil temperatures were warmer at the surface than in depth. This trend reversed in autumn in all sites, and was more drastic in winter, where the temperatures at the SBI were warmer than at the surface.

Soil moisture and temperature are important factors that drive critical zone evolution by controlling the rate of chemical weathering (Amundson et al., 2015; Riebe et al., 2016; White & Blum, 1995). The results in Figure 5-9 imply that the soil acts as a buffer for temperature fluctuations and can even retain some heat through winter which can have a significant effect on soil weathering rates, especially in winter when soil moisture increases (Figure 5-7). Furthermore, higher temperatures on the subsurface across winter has an effect on the overall energy balance of the system, whereas ground heat flux, which is positive across summer (i.e., heat from solar radiation is conducted down the soil profile) becomes negative in winter (i.e., heat from the soil profile is conducted upwards towards temperature gradient). This effect can explain the positive LW_{net}values in winter and the negative values in summer across the sites (Figure 5-4, right column).

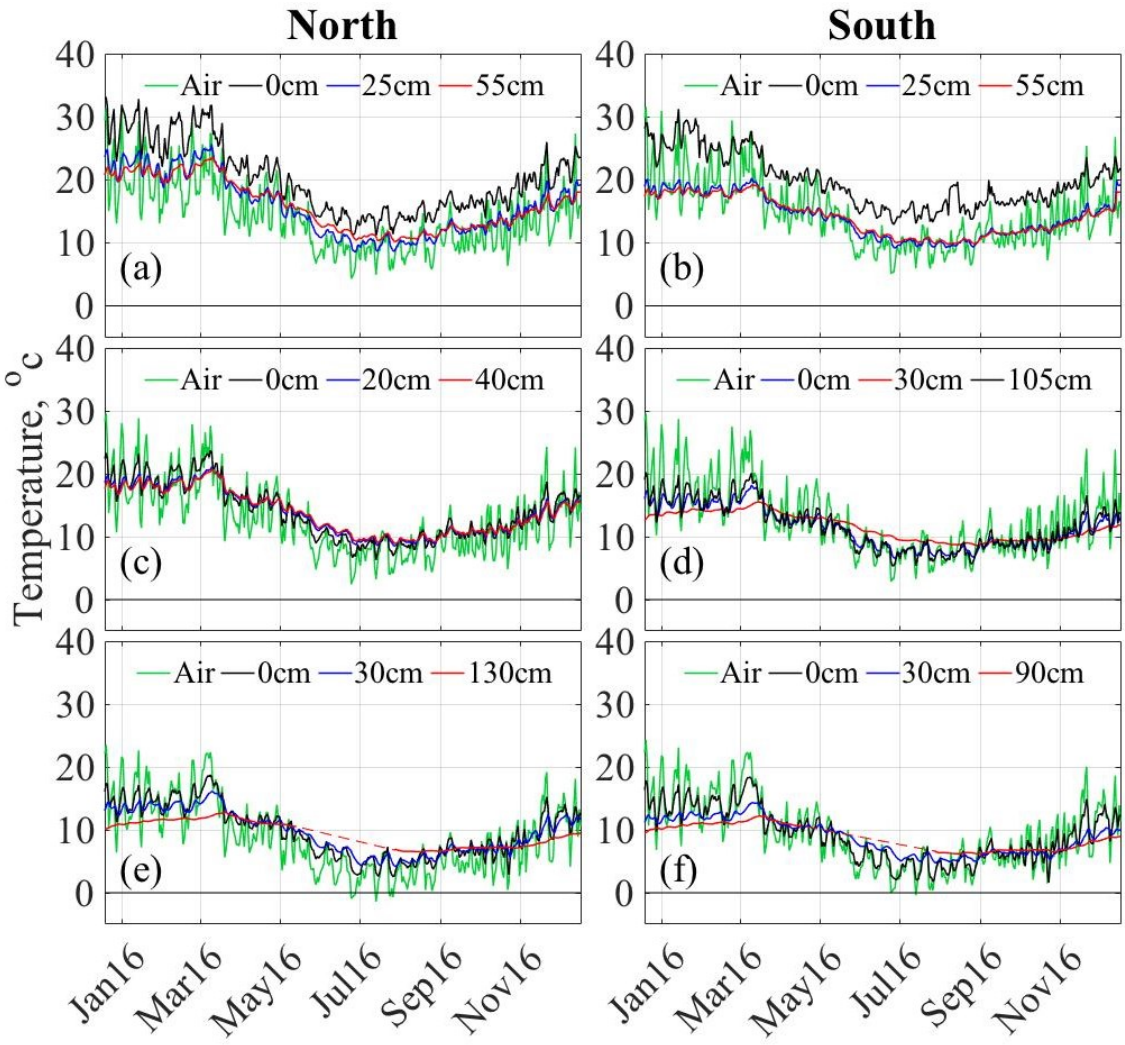

Figure 5-9– Daily mean of air and soil temperatures at the surface, 20-30 cm below and at the soil-bedrock interface on north (left column) and south (right column) facing hillslopes on CH (a-b), RT (c-d) and TT (e-f). Dashed lines at TT sites are a linear interpolation of soil temperatures at the bedrock interface, where data at these depths were unavailable due to sensor malfunction.

Changes in soil temperature are affected by several factors, such as net radiation, heat conduction from the air and latent heat transfer, which occurs as water evaporates from its surface (Hillel, 1982). Figure 5-9 shows that soil temperature responds to (and possibly affects) fluctuations in air temperatures as function of time. The response of soil temperatures to changes in air temperatures is presented in Figure 5-10. Soil surface at all the sites showed most significant response to change in air temperature. As soil became deeper, the effect of

air temperature became less significant (Anderson et al., 2013; Hillel, 1982), which was more apparent in the deepest soils at RT south and both aspects at TT (Figure 5-10d, e and f).

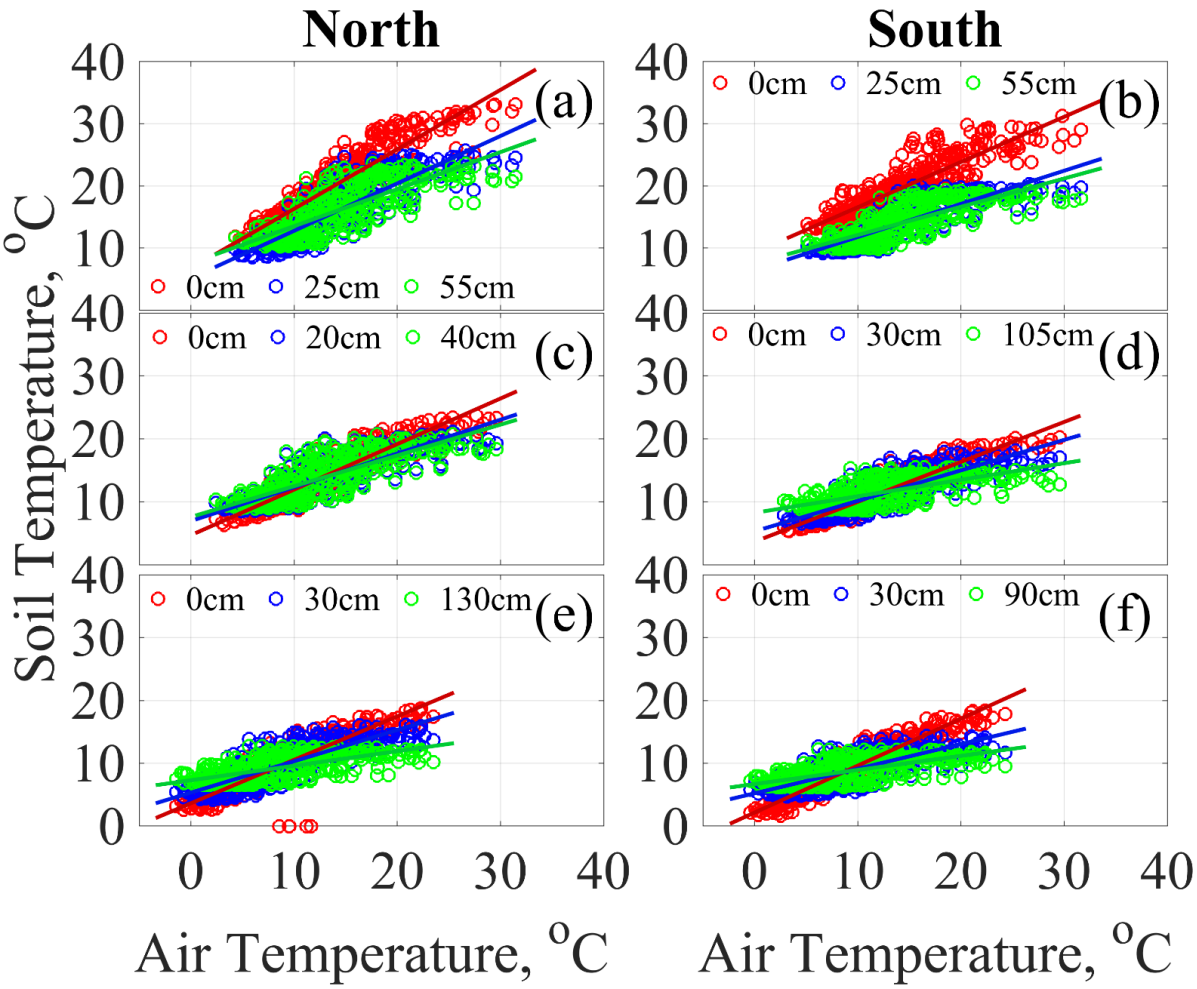

Figure 5-10– Daily mean of soil temperatures at different depths as a function of daily mean of air temperature at CH (a-b), RT (c-d) and TT (e-f) for north and south facing aspects. Each set of data was fitted with a linear function and the slope of this function was used to analyse the response of soil depterature at each depth with change in air temperature (Figure 5-13).

5.5 Discussion

5.5.1 Partitioning of rainfall and energy – summary

The first order control on biomass across the climo-spatial domain is elevation, with its orographic effect on rainfall, shown as increase in PAI (Table 5-1). The increase in elevation also affects throughfall depth across the sites (Figure 5-3). Dry sites and north facing

hillslopes were expected to show higher throughfall ratio (Figure 5-3d), corresponding to the decrease in PAI (Table 5-1) which potentially, should allow more rainfall to go through the canopy. The fact that interception loss (and throughfall ratio) is relatively uniform across the aridity gradient may reject other plausible explanations, such as strong wind that may shake the leaves during and after rainfall, and rainfall angle, that occur locally. In a different study, Mitchell et al. (2012) found similar values of interception loss (1-*throughfall ratio*), regardless of the variable annual rainfall and across topographic positions, while looking at water balance of a post-drought mixed species Eucalyptus forest in SE Australia.

This study looks at how two forms of energy drive evaporation across the sites: SW_{net} and VPD . The results clearly demonstrate that net short wave solar radiation under the canopy SW_{net-bc} is mainly affected by PAI (or canopy closure) and solar exposure (aspect) and not by elevation (Figure 5-6a). VPD on the other hand, is strongly correlated with aridity but not affected by aspect nor PAI, as there is very little difference in temperature and RH in the tree topographic positions and forest cover (Table 5-2). Overall, it seems that the relative importance of VPD as evaporative driver increases with aridity (Figure 5-6d-f).

On *dry* sites, both rainfall and throughfall are low (Table 5-2; Figure 5-3c), which means that there is less water to evaporate, and a relatively larger proportion of energy originated by short wave radiation is used to heating the surface. The low PAI and SW_{net-c} at the drier sites (Table 5-1; Figure 5-6c) means that the open canopy intercepts relatively low amount of radiation, while the rest of it (SW_{net-bc}) is reaching the forest floor (Figure 5-5a, b and c). It is postulated that the sparser vegetation at these dry sites results in lower aerodynamic resistance, which intensifies the relative significance of VPD in the evaporative demand (Lindroth, 1993; Monteith, 1965). It is suggested that canopy water stores empty faster during and between rainstorms on dry sites and on north facing slopes due to higher SW_{net} per leaf area (PAI), the lower aerodynamic resistance and the higher VPD , which could explain the lower than expected throughfall ratio at these sites (Figure 5-3d; Table 5-2). Evaporation of intercepted water during rainfall was found to be a significant process in many cases (Carlyle-Moses & Gash, 2011; Dunkerley, 2008; Muzylo et al., 2009), and a major contributor for the interception loss and water balance (Dunin et al., 1988). At the forest floor, evaporative demand (E_p) is high (Table 5-2) due to low interception of SW_{net} (Figure 5-5a, b and c; Figure 5-6a) and high VPD (Figure 5-6d). All of the above point out to the fact that there is high pressure on water stores to satisfy the evapotranspiration demand at

these drier sites, pointing to their higher sensitivity to actual soil moisture (Figure 5-7; Figure 5-8) and can explain the high abundance of drought tolerant species across these hillslopes (Cheal, 2010).

As climate becomes *wetter* (i.e., lower aridity), throughfall increases despite the denser canopy, and more water is available to evaporate across all water reservoirs in the system. Higher PAI (Table 5-1) also means that more solar radiation is intercepted by the canopy and a smaller proportion reaches the forest floor (Figure 5-6c). Under these conditions, the relative role of (the already low; Figure 5-6) VPD in the evaporative demand becomes lower due to the high aerodynamic resistance (Lindroth, 1993; Monteith, 1965). Thus, on these wet sites, the relative role of solar radiation in evapotranspiration from the canopy is higher than the role of VPD , despite possible night-time transpiration (Gharun et al., 2013b). It is possible that during rainstorms, energy from solar radiation and VPD is not sufficient to evaporate canopy water stores due to the high PAI and complex canopy at these wetter sites. This can explain the higher than expected throughfall ratio on these sites (Figure 5-3d; Table 5-2). Similarly, the high aerodynamic resistance under the canopy reduces the potential effect of VPD on evaporative demand from the soil/litter (Nyman et al., 2018). This means that the relatively low shortwave radiation that penetrates the canopy (SW_{net-bc}) is the main driver that evaporates water from the forest floor in wet forests, followed by the higher proportion of long wave radiation (Figure 5-4f and i). The results support the study of Nyman et al. (2018) who looked at the factors controlling litter moisture dynamics under the canopy during two drying phases in summer.

5.5.2 Soil water stores and productivity

The volume of soil water holding capabilities is determined by its physical properties and its depth. Soils are deeper as climate becomes (Table 5-1). This allows more water to be stored on the wetter (i.e., low aridity) hillslopes compared to drier ones (Figure 5-8b), potentially maintaining higher transpiration rates, productivity and more biomass. Results show that mean annual soil moisture (*Vs*) decreases significantly with aridity (Figure 5-8b). SE Australia host some of the most carbon-dense forests on earth (Keith et al., 2009). The deep soils and very large water stores measured at the *wet* sites (Table 5-2) are required to maintain such high productivity. On the other side of the aridity gradient, the sparser vegetation does not require large amount of moisture to maintain productivity. The big

difference between wet and dry can be seen across the two aspects at the RT site, sharing the same rainfall.

Soil moisture on CH displayed an unexpected pattern in which north facing hillslope was considerably wetter than the south facing one (Figure 5-7c). It is suggested that the difference in vegetation is what causing this pattern, and that PAI at both hillslopes (Table 5-1) is not in equilibrium with soil depth and climatic conditions on the year of measurements (Berry et al., 2005; Eagleson, 1982). These suggest that despite the differences in long-term aridity (Table 5-1), differences in PAI between the two aspects the sites should potentially be smaller in order to express the expected differences in soil moisture.

5.5.3 Effect of microclimate under the canopy on flammability

Soil moisture has been shown to influence fuel moisture in the lower levels of the litter layer (Hatton et al., 1988), was widely used as a proxy for fuel moisture and site flammability (eg., Finkele et al., 2006; Keetch & Byram, 1968; Krueger et al., 2016), and it is often used as a predictor for fuel availability and moisture in fire risk assessments (Walsh et al., 2017). Here I will look at the evaporative conditions that affect the volumetric water content of the soil surface. Results show that short wave radiation under the canopy is highest during summer months (December through send of February, Figure 5-5), which represents the period with the highest probability of wildfire across SE Australia. During that period, net radiation and evaporative demand is at its highest, resulting in low surface soil moisture at the drier sites (Figure 5-7a, b and d). In autumn, net radiation levels drop but soil moisture is not replenished until the beginning of winter (around June; Figure 5-7).

Figure 5-11 shows cumulative distribution functions (CDFs) for volumetric water content at the soil surface (VWC_{surf}) for all the sites throughout the measurement period (Figure 5-11a) and on summer through autumn (Figure 5-11b), while Figure 5-12 shows the number of days VWC_{surf} was below theoretical wilting point (VWC_{wp}). The latter can be regarded as a qualitative indicator of relative flammability throughout the year of measurements. Distributions vary significantly between the sites (Figure 5-11a), a pattern which is exaggerated during summer-autumn period (Figure 5-11b). Overall, the order of surface soil moisture across the sites correspond to their aridity index values (Table 5-1), and their Average Fire Cycle (Table A- II-1 in Appendix II) and Tolerable Fire Intervals known for

such systems (Cheal, 2010; Kennedy & Jamieson, 2007). On summer and Autumn, CDFs of dry forests and wet forest are almost separated by VWC_{wp} (Figure 5-11b), indicating an overall dry conditions at the forest floor at the dry sites (Nyman et al., 2015a). Fuel moisture is very important for fire propagation and connectivity on the landscape scale (Nyman et al., 2015a, 2018). Theoretically, if at any point in time during summer-autumn a fire would have started at a random location, the chance of the TT and RT south to be severely burnt would be considerably low, compared to the dry sites (i.e., CH north and south and RT north), which, according to their soil moisture (Figure 5-7a and Figure 5-7d; and Figure 5-11b), would have been ready to burn at any moment.

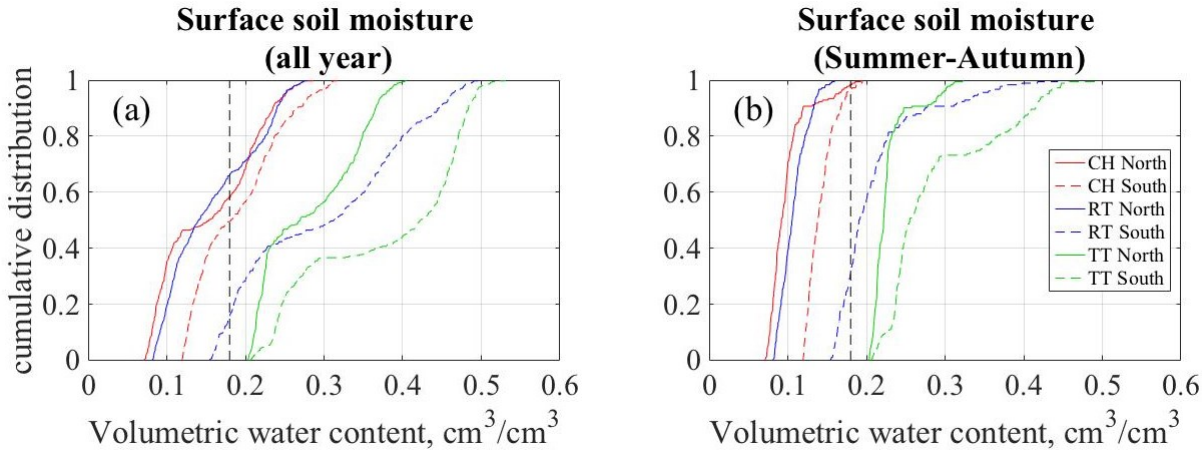

Figure 5-11 – Cumulative Distribution Functions (CDFs) of surface volumetric soil moisture (VWC_{surf}) for all the measurement period (a) and summer (31/12/2015 - 29/2/2016)(b). Vertical line represents theoretical VWC at wilting point (VWC_{wp}) as reference.

The effect of climate on coevolution can be a relatively slow process, which change its rate with climatic fluctuations (Pelletier et al., 2013, 2016). This means that a system that its evolution is driven by climate will take a long time to equilibrate to a state where change in soil depth and biomass is *zero*. It seems that fire holds within it the potential to increase the rates in which a system reaches equilibrium under steady or changing climatic forcings through a set of positive feedbacks. For example, an increase in fire frequency has the potential to affect the coevolution process by changing the soil erosion regime (for example, higher soil erosion rates as seen in Moody & Martin, 2001a; Nyman et al., 2011; Prosser & Williams, 1998 and others), which can alter the soil's biomass holding capacity as a response to long-term changes in soil depth (Fletcher et al., 2014a; Milodowski et al., 2015). A change

in biomass, in turn, can affect fuel load and its dryness (flammability) at a point, due to changes in forest cover and corresponding shortwave radiation fluxes reaching the forest floor (Figure 5-5; Figure 5-6a).

This feedback is hypothesised to be one of the possible drivers for the observed patterns in system states across the study area. A first-order test of the hypothesis would be in showing whether patterns in site flammability correspond with patterns of soil depth (which reflects longer-term balance between soil erosion and production). In order to do that, it is assumed here that the proportion of time soil moisture at the surface for a given site was below VWC_{wp} (defined here as $pVWC_{wp}$) corresponds to its relative flammability (assuming drier soils correspond with higher flammability). $pVWC_{wp}$ is calculated using:

$$pVWC_{wp} = \frac{\sum_{DOY=1}^{365} VWC < VWC_{wp}}{365} \quad 4.1$$

Figure 5-12 shows $pVWC_{wp}$ plotted as a function of aridity. The analysis shows a threshold in $pVWC_{wp}$ value between aridity 1 to 1.4 (between north and south facing hillslopes at RT), similar to observed pattern in soil depth (Table 4-1; Figure 2-3a).

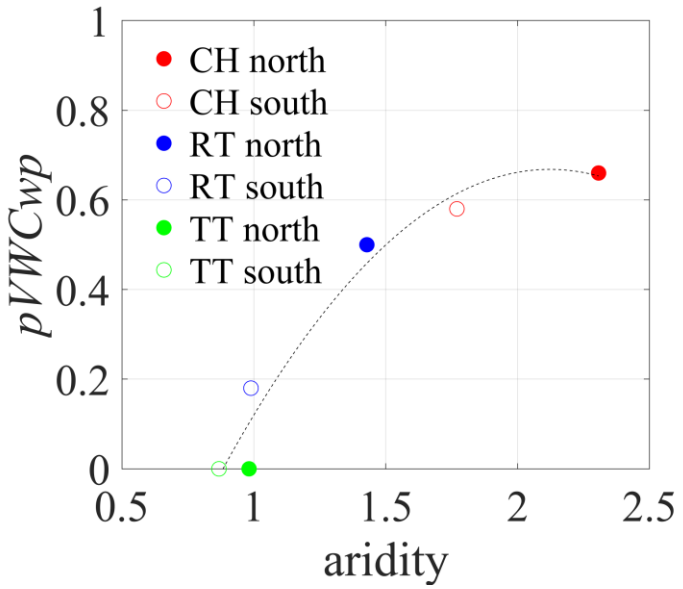

Figure 5-12 - The proportion of time in which the volumetric water content at the soil surface (VWC_{surf}) was under the theoretical wilting point (VWC_{wp}), calculated from the CDF (Figure 5-11a). This metric is proposed to be a qualitative indicator for relatevie flammability only for the year of measurements. Dashed line is a second order polynomial function plotted to the data.

5.5.4 Potential effect of microclimate under the canopy on soil weathering

The main way energy transfer through soils is by heat conduction, and it depends on the mineral composition, particle size distribution and soil moisture, as water is a better heat conductor than mineral soils (Hillel, 1982). As expected, results show that temperatures fluctuated less at the SBI (where bedrock is constantly converted to soil) compared to the surface (Figure 5-9 and Figure 5-13a). These fluctuations had been shown to cause temperature related mechanical breakdown of rock to smaller particles (eg., McFadden et al., 2005; Sharmeen & Willgoose, 2006).

The slope of the dashed lines on Figure 5-10, which are fitted to air and soil temperature data, can be interpreted as the response of soil temperature at a specific depth to changes in air temperature. The less buffered soil temperature is from air temperature, the higher the slope of these curves. Another interpretation for this metric is the heat conduction property of soils. Figure 5-13a show an analysis of the slope of the response curves as a function of aridity and soil depth. Results show that the response of soil temperatures to air temperatures at the surface and at 20-30 cm was higher with increase in aridity. This response can be explained by the higher proportion of shortwave radiation that reaches the forest floor on dry sites compared to wetter ones (Figure 5-5, Figure 5-6a). This energy is spent to evaporate water from the soil surface, to heat the soil surface and the air above it, but can also be used for chemical reactions in weathering and soil production. When the canopy becomes less open (*PAI* increases, Table5-1), the amount of short wave radiation that is entering the canopy is lower (Figure 5-5, Figure 5-6a), and soil temperature becomes less responsive to air temperatures.

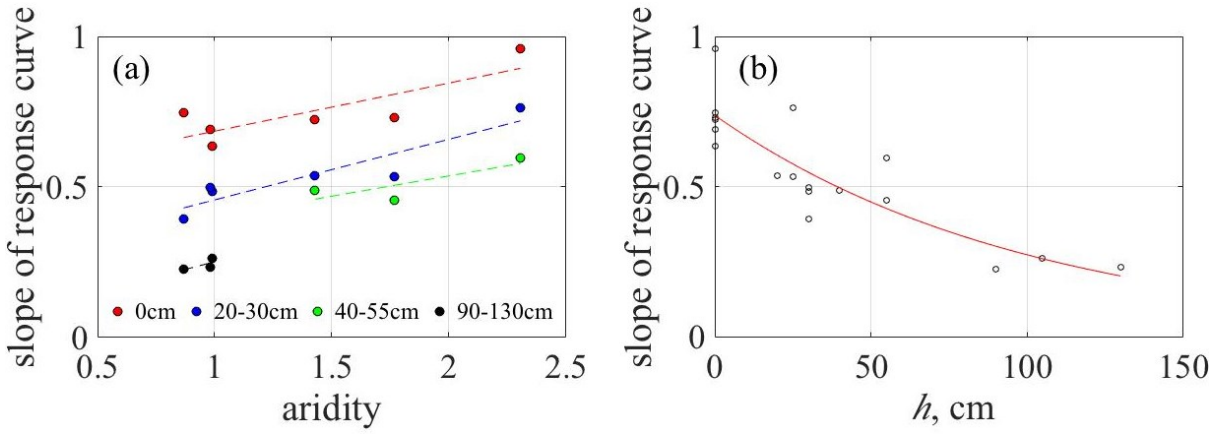

Figure 5-13 – The slope of the response curve of soil to air temperature as (slope of linear function fitted to data at each depth in Figure 5-10) as a function of aridity (a); and as a function of soil depth (b), in all the sites. Dashed colored lines at (a) are 1st order polynomial function fitted to data at similar depths across all the sites (only as visual aid); and the red line on (b) is a fitted exponential function to all data combined ($R^2 = 0.74$).

Soil moisture and temperature dynamics are often regarded as drivers of soil production and development (eg., Amundson et al., 2015; White & Blum, 1995). Here, in order to compare soil production and development between *dry* and *wet* sites, relative rates of these processes are qualitatively inferred by an analysis of measured soil moisture and temperature within the soil and in the SBI. Soil production, which is defined as the *de novo* production soil from the underlying bedrock, is inferred from soil moisture and temperatures at the SBI. Soil development, which is defined as the breakdown of soil and small gravel into smaller parties, is inferred by analysis of soil moisture and temperature within the whole soil profile.

Figure 5-13b shows the slope of the response curves of soil temperature to air temperature (Figure 5-10) at each depth. Similar to other studies, the results show that the magnitude of response decreased with soil depth (Anderson et al., 2013; Hillel, 1982)(Figure 5-13b) which is consistent across all sites. An exponential function explains 74% of the variations across all sites and soil depths. The exponential nature of the function points to the fact that the rates of soil production (caused by mechanical weathering and breakdown of the parent material) decrease exponentially with soil depth. This resembles the empirical soil production function proposed by Heimsath et al., (1997).

Figure 5-13b points to possible differences in soil production rates across the aridity gradient. At the *dry* sites, soils are thin and are less buffered from the outside air temperatures and temperatures at the soil bedrock interface are relatively warm, possibly due to higher shortwave radiation reaching the forest floor (Table 5-2). These conditions at the SBI can point to faster soil production, which is plausible considering the frequent fires and high post-fire erosion rates from these open woodlands (Nyman et al., 2011; Noske et al., 2016; Sheridan et al., 2016). At the *wet* sites, soils are thick and are more buffered to outside air temperatures, and temperatures at the SBI are lower than their dry counterparts, which can point to slower soil production. The higher VWC at SBI at the *wet* sites (Table 5-2) (Figure 5-13b) suggest that soil production across these sites depend on chemical weathering of the bedrock rather than its mechanical breakdown.

During winter, sub-surface soil temperature at the *wet* sites remained high relative to the low air temperatures (Figure 5-9e and f), which indicates that energy was retained within the soil profile which can potentially affect rates of chemical alteration and soil development (i.e., chemical weathering of soil particles) throughout the year. It is suggested that the high soil moisture (Figure 5-7i and Figure 5-8a) and the higher productivity at these sites, are likely to keep rates of soil weathering high due to (i) high soil organic matter content; (ii) higher transpiration rates and fast leaching, which drive chemical alteration processes (Gabet et al., 2006; Lybrand & Rasmussen, 2014; Rasmussen et al., 2015). On the other hand, soil moisture at the *dry* sites only increases in winter (Figure 5-7c, f and Figure 5-8a). It is suggested that, rates of chemical weathering and soil development are slower at these sites despite the warmer soils (Figure 5-9a, b and c).

Overall, results indicate that the partitioning and storage of water and energy by the vegetation and soil is important in the coevolution of the critical zone. Although not directly quantified here, measured microclimatic conditions can point to processes that contribute to the coevolution of the critical zone at a point. Results points to a possible feedback between weathering, productivity and fire (which can potentially leads to erosion) that is controlled by the partitioning and storage of rainfall and energy. It is suggested that this feedback operates at different rates and accelerates the divergence in system states across the aridity gradient.

On *wet* sites, the high moisture content (Figure5-7f and i) and heat retention during winter (Figure 5-9e and f) can favour high chemical weathering rates (Dessert et al., 2003; Dupré et al., 2003) which could in turn lead to higher water holing capacity (per volume of soil). The

higher water holding capacity enables soils to support high levels of productivity and denser vegetation (Figure 1-2a), which could provide more cover, reduces flammability (Nyman et al., 2015a, 2018) and maintain higher infiltration capacity (Sheridan et al., 2016). These conditions favour low fire frequency (Cheal, 2010) and almost no post-fire erosion (Lane et al., 2006; Sheridan et al., 2007), and can explain the deep and weathered soils on these wet sites (Table 4-1; Figure 1-2b).

On *dry* sites, soils are thin and relatively dry (Table 4-1; Table 4-2). These conditions favour low weathering rates (Amundson et al., 2015; Dessert et al., 2003; Dupré et al., 2003) which may keep water holding capacity low . Lower water holding capacity limits productivity (Figure 1-2c), supports an open canopy which makes the system more flammable (Figure 5-12)(Nyman et al., 2015a, 2018), and keeps post-fire infiltration capacity low (Sheridan et al., 2016). These conditions favour high fire frequency (Cheal, 2010) and increased post-fire erosion (Noske et al., 2016; Nyman et al., 2011), and can explain the shallower undeveloped soils on these dry sites (Figure 1-2d). It is suggested that this feedback might be responsible for the extreme differences in vegetation, soils and fire regime across the domain. A more complete picture of the microclimatic conditions that affect soil production and development is needed in order to better understand the role of this feedback in coevolution. One way would be to quantify the rates of soil production and development and compare the developmental state of the soils across the climatic domain. Data from this analysis can be then used to parameterise a numerical model, similar to the one presented in Chapters 3 and 4.

5.6 Conclusions

The aim of this chapter was to evaluate and quantify, using intensive field measurements, the way in which vegetation and soil depth affect the partitioning of rainfall and solar radiation, and to estimate what are the implications of this partitioning on processes in coevolution of the critical zone. The partitioning of rainfall and energy by vegetation and soils was quantified at sites across a climatic gradient, in order to evaluate its implications on coevolution processes. The effect of the partitioning of rainfall and energy on coevolution was estimated by analysing soil moisture and temperature data, known affect key processes in the coevolution of the critical zone: evapotranspiration and productivity; flammability; and weathering. Results show that:

a) throughfall decrease and net shortwave radiation under the canopy increase with aridity due to the lower rainfall and higher canopy openness (respectively). On wet sites, the closed canopy and the deep soil partitions water and energy in a way that results in wetter soils throughout the year, leading to lower flammability and higher productivity. On drier sites, the open canopy and shallow soil partitions water and energy in a way that results in drier soils, mainly in summer and autumn, leading to higher flammability and lower productivity.

b) mean annual soil water stores were found to decrease non-linearly with aridity, being more than 5-fold higher on wet sites compared to dry ones. These results can explain the existence of low productive, dry and open woodlands in close proximity to wet and closed forests, which are claimed to be one of the most productive forests on earth.

c) analysis of soil moisture and temperature suggest that soil temperature is likely to control soil production at the drier sites, while variations in soil moisture are likely to control weathering of the soil profile on the wetter sites. The higher weathering rates on the wet sites are suggested to increase the divergence between system states by keeping water holding capacity high, which feeds back to higher productivity, lower flammability and higher infiltration capacity. The lower weathering rates on the dry sites are suggested to increase the divergence in system states by keeping water holding capacity low, which feeds back to lower productivity, higher flammability and lower infiltration capacity.

Results point to a coevolutionary feedback between weathering, productivity, erosion and fire, which is controlled by the partitioning of water and energy through vegetation and soils. It is suggested that this feedback accelerates the rate of divergence in system states across the domain.

6 Fire and the coevolution of the critical zone – a synthesis

6.1 Summary of findings

The aim of this study is to explore the role of fire in coevolution of soil and vegetation within the critical zone. The high-level question was: what is the role of fire in the coevolution process, and in case it does play a role, what are the mechanisms involved? I argued that SE Australian uplands are an excellent location to answer these questions due to its tectonic stability and the systematic variations of forest types, fire frequency and post fire response across an aridity gradient. The observed conditions, in which higher runoff and erosion rates are originated from drier forests, lead to the hypothesis that in SE Australian uplands, fire has a critical role in the coevolution of the critical zone, and that its contribution increases systematically with aridity. Three different methods were used in order to address the hypothesis, which are described in the chapters. In this section I discuss each of the methods by itself, and how the results contributed to testing the hypothesis and in answering the high-level research questions:

- **Chapter 2** focused on long term fingerprints of coevolution: soil depth and hillslope gradient. Considering the observed climate-related differences in forest type, fire frequency and erosion rates, I hypothesised that soil depth and hillslope gradient are north-south asymmetric and that the magnitude of this asymmetry varies systematically with climate. The first hypothesis was supported by soil depth measurements and topographic analysis, as both pointed to higher erosion efficiency across north facing slopes compared to south facing ones. These differences in erosion rates caused soil depth to be thinner and hillslopes flatter on north facing slopes compared to south facing ones. These results suggested that these erosion processes were driven by the effect of solar radiation on vegetation and soils (Istanbulluoglu et al., 2008; McGuire et al., 2014; Perron, 2017; Rasmussen et al., 2017; Yetemen et al., 2015b). Results showed systematic patterns of soil depth and hillslope asymmetry across an aridity gradient. The biggest difference in asymmetry in soil depth and hillslope gradient occurred close to the climate boundary between water limited to energy limited systems (aridity 1), suggesting that this climatic-microclimatic affect was probably mediated by the effect of climate on vegetation, and that the coevolution process governing the development of soil depth has been taking place in timescales longer than recent fluctuations in climate. From evidence provided in Chapter 2 alone, the effect of fire on soil depth and landform cannot not be explicitly decoupled from that of climate. However, higher

fire frequency and erosion rates measured on drier sites and north facing hillslopes (Noske et al., 2016; Nyman et al., 2011, 2015b) suggest that fire might have a role in controlling landform on the drier side of the aridity spectrum. It is possible that even in periods with low fire frequency due to low ENSO activity during glacial maxima (Petherick et al., 2013), north (equatorial) facing hillslopes and hillslopes in lower elevations might have hosted slightly thicker vegetation due to slightly warmer conditions (McGuire et al., 2014; Rasmussen et al., 2017). These conditions could possibly facilitate enough vegetation as potential fuel for wildfires, which could lead to faster erosion rates compared to hillslopes on colder south facing or higher elevation. This would make the hillslopes that are currently under higher aridity more subjected to fire and erosion throughout history, even if fire frequency would have fluctuated (Mooney, 2012) due to fuel or energy limitation (Bradstock, 2010). Overall, results from this chapter indicate that fingerprints of different trajectories of coevolution in SE Australian uplands can be found in small and intermediate scales, and that it is affected by climate and possibly fire.

- **Chapters 3&4** involved the development of a new numerical model (Chapter 3), designed in order: (i) to test the hypothesis that fire related processes and feedbacks are critical to explain observed patterns and magnitude of difference in system states across the landscape, and that their effect of on coevolution increases with aridity; then, given the hypothesis is supported, (ii) to evaluate the role of fire related mechanisms in coevolution. (Chapter 4). The model was developed and parameterised in order to simulate the coupled ecohydrological and hydro-geomorphological processes typical to SE Australian systems. The model simulates a point on the landscape that contains vegetation and soil that coevolve with time under the influence of rainfall and solar radiation, and stochastic fire driven by soil moisture deficit. The model showed satisfactory results when outputs of hydrological partitioning, fire regime, post-fire vegetation recovery, and post-fire hydro-geomorphic response, were compared to literature values and measured data from SE Australian uplands (Chapter 3).
The model was used to run different sets of numerical experiments in order to test the hypothesis and to evaluate the role of fire related mechanisms in coevolution. A decreasing logistic pattern between soil depth and aridity emerged both from simulations *with* and *without* fire. However, simulations with fire, reproduced values and magnitude of difference between the deepest to the shallowest soil when compared to the measured data, supporting the hypothesis that fire related processes and feedbacks are critical to explain patterns and magnitude in soil depth across the landscape. Furthermore, results showed that the net effect

of fire on soil depth increased non-linearly with aridity, a pattern that was found to be mainly driven by fire frequency and the effect of fire on infiltration capacity. Analysis of simulations designed to isolate key processes and feedback indicated that combination of fire frequency and the effect of fire on infiltration capacity are critical in the coevolution of the critical zone in SE Australia. The dependency of fire frequency on soil depth and climate highlights an important feedback loop in which increased erosion due to higher fire frequency might reinforce it, contributing to higher fire frequency and more erosion. This fire related eco-hydro-geomorphic feedback will eventually stop when climate, vegetation, soil moisture and fire regime reaches a new steady state.

Chapter 5 focused on short term processes and feedbacks related to coevolution under contemporary conditions, which are driven by soil moisture and temperature. It was claimed that small scales the partitioning of energy and water by vegetation and soil can influence important processes in the coevolution of the critical zone. The aim of chapter 5 was to evaluate and quantify the way in which vegetation and soil depth affect the partitioning of rainfall and solar radiation, and to estimate the implications of this on processes in coevolution of the critical zone. The aim was addressed by measuring sub-canopy microclimate (and open reference sites) across a climatic gradient for one year. The effect of the partitioning of water and energy on coevolution was inferred by analysing soil moisture and temperatures data, which affect key processes in the coevolution of the critical zone: (i) evapotranspiration and productivity; (ii) flammability; and (iii) weathering. Results show that on *wet* sites, the closed canopy and the deep soil partitions water and energy in a way that resulted in wetter soils throughout the year, pointing to lower flammability and higher productivity. On *drier* sites, the open canopy and shallow soil partitions water and energy in a way that resulted in drier soils, mainly in summer and autumn, pointing to higher flammability and lower productivity. Mean annual soil water stores were found to decrease non-linearly with aridity, being more than 5-fold higher on wet sites compared to dry ones. At at the SBI, temperature fluctuations are higher (lower) and moisture is lower (higher) at the dry (wet) sites, pointing to potentially higher rates of mechanical (chemical) soil production (weathering). The higher inferred weathering rates on the *wet* sites are suggested to potentially increase the divergence between system states by keeping water holding capacity high, which feeds back to higher productivity, lower flammability and higher infiltration capacity. Conversely, the lower inferred weathering rates on the *dry* sites are suggested to potentially increase the divergence in system states by keeping water holding

capacity low, which feeds back to lower productivity, higher flammability and lower infiltration capacity. This points to a possible coevolutionary feedback between weathering, productivity, erosion and fire, which is controlled by the partitioning of water and energy through vegetation and soils. It is suggested that this feedback accelerates the rate of divergence in system states across the domain.

6.2 Synthesis and discussion points

Overall, results from chapters 2, 3 and 4 support the high-level hypothesis that fire has a critical role in the coevolution in SE Australia, and that its relative role increases with aridity. Analysis of model simulations (chapter 4) highlight specific mechanisms in which fire affect coevolution trajectories, and the data from microclimate sites (chapter 5) gives evidence on how these mechanisms are regulated by contemporary system states across an aridity gradient. Factors affecting soil moisture at a point were found to be important in driving processes and feedbacks in the critical zone both by controlling fire frequency, productivity and soil development. Furthermore, the effect of individual fires on infiltration capacity was found to drive changes in systems states, especially on drier climates, highlighting the importance of soil development to coevolution. As for landform, while results from the modelling exercises indicate that fire is essential to create the observed patterns in soil depth, its physical effect on landform within the coevolution process is unclear. Use of 2D landscape evolution models is suggested in order to answer the question whether fire is essential to landscape evolution.

This study is the first to address the coevolution of coupled soil-vegetation systems in SE Australia and the first to suggest that the role of fire and its effects are critical in driving systems into different trajectories of coevolution. The feedbacks between system states (i.e., vegetation and soil) and processes related to fire within the coevolution point to the fact that fire is an integral part of it. The unique evidence given here of the way contemporary system states partition and store water and energy and how they are being utilized, gave a snapshot of these effects, and gave evidence to the legitimacy of the modelling framework in predicting the role of fire in coevolution in SE Australia. The space-time link between vegetation, soil moisture, climate fluctuations and fire under a modelling framework has been identified as an important avenue of research, as expressed by *Rodriguez-Iturbe* (2000). This contribution pushes the knowledge one step forward toward understanding the interactions

between these key players, and their relationship implications on long-term coevolution. In the next sections I will discuss some of the key findings that were highlighted throughout this dissertation, and will point to interesting new avenues of research to follow.

6.2.1 Fire as a dynamic process in coevolution

The modelling framework (Chapters 3&4) and contemporary evidence (Chapter 5) highlight the fact that fire is a dynamic part of feedbacks in coevolution and not a decoupled stochastic disturbance as it was perceived in the literature. I suggest that once fire becomes more frequent, it turns from being a decoupled disturbance to being part of the system, and a substantial part in its coevolution. In Australia, fire had been part of the system for millions of years (Bowman, 2000), affecting the evolution of plant species (Bowman & Yeates, 2006), and changing the distribution of vegetation (eg., Bowman, 2000; Bowman et al., 2014; Fletcher et al., 2014a). However, in locations where fire hasn't been part of the system changes in its frequency might have significant effects on trajectories of change (Bowman, 2017). For example, based on evidence from *Taufik et al.* (2017), *Bowman* (2017) claimed that fire that is driven by hydrological stress is part of a cycle with a potential to change fire regime and possibly vegetation structure in tropical rainforests. An interesting avenue for future research would be to identify critical thresholds in fire regime (i.e., when will fire start to affect the system state by pushing it in different trajectories that will inforce changes on fire regime) in which it changes from being decoupled, to being incorporated into feedbacks that affect the coevolution of the critical zone. This might be increasingly important area of research given the expected changes in fire regimes due to the changing climate (Moritz et al., 2012).

6.2.2 Applying the model in other systems

This study highlighted important processes and feedbacks that connect fire with the SE Australian coupled soil-vegetation systems. The model results underscore the importance of differentiating between fire regime and the unique effect of individual fires. For example, under dry climate, long-term effect of individual fires on steady-state system states were significantly higher than under wet climates, even when having a similar fire regime (Figure 4-7). These differences in the consequence of individual fires are a result of the relationship

between aridity and post fire effects on infiltration capacity, a phenomenon that might be unique to SE Australia (Sheridan et al., 2016). For example, *Inbar et al.* (2014) found that infiltration capacity increased after heating surface soils sampled from a Mediterranean forest in Israel, to temperatures typical to severe wildfires. The model that is presented in this thesis is constrained to steep forested uplands. It is suggested that the model would not be adequate to areas where fire is more affected by seasonal dryness of biomass regardless of soil moisture levels such as grasslands; and neither on woodlands and savannas across low-relief landscapes where the hydro-geomorphic consequence of fire is negligible. The implications of the model and the findings presented in this thesis are highly important to coevolution studies. However, it is suggested that one should look at location-specific processes and parameters before using the model in other systems.

6.2.3 Fire related eco-hydro-geomorphic feedbacks in the coevolution of the critical zone

In this section I will highlight an important feedback loop between erosion and fire frequency that was identified using the modelling framework (Chapters 3&4), and the evidence obtained from measurements across contemporary systems (Chapter 5). Then, I will discuss an extension of that feedback relating weathering and soil development, which might impact the coevolution process as proposed in chapter 5. The common factor relating these feedbacks is soil moisture, which, I claim is the centre of most of the processes in coevolution of the coupled soil, vegetation and fire regime within the critical zone.

Erosion-Fire frequency feedback

The ecohydrologic importance of soil moisture is essential to understand hydrologic response, mainly due to its control on vegetation (Eagleson, 1982; Eagleson & Tellers, 1982; Rodriguez-Iturbe et al., 1999). Using cellular automata (Caracciolo et al., 2014; Zhou et al., 2013) or other modelling approaches (eg., Brolsma & Bierkens, 2007; Istanbulluoglu et al., 2012; Yetemen et al., 2015b) spatial and temporal distribution of soil moisture was found to control patterns of vegetation seen in nature, an outcome that is to be expected. However, up to this point, only handful of studies looked at the effect of short-term ecohydrological processes on long-term geomorphology and landscape evolution (eg., Baartman et al., 2018;

Istanbulluoglu & Bras, 2006; Saco & Moreno-De Las Heras, 2013; Yetemen et al., 2015b). For example, *Yetemen et al*. (2015b) illustrated the importance of climatic and topographic conditions in affecting soil moisture and how it translated to vegetation (grass) and erosion patterns, which ended up with different landform in the geological timescales. *Saco and Moreno-De Las Heras*(2013) used an inter-linked dynamic vegetation and an ecohydrogeomorphic models in order to explain the devlopment of banded vegetation patterns, typical to gentle slopes across some semi arid landscapes. Similarly, in the conceptual model presented here, soil moisture acts as a link between climate, vegetation and fire (Eqns 3.32-3.34 and 3.42-3.43), a role that is key to coevolution process at a point (Eagleson, 1982; Rodriguez-Iturbe et al., 1999). This contribution is the first to relate soil moisture to the development of landscape-scale geomorphic patterns across the temperate forests of SE Australia, and the first to link fire into this framework.

The model presented in this work shows the co-evolutionary potential of how short-term microclimatic conditions created by the vegetation, affect fire frequency, with longer-term eco-hydro-geomorphological implications across a fire-prone landscape such as the forested uplands of SE Australia (Chapter 4). The model predicts an important feedback relating local ecohydrology, fire and soil depth (Figure 4-7 and Figure 4-8), and highlights the importance of incorporating such processes in a coevolution model, especially ones which deal with the effects of fire on short and long-term processes in coevolution. Field observations that were presented in Chapter 5 give some evidence on these short-term coevolution processes. One good example is the relationship between aridity and mean annual soil moisture, (*Vs*, Figure 5-8b), which is defined as the total amount of water that is stored in the soil (including water that is inaccessible to plants) and suggested to support contemporary vegetation at each site (see Ecological Vegetation Class for each site on Table 5-1). Vegetation, in turn, partitions solar radiation (Figure 5-4, Figure 5-5 and Figure 5-6a) and rainfall (Figure 5-3) and control the microclimatic conditions and the moisture state of the system under the canopy (Figure 5-8b)(Nyman et al., 2015a). Figure 5-11 and Figure 5-12 show that these conditions, as expressed in soil moisture distributions, express the relative order in which fire frequency is distributed across the aridity gradient (Cheal, 2010; Kennedy & Jamieson, 2007) (Table A-II-1 in Appendix II). The analysis showed an unexpected feedback in which fire-induced erosion, that in the long-term changes soil depth, not only changes vegetation density, but also fire frequency itself (Figure 4-8a). In this feedback, long-term increase in erosion rates (which overcomes rates of soil production) will cause an increase in fire frequency, due to the

overall lower water holding capacity of the soil. These findings may have significant long-term implications in areas that experience an increasing number of fires, especially with the changing climate.

This work proposes that fire regime has a role beyond that of what it has been perceived before, which is its long-term effect on soil depth and its water holding capacity, and how it feeds back to vegetation, soil moisture and the fire regime itself. This work proposes a new fire related eco-hydro-geomorphic feedback loop in the coevolution process (Figure 6-1):

- In steady state conditions (when climate is steady, designated here as steady rainfall - *P*), fire frequency (*Ff*), biomass (*B*), soil depth (*h*), soil moisture (*s*), are in equilibrium:

$$\frac{dP}{dt} = 0\ ; \quad \frac{dFf}{dt} = 0; \quad \frac{dB}{dt} = 0; \quad \frac{dh}{dt} = 0; \quad hn\frac{ds}{dt} = 0; \tag{6.1}$$

- In the short term (up to a few years), fire slightly affects soil depth (*h* in the figure) by temporarily changing soil hydrological properties (mainly infiltration capacity). The effect of fire on the soil hydraulic properties varies with climate (Sheridan et al., 2016; Van der Sant, 2016), and was found to be critical to the observed differences in system states across the landscape, as described in Chapter 4.

- When climate changes it affects soil moisture and with it biomass and fire frequency (Taufik et al., 2017).

- In short term, change in fire frequency increases erosion, which, when aggregated over longer timescales, makes changes to soil depth and its water holding capacity.

- Assuming optimality (Eagleson, 1982), vegetation arranges itself in intermediate timescales according to climate and plant available water (which also depend on soil depth).

- The pseudo steady-state vegetation community is controlled by but also affect soil moisture (depending on LAI; Chapter 5), feeding back to frequency and soil depth.

- Cycle stops when steady state between all components is reached (Eqn. 6.1).

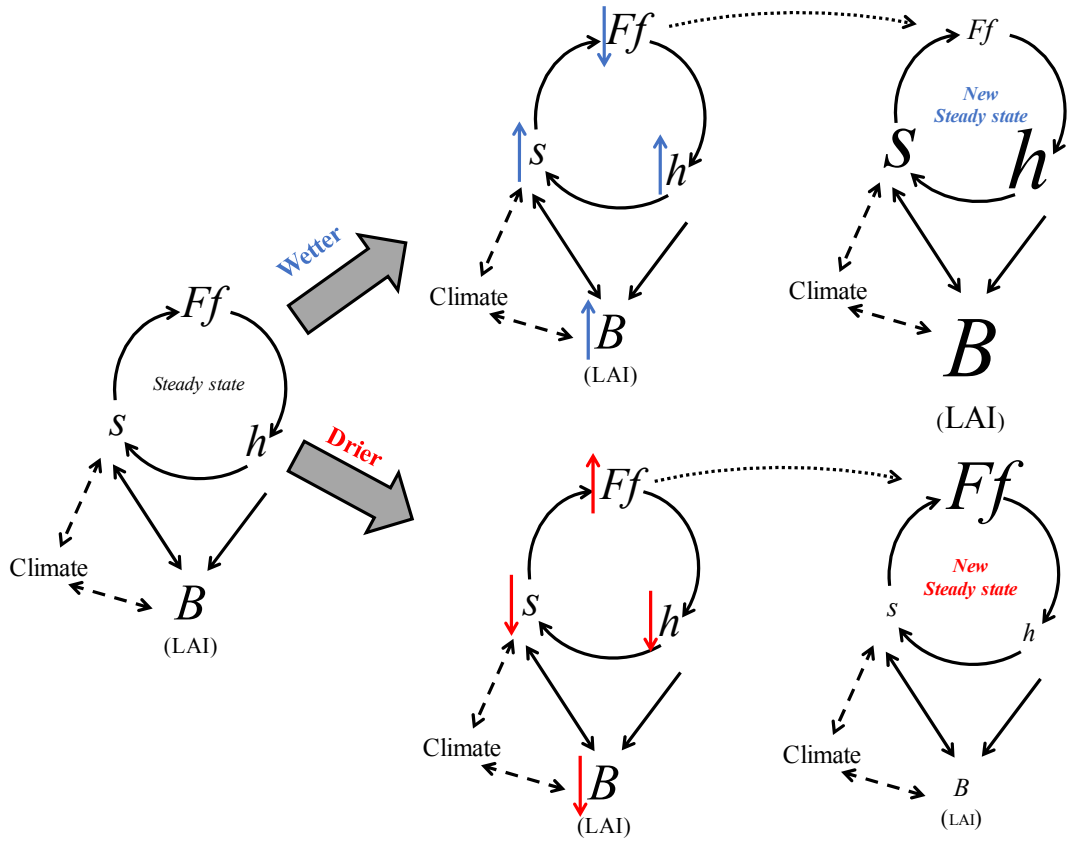

Figure 6-1 – Fire related eco-hydro-geomorphic feedback. When changes in climate are imposed (either wetter or drier conditions), steady state conditions (Eqn.6.1) are breached, and the system will coevolve until a new steady state will be reached. In the figure, *Ff* is fire frequency; *s* is soil moisture; *h* is soil depth; and *B* is biomass. For simplicity, all variables in this figure are unitless, and that smaller (larger) font refers to a decrease (increase) in mass, depth or frequency.

This study is the first to report such a feedback in the coevolution of the coupled soil-vegetation systems. This findings coincides with a recent study relating lowering groundwater levels to an increase fire frequency in Borneo's wet rainforests (Bowman, 2017; Taufik et al., 2017), and can have implications on understanding trajectories of coevolution with changes in climate.

Adding another dimension: Fire-Soil development feedback

Data presented on chapter 5 give rise to another dimension to the feedback presented above. In the model (as described on chapter 3), in order to keep the model as simple as possible,

soil depth was chosen to be the only dynamic soil property that controls plant available water (PAW) capacity. However, in nature, weathering of bedrock and soil particles make changes in soil properties that control water holding capacity (WHC) and PAW, hydraulic conductivity and infiltration capacity (Clapp & Hornberger, 1978; Saxton & Rawls, 2006). Chapter 5 gives evidence on possible drivers for soil production and development across the aridity gradient. Analysis of soil moisture and temperature data measured in depths showed that while fluctuations in soil temperature decrease exponentially with depth (Figure 5-13b) soil moisture across all sites was significantly different (Figure 5-8). This suggests that in contemporary climatic conditions, soil moisture holds a dominant control on weathering rates across the sites. These findings suggest that moisture-related weathering of the soil profile is occurring at faster rates on the wetter sites than on dry ones. *Could this have implications on the fire related eco-hydro-geomorphic feedback that was identified?*

In this section I will elaborate how weathering processes can influence fire frequency. Here I claim that effect of changes in water holding capacity (WHC) of the soil on coevolution is nonlinear, and can increase the difference between system states even further. The model shows that under drier conditions, fire frequency increases and soils becomes increasingly thinner (eg., Figure 4-6a) and as a result soil is produced at a faster rate due to the exponential relationship between soil depth and soil production (Eqn. 3.46; (Heimsath et al., 1997)). The combination of drier conditions (Figure 5-8) and the fast removal and production of soil, keeps the soil profile gravelly and unweathered (as seen in Figure 1-2c), and WHC (per unit volume of soil) relatively low. These conditions are expected to have several effects on feedbacks between soil moisture and fire: (i) lower WHC and dry conditions will cause an increases in fire frequency; (ii) lower plant available water reduces forest cover which will eventually causes a reduction in background and post-fire infiltration capacity (due to fewer macropores, thin litter layer, slower decomposition rates and lower organic matter content); and (iii) the relatively large gavel content across the soil profile could increase the quantity and size of non-cohesive material that is covering the hillslopes after severe fires (Figure 3-4; (Nyman et al., 2013)), and the potential for post fire hillslope debris flow, a process that have been identified after fires across SE Australia (eg., Langhans et al., 2017), and results in extremely high hillslope erosion rates. In this way, both fire frequency and post fire erosion per event will increase. This feedback is expected to create faster transitions between steady state conditions than that is predicted by the model.

On the other side of the aridity spectrum, the model shows that if climate becomes wetter, fire frequency decreases and soils becomes increasingly thicker (eg., Figure 4-2) which in turn slows soil production (Eqn. 3.46; (Heimsath et al., 1997)). The combination of higher soil moisture (Figure 5-8) with the slow removal and production of soil, keeps the soil profile weathered (as seen in Figure 1-2b), and WHC (per unit volume of soil) high. As with the drier conditions, at wet sites, several effects on soil moisture-fire feedbacks are expected: (i) higher WHC and wetter conditions will reduce in fire frequency; (ii) higher plant available water will increase forest cover, which will eventually keep background and post-fire infiltration capacity high (due to more and larger macropores, more litter, faster decomposition rates and higher organic matter content); and (iii) the lack of gravel will decrease the quantity and size of non-cohesive material covering the hillslopes after fires (Figure 3-4; (Nyman et al., 2013)), reducing the potential for fluvial hillslope erosion events to transition into higher magnitude hillslope debris flows (eg., Langhans et al., 2017). In this way, fire frequency and post fire erosion per event will decrease even further. However, it is possible that this feedback will be limited as soil becomes more clayey due to the reduction in plant available water in higher clay contents.

It is suggested that this fire-soil development feedback has the potential to magnify the differences between system states across an aridity gradient even further, especially on wetter sites, where soil residence time is estimated to be over 100kyr (Figure 4-4a). Future endeavours in this direction are encouraged to include an additional soil development module, to represent the development of soil hydraulic properties and particle size distribution (Cohen et al., 2009; Temme & Vanwalleghem, 2016).

6.2.4 Rates of soil production and erosion throughout the Quaternary – how valid are the model's predictions?

Soil production and development depend on the combination of several factors including: climate, organisms, parent material, topography and time (Jenny, 1941). The soil depth patterns that were reproduced by the model emerged by holding soil hydraulic properties (Table 3-1) and the maximum soil production rate ($\in_o$, Eqn 3.46) constant across the climatic domain, soil depth controlled mainly by erosion (or the lack thereof). Measurements show that soil temperature fluctuations for a given soil depth do not vary much between the sites (Figure 5-13b), and that the temperature at the bedrock interface wasn't extremely different

(in a way that would have significant differences in weathering), indicating that differences in soil production and development across the aridity gradient are mostly controlled by soil moisture (Figure 5-8). However, these conditions might have been different during the colder and drier glacial periods, when variations in elevation and aspect might have had bigger influences on the type and rate of geomorphic processes across the region. For example, while examining soils across a range of cinder cones in Arizona, USA, *Rasmussen et al.* (2017) found that soils on the south (polar) facing hillslopes contains more eaolian-delivered dust particles despite having higher erosion rates. This finding was then attributed to different microclimatic conditions across north and south facing hillslopes during the Quaternary, which favoured the existence of dust-trapping vegetation on south facing hillslopes. It was suggested that these dust particles increase water retention, bioturbation and freeze-thaw creep processes in a positive feedback, resulting in shallower slopes on these hillslopes (McGuire et al., 2014; Rasmussen et al., 2017).

Modelling results showed that the it takes ~37kyr and ~120kyr for soils to reach steady state in dry and wet sites, respectively (Figure 4-4b), without taking into account changes in rainfall, temperatures and fire regime. Although these results are within the range of measured soil residence time in SE Australia reported by *Dosseto et al.* (2010) (27±8 to 420±78 kyr), how *does it coincide with soil erosion and production during times when climate was colder?* In this section I will discuss the possible effects of fluctuations in climate on the contemporary soil depths and how it coincide with the model's predictions.

Soils on the south (polar) facing slopes in intermediate and high elevations

The steep terrain at high elevations and the lack of deep-rooting trees during LGM (McKenzie, 1997) might suggest that mass failure and other high magnitude erosion events were likely to have occurred during transitions between warmer and wetter to colder and direr conditions, as shown by some studies (Heimsath et al., 2001). This contradicts the model's predictions of ~120kyr on average in building the soil profile (Figure 4-4b), if initial soil depths were below 0.8 m (Figure 4-4a). Assuming the model's predictions are correct, soil depth must have been deep (above 1m) to be able to build the soil profile since last deglaciation (Figure 4-4a).

One possible explanation for this contradiction is that mass losses were not common and that soils on high elevations remain constantly deep. In order for that to happen, soil must have remained very porous during the glacial times, but on the other hand very cohesive, which is

possible, considering the fact that these soils are very rich in clay from the top of their thick B horizon towards the SBI. This possibility is unlikely to have occurred, as it contradicts studies reporting high sediment erosion during late Pleistocene (Kemp & Rhodes, 2010). Another possible explanation is that erosion/soil stripping was indeed higher in these sites, but soils only lost a small portion of its profile (say the O and A horizon), which was quickly built back (from top or bottom) during the recolonization with vegetation during the Holocene, a process that is supported by measurements in locations across the Snowy mountains (NSW) (Stromsoe et al., 2016). This might indicate the B and C horizons in these soils are hundreds of thousands of years old, and that the O and A horizons are Holocene by age.

Soils on the north (equatorial) facing slopes in low and intermediate elevations

The model predicted ~37kyr on average for sites at the driest end of the aridity spectrum to reach steady state, which is shorter than the time between glacial maxima (Augustin et al., 2004; Petit et al., 1999). It was suggested earlier that the north facing hillslopes and hillslope of low elevations might have had slightly warmer conditions, more vegetation and higher chances of fire during LGM, due to their solar exposure. Furthermore, more vegetation also suggests higher bioturbation and freeze-thaw processes, that may have prevailed during these colder and drier period (McGuire et al., 2014; Rasmussen et al., 2017), further increasing soil production and erosion across these slopes. These conditions might have kept erosion relatively high and soils relatively shallow and young also during LGM, and might explain the persistent hillslope asymmetry across the domain (Figure 2-3) despite the fluctuations in climate (McGuire et al., 2014).

Overall, the discussion points and evidence presented above indicate that the model's soil depths predictions on the driest and wettest sites are reasonable, despite the dramatic climatic fluctuations during the Quaternary. Nevertheless, it is important remember that the model was created in order to predict trends and patterns of system states rather than actual values, similar to other coevolution models (Pelletier et al., 2013). The current data on the rates of erosion and production across the domain is limited. This study might open some interesting avenues for future research that can shed light on soil erosion and formation processes across the uplands.

6.2.5 Fire and Eagleson's optimality – a new theory proposed

The concept that vegetation is optimized with available resources (i.e., soil moisture, nutrients etc) has been formulated by *Eagleson* (1982, 2005) in order to improve hydrological predictions with using minimal number of parameters, and was used in order to solve some theoretical questions in ecohydrology (eg., Berry et al., 2005; Brolsma & Bierkens, 2007; Huang et al., 2006). The theory proposes a three-stage process occurring at different timescales (from short-term ecosystem to geological timescales) in which vegetation properties and soil properties are optimized in a way that equilibrium soil moisture (evaporation) will be maximized (minimized). The three stages were later described by (Hatton et al., 1997). In order to achieve the above conditions: (i) First, on short timescales (within one or few generations), the canopy structure will be optimized; then (ii) after a few generations vegetation species with specific properties will be selected; and (iii) in even longer timescale vegetation will alter soil properties (such as soil-pore disconnectedness or saturated intrinsic permeability). The findings described here raises an interesting theoretical question: *how fire incorporates in the optimality of systems to the available resources?*.

The relationship between soil moisture and fire is not straight forward, however, some empirical work had shown that moist soil does in fact affect the moisture content at the bottom of dead fuel (Hatton et al., 1988), and that soil moisture deficit can predict wildfire probability (eg., Finkele et al., 2006; Keetch & Byram, 1968; Krueger et al., 2016), an approach that was used in order to predict fire risk in drought indexes such as Keetch–Byram Drought Index (KBDI; (Keetch & Byram, 1968))(eg., Nyman et al., 2015a; Walsh et al., 2017).

Conditions in which canopy and soil moisture are not in equilibrium are theoretically possible. For example, in south facing hillslopes at Christmas Hills (CH), soil moisture was below wilting point most of the year, while it's north facing counterpart was above it (Figure 5-7 and Figure 5-8a). It was suggested that vegetation and canopy (PAI) in both hillslopes are not in equilibrium with soil depth and current climatic conditions, which causes higher demand for transpiration than what the system can supply according to its water holding capacity. According to *Eagleson's* theory, assuming these conditions are constant, either canopy structure or soil properties need to change in order to reach equilibrium between the soil, vegetation and climate. Interestingly, Figure 4-8 shows a hypothetical situation in which sites with higher LAI than the "optimal" have increased flammability and lower fire return

interval. Could it be that fire, as a ecohydrological-dependent geomorphic agent, acts as an "accelerator" between the temporal stages in *Eagleson's* hypothesis of optimality?

Here I propose a theory in which fire (or the lack thereof) acts as a possible option towards optimality of the coupled soil-vegetation system. For example, fire can bring the system to a new equilibrium by its effect soil depth in case vegetation is consistently out of equilibrium with climate (for example, if rainfall is lower than mean averages for a considerable amount of time). The theory suggests that in optimized conditions, the canopy acts in order to minimize fire risk, at least to levels that are equilibrium with the climate, soil water holding capacity and recovery strategy (Figure 3-3). This could also be a mechanism in which fire eliminates excess burden on the available resources, which could serve as an advantage to the local regenerating woody species. Here, fire's geomorphic implications (Moody & Martin, 2001a; Nyman et al., 2011; Prosser & Williams, 1998; Shakesby & Doerr, 2006) comes to the "advantage" of the vegetation community.

Eagleson's hypothesised that in a matter of few generations, vegetation community could change into a new one with species that has potential transpiration efficiency more optimized to the soil-climate conditions (Hatton et al., 1997). Here, another question comes to mind: *could fire act to speed up evolutionary changes within each specie with changing climatic drivers*? And, *when will fire push towards change in vegetation community rather than speeding up the evolution of a species*?

Could fire accelerate long-term optimality between vegetation and available resources?

In wet (i.e., with low aridity) areas in SE Australia, vegetation are often occupied by "*fire sensitive*" species (eg., *Eucalyptus regnans and Eucalyptus delegatensis*) which die when exposed to wildfire (Fairman et al., 2016). Given the model's predictions are true (i.e., Figure 4-8), "*fire sensitive*" specie at a point gains two potential avenues for better optimization to climate-soil conditions: Either by post-fire reduction in soil depth (by erosion processes) and by that adjusting the plant available water to the existing specie; and/or the sprouting of better "evolved" species that use the available resources better and by that adjusting the specie to the existing plant available water.

Changes in vegetation

It is very common that "fire sensitive" forests show a single aged stands, due to the nature of their recovery from fire (being obligate seeders). *Fairman et al.* (2016) discussed changes in

structure from forest to non-forest in these type of forests due to repeated fire, given that fire occurs before the trees reaches reproductive age (~20 years). Evidence of the effect of repeated fires on the transition between forest to non-forest and between forest species can be observed today and had been shown to occur during the recent deglaciation period (Fletcher et al., 2014a). According to the Eagleson's optimality theory (Eagleson, 1982), in case a changes in vegetation, the system could step into a dis-equilibrium state between the newly established vegetation and climate-soil conditions, which could lead to increase in erosion processes or the re-establishment of the "old" vegetation (Fairman et al., 2016) before it even could take place. It is possible that in situations when repeated fires and replacement of vegetation can trigger shallow landslides due to decomposition of dead roots, as modelled elsewhere (Istanbulluoglu & Bras, 2005), however, these processes are very rare in the SE Australian uplands compared to debris flows, for example (Nyman et al., 2011; Rutherfurd et al., 1994).

Results from the modelling experiments show that changes in fire frequency results in changes in biomass, but without any effect on soil depth (Figure 4-7). This response occurs due to the fact that Infiltration capacity (*Ic*) values remain very high on wet sites (Appendix IV) regardless the of number of fires that the site experienced and the amount of biomass it carries (Figure 4-7). A lesson needs to be learnt from this experience and to incorporate a soil development module, in which soil hydraulic properties are developed independent of climate, but depending on intermediate-term biomass values (assuming smaller biomass in the intermediate-term would result in less porosity and higher erosion rates).

6.3 Implications of this study

Evidence show that there was a recent global-scale increase in fire frequency and severity (Moritz et al., 2012), even in places that are unlikely to burn (eg., Taufik et al., 2017), with large proportions of this trend attributed to deforestation, climate change and other human activity (Bowman et al., 2009). This work contributes to the knowledge of how change in fire regime could cause a shift in ecosystems through its effects on soils and their biomass holding capacity. The fire related eco-hydro-geomorphological cycle presented here could potentially be implemented into hydrological models to get insights into long-term trends in hydrological response to changes in fire regimes. By extending this work and looking into the effect of fire on changing of ecosystems (Fairman et al., 2016) based on evidence from the

past (eg., Fletcher et al., 2014a; Fletcher & Moreno, 2012), researchers could understand and identify areas that are sensitive and resilient to these changes in fire regime especially in the flammable Australian systems.

7 Conclusions

Fire affects biological, ecological, hydrological and geomorphological processes. However, its effect on the coevolution of the critical zone has been largely overlooked. The aim of this study was to explore the role of fire in the coevolution of the critical zone by answering these two high level questions: (i) what is the role of fire in coevolution of the critical zone?; and (ii) if it does play a role, what are the mechanisms involved?. It has been suggested that the effect of fire on coevolution involves feedbacks between its hydro-geomorphic consequences on soil depth and vegetation, and their ecohydrological effects on flammability. In the introduction, I claimed that SE Australian uplands are an excellent natural laboratory to answer these questions, as forest type, fire frequency and its effects on hydro-geomorphological consequences vary systematically with climate. Observations in which drier forests burn more frequently and yield more post-fire runoff and erosion, were used to hypothesize that in SE Australia, fire has a critical role in the coevolution of the critical zone, and that its contribution increases systematically with aridity. I used three independent methods that focus on different timescales in order to address the hypothesis.

In chapter 2 I focused on fingerprints of long term coevolution: soil depth and landform. Building on the observed systematic differences in forest type, fire frequency and post-fire erosion in SE Australian uplands, I hypothesized that (i) soil depth and hillslope gradient are north-south asymmetric; and that (ii) the magnitude of that asymmetry varies systematically with climate. Patterns of asymmetry in soil depth and landform were quantified using soil depth measurements and topographic analysis across a contemporary rainfall gradient. Soil depth was found to decrease non-linearly with aridity, and that south (polar) facing hillslopes are persistently steeper and have greater soil depth than north (equatorial) facing slopes, pointing to higher erosion efficiency across drier north facing slopes compared to south facing ones. These results suggest that the erosion processes that shaped the landscape are driven by the effect of solar radiation on vegetation and soils. Furthermore, both soil depth and landform asymmetry were found to trend non-linearly with climate, with a maximum near the water-limited boundary, where vegetation cover varies most rapidly with aridity, suggesting a possible long-term role for vegetation in coevolution and hillslope development. Although the effect of fire on these-long term fingerprints of coevolution could not be decoupled from that of climate, local observation suggest that fire might have a role in controlling soil depth and landform on the drier end of the aridity spectrum.

On chapters 3 and 4 I used a new numerical model, which was developed in order to: (i) test the hypothesis that fire related processes and feedbacks are critical to explain observed patterns and magnitude of difference in system states across the landscape, and (ii) to evaluated the role of fire related mechanisms in coevolution. The model was developed and parameterised in order to simulate coupled ecohydrological and geomorphological processes typical to the SE Australian systems. The model simulates a point in the landscape which consists of vegetation and soil, that evolves under prescribed climatic conditions (rainfall and solar radiation) and stochastic fire regime, driven by soil moisture deficit. After evaluating the model's performance, different sets of numerical experiments were used in order to test the hypothesis and to evaluate the role of fire related mechanisms in coevolution. Simulations with fire reproduced similar pattern and magnitude of difference in soil depth across an aridity gradient when compared to field measurements. Stochastic fire was found to exaggerate the differences in soil depth, particularly at higher aridity, when compared to simulation without fire. Fire frequency and the effect of fire on infiltration capacity were identified to be the most important parameters in reproducing the observed trends. Using model simulations, a fire-related eco-hydro-geomorphic feedback was identified in which a long-term increase in post-fire erosion might contribute to more frequent fires and more erosion. This feedback puts the focus on ecohydrologic controls on soil moisture at the centre of coevolution of vegetation, soils and fire.

On chapter 5 focused at short term processes and feedback related to coevolution under contemporary conditions. It was claimed that at small scales, the partitioning of water and energy by the vegetation and soils influence important processes in the coevolution of the critical zone. The aim of this chapter was to evaluate and quantify, using intensive field measurements, the way in which vegetation and soil depth affect the partitioning of rainfall and solar radiation, and to estimate what are the implications of this on processes in coevolution of the critical zone. The partitioning of rainfall and solar radiation was quantified by measuring sub-canopy microclimate (and open reference sites) across an aridity gradient for one year, while the effect of the partitioning of these climatic forcings on coevolution was investigated by analysing soil moisture and temperature data, which are central to several processes in coevolution: productivity, flammability and weathering. Results show that throughfall decrease and net shortwave radiation under the canopy increase with aridity due to the lower rainfall and higher canopy openness (respectively). On wet sites, high throughfall rates and lower solar radiation levels penetrating the canopy allowed moisture to

be stored in the deep soils, pointing to high productivity and low flammability. On dry sites low throughfall rates and high levels of penetrating solar radiation kept the thin soils drier, which points to lower productivity and higher flammability. Mean annual soil water stores were found to decrease non-linearly with aridity, being more than 5-fold higher on wet sites compared to the dry sites, despite annual rainfall only differing by a factor of ~2. Soil weathering was found to be controlled by soil moisture, and was suggested to further increasing the differences between system states, through its control on water holding capacity. The results points to another coevolutionary feedback between weathering, productivity, erosion and fire, controlled by the partitioning of water and energy through vegetation and soils. It is suggested that this feedback accelerates the rate of divergence in system states across the domain.

Overall, results from chapters 2, 3 and 4 support the high-level hypothesis that fire has a critical role in the coevolution in SE Australia, and that its relative role increases with aridity. Analysis of model simulations (chapter 4) highlight specific mechanisms in which fire affect coevolution trajectories, and the data from microclimate sites (chapter 5) gives evidence on how these mechanisms are regulated by contemporary system states across an aridity gradient. Factors affecting soil moisture at a point were found to be important in driving processes and feedbacks in the critical zone both by controlling fire frequency, productivity and soil development. Furthermore, the effect of individual fires on infiltration capacity was found to drive changes in systems states, especially on drier climates, highlighting soil development as an important process in coevolution. As for landform, while results indicate that fire is essential to create the observed asymmetry in soil depth, its effect on hillslope asymmetry could only be estimated. Use of landscape evolution models is suggested in order to answer the question whether fire is essential to landscape evolution.

8 References

Adams, M. A. (1995). *Distribution of eucalypts in Australian landscapes: landforms, soils, fire and nutrition*. (P. M. Attiwill & M. A. Adams, Eds.). Melbourne: CSIRO.

Amundson, R., Heimsath, A., Owen, J., Yoo, K., & Dietrich, W. E. (2015). Hillslope soils and vegetation. *Geomorphology*, *234*, 122–132. https://doi.org/https://doi.org/10.1016/j.geomorph.2014.12.031

Amundson, R., Richter, D., Humphreys, G., Jobbagy, E., & Gaillardet, J. (2007). Coupling between Biota and Earth Materials in the Critical Zone. *Elements*, *3*(5), 327–332.

Anderson, R. S., Anderson, S. P., & Tucker, G. E. (2013). Rock damage and regolith transport by frost: An example of climate modulation of the geomorphology of the critical zone. *Earth Surface Processes and Landforms*, *38*(3), 299–316. https://doi.org/10.1002/esp.3330

Archer, N. A. L., Otten, W., Schmidt, S., Bengough, A. G., Shah, N., & Bonell, M. (2016). Rainfall infiltration and soil hydrological characteristics below ancient forest, planted forest and grassland in a temperate northern climate. *Ecohydrology*, *9*(4), 585–600. https://doi.org/10.1002/eco.1658

Augustin, L., Barbante, C., Barnes, P. R. F., Marc Barnola, J., Bigler, M., Castellano, E., et al. (2004). Eight glacial cycles from an Antarctic ice core. *Nature*, *429*(6992), 623–628. https://doi.org/10.1038/nature02599

Australian Bureau of Meteorology. (2017). Gridded climate data. Retrieved from http://www.bom.gov.au/climate/averages/climatology/gridded-data-info/gridded_datasets_summary.shtml

Baartman, J. E. M., Temme, A. J. A. M., & Saco, P. M. (2018). The effect of landform variation on vegetation patterning and related sediment dynamics. *Earth Surface Processes and Landforms*. https://doi.org/10.1002/esp.4377

Bale, C. L., Williams, J. B., & Charley, J. L. (1998). The impact of aspect on forest structure and floristics in some Eastern Australian sites. *Forest Ecology and Management*, *110*, 363–377.

Barrows, T. T., Stone, J. O., Fifield, L. K., & Cresswell, R. G. (2001). Late Pleistocene Glaciation of the Kosciuszko Massif, Snowy Mountains, Australia. *Quaternary Research*, *55*(02), 179–189. https://doi.org/10.1006/qres.2001.2216

Ben-Asher, M., Haviv, I., Roering, J. J., & Crouvi, O. (2017). The influence of climate and microclimate (aspect) on soil creep efficiency: Cinder cone morphology and evolution along the eastern Mediterranean Golan Heights. *Earth Surface Processes and Landforms*, *42*(15), 2649–2662. https://doi.org/10.1002/esp.4214

Benda, L., & Dunne, T. (1997). Stochastic forcing of sediment routing and storage in channel networks. *Water Resources Research*, *33*(12), 2865–2880. https://doi.org/10.1029/97WR02387

Benyon, R. G., & Lane, P. N. J. (2013). Ground and satellite-based assessments of wet eucalypt forest survival and regeneration for predicting long-term hydrological responses to a large wildfire. *Forest Ecology and Management*, *294*, 197–207. https://doi.org/10.1016/j.foreco.2012.04.003

Berry, S. L., Farquhar, G. D., & Roderick, M. L. (2005). Co- Evolution of Climate, Soil and Vegetation. In M. G. Anderson (Ed.), *Encyclopedia of hydrological sciences*. Indianapolis: John Wiley And Sons, Ltd.

Beven, K., & Germann, P. (1982). Macropores and water flow in soils. *Water Resources Research*, *18*(5), 1311–1325. https://doi.org/10.1029/WR018i005p01311

Bishop, P. (1985). Southeast Australian late Mesozoic and Cenozoic denudation rates: a test for late Tertiary increases in continental denudation. *Geology*, *13*(7), 479–482.

Boer, M. M., Bowman, D. M. J. S., Murphy, B. P., Cary, G. J., Cochrane, M. A., Fensham, R. J., et al. (2016). Future changes in climatic water balance determine potential for transformational shifts in Australian fire regimes. *Environmental Research Letters*, *11*(6), 065002. https://doi.org/10.1088/1748-9326/11/6/065002

Bond, W. J., Woodward, F. I., & Midgley, G. F. (2005). The global distribution of ecosystems in a world without fire. *New Phytologist*, *165*(2), 525–538. https://doi.org/10.1111/j.1469-8137.2004.01252.x

Bowman, D. M. J. S. (2000). *Australian Rainforests: Islands of Green in a Land of Fire: By*

David M.J.S. Bowman. (D. M. J. S. Bowman, Ed.). Cambridge, United Kingdom: Cambridge University Press. https://doi.org/10.1111/j.1745-7939.2001.tb01610.x

Bowman, D. M. J. S. (2017). When will the jungle burn ? *Nature Publishing Group*, *7*(6), 390–391. https://doi.org/10.1038/nclimate3284

Bowman, D. M. J. S., Balch, J. K., Artaxo, P., Bond, W. J., Carlson, J. M., Cochrane, M. A., et al. (2009). Fire in the Earth system. *Science*, *324*, 481–484.

Bowman, D. M. J. S., Murphy, B. P., Neyland, D. L. J., Williamson, G. J., & Prior, L. D. (2014). Abrupt fire regime change may cause landscape- wide loss of mature obligate seeder forests. *Global Change Biology*, *20*(3), 1008–1015.

Bowman, D. M. J. S., & Yeates, D. (2006). A remarkable moment in Australian biogeography. In *New Phytologist* (Vol. 170, pp. 208–212). Blackwell Publishing Ltd. https://doi.org/10.1111/j.1469-8137.2006.01699.x

Boyle, M., Frankenberger, W. T., & Stolzy, L. H. (1989). The influence of organic matter on soil aggregation and water infiltration. *Journal of Production Agriculture*, *2*(4), 290–299.

Bradstock, R. A. (2010). A biogeographic model of fire regimes in Australia: current and future implications. *Global Ecology and Biogeography*, *19*(2), 145–158. https://doi.org/10.1111/j.1466-8238.2009.00512.x

Bren, L. J., & Turner, A. (1979). Overland flow on a steep, forested infiltrating slope. *Australian Journal of Soil Research*, *17*(1), 43. https://doi.org/10.1071/SR9790043

Brolsma, R. J., & Bierkens, M. F. P. (2007). Groundwater–soil water–vegetation dynamics in a temperate forest ecosystem along a slope. *Water Resources Research*, *43*(1).

Brown, J. A. H. (1972). Hydrologic effects of a bushfire in a catchment in south-eastern New South Wales. *Journal of Hydrology*, *15*(1), 77–96. https://doi.org/10.1016/0022-1694(72)90077-7

Budyko, M. I. (1974). *Climate and life*. San Diego, California: Academic Press.

Burch, G. J., Moore, I. D., & Burns, J. (1989). Soil hydrophobic effects on infiltration and catchment runoff. *Hydrological Processes*, *3*(3), 211–222.

https://doi.org/10.1002/hyp.3360030302

Burrows, G. E. (2013, August 29). Buds, bushfires and resprouting in the eucalypts. *Australian Journal of Botany*. CSIRO PUBLISHING. https://doi.org/10.1071/BT13072

Camici, S., Tarpanelli, A., Brocca, L., Melone, F., & Moramarco, T. (2011). Design soil moisture estimation by comparing continuous and storm-based rainfall-runoff modeling. *Water Resources Research*, *47*(5). https://doi.org/10.1029/2010WR009298

Caracciolo, D., Noto, L. V., Istanbulluoglu, E., Fatichi, S., & Zhou, X. (2014). Climate change and Ecotone boundaries: Insights from a cellular automata ecohydrology model in a Mediterranean catchment with topography controlled vegetation patterns. *Advances in Water Resources*, *73*, 159–175. https://doi.org/10.1016/j.advwatres.2014.08.001

Carlyle-Moses, D. E., & Gash, J. H. C. (2011). Rainfall interception loss by forest canopies. In L. D., C.-M. D., & T. T. (Eds.), *Forest Hydrology and Biogeochemistry. Ecological Studies (Analysis and Synthesis)* (pp. 407–423). Springer. https://doi.org/https://doi.org/10.1007/978-94-007-1363-5_20

Carson, M. A., & Kirkby, M. J. (1972). *Hillslope form and process*. London: Cambridge University Press.

Cawson, J. G., Nyman, P., Smith, H. G., Lane, P. N. j, & Sheridan, G. J. (2016). How soil temperatures during prescribed burning affect soil water repellency, infiltration and erosion. *Geoderma*, *278*, 12–22. https://doi.org/10.1016/j.geoderma.2016.05.002

Cawson, J. G., Sheridan, G. J., Smith, H. G., & Lane, P. N. J. (2013). Effects of fire severity and burn patchiness on hillslope-scale surface runoff, erosion and hydrologic connectivity in a prescribed burn. *Forest Ecology and Management*, *310*, 219–233. https://doi.org/10.1016/j.foreco.2013.08.016

Certini, G. (2005). Effects of fire on properties of forest soils: A review. *Oecologia*, *143*(1), 1–10. https://doi.org/10.1007/s00442-004-1788-8

Chadwick, O. A., Roering, J. J., Heimsath, A. M., Levick, S. R., Asner, G. P., & Khomo, L. (2013). Shaping post-orogenic landscapes by climate and chemical weathering. *Geology*, *41*(11), 1171–1174. https://doi.org/10.1130/G34721.1

Cheal, D. (2010). *Growth stages and tolerable fire intervals for Victoria's native vegetation*

data sets. Fire and Adaptive Management. Report No. 84.

Chorover, J., Troch, P. A., Rasmussen, C., Brooks, P. D., Pelletier, J. D., Breshears, D. D., et al. (2011). How water, carbon, and energy drive critical zone evolution: The Jemez–Santa Catalina Critical Zone Observatory. *Vadose Zone Journal*, *10*(3), 884–899. https://doi.org/10.2136/vzj2010.0132

Clapp, R. B., & Hornberger, G. M. (1978). Empirical equations for some soil hydraulic properties. *Water Resources Research*, *14*(4), 601–604. https://doi.org/10.1029/WR014i004p00601

Clarke, P. J., Lawes, M. J., Midgley, J. J., Lamont, B. B., Ojeda, F., Burrows, G. E., et al. (2013). Resprouting as a key functional trait: how buds, protection and resources drive persistence after fire. *New Phytologist*, *197*(1), 19–35. https://doi.org/10.1111/nph.12001

Clarke, P. J., Lawes, M. J., Murphy, B. P., Russell-Smith, J., Nano, C. E. M., Bradstock, R. A., et al. (2015). A synthesis of postfire recovery traits of woody plants in Australian ecosystems. *Science of The Total Environment*, *534*, 31–42. https://doi.org/10.1016/j.scitotenv.2015.04.002

Cohen, S., Willgoose, G., & Hancock, G. (2009). The mARM spatially distributed soil evolution model: A computationally efficient modeling framework and analysis of hillslope soil surface organization. *Journal of Geophysical Research: Earth Surface (2003–2012)*, *114*(F3). https://doi.org/10.1029/2008JF001214

Cohen, S., Willgoose, G., & Hancock, G. (2010). The mARM3D spatially distributed soil evolution model: Three-dimensional model framework and analysis of hillslope and landform responses. *Journal of Geophysical Research: Earth Surface (2003–2012)*, *115*(F4). https://doi.org/https://doi.org/10.1029/2009JF001536

Cohen, S., Willgoose, G., & Hancock, G. (2013). Soil–landscape response to mid and late Quaternary climate fluctuations based on numerical simulations. *Quaternary Research*, *79*(3), 452–457. https://doi.org/https://doi.org/10.1016/j.yqres.2013.01.001

Collins, D. B. G., Bras, R. L., & Tucker, G. E. (2004). Modeling the effects of vegetation-erosion coupling on landscape evolution. *Journal of Geophysical Research: Earth Surface (2003–2012)*, *109*(F03004). https://doi.org/10.1029/2003JF000028

Collins, D. B. G., Collins, R. L., & Bras, R. L. (2008). Climatic control of sediment yield in dry lands following climate and land cover change. *Water Resources Research*, *44*(10).

Coon, W. F. (1997). *Estimation of roughness coefficients for natural stream channels with vegetated banks*. *U.S. Geological Survey water-supply paper*. U.S. Geological Survey. Retrieved from https://pubs.er.usgs.gov/publication/wsp2441

Corenblit, D., Baas, A. C. W., Bornette, G., Darrozes, J., Delmotte, S., Francis, R. A., et al. (2011). Feedbacks between geomorphology and biota controlling Earth surface processes and landforms: A review of foundation concepts and current understandings. *Earth-Science Reviews*, *106*(3), 307–331. https://doi.org/10.1016/j.earscirev.2011.03.002

Corenblit, D., & Steiger, J. (2009). Vegetation as a major conductor of geomorphic changes on the Earth surface: toward evolutionary geomorphology. *Earth Surface Processes and Landforms*, *34*(6), 891–896. https://doi.org/10.1002/esp.1788

Corenblit, D., Steiger, J., Gurnell, A., & Tabacchi, E. (2007). Darwinian origin of landforms. *Earth Surface Processes and Landforms*, *32*(13), 2070–2073. https://doi.org/10.1002/esp.1536

Costermans, L. (2006). *Native Trees and Shrubs of South-eastern Australia*. Reed New Holland.

Cowpertwait, P. S. P., O'Connell, P. E., Metcalfe, A. V., & Mawdsley, J. A. (1996). Stochastic point process modelling of rainfall. I. Single-site fitting and validation. *Journal of Hydrology*, *175*(1–4), 17–46. https://doi.org/10.1016/S0022-1694(96)80004-7

Cramer, W., Bondeau, A., Woodward, F. I., Prentice, I. C., Betts, R. A., Brovkin, V., et al. (2001). Global response of terrestrial ecosystem structure and function to CO2 and climate change: results from six dynamic global vegetation models. *Global Change Biology*, *7*(4), 357–373. https://doi.org/10.1046/j.1365-2486.2001.00383.x

Davis, M. B., & Shaw, R. G. (2001, April 27). Range shifts and adaptive responses to quaternary climate change. *Science*. American Association for the Advancement of Science. https://doi.org/10.1126/science.292.5517.673

DeBano, L. F. (2000a). The role of fire and soil heating on water repellency in wildland environments: a review. *Journal of Hydrology*, *231*, 195–206. https://doi.org/10.1016/S0022-1694(00)00194-3

DeBano, L. F. (2000b). Water repellency in soils: a historical overview. *Journal of Hydrology*, *231*, 4–32. https://doi.org/10.1016/S0022-1694(00)00180-3

DeBano, L. F., Neary, D. G., & Ffolliott, P. F. (1998). *Fire effects on ecosystems*. John Wiley & Sons.

Dessert, C., Dupré, B., Gaillardet, J., François, L. M., & Allègre, C. J. (2003). Basalt weathering laws and the impact of basalt weathering on the global carbon cycle. *Chemical Geology*, *202*(3–4), 257–273. https://doi.org/10.1016/J.CHEMGEO.2002.10.001

Dietrich, W. E., Bellugi, D. G., Sklar, L. S., Stock, J. D., Heimsath, A. M., & Roering, J. J. (2003). Geomorphic transport laws for predicting landscape form and dynamics. In P. R. Wilcock & R. Iverson (Eds.), *Prediction in geomorphology* (pp. 103–132). Florida, US: AGU.

Dietrich, W. E., & Perron, J. T. (2006). The search for a topographic signature of life. *Nature*, *439*(7075), 411–418. https://doi.org/10.1038/nature04452

Dixon, J. L., Heimsath, A. M., & Amundson, R. (2009a). The critical role of climate and saprolite weathering in landscape evolution. *Earth Surface Processes and Landforms*, *34*(11), 1507–1521. https://doi.org/10.1002/esp.1836

Dixon, J. L., Heimsath, A. M., Kaste, J., & Amundson, R. (2009b). Climate-driven processes of hillslope weathering. *Geology*, *37*(11), 975–978. https://doi.org/10.1130/G30045A.1

Dixon, J. L., & von Blanckenburg, F. (2012). Soils as pacemakers and limiters of global silicate weathering. *Comptes Rendus Geoscience*, *344*, 597–609. https://doi.org/10.1016/j.crte.2012.10.012

Doerr, S. H., Shakesby, R. A., Blakeb W. H, Chaferc C. J., Humphreys G. S., & Wallbrink, P. J. (2006). Effects of differing wildfire severities on soil wettability and implications for hydrological response. *Journal of Hydrology*, *319*(1–4), 295–311. https://doi.org/10.1016/J.JHYDROL.2005.06.038

Dohrenwend, J. C. (1978). Systematic valley asymmetry in the central California Coast Ranges. *Geological Society of America Bulletin*, *89*(6), 891–900. https://doi.org/https://doi.org/10.1130/0016-7606(1978)89<891:SVAITC>2.0.CO;2

Donohue, R., Roderick, M., & McVicar, T. (2012). Roots, storms and soil pores: Incorporating key ecohydrological processes into Budyko's hydrological model. *Journal of Hydrology*, *436*, 35–50. https://doi.org/10.1016/j.jhydrol.2012.02.033

Dosseto, A., Hesse, P. P., Maher, K., Fryirs, K., & Turner, S. (2010). Climatic and vegetation control on sediment dynamics during the last glacial cycle. *Geology*, *38*(5), 395–398. https://doi.org/10.1130/G30708.1

Dosseto, A., & Schaller, M. (2016). The erosion response to Quaternary climate change quantified using uranium isotopes and in situ-produced cosmogenic nuclides. *Earth-Science Reviews*, *155*, 60–81. https://doi.org/10.1016/j.earscirev.2016.01.015

Dunin, F. X., O'Loughlin, E. M., & Reyenga, W. (1988). Interception loss from eucalypt forest: Lysimeter determination of hourly rates for long term evaluation. *Hydrological Processes*, *2*(4), 315–329. https://doi.org/10.1002/hyp.3360020403

Dunkerley, D. (2015). Percolation through leaf litter: What happens during rainfall events of varying intensity? *Journal of Hydrology*, *525*, 737–746.

Dunkerley, D. L. (1997). Banded vegetation: development under uniform rainfall from a simple cellular automaton model. *Plant Ecology*, *129*(2), 103–111. https://doi.org/10.1023/A:1009725732740

Dunkerley, D. L. (2008). Intra-storm evaporation as a component of canopy interception loss in dryland shrubs: observations from Fowlers Gap, Australia. *Hydrological Processes*, *22*(12), 1985–1995. https://doi.org/10.1002/hyp.6783

Dupré, B., Dessert, C., Oliva, P., Goddéris, Y., Viers, J., François, L., et al. (2003). Rivers, chemical weathering and Earth's climate. *Comptes Rendus Geoscience*, *335*(16), 1141–1160. https://doi.org/10.1016/j.crte.2003.09.015

Eagleson, P. S. (1982). Ecological optimality in water-limited natural soil-vegetation systems: 1. Theory and hypothesis. *Water Resources Research*, *18*(2), 325–340. https://doi.org/10.1029/WR018i002p00325

Eagleson, P. S. (2005). *Ecohydrology - Darwinian expression of vegetation form and function*. (S. Eagleson, Peter, Ed.). Cambridge, United Kingdom: Cambridge University Press.

Eagleson, P. S., & Tellers, T. E. (1982). Ecological optimality in water-limited natural soil-vegetation systems: 2. Tests and applications. *Water Resources Research*, *18*(2), 341–354. https://doi.org/10.1029/WR018i002p00341

Eamus, D. (2003). How does ecosystem water balance affect net primary productivity of woody ecosystems? *Functional Plant Biology*, *30*(2), 187. https://doi.org/10.1071/FP02084

Eamus, D., Hatton, T., Cook, P., & Colvin, C. (2006). *Ecohydrology: Vegetation Functions, Water and Resource Management*. *Book*. Collingwood, Victoria, Australia: CSIRO. https://doi.org/10.1111/j.1442-9993.2006.01703.x

Ebel, B. A. (2013). Simulated unsaturated flow processes after wildfire and interactions with slope aspect. *Water Resources Research*, *49*(12), 8090–8107.

Egli, M., Mirabella, A., & Sartori, G. (2008). The role of climate and vegetation in weathering and clay mineral formation in late Quaternary soils of the Swiss and Italian Alps. *Geomorphology*, *102*(3), 307–324. https://doi.org/10.1016/j.geomorph.2008.04.001

Fairman, T. A., Nitschke, C. R., & Bennett, L. T. (2016). Too much, too soon? A review of the impacts of increasing wildfire frequency on tree demography and structure in temperate forests. *International Journal of Wildland Fire*, *25*(8), 831–848. https://doi.org/10.1071/WF15010

Fifield, L. K., Wasson, R. J., Pillans, B., & Stone, J. O. H. (2010). The longevity of hillslope soil in SE and NW Australia. *Catena*, *81*(1), 32–42. https://doi.org/10.1016/j.catena.2010.01.003

Finkele, K., Mills, G. A., Beard, G., & Jones, D. A. (2006). National gridded drought factors and comparison of two soil moisture deficit formulations used in prediction of Forest Fire Danger Index in Australia. *Australian Meteorological Magazine*, *55*, 183–197.

Fletcher, M. S., & Moreno, P. I. (2012). Have the Southern Westerlies changed in a zonally

symmetric manner over the last 14,000 years? A hemisphere-wide take on a controversial problem. *Quaternary International*, *253*, 32–46. https://doi.org/10.1016/j.quaint.2011.04.042

Fletcher, M. S., Wood, S. W., & Haberle, S. H. (2014a). A fire-driven shift from forest to non-forest: evidence for alternative stable states? *Ecology*, *95*(9), 2504–2513. https://doi.org/10.1890/12-1766.1

Fletcher, M., Wolfe, B. B., Whitlock, C., Pompeani, D. P., Heijnis, H., Haberle, S. G., et al. (2014b). The legacy of mid-Holocene fire on a Tasmanian montane landscape. *Journal of Biogeography*, *41*(3), 476–488.

Gabet, E. J., & Dunne, T. (2003). A stochastic sediment delivery model for a steep Mediterranean landscape. *Water Resources Research*, *39*(9). https://doi.org/10.1029/2003WR002341

Gabet, E. J., Edelman, R., & Langner, H. (2006). Hydrological controls on chemical weathering rates at the soil-bedrock interface. *Geology*, *34*(12), 1065–1068. https://doi.org/10.1130/G23085A.1

Gabet, E. J., & Mudd, S. M. (2010). Bedrock erosion by root fracture and tree throw: A coupled biogeomorphic model to explore the humped soil production function and the persistence of hillslope soils. *Journal of Geophysical Research: Earth Surface*, *115*(F4), F04005. https://doi.org/10.1029/2009JF001526

Gabet, E. J., Reichman, O. J., & Seabloom, E. W. (2003). The effects of bioturbation on soil processes and sediment transport. *Annual Review of Earth and Planetary Sciences*, *31*, 249–273. https://doi.org/10.1146/annurev.earth.31.100901.141314

Gao, H., Hrachowitz, M., Schymanski, S. J., Fenicia, F., Sriwongsitanon, N., & Savenije, H. H. G. (2014). Climate controls how ecosystems size the root zone storage capacity at catchment scale. *Geophysical Research Letters*, *41*(22), 7916–7923. https://doi.org/10.1002/2014GL061668

Gharun, M., Turnbull, T. L., & Adams, M. A. (2013a). Stand water use status in relation to fire in a mixed species eucalypt forest. *Forest Ecology and Management*, *304*, 162–170. https://doi.org/10.1016/j.foreco.2013.05.002

Gharun, M., Turnbull, T. L., & Adams, M. A. (2013b). Validation of canopy transpiration in a mixed-species foothill eucalypt forest using a soil–plant–atmosphere model. *Journal of Hydrology*, *492*, 219–227. https://doi.org/10.1016/j.jhydrol.2013.03.051

Gibson, R. K., Bradstock, R. A., Penman, T., Keith, D. A., & Driscoll, D. A. (2015). Climatic, vegetation and edaphic influences on the probability of fire across mediterranean woodlands of south-eastern Australia. *Journal of Biogeography*, *42*(9), 1750–1760. https://doi.org/10.1111/jbi.12547

Gill, A. M., & McCarthy, M. A. (1998). Intervals between prescribed fires in Australia: what intrinsic variation should apply? *Biological Conservation*, *85*(1–2), 161–169. https://doi.org/10.1016/S0006-3207(97)00121-3

Givnish, T., Wond, S. C., Stuart-Williams, H., Holloway-Phillips, M., & Farquhar, G. (2014). Determinants of maximum tree height in Eucalyptusspecies along a rainfall gradient in Victoria, Australia. *Ecology*, *95*(11), 2991–3007. https://doi.org/10.1890/14-0240.1

Grierson, P. F., Adams, M. A., & Attiwill, P. M. (1992). Estimates of Carbon Storage in the Aboveground Biomass of Victorias Forests. *Australian Journal of Botany*, *40*(4–5), 631–640. https://doi.org/https://doi.org/10.1071/BT9920631

Grieve, S. W. D., Mudd, S. M., & Hurst, M. D. (2016). How long is a hillslope? *Earth Surface Processes and Landforms*, *41*(8), 1039–1054. https://doi.org/10.1002/esp.3884

Gutiérrez-Jurado, H. A., & Vivoni, E. R. (2013a). Ecogeomorphic expressions of an aspect-controlled semiarid basin: I. Topographic analyses with high-resolution data sets. *Ecohydrology*, *6*(1), 8–23. https://doi.org/10.1002/eco.280

Gutiérrez-Jurado, H. A., & Vivoni, E. R. (2013b). Ecogeomorphic expressions of an aspect-controlled semiarid basin: II. Topographic and vegetation controls on solar irradiance. *Ecohydrology*, *6*(1), 24–37. https://doi.org/10.1002/eco.1263

Gutiérrez-Jurado, H. A., Vivoni, E. R., Cikoski, C., Harrison, J. B. J., Bras, R. L., & Istanbulluoglu, E. (2013). On the observed ecohydrologic dynamics of a semiarid basin with aspect-delimited ecosystems. *Water Resources Research*, *49*(12), 8263–8284. https://doi.org/Doi 10.1002/2013wr014364

Gutiérrez-Jurado, H. A., & Vivoni, E. R. (2013). Ecogeomorphic expressions of an aspect-

controlled semiarid basin: I. Topographic analyses with high-resolution data sets. *Ecohydrology*, *6*(1), 8–23. https://doi.org/10.1002/eco.280

Gutiérrez-Jurado, H. A., Vivoni, E. R., Istanbulluoglu, E., & Bras, R. L. (2007). Ecohydrological response to a geomorphically significant flood event in a semiarid catchment with contrasting ecosystems. *Geophysical Research Letters*, *34*(24).

Hancock, G. R., Hugo, J., Webb, A. A., & Turner, L. (2017). Sediment transport in steep forested catchments – An assessment of scale and disturbance. *Journal of Hydrology*, *547*, 613–622. https://doi.org/10.1016/j.jhydrol.2017.02.022

Hatton, T. J., Viney, N. R., Catchpole, E. A., & De Mestre, N. J. (1988). The influence of soil moisture on Eucalyptus leaf litter moisture. *Forest Science*, *34*(2), 292–301. https://doi.org/https://doi.org/10.1093/forestscience/34.2.292

Hatton, T., Salvucci, G., & Wu, H. (1997). Eagleson's optimality theory of an ecohydrological equilibrium: quo vadis? *Functional Ecology*, *11*(1945), 665–674. https://doi.org/10.1046/j.1365-2435.1997.00159.x

Heimsath, A. M., Chappell, J., Dietrich, W. E., Nishiizumi, K., & Finkel, R. C. (2001). Late Quaternary erosion in southeastern Australia: a field example using cosmogenic nuclides. *Quaternary International*, *83*, 169–185. https://doi.org/https://doi.org/10.1016/S1040-6182(01)00038-6

Heimsath, A. M., Dietrich, W. E., Nishiizumi, K., & Finkel, R. C. (1997). The soil production function and landscape equilibrium. *Nature*, *388*(6640), 358–361. https://doi.org/10.1038/41056

Heimsath, A. M., Fink, D., & Hancock, G. R. (2009). The 'humped'soil production function: eroding Arnhem Land, Australia. *Earth Surface Processes and Landforms*, *34*(12), 1674–1684. https://doi.org/https://doi.org/10.1002/esp.1859

Hillel, D. (1982). *Introduction to soil physics*. New York: Academic Press.

Huang, X., Huang, J., & Niemann. (2006). Modelling the potential impacts of groundwater hydrology on long-term drainage basin evolution. *Earth Surface Processes and Landforms*, *31*(14), 1802–1823. https://doi.org/https://doi-org.ezp.lib.unimelb.edu.au/10.1002/esp.1369

Inbar, A., Lado, M., Sternberg, M., Tenau, H., & Ben-Hur, M. (2014). Forest fire effects on soil chemical and physicochemical properties, infiltration, runoff, and erosion in a semiarid Mediterranean region. *Geoderma*, *221*, 131–138. https://doi.org/https://doi.org/10.1016/j.geoderma.2014.01.015

Istanbulluoglu, E., & Bras, R. L. (2005). Vegetation-modulated landscape evolution: Effects of vegetation on landscape processes, drainage density, and topography. *Journal of Geophysical Research: Earth Surface*, *110*(2), 1–19. https://doi.org/10.1029/2004JF000249

Istanbulluoglu, E., & Bras, R. L. (2006). On the dynamics of soil moisture, vegetation, and erosion: Implications of climate variability and change. *Water Resources Research*, *42*(6). https://doi.org/10.1029/2005WR004113

Istanbulluoglu, E., Tarboton, D. G., Pack, R. T., & Luce, C. H. (2004). Modeling of the interactions between forest vegetation, disturbances, and sediment yields. *Journal of Geophysical Research: Earth Surface*, *109*, F01009. https://doi.org/0148-0227/04/2003JF000041$09.00

Istanbulluoglu, E., Wang, T., & Wedin, D. A. (2012). Evaluation of ecohydrologic model parsimony at local and regional scales in a semiarid grassland ecosystem. *Ecohydrology*, *5*(1), 121–142. https://doi.org/https://doi.org/10.1002/eco.211

Istanbulluoglu, E., Yetemen, O., Vivoni, E. R., Gutiérrez-Jurado, H. A., & Bras, R. L. (2008). Eco-geomorphic implications of hillslope aspect: Inferences from analysis of landscape morphology in central New Mexico. *Geophysical Research Letters*, *35*(14), 1–6. https://doi.org/10.1029/2008GL034477

Ivanov, V. Y., Bras, R. L., & Vivoni, E. R. (2008). Vegetation-hydrology dynamics in complex terrain of semiarid areas: 1. A mechanistic approach to modeling dynamic feedbacks. *Water Resources Research*, *44*(3), W03429. https://doi.org/10.1029/2006WR005588

Jenny, H. (1941). *Factors of Soil Formation: A System of Quantitative Pedology*. New York: Dover Publication, INC.

Johnson, E. A., & Wagner, C. E. Van. (1985). The theory and use of two fire history models. *Canadian Journal of Forest Research*, *15*(1), 214–220. https://doi.org/10.1139/x85-039

Kandel, D. D., Western, A. W., & Grayson, R. B. (2005). Scaling from process timescales to daily time steps: A distribution function approach. *Water Resources Research*, *41*(2), W02003. https://doi.org/https://doi.org/10.1029/2004WR003380

Kean, J. W., Staley, D. M., & Cannon, S. H. (2011). In situ measurements of post-fire debris flows in southern California: Comparisons of the timing and magnitude of 24 debris-flow events with rainfall and soil moisture conditions. *Journal of Geophysical Research: Earth Surface*, *116*(4), 1–21. https://doi.org/10.1029/2011JF002005

Keetch, J. J., & Byram, G. M. (1968). *A Drought Index for Forest Fire Control*. *USDA Forest Service Research Paper* (Vol. 038). Retrieved from https://www.srs.fs.usda.gov/pubs/viewpub.php?index=40

Keith, H., Mackey, B. G., & Lindenmayer, D. B. (2009). Re-evaluation of forest biomass carbon stocks and lessons from the world's most carbon-dense forests. *Proceedings of the National Academy of Sciences*, *106*(28), 11635–11640. https://doi.org/https://doi.org/10.1073/pnas.0901970106

Kemp, J., & Rhodes, E. J. (2010). Episodic fluvial activity of inland rivers in southeastern Australia: Palaeochannel systems and terraces of the Lachlan River. *Quaternary Science Reviews*, *29*(5–6), 732–752. https://doi.org/10.1016/j.quascirev.2009.12.001

Kennedy, A., & Jamieson, D. (2007). Ecological Fire Management in North East Victoria. In *Proceedings of the Joint AFAC/Bushfire CRC Conference* (pp. 18–20).

Kennet, B. L. N., & Blewett, R. S. (2012). *Lithospheric Framework of Australia*. *Episodes* (Vol. 35). International Union of Geological Sciences. Retrieved from http://52.172.159.94/index.php/epi/article/view/59835

Klute, A., Cassel, D. K., & Nielsen, D. R. (1986). Field Capacity and Available Water Capacity. In *Methods of Soil Analysis: Part 1—Physical and Mineralogical Methods* (pp. 901–926). Madison, USA: Soil Science Society of America, American Society of Agronomy. https://doi.org/10.2136/sssabookser5.1.2ed.c36

Kosmas, C., Gerontidis, S., & Marathianou, M. (2000). The effect of land use change on soils and vegetation over various lithological formations on Lesvos (Greece). *Catena*, *40*(1), 51–68. https://doi.org/10.1016/S0341-8162(99)00064-8

Krueger, E. S., Ochsner, T. E., Carlson, J. D., Engle, D. M., Twidwell, D., & Fuhlendorf, S. D. (2016). Concurrent and antecedent soil moisture relate positively or negatively to probability of large wildfires depending on season. *International Journal of Wildland Fire*, *25*(2), 257–668. https://doi.org/10.1071/WF15104

Kuczera, G. (1987). Prediction of water yield reductions following a bushfire in ash-mixed species eucalypt forest. *Journal of Hydrology*, *94*(3), 215–236. https://doi.org/https://doi.org/10.1016/0022-1694(87)90054-0

Lado, M., Lado, A., Paz, M., & Ben, H. (2004). Organic Matter and Aggregate Size Interactions in Infiltration, Seal Formation, and Soil Loss. *Soil Science Society of America Journal*, *68*(3), 935. https://doi.org/doi:10.2136/sssaj2004.9350

Laio, F., D'Odorico, P., & Ridolfi, L. (2006). An analytical model to relate the vertical root distribution to climate and soil properties. *Geophysical Research Letters*, *33*(18). https://doi.org/https://doi.org/10.1029/2006GL027331

Lane, P. N. J., Croke, J. C., & Dignan, P. (2004). Runoff generation from logged and burnt convergent hillslopes: rainfall simulation and modelling. *Hydrological Processes*, *18*(5), 879–892. https://doi.org/10.1002/hyp.1316

Lane, P. N. J., Sheridan, G. J., & Noske, P. J. (2006). Changes in sediment loads and discharge from small mountain catchments following wildfire in south eastern Australia. *Journal of Hydrology*, *331*(3–4), 495–510. https://doi.org/10.1016/j.jhydrol.2006.05.035

Langbein, W. B., & Schumm, S. A. (1958). Yield of sediment in relation to mean annual precipitation. *Eos, Transactions American Geophysical Union*, *39*(6), 1076–1084. https://doi.org/https://doi.org/10.1029/TR039i006p01076

Langhans, C., Lane, P. N. J., Nyman, P., Noske, P. J., Cawson, J. G., Oono, A., & Sheridan, G. J. (2016a). Scale-dependency of effective hydraulic conductivity on fire-affected hillslopes. *Water Resources Research*, *52*(7), 5041–5055. https://doi.org/10.1002/2016WR018998

Langhans, C., Nyman, P., Noske, P. J., Van der Sant, R. E., Lane, P. N. J., & Sheridan, G. J. (2017). Post-fire hillslope debris flows: Evidence of a distinct erosion process. *Geomorphology*, *295*, 55–75. https://doi.org/10.1016/j.geomorph.2017.06.008

Langhans, C., Smith, H. G., Chong, D. M. O., Nyman, P., Lane, P. N. J., & Sheridan, G. J. (2016b). A model for assessing water quality risk in catchments prone to wildfire. *Journal of Hydrology*, *534*, 407–426. https://doi.org/https://doi.org/10.1016/j.jhydrol.2015.12.048

Larsen, I. J., MacDonald, L. H., Brown, E., Rough, D., Welsh, M. J., Pietraszek, J. H., et al. (2009). Causes of Post-Fire Runoff and Erosion: Water Repellency, Cover, or Soil Sealing? *Soil Science Society of America Journal*, *73*(4), 1393. https://doi.org/10.2136/sssaj2007.0432

Lawlor, L. R., & Smith, J. M. (1976). The Coevolution and Stability of Competing Species. *The American Naturalist*, *110*(971), 79–99. https://doi.org/10.1086/283049

Lin, H. (2011). Three Principles of Soil Change and Pedogenesis in Time and Space. *Soil Science Society of America Journal*, *75*(6), 2049. https://doi.org/10.2136/sssaj2011.0130

Lindroth, A. (1993). Aerodynamic and canopy resistance of short-rotation forest in relation to leaf area index and climate. *Boundary-Layer Meteorology*, *66*(3), 265–279. https://doi.org/10.1007/BF00705478

Lohse, K. A., & Dietrich, W. E. (2005). Contrasting effects of soil development on hydrological properties and flow paths. *Water Resources Research*, *41*(12). https://doi.org/10.1029/2004WR003403

Lybrand, R., & Rasmussen, C. (2014). Linking soil element-mass-transfer to microscale mineral weathering across a semiarid environmental gradient. *Chemical Geology*, *381*, 26–39. https://doi.org/https://doi.org/10.1016/j.chemgeo.2014.04.022

Lybrand, R., & Rasmussen, C. (2015). Quantifying climate and landscape position controls on soil development in semiarid ecosystems. *Soil Science Society of America Journal*, *79*(1), 104–116. https://doi.org/10.2136/sssaj2014.06.0242

Lybrand, R., Rasmussen, C., Jardine, A., Troch, P., & Chorover, J. (2011). The effects of climate and landscape position on chemical denudation and mineral transformation in the Santa Catalina mountain critical zone observatory. *Applied Geochemistry*, *26*, S80–S84. https://doi.org/10.1016/j.apgeochem.2011.03.036

Lynch, A. H., Beringer, J., Kershaw, P., Marshall, A., Mooney, S., Tapper, N., et al. (2007).

Using the paleorecord to evaluate climate and fire interactions in Australia. *Annu. Rev. Earth Planet. Sci.*, *35*, 215–239. https://doi.org/https://doi.org/10.1146/annurev.earth.35.092006.145055

Mariani, M., & Fletcher, M. S. (2016). The Southern Annular Mode determines inter-annual and centennial-scale fire activity in temperate southwest Tasmania, Australia. *Geophysical Research Letters*, *43*(4), 1702–1709. https://doi.org/10.1002/2016GL068082

Mariani, M., Fletcher, M. S., Holz, A., & Nyman, P. (2016). ENSO controls interannual fire activity in southeast Australia. *Geophysical Research Letters*, *43*(20), 10,891-10,900. https://doi.org/10.1002/2016GL070572

McCarthy, M. A., Gill, A. M., & Bradstock, R. A. (2001). Theoretical fire-interval distributions. *International Journal of Wildland Fire*, *10*(1), 73–77. https://doi.org/10.1071/WF01013

McCarthy, M. A., Malcolm Gill, A., & Lindenmayer, D. B. (1999). Fire regimes in mountain ash forest: Evidence from forest age structure, extinction models and wildlife habitat. *Forest Ecology and Management*, *124*(2–3), 193–203. https://doi.org/10.1016/S0378-1127(99)00066-3

McFadden, L. D., Eppes, M. C., Gillespie, A. R., & Hallet, B. (2005). Physical weathering in arid landscapes due to diurnal variation in the direction of solar heating. *Geological Society of America Bulletin*, *117*(1), 161. https://doi.org/10.1130/B25508.1

McGuire, L. A., Pelletier, J. D., & Roering, J. J. (2014). Development of topographic asymmetry: Insights from dated cinder cones in the western United States. *Journal of Geophysical Research: Earth Surface*, *119*(8), 1725–1750. https://doi.org/10.1002/2014JF003081

McKenzie, G. M. (1997). The late Quaternary vegetation history of the south-central highlands of Victoria, Australia. I. Sites above 900 m. *Austral Ecology*, *22*(1), 19–36. https://doi.org/10.1111/j.1442-9993.1997.tb00638.x

McKenzie, G. M. (2002). The late Quaternary vegetation history of the south-central highlands of Victoria, Australia. II. Sites below 900 m. *Austral Ecology*, *27*(1), 32–54. https://doi.org/10.1046/j.1442-9993.2002.01155.x

Meyer, G. A., Wells, S. G., Balling, R. C., & Jull, A. J. T. (1992). Response of alluvial systems to fire and climate change in Yellowstone National Park. *Nature*, *357*(6374), 147–150. https://doi.org/10.1038/357147a0

Meyer, M. D., North, M. P., Gray, A. N., & Zald, H. S. J. (2007). Influence of soil thickness on stand characteristics in a Sierra Nevada mixed-conifer forest. *Plant and Soil*, *294*(1–2), 113–123. https://doi.org/10.1007/s11104-007-9235-3

Milodowski, D. T., Mudd, S. M., & Mitchard, E. T. A. (2015). Erosion rates as a potential bottom-up control of forest structural characteristics in the Sierra Nevada Mountains. *Ecology*, *96*(1), 31–38. https://doi.org/https://doi.org/10.1890/14-0649.1

Minasny, B., Finke, P., Stockmann, U., Vanwalleghem, T., & McBratney, A. B. (2015). Resolving the integral connection between pedogenesis and landscape evolution. *Earth-Science Reviews*, *150*, 102–120. https://doi.org/https://doi.org/10.1016/j.earscirev.2015.07.004

Mitchell, P. J., Benyon, R. G., & Lane, P. N. J. (2012). Responses of evapotranspiration at different topographic positions and catchment water balance following a pronounced drought in a mixed species eucalypt forest, Australia. *Journal of Hydrology*, *440*, 62–74. https://doi.org/10.1016/j.jhydrol.2012.03.026

Montaldo, R., Rondena, J. D., Albertson, M., & Mancini. (2005). Parsimonious modeling of vegetation dynamics for ecohydrologic studies of water-limited ecosystems. *Water Resources Research*, *41*(10). https://doi.org/https://doi.org/10.1029/2005WR004094

Monteith, J. L. (1965). Evaporation and environment. The state and movement of water in livilng organisms. In *Symposia of the Society for Experimental Biology* (Vol. 19, pp. 205–234). https://doi.org/10.1613/jair.301

Moody, J. A., & Martin, D. A. (2001a). *Hydrologic and sedimentologic response of two burned watersheds in Colorado*. US Department of the Interior, US Geological Survey.

Moody, J. A., & Martin, D. A. (2001b). Initial hydrologic and geomorphic response following a wildfire in the Colorado Front Range. *Earth Surface Processes and Landforms*, *26*(10), 1049–1070. https://doi.org/10.1002/esp.253

Mooney, S. (2012). Late Quaternary fire regimes of Australasia. *Quaternary International*,

279, 334.

Moritz, M. A., Parisien, M.-A., Batllori, E., Krawchuk, M. A., Van Dorn, J., Ganz, D. J., & Hayhoe, K. (2012). Climate change and disruptions to global fire activity. *Ecosphere*, *3*(6). https://doi.org/10.1890/ES11-00345.1

Muzylo, A., Llorens, P., Valente, F., Keizer, J. J., & Domingo, F. (2009). A review of rainfall interception modelling. *Journal of Hydrology*, *370*(1–4), 191–206. https://doi.org/https://doi.org/10.1016/j.jhydrol.2009.02.058

Nolan, R. H., Lane, P. N. J., Benyon, R. G., Bradstock, R. A., & Mitchell, P. J. (2014). Changes in evapotranspiration following wildfire in resprouting eucalypt forests. *Ecohydrology*, *7*(5), 1363–1377. https://doi.org/10.1002/eco.1463

Nolan, R. H., Lane, P. N. J., Benyon, R. G., Bradstock, R. A., & Mitchell, P. J. (2015). Trends in evapotranspiration and streamflow following wildfire in resprouting eucalypt forests. *Journal of Hydrology*, *524*, 614–624. https://doi.org/10.1016/j.jhydrol.2015.02.045

Norton, K. P., Molnar, P., & Schlunegger, F. (2014). The role of climate-driven chemical weathering on soil production. *Geomorphology*, *204*, 510–517. https://doi.org/10.1016/j.geomorph.2013.08.030

Noske, P. J., Nyman, P., Lane, P. N. J., & Sheridan, G. J. (2016). Effects of aridity in controlling the magnitude of runoff and erosion after wildfire. *Water Resources Research*, *52*, 4338–4357. https://doi.org/10.1002/2015WR017611.Received

Nyman, P., Baillie, C. C., Duff, T. J., & Sheridan, G. J. (2018). Eco-hydrological controls on microclimate and surface fuel evaporation in complex terrain. *Agricultural and Forest Meteorology*, *252*, 49–61. https://doi.org/10.1016/j.agrformet.2017.12.255

Nyman, P., Metzen, D., Hawthorne, S. N. D., Duff, T. J., Inbar, A., Lane, P. N. J., & Sheridan, G. J. (2017). Evaluating models of shortwave radiation below Eucalyptus canopies in SE Australia. *Agricultural and Forest Meteorology*, *246*, 51–63. https://doi.org/10.1016/j.agrformet.2017.05.025

Nyman, P., Metzen, D., Noske, P. J., Lane, P. N. J., & Sheridan, G. J. (2015a). Quantifying the effects of topographic aspect on water content and temperature in fine surface fuel.

International Journal of Wildland Fire, *24*(8), 1129–1142. https://doi.org/10.1071/WF14195

Nyman, P., Sheridan, G. J., & Lane, P. N. J. (2010). Synergistic effects of water repellency and macropore flow on the hydraulic conductivity of a burned forest soil, south-east Australia. *Hydrological Processes*, *24*(20), 2871–2887. https://doi.org/10.1002/hyp.7701

Nyman, P., Sheridan, G. J., Moody, J. A., Smith, H. G., Noske, P. J., & Lane, P. N. J. (2013). Sediment availability on burned hillslopes. *Journal of Geophysical Research: Earth Surface*, *118*(4), 2451–2467. https://doi.org/https://doi.org/10.1002/jgrf.20152

Nyman, P., Sheridan, G. J., Smith, H. G., & Lane, P. N. J. (2011). Evidence of debris flow occurrence after wildfire in upland catchments of south-east Australia. *Geomorphology*, *125*(3), 383–401. https://doi.org/10.1016/j.geomorph.2010.10.016

Nyman, P., Sheridan, G. J., Smith, H. G., & Lane, P. N. J. (2014a). Modeling the effects of surface storage, macropore flow and water repellency on infiltration after wildfire. *Journal of Hydrology*, *513*, 301–313.

Nyman, P., Sherwin, C. B., Langhans, C., Sheridan, G. J., & Lane, P. N. J. (2014b). Downscaling regional climate data to calculate the radiative index of dryness in complex terrain. *Australian Metrological and Oceanographic Journal*, *64*(2), 109–122. https://doi.org/10.22499/2.6402.003

Nyman, P., Smith, H. G., Sherwin, C. B., Langhans, C., Lane, P. N. J., & Sheridan, G. J. (2015b). Predicting sediment delivery from debris flows after wildfire. *Geomorphology*, *250*, 173–186. https://doi.org/http://dx.doi.org/10.1016/j.geomorph.2015.08.023

Parsons, A. J. (1988). *Hillslope form*. Routledge London.

Pausas, J. G., & Keeley, J. E. (2014). Evolutionary ecology of resprouting and seeding in fire-prone ecosystems. *New Phytologist*, *204*(1), 55–65. https://doi.org/10.1111/nph.12921

Pausas, J. G., & Paula, S. (2012). Fuel shapes the fire–climate relationship: evidence from Mediterranean ecosystems. *Global Ecology and Biogeography*, *21*(11), 1074–1082. https://doi.org/10.1111/j.1466-8238.2012.00769.x

Pawlik, Ł., Phillips, J. D., & Šamonil, P. (2016). Roots, rock, and regolith: Biomechanical and biochemical weathering by trees and its impact on hillslopes—A critical literature review. *Earth-Science Reviews*, *159*, 142–159. https://doi.org/10.1016/j.earscirev.2016.06.002

Pelletier, J. D., Barron-Gafford, G. A., Breshears, D. D., Brooks, P. D., Chorover, J., Durcik, M., et al. (2013). Coevolution of nonlinear trends in vegetation, soils, and topography with elevation and slope aspect: A case study in the sky islands of southern Arizona. *Journal of Geophysical Research:Earth Surface*, *118*(2), 741–758. https://doi.org/Doi 10.1002/Jgrf.20046

Pelletier, J. D., Nichols, M. H., & Nearing, M. A. (2016). The influence of Holocene vegetation changes on topography and erosion rates: A case study at Walnut Gulch Experimental Watershed, Arizona. *Earth Surface Dynamics*, *4*(2), 471–488. https://doi.org/10.5194/esurf-4-471-2016

Pelletier, J. D., & Swetnam, T. L. (2017). Asymmetry of weathering-limited hillslopes: The importance of diurnal covariation in solar insolation and temperature. *Earth Surface Processes and Landforms*, *42*(9), 1408–1418. https://doi.org/10.1002/esp.4136

Perron, J. T. (2017). Climate and the Pace of Erosional Landscape Evolution Department of Earth , Atmospheric and Planetary Sciences Massachusetts Institute of Technology Short title : Climate and Landscape Evolution. *Annual Review of Earth and Planetary Sciences*, *45*, 1–71. https://doi.org/https://doi.org/10.1146/annurev-earth-060614-105405

Petherick, L., Bostock, H., Cohen, T. J., Fitzsimmons, K., Tibby, J., Fletcher, M. S., et al. (2013). Climatic records over the past 30 ka from temperate Australia – a synthesis from the Oz-INTIMATE workgroup. *Quaternary Science Reviews*, *74*, 58–77.

Petit, J. R., Jouzel, J., Raynaud, D., Barkov, N. I., Barnola, J.-M., Basile, I., et al. (1999). Climate and atmospheric history of the past 420,000 years from the Vostok ice core, Antarctica. *Nature*, *399*(6735), 429–436. https://doi.org/10.1038/20859

Phillips, J. D. (2016). Landforms as extended composite phenotypes. *Earth Surface Processes and Landforms*, *41*(1), 16–26. https://doi.org/10.1002/esp.3764

Pierce, J. L., Meyer, G. A., & Timothy Jull, A. J. (2004). Fire-induced erosion and millennial-scale climate change in northern ponderosa pine forests. *Nature*, *432*(7013),

87–90. https://doi.org/10.1038/nature03058

Porder, S. (2014). Coevolution of life and landscapes. *Proceedings of the National Academy of Sciences*, *111*(9), 3207–3208. https://doi.org/https://doi.org/10.1073/pnas.1400954111

Poulos, M. J., Pierce, J. L., Flores, A. N., & Benner, S. G. (2012). Hillslope asymmetry maps reveal widespread, multi-scale organization. *Geophysical Research Letters*, *39*(6). https://doi.org/10.1029/2012gl051283

Power, M. J., Marlon, J., Ortiz, N., Bartlein, P. J., Harrison, S. P., Mayle, F. E., et al. (2008). Changes in fire regimes since the Last Glacial Maximum: an assessment based on a global synthesis and analysis of charcoal data. *Climate Dynamics*, *30*(7–8), 887–907. https://doi.org/10.1007/s00382-007-0334-x

Priestley, C., & Taylor, R. (1972). On the Assessment of Surface Heat Flux and Evaporation Using Large-Scale Parameters'. *Monthly Weather Review*, *100*, 81–92. https://doi.org/https://doi.org/10.1175/1520-0493(1972)100<0081:OTAOSH>2.3.CO;2

Prosser, I. P., & Williams, L. (1998). The effect of wildfire on runoff and erosion in native Eucalyptus forest. *Hydrological Processes*, *12*(2), 251–265. https://doi.org/https://doi.org/10.1002/(SICI)1099-1085(199802)12:2<251::AID-HYP574>3.0.CO;2-4

Rasmussen, C., McGuire, L. A., Dhakal, P., & Pelletier, J. D. (2017). Coevolution of soil and topography across a semiarid cinder cone chronosequence. *Catena*, *156*, 338–352. https://doi.org/10.1016/j.catena.2017.04.025

Rasmussen, C., Pelletier, J. D., Troch, P. A., Swetnam, T. L., & Chorover, J. (2015). Quantifying Topographic and Vegetation Effects on the Transfer of Energy and Mass to the Critical Zone. *Vadose Zone Journal*, *14*(11). https://doi.org/10.2136/vzj2014.07.0102

Rasmussen, C., & Tabor, N. J. (2007). Applying a quantitative pedogenic energy model across a range of environmental gradients. *Soil Science Society of America Journal*, *71*(6), 1719–1729. https://doi.org/10.2136/sssaj2007.0051

Rasmussen, C., Troch, P. A., Chorover, J., Brooks, P. D., Pelletier, J. D., & Huxman, T. E. (2011). An open system framework for integrating critical zone structure and function.

Biogeochemistry, *102*(1–3), 15–29. https://doi.org/10.1007/s10533-010-9476-8

Rees, D. B. (1982). *A study of soils in the Reefton experimental area; with particular reference to hydrological properties*. Melbourne.

Reubens, B., Poesen, J., Danjon, F., Geudens, G., & Muys, B. (2007). The role of fine and coarse roots in shallow slope stability and soil erosion control with a focus on root system architecture: a review. *Trees*, *21*(4), 385–402. https://doi.org/10.1007/s00468-007-0132-4

Richardson, P. W. (2015). *Topographic Asymmetry and Climate Controls on Landscape Evolution*. Massachusetts Institute of Technology.

Riebe, C. S., Hahm, W. J., & Brantley, S. L. (2016). Controls on deep critical zone architecture: a historical review and four testable hypotheses. *Earth Surface Processes and Landforms*. https://doi.org/10.1002/esp.4052

Rodriguez-Iturbe, I. (2000). Ecohydrology : A hydrologic perspective of climate-soil-vegetation dynamics. *Water Resources Research*, *36*(1), 3–9. https://doi.org/https://doi.org/10.1029/1999WR900210

Rodriguez-Iturbe, I., D'Odorico, P., Porporato, A., & Ridolfi, L. (1999). On the spatial and temporal links between vegetation, climate, and soil moisture. *Water Resources Research*, *35*(12), 3709–3722. https://doi.org/10.1029/1999WR900255

Rodríguez-Iturbe, I., Power, B. F., & Valdés, J. B. (1987). Rectangular pulses point process models for rainfall: Analysis of empirical data. *Journal of Geophysical Research: Atmospheres*, *92*(D8), 9645–9656. https://doi.org/10.1029/JD092ID08P09645

Roering, J. J. (2008). How well can hillslope evolution models "explain" topography? Simulating soil transport and production with high-resolution topographic data. *Geological Society of America Bulletin*, *120*(9–10), 1248–1262. https://doi.org/10.1130/B26283.1

Roering, J. J., & Gerber, M. (2005). Fire and the evolution of steep, soil-mantled landscapes. *Geology*, *33*(5), 349–352. https://doi.org/10.1130/G21260.1

Roering, J. J., Kirchner, J. W., & Dietrich, W. E. (1999). Evidence for nonlinear, diffusive sediment transport on hillslopes and implications for landscape morphology. *Water*

Resources Research, *35*(3), 853–870. https://doi.org/10.1029/1998WR900090

Roering, J. J., Marshall, J., Booth, A. M., Mort, M., & Jin, Q. (2010). Evidence for biotic controls on topography and soil production. *Earth and Planetary Science Letters*, *298*(1), 183–190. https://doi.org/https://doi.org/10.1016/j.epsl.2010.07.040

Rutherfurd, I. D., Bishop, P., & Loffler, T. (1994). Debris flows in northeastern Victoria, Australia: occurrence and effects on the fluvial system. *IAHS Publications-Series of Proceedings and Reports-Intern Assoc Hydrological Sciences*, *224*, 359–372.

Saco, P. M., & Moreno-De Las Heras, M. (2013). Ecogeomorphic coevolution of semiarid hillslopes: Emergence of banded and striped vegetation patterns through interaction of biotic and abiotic processes. *Water Resources Research*, *49*(1), 115–126. https://doi.org/10.1029/2012WR012001

Saco, P. M., Willgoose, G. R., & Hancock, G. R. (2007). Eco-geomorphology of banded vegetation patterns in arid and semi-arid regions. *Hydrology and Earth System Sciences Discussions*, *11*(6), 1717–1730. https://doi.org/10.5194/hess-11-1717-2007

Saiz, G., Bird, M. I., Domingues, T., Schrodt, F., Schwarz, M., Feldpausch, T. R., et al. (2012). Variation in soil carbon stocks and their determinants across a precipitation gradient in West Africa. *Global Change Biology*, *18*(5), 1670–1683. https://doi.org/10.1111/j.1365-2486.2012.02657.x

Saxton, K. E., & Rawls, W. J. (2006). Soil Water Characteristic Estimates by Texture and Organic Matter for Hydrologic Solutions. *Soil Science Society of America Journal*, *70*(5), 1569. https://doi.org/10.2136/sssaj2005.0117

Schwanghart, W., & Scherler, D. (2014). Short Communication: TopoToolbox 2–MATLAB-based software for topographic analysis and modeling in Earth surface sciences. *Earth Surface Dynamics*, *2*(1), 1–7. https://doi.org/10.5194/esurf-2-1-2014

Scott, A. C., & Glasspool, I. J. (2006). The diversification of Paleozoic fire systems and fluctuations in atmospheric oxygen concentration. *Proceedings of the National Academy of Sciences*, *103*(29), 10861–10865. https://doi.org/10.1073/pnas.0604090103

Shakesby, R. A., Blakeb W. H, Doerr, S. H., Humphreys, G. S., Wallbrink, P. J., Chafer, C. J., et al. (2006). Hillslope soil erosion and bioturbation after the Christmas 2001 forest

fires near Sydney, Australia. *Soil Erosion and Sediment Redistribution in River Catchments: Measurement, Modelling and Management*, 51–61.

Shakesby, R. A., & Doerr, S. H. (2006). Wildfire as a hydrological and geomorphological agent. *Earth-Science Reviews*, *74*(3), 269–307. https://doi.org/10.1016/j.earscirev.2005.10.006

Shakesby, R. A., Shakesby, P. J., Wallbrink, S. H., Doerr, P. M., English, C. J., Chafer, G. S., et al. (2007). Distinctiveness of wildfire effects on soil erosion in south-east Australian eucalypt forests assessed in a global context. *Forest Ecology and Management*, *238*(1), 347–364. https://doi.org/10.1016/j.foreco.2006.10.029

Sharmeen, S., & Willgoose, G. R. (2006). The interaction between armouring and particle weathering for eroding landscapes. *Earth Surface Processes and Landforms*, *31*(10), 1195–1210. https://doi.org/10.1002/esp.1397

Shepard, C., Schaap, M. G., Crimmins, M. A., van Leeuwen, W. J. D., & Rasmussen, C. (2015). Subsurface soil textural control of aboveground productivity in the US Desert Southwest. *Geoderma Regional*, *4*, 44–54. https://doi.org/10.1016/j.geodrs.2014.12.003

Sheridan, G. J., Lane, P. N. J., & Noske, P. J. (2007). Quantification of hillslope runoff and erosion processes before and after wildfire in a wet Eucalyptus forest. *Journal of Hydrology*, *343*(1), 12–28. https://doi.org/10.1016/j.jhydrol.2007.06.005

Sheridan, G. J., Nyman, P., Langhans, C., Cawson, J., Noske, P. J., Oono, A., et al. (2016). Is aridity a high-order control on the hydro-geomorphic response of burned landscapes? *International Journal of Wildland Fire*, *25*(3), 262–267. https://doi.org/10.1071/WF14079

Sicart, J. E., Pomeroy, J. W., Essery, R. L. H., & Bewley, D. (2006). Incoming longwave radiation to melting snow: observations, sensitivity and estimation in Northern environments. *Hydrological Processes*, *20*(17), 3697–3708. https://doi.org/10.1002/hyp.6383

Sivapalan, M. (2003). Prediction in ungauged basins: a grand challenge for theoretical hydrology. *Hydrological Processes*, *17*(15), 3163–3170. https://doi.org/10.1002/hyp.5155

Slijepcevic, A., Anderson, W. R., & Matthews, S. (2013). Testing existing models for predicting hourly variation in fine fuel moisture in eucalypt forests. *Forest Ecology and Management*, *306*, 202–215. https://doi.org/10.1016/j.foreco.2013.06.033

Smith, H. G., Sheridan, G. J., Lane, P. N. J., & Bren, L. J. (2011a). Wildfire and salvage harvesting effects on runoff generation and sediment exports from radiata pine and eucalypt forest catchments, south-eastern Australia. *Forest Ecology and Management*, *261*(3), 570–581. https://doi.org/10.1016/j.foreco.2010.11.009

Smith, H. G., Sheridan, G. J., Lane, P. N. J., Noske, P. J., & Heijnis, H. (2011b). Changes to sediment sources following wildfire in a forested upland catchment, southeastern Australia. *Hydrological Processes*, *25*(18), 2878–2889. https://doi.org/https://doi-org.ezp.lib.unimelb.edu.au/10.1002/hyp.8050

Smith, H. G., Sheridan, G. J., Lane, P. N. j, Nyman, P., & Haydon, S. (2011c). Wildfire effects on water quality in forest catchments: A review with implications for water supply. *Journal of Hydrology*, *396*(1–2), 170–192. https://doi.org/10.1016/j.jhydrol.2010.10.043

Smith, H. G., Sheridan, G. J., Nyman, P., Child, D. P., Lane, P. N. J., Hotchkis, M. A. C., & Jacobsen, G. E. (2012). Quantifying sources of fine sediment supplied to post-fire debris flows using fallout radionuclide tracers. *Geomorphology*, *139*, 403–415. https://doi.org/https://doi.org/10.1016/j.geomorph.2011.11.005

Specht, R. L., & Wood, J. G. (1972). *The vegetation of South Australia, 2nd edition*. Adelaide, Ausralia: Government Printer.

Stern, H., de Hoedt, G., & Ernst, J. (2000). Objective classification of Australian climates. *Australian Meteorological Magazine*, *49*(2), 87–96.

Stockmann, U., Minasny, B., & McBratney, A. B. (2014). How fast does soil grow? *Geoderma*, *216*, 48–61. https://doi.org/10.1016/j.geoderma.2013.10.007

Stromsoe, N., Marx, S., Callow, N., McGowan, H., & Heijnis, H. (2016). Estimates of late Holocene soil production and erosion in the Snowy Mountains, Australia. *Catena*, *145*, 68–82. https://doi.org/https://doi.org/10.1016/j.catena.2016.05.013

Suresh, P. O., Dosseto, A., Hesse, P. P., & Handley, H. K. (2014). Very long hillslope

transport timescales determined from uranium-series isotopes in river sediments from a large, tectonically stable catchment. *Geochimica et Cosmochimica Acta*, *142*, 442–457. https://doi.org/https://doi.org/10.1016/j.gca.2014.07.033

Tarpanelli, A., Franchini, M., Brocca, L., Camici, S., Melone, F., & Moramarco, T. (2012). A simple approach for stochastic generation of spatial rainfall patterns. *Journal of Hydrology*, *472*, 63–76. https://doi.org/10.1016/j.jhydrol.2012.09.010

Taufik, M., Torfs, P. J. J. F., Uijlenhoet, R., Jones, P. D., Murdiyarso, D., & Lanen, H. A. J. Van. (2017). Amplification of wildfire area burnt by hydrological drought in the humid tropics. *Nature Climate Change*, *7*, 428–433. https://doi.org/10.1038/NCLIMATE3280

Temme, A. J. A. M., & Vanwalleghem, T. (2016). LORICA – A new model for linking landscape and soil profile evolution: Development and sensitivity analysis. *Computers & Geosciences*, *90*, 131–143. https://doi.org/10.1016/j.cageo.2015.08.004

Tesemma, Z. K., Wei, Y., Western, A. W., & Peel, M. C. (2014). Leaf area index variation for cropland, pasture and tree in response to climatic variation in the Goulburn-Broken catchment, Australia. *Journal of Hydrometeorology*, *15*, 1592–1606. https://doi.org/10.1175/JHM-D-13-0108.1

Thomas, P. B., Watson, P. J., Bradstock, R. A., Penman, T. D., & Price, O. F. (2014). Modelling surface fine fuel dynamics across climate gradients in eucalypt forests of south-eastern Australia. *Ecography*, *37*(9), 827–837. https://doi.org/10.1111/ecog.00445

Thompson, J. N., & Cunningham, B. M. (2002). Geographic structure and dynamics of coevolutionary selection. *Nature*, *417*(6890), 735–738. https://doi.org/10.1038/nature00810

Thompson, S. E., Harman, C. J., Heine, P., & Katul, G. G. (2010). Vegetation-infiltration relationships across climatic and soil type gradients. *Journal of Geophysical Research: Biogeosciences*, *115*(G2). https://doi.org/10.1029/2009JG001134

Troch, P. A., Carrillo, G., Sivapalan, M., Wagener, T., & Sawicz, K. (2013). Climate-vegetation-soil interactions and long-term hydrologic partitioning: signatures of catchment co-evolution. *Hydrology and Earth System Sciences Discussions*, *10*(3), 2927–2954.

Troch, P. A., Lahmers, A., Meira, R., Mukherjee, J. W., Pedersen, T., Roy, R., & Valdés, P. (2015). Catchment coevolution: A useful framework for improving predictions of hydrological change? *Water Resources Research*, *51*(7), 4903–4922.

Tromp-van Meerveld, H. J., & McDonnell, J. J. (2006). On the interrelations between topography, soil depth, soil moisture, transpiration rates and species distribution at the hillslope scale. *Advances in Water Resources*, *29*(2), 293–310. https://doi.org/10.1016/j.advwatres.2005.02.016

Trouvé, R., Nitschke, C. R., Robinson, A. P., & Baker, P. J. (2017). Estimating the self-thinning line from mortality data. *Forest Ecology and Management*, *402*, 122–134. https://doi.org/10.1016/j.foreco.2017.07.027

Tucker, G. E., Gasparini, N. ., Bras, R. L., & Lancaster, S. L. (1999). A 3D computer simulation model of drainage basin and floodplain evolution: theory and applications. *Technical Report Prepared for U.S. Army Corps of Engineers Construction Engineering Research Laboratory*.

Tucker, G. E., & Hancock, G. R. (2010). Modelling landscape evolution. *Earth Surface Processes and Landforms*, *35*(1), 28–50.

Tucker, G., Lancaster, S., Gasparini, N., & Bras, R. (2001). The Channel-Hillslope Integrated Landscape Development Model (CHILD). In *Landscape Erosion and Evolution Modeling* (pp. 349–388). Boston, MA: Springer US. https://doi.org/10.1007/978-1-4615-0575-4_12

Van der Sant, R. E. (2016). *Aridity index as a predictor of the hydrogeomorphic response of burnt landscapes*. University of Melbourne.

Van Dijk, A. I. J. M., Gash, J. H., Van Gorsel, E., Blanken, P. D., Cescatti, A., Emmel, C., et al. (2015). Rainfall interception and the coupled surface water and energy balance. *Agricultural and Forest Meteorology*, *214–215*, 402–415. https://doi.org/10.1016/j.agrformet.2015.09.006

van Wijk, M. T., & Rodriguez-Iturbe, I. (2002). Tree-grass competition in space and time: Insights from a simple cellular automata model based on ecohydrological dynamics. *Water Resources Research*, *38*(9), 15–18.

Verboom, W. H., & Pate. (2013). Exploring the biological dimension to pedogenesis with emphasis on the ecosystems, soils and landscapes of southwestern Australia. *Geoderma*, *211*, 154–183. https://doi.org/https://doi.org/10.1016/j.geoderma.2012.03.030

Vertessy, R. A., Watson, F. G. R., & Sharon, K. O. (2001). Factors determining relations between stand age and catchment water balance in mountain ash forests. *Forest Ecology and Management*, *143*(1), 13–26. https://doi.org/https://doi.org/10.1016/S0378-1127(00)00501-6

Vertessy, R., Watson, F., O 'sullivan, S., Davis, S., Campbell, R., Benyon, R. G., & Haydon, S. (1998). *Predicting Water Yield From Mountain Ash Forest Catchments*. Clayton, Melbourne. Retrieved from http://ewater.org.au/archive/crcch/archive/pubs/pdfs/industry199804.pdf

Volkova, L., Bi, H., Murphy, S., & Weston, C. J. (2015). Empirical Estimates of Aboveground Carbon in Open Eucalyptus Forests of South-Eastern Australia and Its Potential Implication for National Carbon Accounting. *Forests*, *6*(10), 3395–3411. https://doi.org/10.3390/f6103395

Wagenbrenner, J. W., Robichaud, P. R., & Elliot, W. J. (2010). Rill erosion in natural and disturbed forests: 2. Modeling approaches. *Water Resources Research*, *46*(10).

Wagener, T., Sivapalan, M., Troch, P. A., McGlynn, B. L., Harman, C. J., Gupta, H. V., et al. (2010). The future of hydrology: An evolving science for a changing world. *Water Resources Research*, *46*(5), W05301. https://doi.org/10.1029/2009WR008906

Walling, D. E., & He, Q. (1999). Improved Models for Estimating Soil Erosion Rates from Cesium-137 Measurements. *Journal of Environment Quality*, *28*(2), 611. https://doi.org/10.2134/jeq1999.00472425002800020027x

Walsh, S. F., Nyman, P., Sheridan, G. J., Baillie, C. C., Tolhurst, K. G., & Duff, T. J. (2017). Hillslope-scale prediction of terrain and forest canopy effects on temperature and near-surface soil moisture deficit. *International Journal of Wildland Fire*, *26*(3), 191–208. https://doi.org/10.1071/WF16106

Wellman, P. (1987). Eastern highlands of Australia; their uplift and erosion. *Journal of Australian Geology & Geophysics*, *10*, 277–286.

West, N., Kirby, E., Bierman, P. R., & Clarke, B. A. (2014). Aspect-dependent variations in regolith creep revealed by meteoric 10Be. *Geology*, *42*(6), 507–510. https://doi.org/10.1130/G35357.1

White, A. F., & Blum, A. E. (1995). Effects of climate on chemical_ weathering in watersheds. *Geochimica et Cosmochimica Acta*, *59*(9), 1729–1747. https://doi.org/https://doi.org/10.1016/0016-7037(95)00078-E

Whitehead, D., & Beadle, C. L. (2004). Physiological regulation of productivity and water use in Eucalyptus: a review. *Forest Ecology and Management*, *193*(1), 113–140. https://doi.org/https://doi.org/10.1016/j.foreco.2004.01.026

Wilkinson, M. T., Richards, P. J., & Humphreys, G. S. (2009). Breaking ground: pedological, geological, and ecological implications of soil bioturbation. *Earth-Science Reviews*, *97*(1), 257–272. https://doi.org/10.1016/j.earscirev.2009.09.005

Willgoose, G., Bras, R. L., & Rodriguez Iturbe, I. (1991a). A coupled channel network growth and hillslope evolution model: 1. Theory. *Water Resources Research*, *27*(7), 1671–1684. https://doi.org/10.1029/91WR00935

Willgoose, G., Bras, R. L., & Rodriguez Iturbe, I. (1991b). A physical explanation of an observed link area-slope relationship. *Water Resources Research*, *27*(7), 1697–1702. https://doi.org/10.1029/91WR00937

Williams, C., & Albertson, J. (2005). Contrasting short- and long-timescale effects of vegetation dynamics on water and carbon fluxes in water-limited ecosystems. *Water Resources Research*, *41*(6). https://doi.org/https://doi.org/10.1029/2004WR003750

Wilson, C. J. (1999). Effects of logging and fire on runoff and erosion on highly erodible granitic soils in Tasmania. *Water Resources Research*, *35*(11), 3531–3546. https://doi.org/10.1029/1999WR900181

Yetemen, O., Istanbulluoglu, E., & Duvall, A. (2015a). Solar radiation as a global driver of hillslope asymmetry: Insights from an ecogeomorphic landscape evolution model. *Water Resources Research*, *51*(12), 9843–9861. https://doi.org/10.1002/ 2015WR017103

Yetemen, O., Istanbulluoglu, E., Flores-Cervantes, J. H., Vivoni, E. R., & Bras, R. L. (2015b). Ecohydrologic role of solar radiation on landscape evolution. *Water Resources*

Research, *51*(2), 1127–1157. https://doi.org/doi:10.1002/2014WR016169

Yetemen, O., Istanbulluoglu, E., & Vivoni, E. R. (2010). The implications of geology, soils, and vegetation on landscape morphology: Inferences from semi-arid basins with complex vegetation patterns in Central New Mexico, USA. *Geomorphology*, *116*(3), 246–263. https://doi.org/10.1016/j.geomorph.2009.11.026

Yoshida, T., & Troch, P. A. (2016a). A process-based diagnosis of catchment coevolution in volcanic landscapes: synthesis of Newtonian and Darwinian approaches. *Hydrology and Earth System Sciences Discussions*, (July), 1–20. https://doi.org/10.5194/hess-2016-263

Yoshida, T., & Troch, P. A. (2016b). Coevolution of volcanic catchments in Japan. *Hydrology and Earth System Sciences*, *20*(3), 1133. https://doi.org/10.5194/hess-20-1133-2016

Young, M. H., McDonald, E. V., Caldwell, T. G., Benner, S. G., & Meadows, D. G. (2004). Hydraulic Properties of a Desert Soil Chronosequence in the Mojave Desert, USA. *Vadose Zone Journal*, *3*(3), 956. https://doi.org/10.2136/vzj2004.0956

Zhang, L., Hickel, K., Dawes, W. R., Chiew, F. H. S., Western, A. W., & Briggs, P. R. (2004). A rational function approach for estimating mean annual evapotranspiration. *Water Resources Research*, *40*(2). https://doi.org/10.1029/2003WR002710

Zhou, X., Istanbulluoglu, E., & Vivoni, E. R. (2013). Modeling the ecohydrological role of aspect-controlled radiation on tree-grass-shrub coexistence in a semiarid climate. *Water Resources Research*, *49*(5), 2872–2895. https://doi.org/https://doi.org/10.1002/wrcr.20259

9 Appendices

Appendix I Supplementary material for chapter 2

I.1 Introduction

The first two sections in the supporting information comes as an aid to the methods section in Chapter 2 and includes a Digital Elevation Model (DEM) Quality analysis for the Slope-Area (S-A) curves (Figure 2-2) and for Hillslope Asymmetry Index (*HAI*) calculation (Figure 2-3c); and a description of the method used in calculating the "expected" soil depth asymmetry index (*SAI*; Figure 2-3b). The closing figure is composed of three satellite images (Nearmap 2017) that illustrates the differences in vegetation between equatorial (north) and polar (south) facing hillslopes across a rainfall gradient

I.2 DEM quality for the S-A Analysis

Data for the S-A curves for the wet and damp focus sites was acquired by resampling of a ground surface DEM of 1m airborne light detection and ranging (lidar) into a 10m grid. The airborne lidar was acquired on 2007-2008 on a campaign made possible by Department of Environment, Land, Water and Planning (DELWP; former Victorian Department of Environment and Primary Industries) at an average density of 0.9 points per meter with a vertical and horizontal accuracy of 35 cm and 50 cm respectively. Due to the scarcity of lidar data, no lidar coverage was available for dry areas within the Norton Gully Sandstone formation, thus a lower quality 10m DEM was used for the S-A analysis for this specific location. The lower-quality DEM was provided by DELWP, and comprises of several methods of acquisition, aggregated into a 10m DEM. By comparing the two types of DEM in locations where both were available, the lidar derived 10m DEM was generally steeper than the lower-quality one, however, the shape and difference in median slope of the gradient (to derive the Hillslope Asymmetry Index) were similar. Nevertheless, the S-A analysis (Figure 2-2 in the chapter) is used here with cation as a visual aid rather than a quantitative metric.

I.2.1 Normalizing DEM Quality

Similar as for the S-A curves, same two DEM types were used for *HAI* calculations. In order to normalize the output of the two DEM types, *HAI* for 32 locations overlapping the two DEM types, was calculated and plot together in order to produce a function that can be used for normalization (Figure A- I-1). Out of the 81 DEMs analysed, HAI of 49 were normalized using $\mathrm{HAI_{lq}} = 1.04\,\mathrm{HAI_{li}} - 0.01$, where $\mathrm{HAI_{lq}}$ and $\mathrm{HAI_{li}}$ are HAI for lower-quality and lidar derived DEM types, respectively.

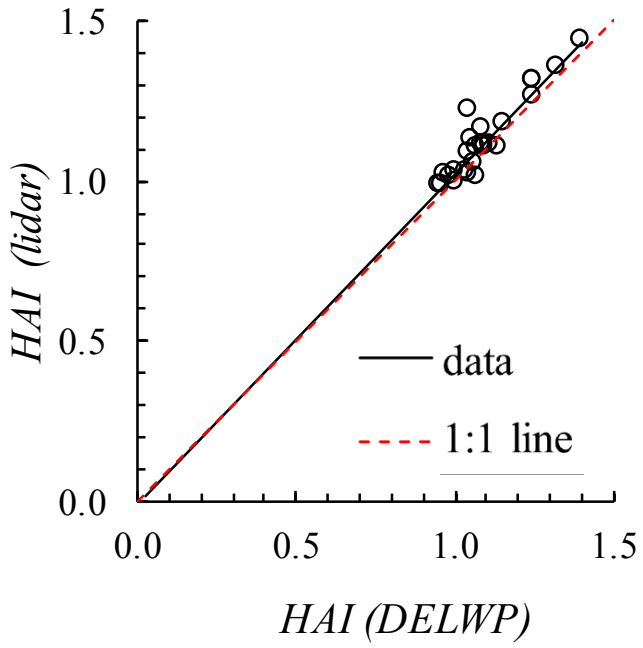

Figure A- I-1 - Comparison between the *HAI* Values obtained from the lower-quality and the lidar derived DEM (R^2=0.87).

I.3 Calculating "expected" soil depth asymmetry index (SAI)

An analytical solution for expected SAI values (Figure 2-3b) was made by combining Eqn 2.1 and SAI, and is presented as a dashed line in Figure 2-3b. The purpose is to have a continuous estimation of SAI with AI within the domain. A function that relates the change in mean AI ($\overline{\mathrm{AI}}$) for north and south aspects ($\partial\overline{\mathrm{AI}_\mathrm{e}}$ and $\partial\overline{\mathrm{AI}_\mathrm{p}}$, respectively), was derived using AI data extracted for seven 5x5 km square polygons of downscaled AI layer (Nyman et al., 2014b) across an rainfall gradient. For each polygon $\overline{\mathrm{AI}_\mathrm{e}}$ and $\overline{\mathrm{AI}_\mathrm{p}}$ were calculated by

averaging all the pixels within north and south facing aspect bins (i.e., 270°-90° and 90°-270°, respectively). Areas larger than 0.1 km^2 and slope gradient larger outside the range 5° -45° were removed from the calculation. $\overline{AI_e}$ and $\overline{AI_p}$ were plotted as a function of $\overline{AI}$ (Figure A-I-2). Best fit for each aspect derived the functions (R^2=0.99): $\overline{AI_e} = 1.19\,\overline{AI} - 0.02$ for north facing hillslopes; and $\overline{AI_p} = 0.89\,\overline{AI} - 0.02$ for south facing hillslopes.

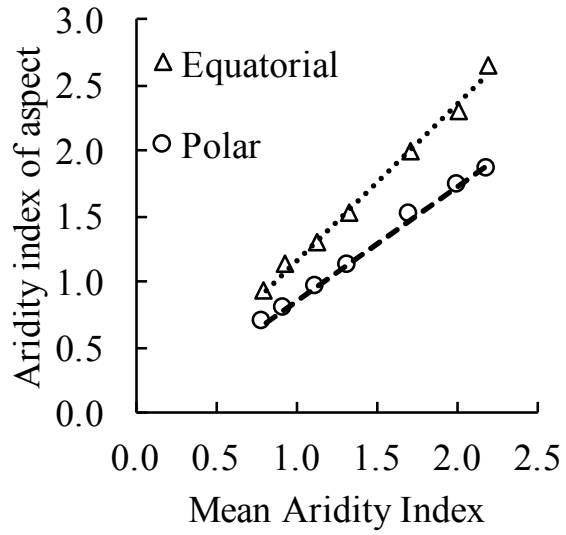

Figure A- I-2 - AI value for each aspect as a function of mean AI for seven 5x5 km square polygons under an AI gradient. The difference between the AI between the aspects increases with mean AI despite the overall reduction in slope (Table 2-1) is due to higher direct/diffuse radiation ratio in lower elevations (Nyman et al., 2014b).

The hypothetical AI values for each aspect for a given $\overline{AI}$ were then used in Eqn. 2.1 to calculate hypothetical soil depths, which were then used to calculate the expected SAI as a function of $\overline{AI}$ (Figure 2-3).

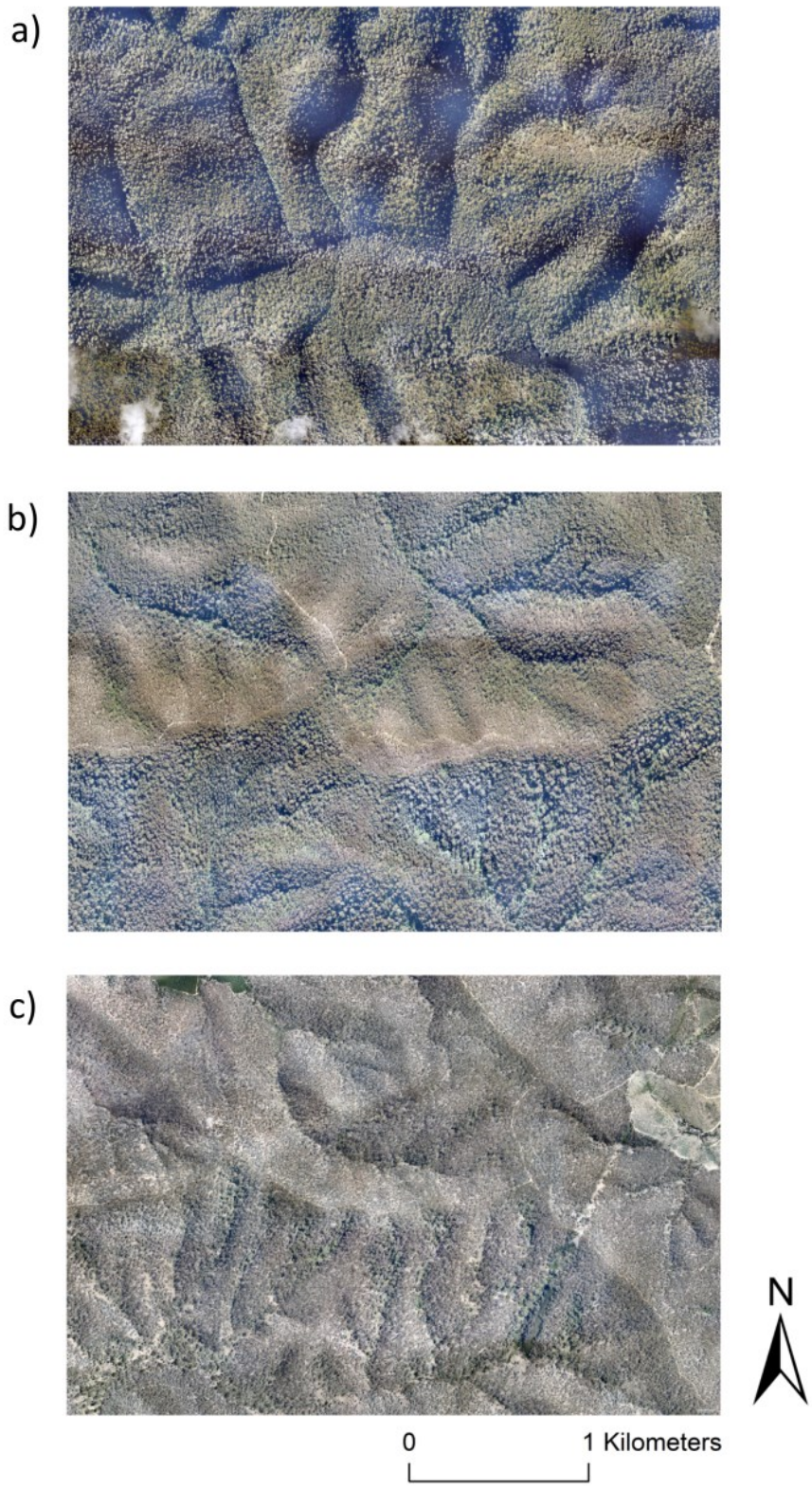

Figure A- I-3 - Example illustrating vegetation differences between south (polar) and north (equatorial) facing hillslopes across an aridity gradient across the Eastern Uplands using Nearmap, 2017. In the wet site (a), vegetation is dense and the differences in vegetation between the aspects is barely noticeable. On the damp site (b) vegetation on the south facing

hillslope is dense, while on the north facing hillslope is relatively sparse. The dry site (c) vegetation is relatively sparse overall, and differences in vegetation between south and north facing aspects are noticeable.

Appendix II Theory and calibration of the fire model

II.1 - Theory and equations

The method is based on the assumption that mean soil moisture at a site can be considered as a proxy for flammability (i.e., probability of a site to be ignited due to the dryness state of the combustible fuel (Nyman et al., 2015a; Walsh et al., 2017). This assumption is based on the fact that probability of fire is higher when plant water stress is higher, indicating that evapotranspiration levels are reduced due to lack of moisture in the litter/soil system (Finkele et al., 2006). Higher fire probability conditions are more frequent in dry areas, where soils are thin and canopy cover is low, allowing increased evaporation from the litter/soil system, and vice versa (Cheal, 2010).

II.2 - Model description

The method defines a daily cutoff value for soil moisture (s_{cut}), below which a site is considered to be under water stress. The annual probability for water deficit (P_{wd}) is then calculated by dividing the number of days that the soil moisture was below s_{cut}:

$$P_{wd} = \frac{\bar{s}}{365} \tag{3.43}$$

where $\bar{s}$ is the number of days in which soil moisture will be below the cutoff [s_{cut} $\bar{s} = \sum_{365}^{DOY=1}(s \leq s_{cut})$].

Every year, at the 1st of January, the model calculates fire probability (P_f), using P_{wd} using the following linear function (Appendix II):

$$\mathrm{P_f} = \kappa_\mathrm{f}\, \mathrm{P_{wd}} + \delta \tag{3.42}$$

where κ_f and δ are calibration parameters (0.1469 and 0.0015, respectively).

Every year, an ignition probability (σ) is calculated using random number generator. When $\sigma \leq \mathrm{P_f}$ a severe fire occurs, altering some key system properties as a response.

II.3 - Calibration process

II.3.1 - Fire return interval

The average fire return interval between forest types is believed to differ substantially (Cheal, 2010), however defining accurately it for a given forest type is almost impossible. A rough estimate of the average fire cycle had been used in fire management in order to estimate the tolerable (i.e. minimum and maximum) fire interval based on key fire-response species (Kennedy & Jamieson, 2007). Table A- II-1 presents average fire cycle (AFC) for selected Ecological Vegetation Classes (EVC) in Victoria, which are compared to the EVC of the ten grounding sites. Since the both EVCs did not exactly align, the sites were grouped into the closest category defined by *Kennedy and Jamieson* (2007) as detailed in Appendix II . In order to achieve a relationship between the AFC and aridity, mean aridity values were calculated for all the sites within one EVC definition.

Table A- II-1 - Average Fire Cycle estimation for the sites based on the EVC categories defined by *Kennedy and Jamieson*, (2007).

K&J[*1] (2007) EVC category	Sites estimated to be within K&J[*1] (2007) EVC category	EVC type of sites	Mean aridity[*3]	AFC estimation
				[yr]
Heathy dry forest/Shrubby dry forest	ELD north, CH south	Grassy dry forest	2.4	20
Herb-rich foothill forest	ELD north, CH south, RT north	Herb-rich foothill forest	1.77	30
Damp Forest	RT South, FS South[*2]	Damp forest, Wet forest	1.04	60[*4]
Wet Forest	TT north, RT south[*2]	Wet forest	0.96	70
Cool Temperate Rainforest	TT south, FS north	Cool Temperate Rainforest/ Montane wet forest/ Montane damp forest	0.81	100

[*1] (Kennedy & Jamieson, 2007)

[*2] Reefton RT south was classified as both Damp and Wet forest, and was used in both categories

[*3] mean aridity of all the sites within the category

[*4] (McCarthy et al., 1999)

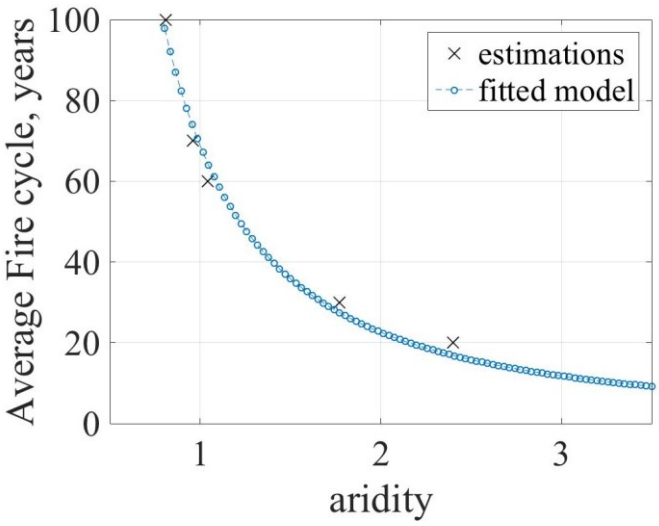

Figure A- II-1 - Site estimates and fitted plot of the Average Fire Cycle as a function of aridity.

Using the best fit for the data in Figure A- II-1, the following function was used in order to calculate the AFC for each of the sites:

$$AFC = 68.75\ aridity^{-1.605} \qquad \text{(AII-1)}$$

II.3.2 - Determining soil moisture deficit cutoff

The model calculates degree of saturation (s) in daily time steps, whereas s values constrain daily ET (Eqn 3.31 and 3.32). Long term (~10k years) modelled mean annual probability of water deficit occurrences ($\overline{P_{wd}}$) for each of the six sites (ELD north and south, RT north and south and FS north and south) were calculated for different water deficit cutoff values (s_{cut}; varying between s_w and s^*), under steady state conditions (i.e., no change in soil depth) (Figure A- II-3).

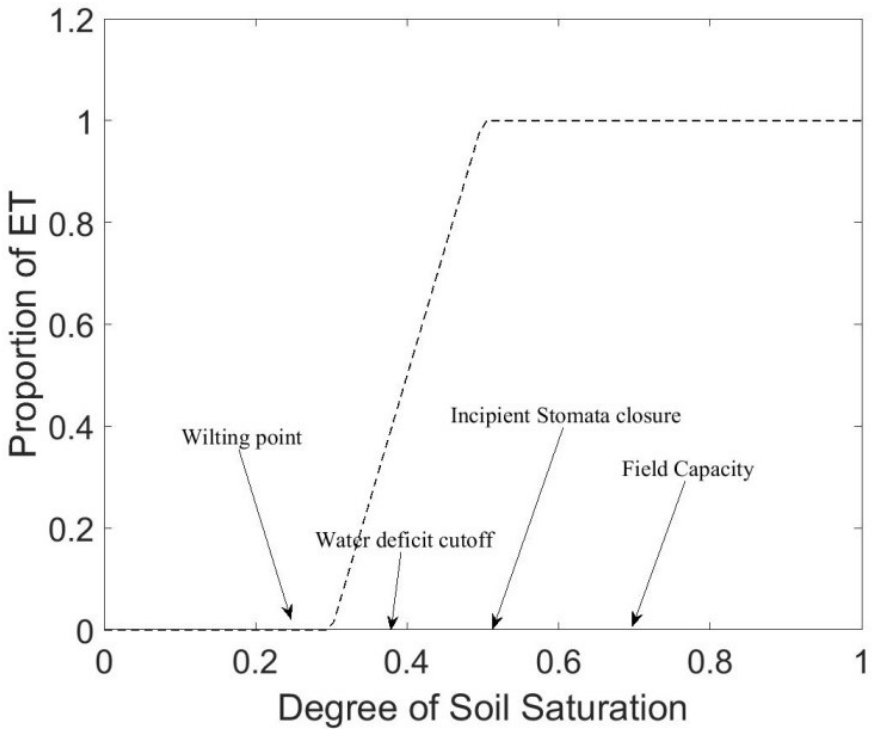

Figure A- II-2- A schematic representation of the way the actual ET is calculated as a proportion of potential ET, using the degree of soil saturation. For simplicity, degree of saturation at: wilting point (s_w), incipient stomata closure (s^*) and field capacity (s_{cap}); and porosity (n) were assumed constant within the domain, regardless of climatic forcing. Water deficit cutoff (s_{cut}) was assumed to be somewhere between s_w and s^* values.

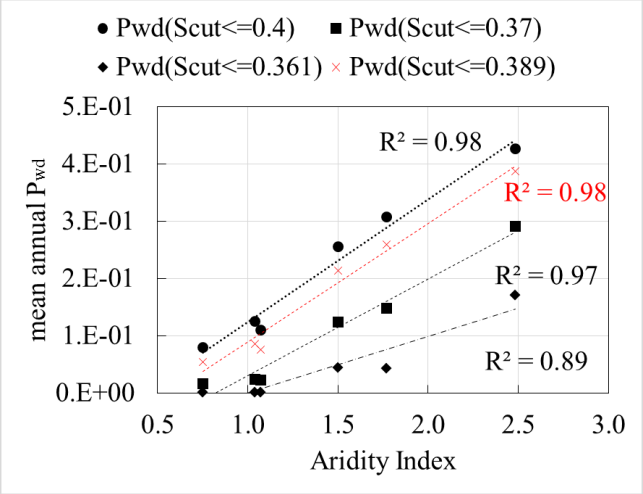

Figure A- II-3 - Modelled mean annual probability of water deficit occurrences ($\overline{P_{wd}}$) for each of the six sites for different s_{cut} values. Data in red represent the selected $\overline{s_{cut}}$ value.

In order to select an appropriate cutoff value ($\overline{s_{cut}}$), an assumption was posed that the ratio between the long term $\overline{P_{wd}}$ at the dry site and that of the wet site for a given s_{cut} (i.e., $\overline{P_{wd}}_{Scut \leq n}$), is expected to be similar to the ratio between fire frequency between these sites. The ratio between the $\overline{P_{wd}}$ of the sites at the two climatic extremes ($r_{P_{wd}}$) for a given s_{cut} value is calculated by:

$$r_{P_{wd}} = \frac{\overline{P_{wd}}_{Scut \leq n_{driest}}}{\overline{P_{wd}}_{Scut \leq n_{wettest}}} \quad \text{(AII-2)}$$

The value $r_{P_{wd}}$ signifies the how higher is the probability of the soil at the dry site to be in water deficit compared that of the wet site, for a given s_{cut} value. The ratio between average fire cycle of the driest to that of the wettest (r_{RI}) is calculated using:

$$r_{RI} = \frac{AFC_{driest}}{AFC_{wettest}} \quad \text{(AII-3)}$$

where AFC_{driest} and $AFC_{wettest}$ were calculated using Eqn AII-1. The value for r_{RI} signifies how higher is the fire return interval of the driest site (Eildon North; AI 2.49) than that of the wettest site (Frenchman's Spur; AI 0.75), and was found to be 6.84.

Figure A- II-4 shows several $r_{P_{wd}}$ values as a function of the respective s_{cut} value used for this calculation by running the model for 10kyr in calibration mode, for driest and wettest sites. Then, the function from the best fit was solved using $r_{RI} = 6.84$ in order to find the wanted $\overline{s_{cut}}$ value, 0.389.

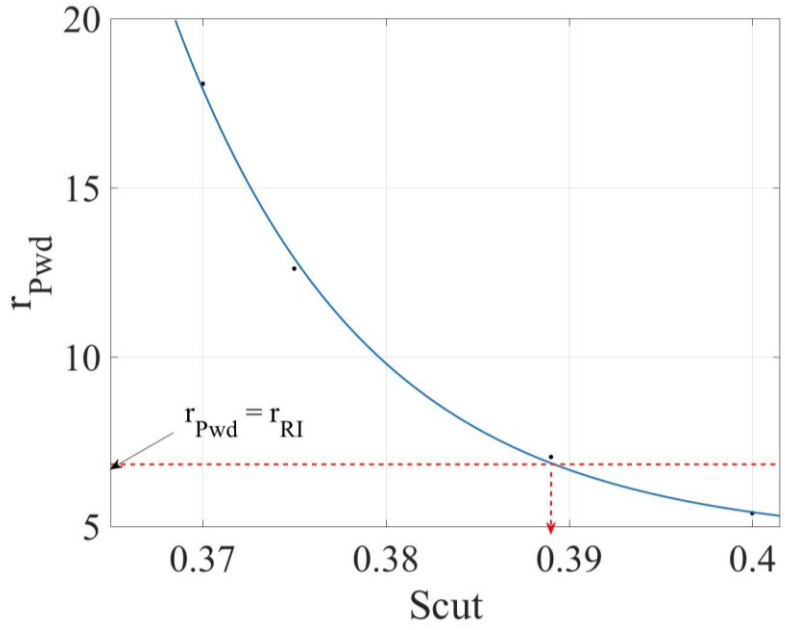

Figure A- II-4 - The ratio between the mean annual probabilities of water deficit occurrences ($r_{P_{wd}}$) of the dry site ($\overline{P_{wd}}_{driest}$) by that of the wet sites ($\overline{P_{wd}}_{wettest}$), as a function of different s_{cut} values. The dashed red line represents the $r_{P_{wd}}$ which is equal to the ratio between the fire frequency of the dry site with that of the wet one (r_{RI}), which is 6.84 (both calculated using using Eqn AII-1)

II.3.3 Calculating fire probability, P_f

Practically, the model counts the number of days which soil moisture (degree of saturation, *s*) is below $\overline{s_{cut}} = 0.389$ to get annual P_{wd} value Eqn 3.43, which is then used to calculate fire probability (*Pf*; Eqn 3.42). values were plotted against fire probability for the 6 sites, calculated by $1/AFC$ (calculated using Eqn AII-1). Modelled $\overline{P_{wd}}$ values (after a 10kyr simulation in calibration mode) for the all the parameterisation sites using $s_{cut} = 0.389$ and optional trend lines, are presented in Table A II-1 and Figure A- I-1.

Table A II-1 - Modelled $\overline{P_{wd}}$ values for the all the parameterisation sites using $s_{cut} = 0.389$

Site name	aspect	aridity	Fire probability*1	*AFC**2	$\overline{P_{wd}}$ using ($\overline{s_{cut}} \leq$ 0.389)
				[yr]	
Frenchman's Spur	S	0.75	9.16E-03	109.23	5.50E-02
	N	1.07	1.62E-02	61.67	7.62E-02
Upper Yarra	S	1.04	1.55E-02	64.58	8.66E-02
	N	1.50	2.79E-02	35.80	2.14E-01
Eildon	S	1.77	3.63E-02	27.56	2.60E-01
	N	2.49	6.26E-02	15.96	3.88E-01

*1 calculated using $1/AFC$ using Eqn. AII-1.

*2 calculated using Eqn AII-1 for each site

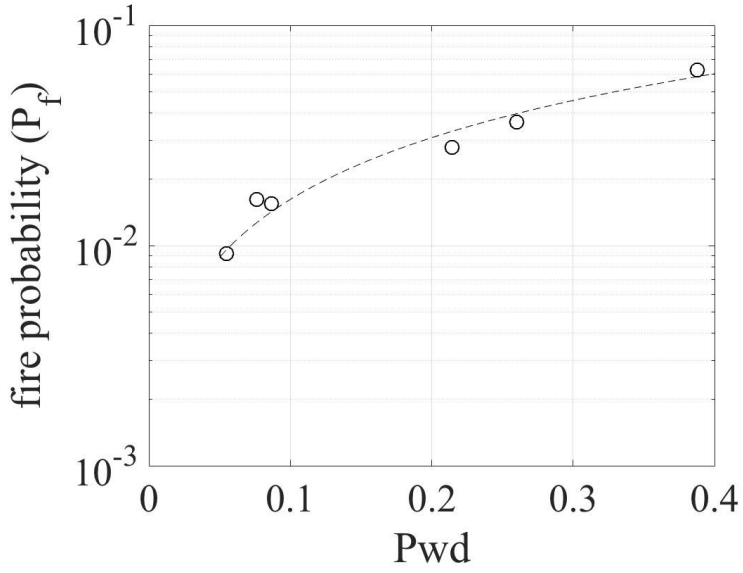

Figure A- II-5 - Modelled $\overline{P_{wd}}$ values for the parameterisation sites using $\overline{s_{cut}} = 0.389$. line represents the best fit (Eqn 3.42) for the model (linear) after validation of modelled results (R^2=0.96; RMSE=0.004).

A linear fit (R^2=0.96; RMSE=0.004) was chosen to represent the relationship between Pwd and Pf (Eqn 3.42) over several other alternatives. The primary reason for choosing a linear function was in order to have a finite (even if low) Pf when *Pwd*=0. Theoretically, *Pwd* could be 0 in wet sites when the soil moisture never gets below *Scut=0.389*. In this case, *Pf* would

be 0.0015 and fire frequency would be roughly equal to *1/Pf*=666.67 years. This is argued to be a logical fire frequency for a very wet site (i.e., temperate rainforest, (Cheal, 2010)), and represent a fire that occurs despite an extreme wet conditions in the site which could be generated due to severe fire weather and an intense fire that goes through a relatively wet site. Furthermore, the linear model was found to have the lowest RMSE (Figure A- II-6a) when validated against two other function types (exponential and linear with b=0) in predicting the "observed" fire frequencies for the 6 sites as detailed in Table A II-1.

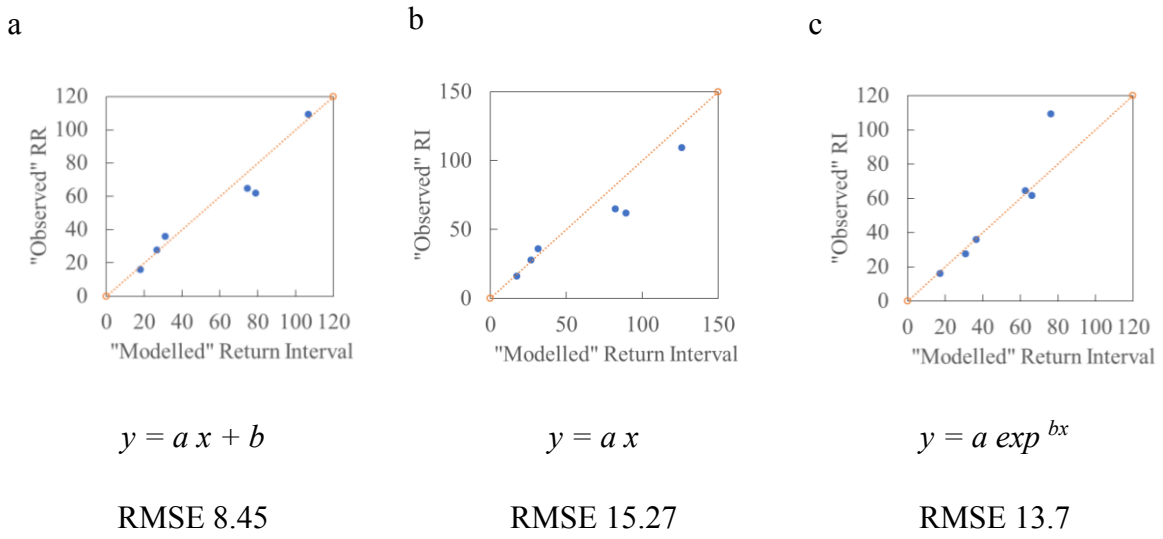

Figure A- II-6 - Module validation. The modelled fire return interval (RI) was calculated by counting the number of fires using both models ("old" and "new") in a 100k year simulation. Here, the "old" model represents the "observed" return interval as it is derived from the data in Table A- II-1.

Appendix III Calibration of NSRP model

Simulated rainfall is fed into the model by using the single-site Neyman-Scott Rectangular Pulse (NSRP) model (Cowpertwait et al., 1996). Previous work has shown that the model is capable of preserving statistical properties of rainfall time series over a range of time scales (Rodríguez-Iturbe et al., 1987). The model uses five parameters: it assumes that the storm origin follow a Poissonian process with parameter λ, with random number of call origins (C). Each storm is displaced independently from the origin by distances that are exponentially distributed with parameter β. A rectangular pulse is associated with each cell origin, with duration that is represented by an independent exponential random variable (η) with intensity X. A method proposed and coded by *Camici et al.* (2011) is used in order to simulate hourly rainfall using measured rainfall data. Sites that that were used for the calibration of the NSRP model were chosen using the following criteria: (i) represent a gradient in rainfall suitable for simulations within the climatic/spatial domain; (ii) the least number of years with intact rainfall data; and (iii) be within a reasonable range in mean hourly rainfall (after removing *zero* values). The last criteria was chosen due to the high sensitivity of the model to rainfall intensity (data no shown).

Table A- III-1– Hourly rainfall data source for calibration of the NSRP model.

Site name	Source Data	Number of full data years	Mean annual precipitation	Mean hourly rainfall
			[mm]	[mm/h]
Rocklands Reservoir	Bureau of Meteorology	42	542	1.26
Christmas Hills	Melbourne Water	38	721	1.35
Mt. St. Leonard	Melbourne Water	30	942	1.32
Noojee	Bureau of Meteorology	19	1261	1.46
Myrrhee	Melbourne Water	24	1610	1.47

The calibration method produces the five parameters described above for each month from analysis of the measured rainfall, and generate simulated rainfall for predefined number of years. Details about the NSRP model and its parameters could be found in *Cowpertwait et al* (1996). Simulated rainfall was generated by a code downloaded for this purpose (Camici et al., 2011; Tarpanelli et al., 2012) and was used to simulate 1000 year simulations using the calibration data (Table A- II-1) The accuracy of the model is tested by analysing the statistical properties used in the calibration process. Figure A- III-1 - Figure A- III-10 show the model performance for each site listed in Table A- II-1. Results show that, overall, model simulations reasonably predicts observed parameters.

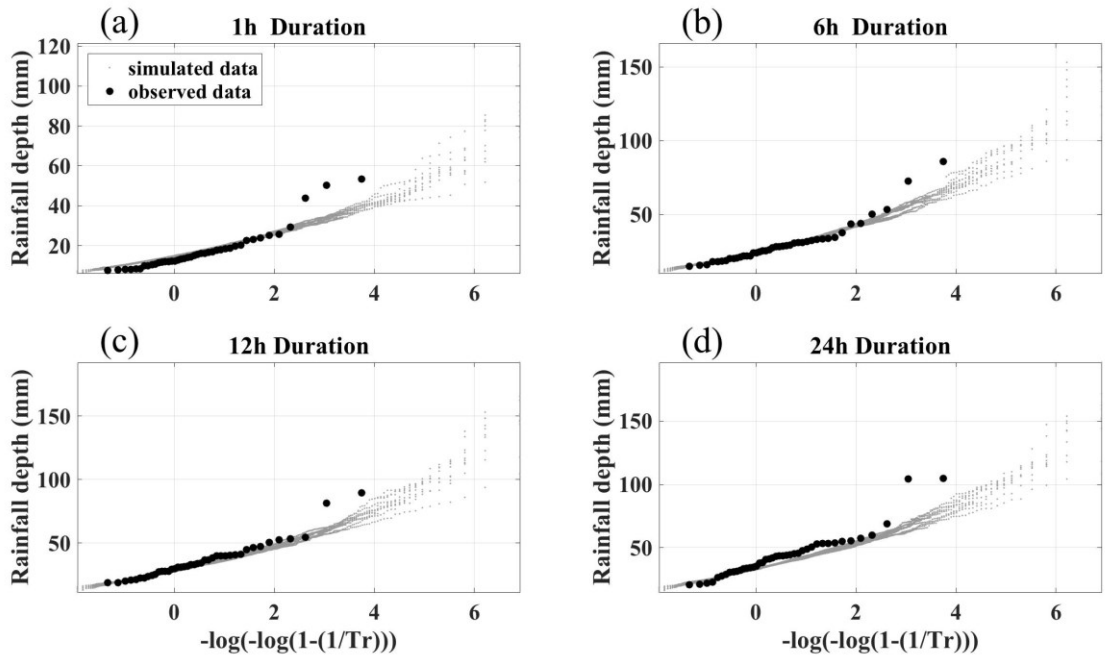

Figure A- III-1– Comparison of return period (Tr) of extreme events (as rainfall maxima values) at four different time aggregations (1, 6, 12 and 24h) between observed and modelled values, calibrated using hourly rainfall data from *Rockland Reservoir* (Table A- II-1)

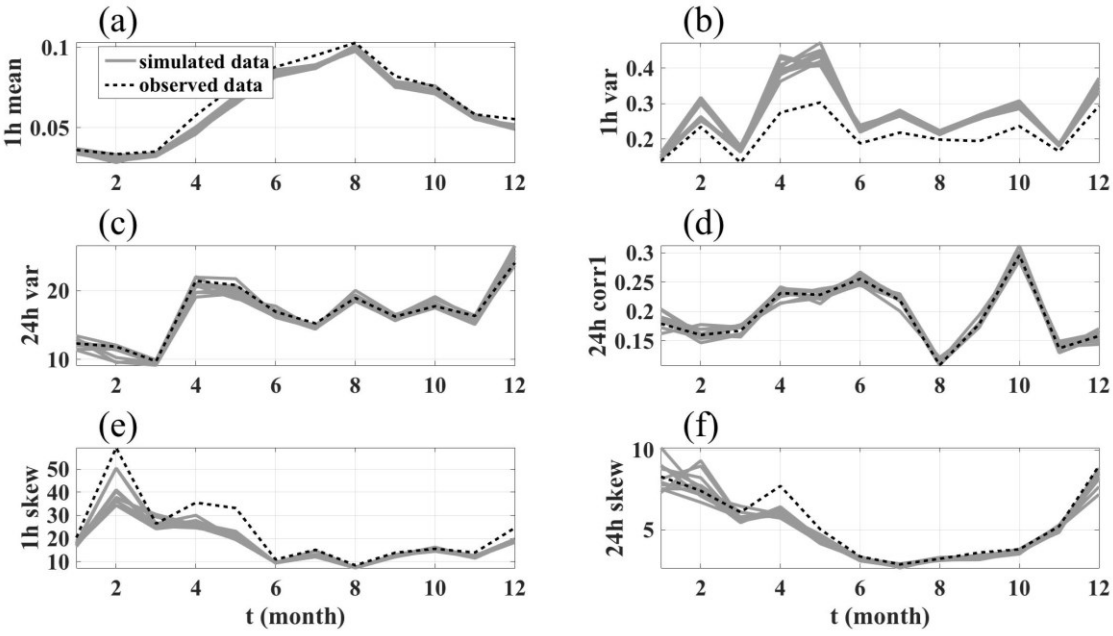

Figure A- III-2– Evaluation for simulated rainfall, calibrated using hourly rainfall data from *Rockland Reservoir* (Table A- II-1). Figure shows: Mean and variance of one hourly rainfall

(a) and (b), respectively; 24 hour and 24h autocorrelation (c) and (d) , respectively; and one and 24 hour skewness (e) and (f), respectively.

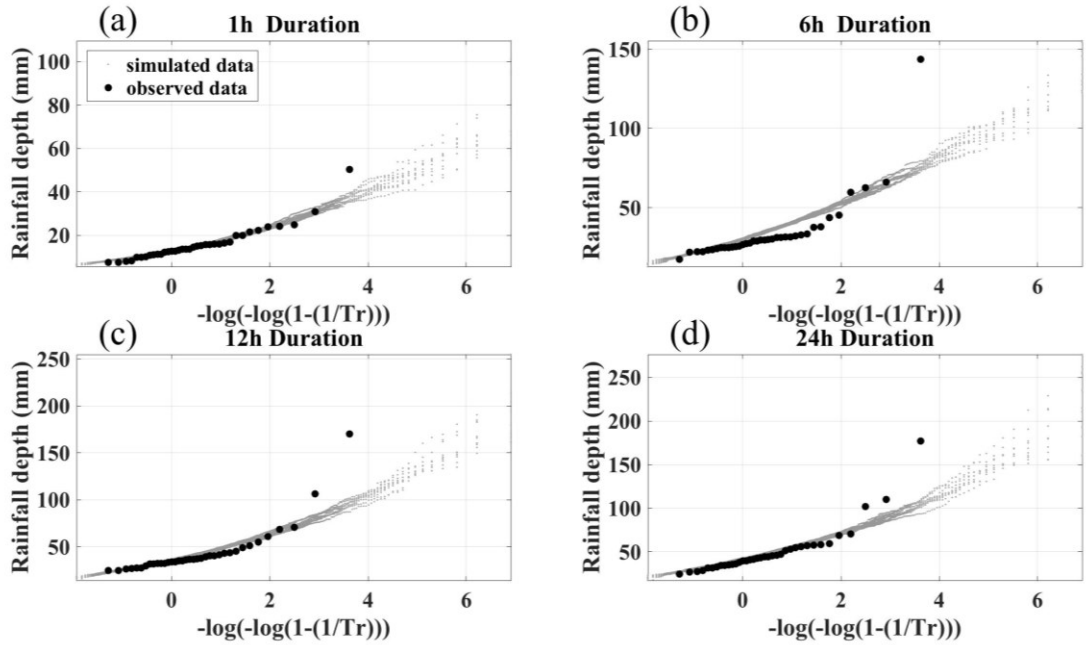

Figure A- III-3– Comparison of return period (*Tr*) of extreme events (as rainfall maxima values) at four different time aggregations (1, 6, 12 and 24h) between observed and modelled values, calibrated using hourly rainfall data from *Christmas Hills* (Table A- II-1)

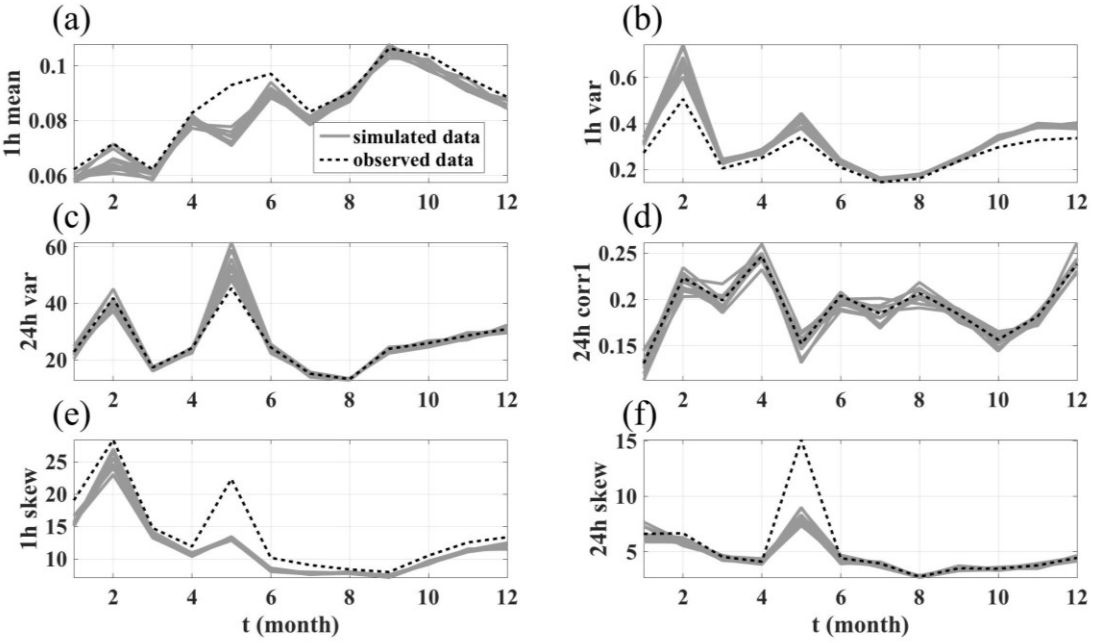

Figure A- III-4 – Evaluation for simulated rainfall, calibrated using hourly rainfall data from *Christmas Hills* (Table A- II-1). Figure shows: Mean and variance of one hourly rainfall (a) and (b), respectively; 24 hour and 24h autocorrelation (c) and (d) , respectively; and one and 24 hour skewness (e) and (f), respectively.

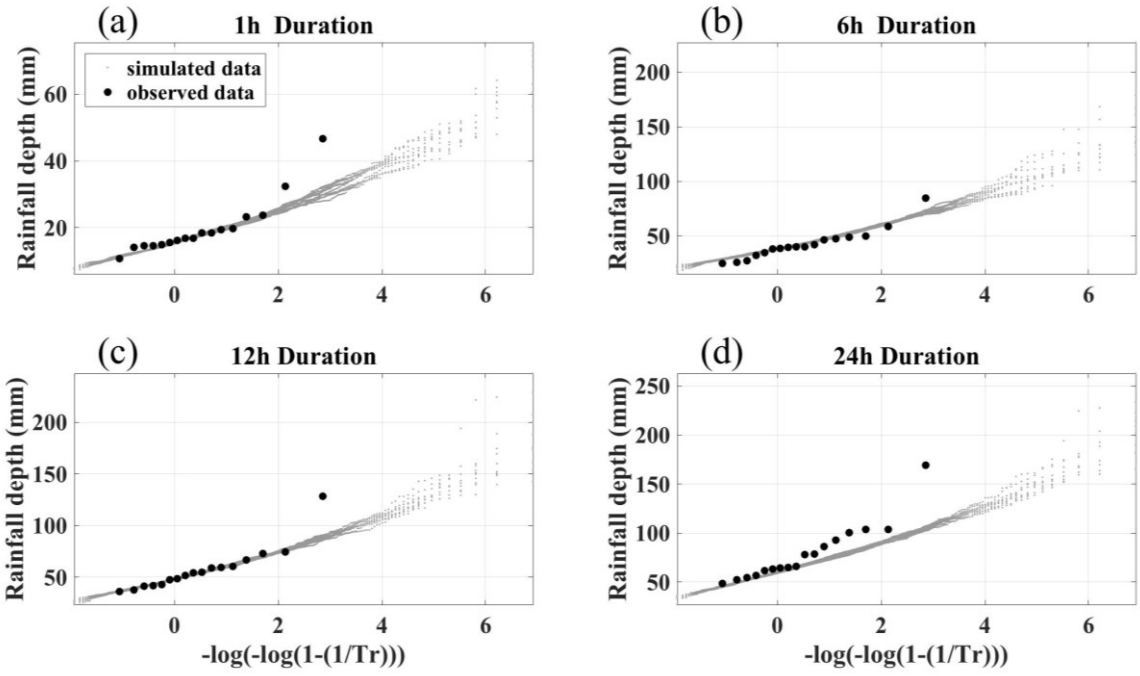

Figure A- III-5 - Comparison of return period (*Tr*) of extreme events (as rainfall maxima values) at four different time aggregations (1, 6, 12 and 24h) between observed and modelled values, calibrated using hourly rainfall data from *Mt. St Leonard* (Table A- II-1)

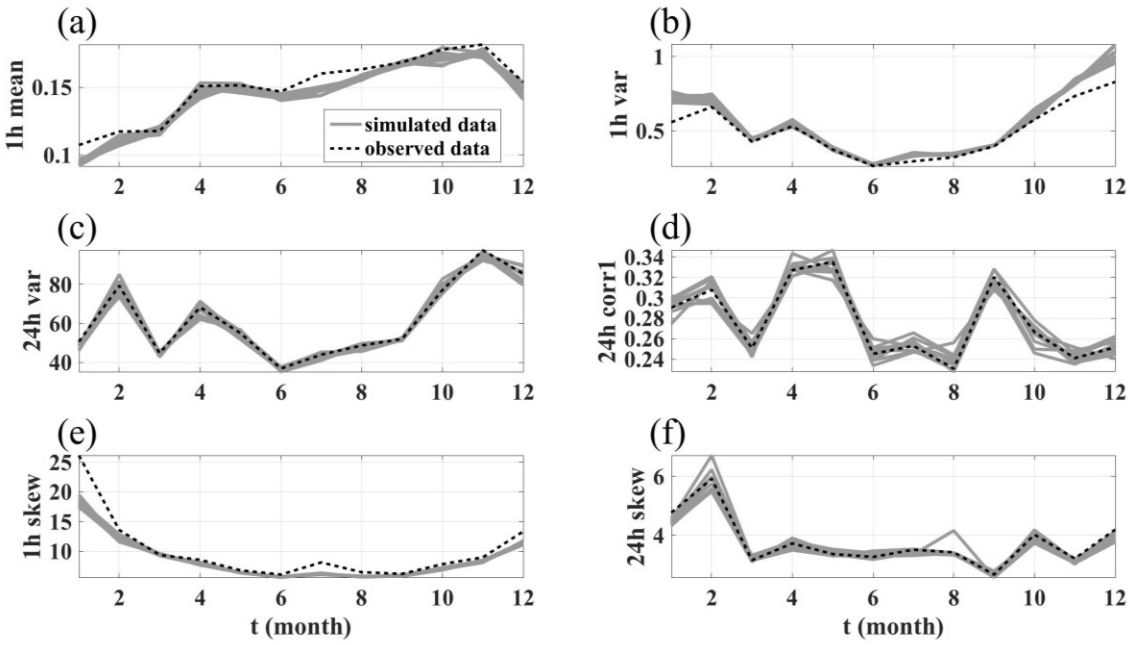

Figure A- III-6 - Evaluation for simulated rainfall, calibrated using hourly rainfall data from *Mt. St Leonard* (Table A- II-1). Figure shows: Mean and variance of one hourly rainfall (a) and (b), respectively; 24 hour and 24h autocorrelation (c) and (d) , respectively; and one and 24 hour skewness (e) and (f), respectively.

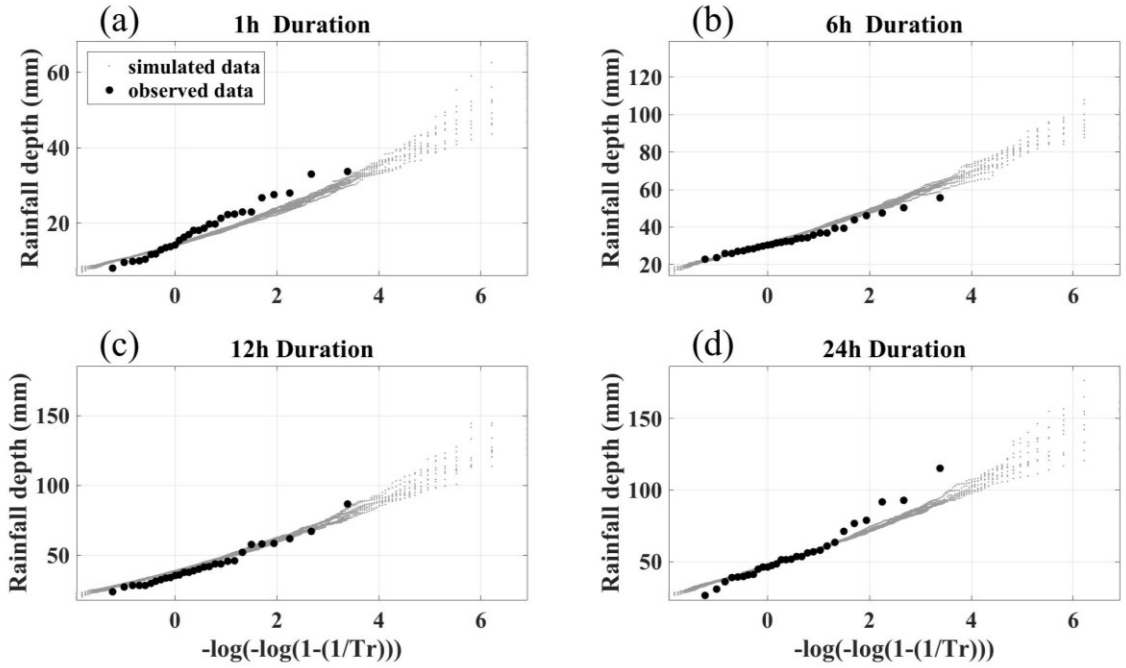

Figure A- III-7- Comparison of return period (*Tr*) of extreme events (as rainfall maxima values) at four different time aggregations (1, 6, 12 and 24h) between observed and modelled values, calibrated using hourly rainfall data from *Noojee* (Table A- II-1).

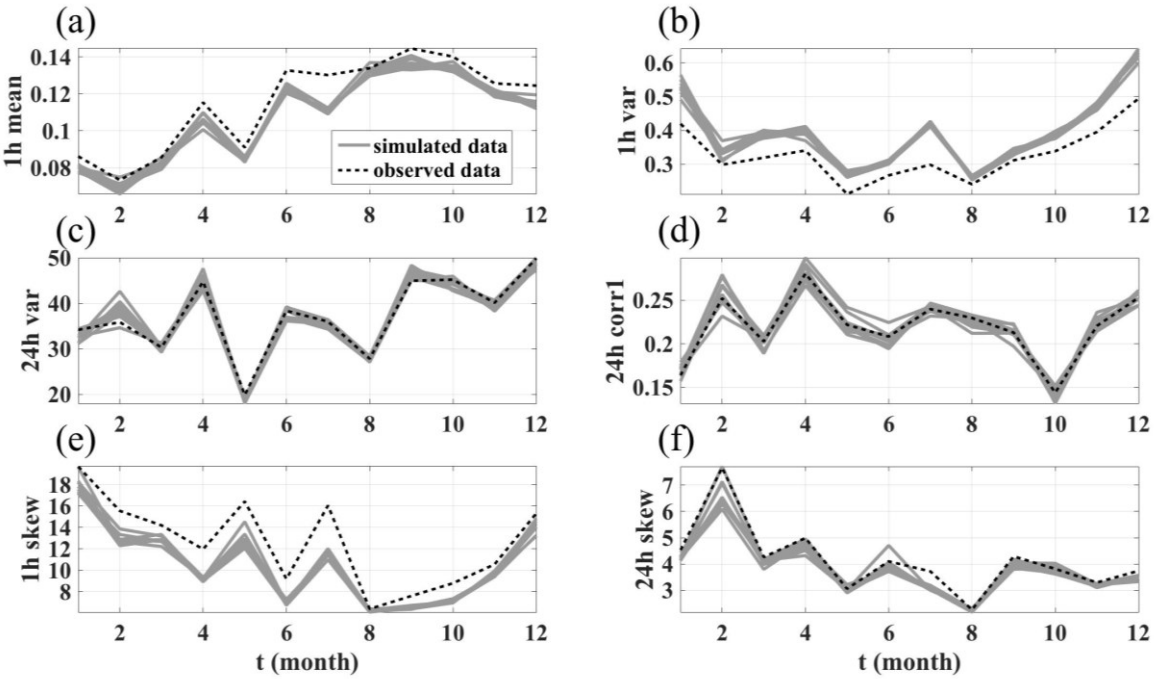

Figure A- III-8- Evaluation for simulated rainfall, calibrated using hourly rainfall data from *Noojee* (Table A- II-1). Figure shows: Mean and variance of one hourly rainfall (a) and (b), respectively; 24 hour and 24h autocorrelation (c) and (d) , respectively; and one and 24 hour skewness (e) and (f), respectively.

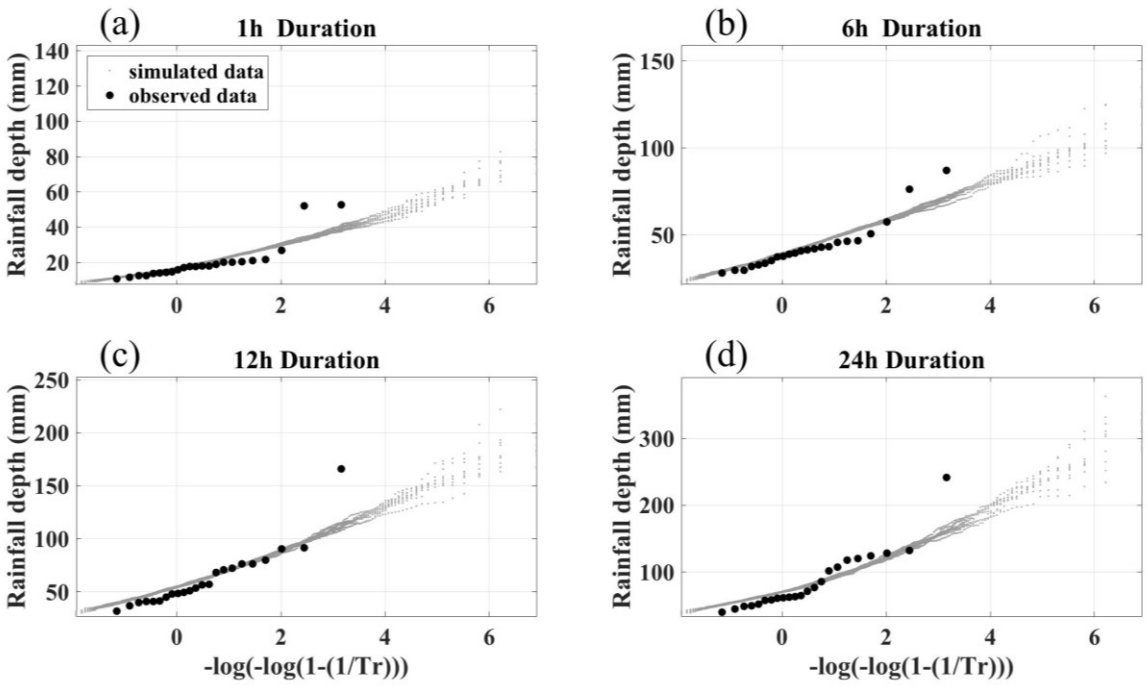

Figure A- III-9- Comparison of return period (*Tr*) of extreme events (as rainfall maxima values) at four different time aggregations (1, 6, 12 and 24h) between observed and modelled values, calibrated using hourly rainfall data from *Myrrhee* (Table A- II-1).

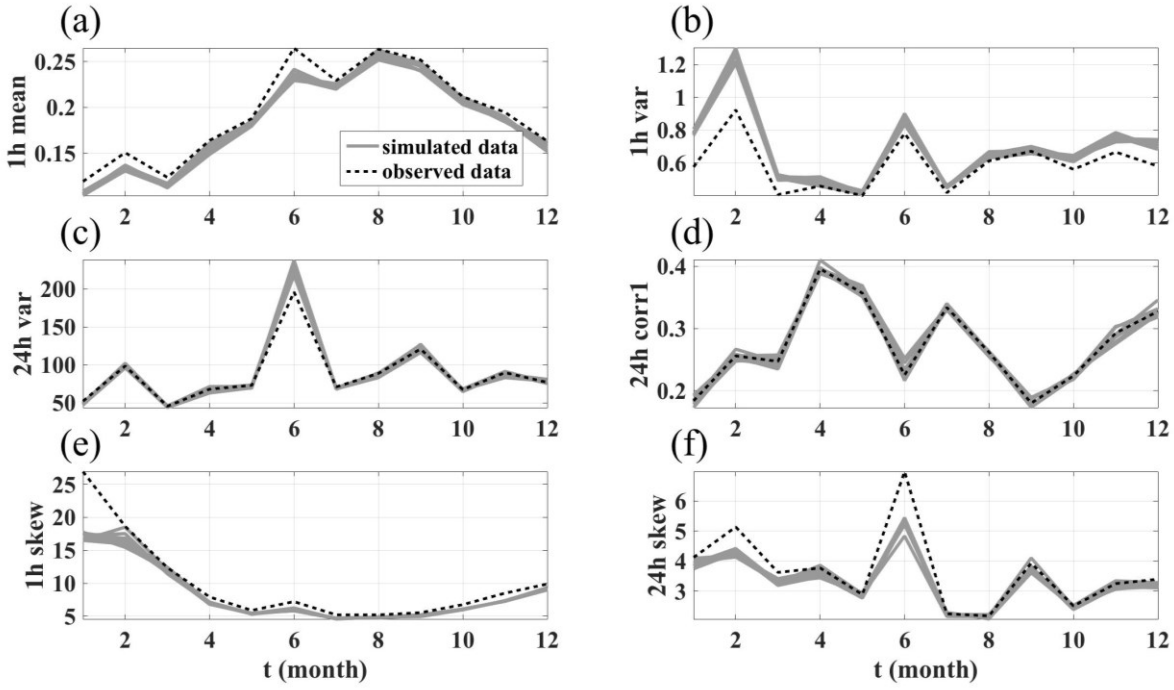

Figure A- III-10– Evaluation for simulated rainfall, calibrated using hourly rainfall data from *Myrrhee* (Table A- II-1). Figure shows: Mean and variance of one hourly rainfall (a) and (b),

respectively; 24 hour and 24h autocorrelation (c) and (d) , respectively; and one and 24 hour skewness (e) and (f), respectively.

Appendix IV Calibration of infiltration capacity model

The infiltration capacity of the soil affects its hydrological response to rainfall. Even though many factors affect the variations of *Ic* (Beven & Germann, 1982; Boyle et al., 1989; Clapp & Hornberger, 1978; Saxton & Rawls, 2006; Thompson et al., 2010), in this exercise fire and aridity have been proposed to have the biggest effect. It is assumed that aridity affects the developmental state of the soil (Jenny, 1941), and its biomass carrying capacity, both have major affect on soil hydraulic properties (Boyle et al., 1989; Jenny, 1941; Lohse & Dietrich, 2005). Fire changes the physical and chemical properties of the soil (Inbar et al., 2014), and in SE Australia (amongst a handful of other places), causes an increase in water repellence which had been proposed to have a direct influence on infiltration capacity (Langhans et al., 2016a; Nyman et al., 2010, 2014a) and runoff generation on burnt landscapes (DeBano, 2000b; Noske et al., 2016; Sheridan et al., 2007). In SE Australia, the recovery of *Ic* after fire is considered to be relatively rapid due to rainfall and vegetation recovery (Langhans et al., 2016a; Noske et al., 2016).

In order to calculate infiltration capacity (*Ic*), this model uses the following equation:

$$\ln(I_c) = r_{a_{y=i}}\,\overline{AI} + r_{b_{y=i}} \qquad (3.17)$$

where $r_{a_{y=i}}$ and $r_{b_{y=i}}$ are constants with values depending on number of years since fire (i.e., 1st year, 2nd year and unburnt, Table A- II-1); and $\overline{AI}$ is mean aridity index calculated for a century. Eqn 3.17 was calibrated using a published data from the area for burnt forest (Table 2 in Langhans et al., 2016b) and from other sources (Noske et al., 2016; Nyman et al., 2014a) for unburnt forests. Table A- II-1 contains data taken from Langhans et al. 2016; and Table A-IV-2 contains the parameters used for $r_{a_{y=i}}$ and $r_{b_{y=i}}$ (Figure A- IV-1).

During model simulations $\overline{AI}$ is calculated annually (starting from year 101) and combined with time since fire (Table A- IV-1) to calculate *Ic* (Eqn. 3.17). Mean century aridity is considered here assuming an estimated 100 lag between changes in climate to changes in soil hydraulic properties. In case $\overline{AI}$ exceeds the values stated in Table A- IV-1, *Ic* remains constant . This is based on the assumption that changes in infiltration rate within the domain (i.e., 0.7<aridity<3.5) would not change much in both extremes, and *Ic* values are expected to be at least as the ones in the defined extremes. In other words, in sites wetter than aridity 0.8,

infiltration rates are not expected to be lower than those of sites soils with aridity 0.8. Similarly, in drier sites than 2.5, infiltration rates are not expected to be lower than those of sites with aridity of 2.5.

Table A- IV-1 – Infiltration capacity values used to calibrate the infiltration model (Eqn 3.17).

aridity	Years since fire		
	0-1[1]	1-2[1]	>2
	[mm/h]	[mm/h]	[mm/h]
2.5	7.7	7.5	22.3[2]
1.5	33.7	96.1	279.67[3]
0.8	148.3	1228	1228[4]

[1](Langhans et al., 2016b)

[2](Noske et al., 2016)

[3](Nyman et al., 2014a)

[4]assumed to be at least as low as second year after the fire for such a wet site (Langhans et al., 2016b).

Table A- IV-2 – Parameters used in the model after calibration (Eqn 3.17).

Years since fire	$r_{a_{y=i}}$	$r_{b_{y=i}}$
0-1	-1.72	6.27
1-2	-2.97	9.31
>2	-2.37	9.08

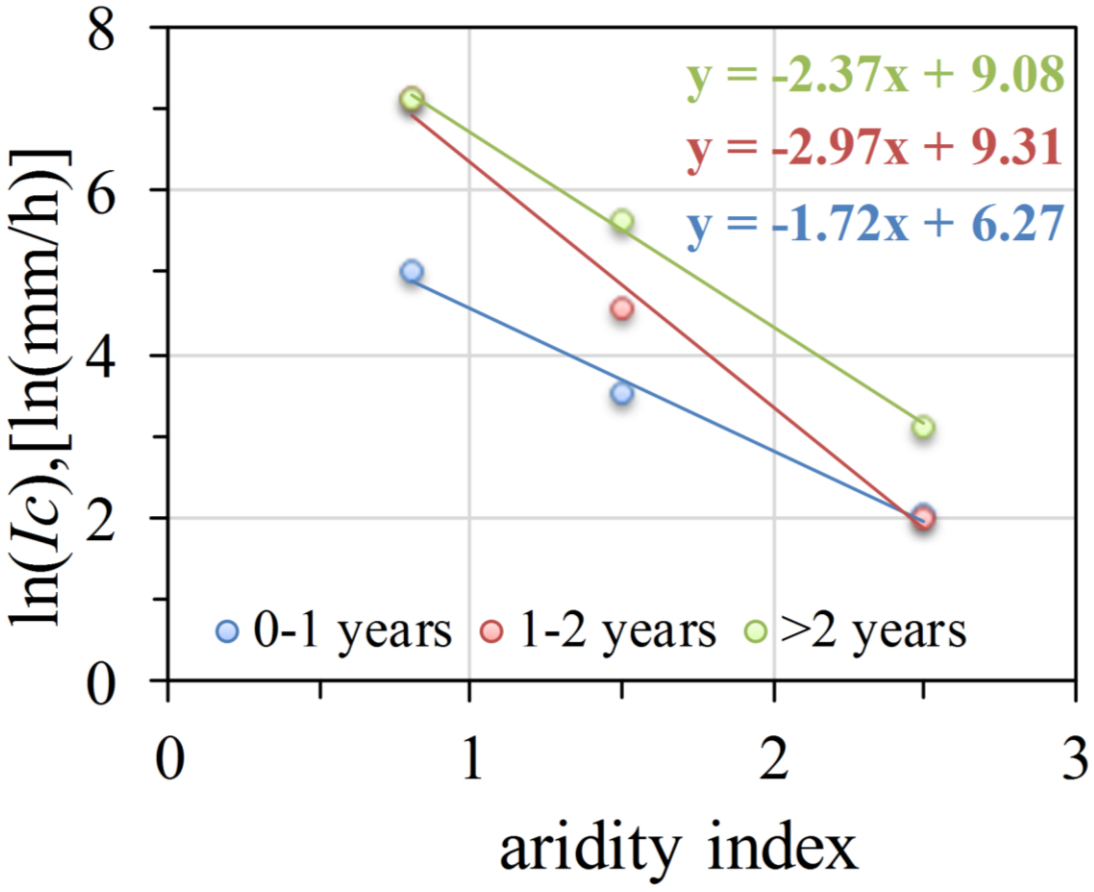

Figure A- IV-1– Calibration of parameters for the infiltration capacity model (Eqn 3.17).

Appendix V - Coevolution of north and south facing slopes

Highlight

The effect of abrupt changes in rainfall on north and south facing hypothetical systems was used in order to explore the interactions and feedbacks between climate, system states and fire frequency throughout the coevolution process. Results were analysed by examining evolution of systems with coupled soil depth-biomass-fire regime with time.

Methods

Temporal changes in soil depth and biomass were explored by simulating coevolution of two systems that only vary in solar radiation (facing north or south). Both simulations started with MAP of 721mm/yr, and were forced by an abrupt change in rainfall after 50kyr to 1621mm/yr and back to 721mm/yr after 300kyr. Temporal changes were analysed by plotting 1000-yearlong bins of biomass and fire frequency as a function of soil depth for each of the two systems. This experiment does not intend to simulate real conditions. The extreme changes in rainfall regime (i.e., 721mm→1610mm→721mm) were chosen in order to maximize the impact of climate on the coevolution process, whilst observing how soil depth, biomass and fire regime coevolve from one steady state to another.

Results and discussion

North facing slope

On the north facing slope, soil depth and biomass started to increase only when MAP change from 721mm to 1610mm (at 50kyr), indicating that both state variables fluctuated around steady state conditions until then (Figure A- V-1b and c). During these early years, fire return interval (FRI) were low (i.e., fire is more frequent) and soil depth fluctuated according to fire frequency. Soil depth and biomass gradually increased when rainfall abruptly changed to 1610mm/yr after 50k years. At this point, despite the change in MAP and the shallow soil, fire frequency remained high, as shown in Figure 4-7 (i.e., low FRI when aridity is low and soil is shallow). Figure A- V-1 shows that the coevolution process that followed the first abrupt change in MAP lasted just over 100kyr (see also Figure 4-4), during which FRI

increased until soil depth, biomass and fire regime reached new steady state conditions corresponding to MAP of 1610mm. Fluctuations in biomass increased with soil depth due to different type of vegetation response to fire, where fire-tolerant *resprouter* species were replaced by *obligate seeders* as aridity decreased from 2.49 to 1.17 (aridity decreased at the first change in MAP between 721mm to 1610mm).

The reduction in MAP to 721mm after 300kyr, was followed by an abrupt reduction in biomass to half its final values (which happens within 1 kyr), while soil remained relatively deep (a). At this point, fire frequency increased immediately when MAP dropped to its new value regardless of the deep soil (as shown in Figure 4-7). The reduction in soil depth to the new steady state condition occurred within 30-50kyr (Figure A- V-1b), which is significantly shorter than the time it took to build the soil profile (see also Figure 4-4). During this period, fire frequency increased and soil depth and biomass fluctuated around a new steady state. In this simulation of a hypothetical north facing system, soil depth and biomass started and finished with the same system states, but performed a complete hysteresis cycle as a response to changes in rainfall.

On the north facing slope, both changes in climate followed similar patterns, in which increase (decrease) in rainfall followed a steep increase (decrease) in biomass with little to no change in soil depth. It is suggested that these changes in biomass are mainly climate controlled (Figure A- V-1a). In periods when soil depth changed more rapidly due to change in fire frequency and erosion regime, biomass values were limited by soil depth and its ability to store water. This hysteresis-type pattern is suggested to be the caused due to infiltration capacity (*Ic*) values and their effect on runoff and erosion processes. For example, when MAP abruptly increased from 721mm/yr to 1610mm/yr, aridity changed from ~2.49 to ~1.17, instantaneously changing post-fire *Ic* from 7.16 mm/h to 70.76 mm/h, and of 23.45mm/h to 548.45mm/h when unburnt, respectively. These reductions in *Ic* caused an immediate decrease in runoff and erosion rates, despite the fact that fire frequency remained relatively high (Figure A- V-1a). It is suggested that the gradual reduction in soil depth as the wet climate progressed (Figure A- V-1b) occurred due to the low fluvial erosion rates (Figure 4-3) and the reduction in soil production with depth caused by the exponential nature of the soil production function (Heimsath et al., 1997). When climate changed from wet to dry after 300kyr, fire became more frequent and *Ic* dropped back what it was before the first increases in MAP. The synergistic effect of the increase in fire frequency and reduction of infiltration capacity caused a sharp reduction in soil depth, that took place about 20-30 kyr (Figure 4-4b).

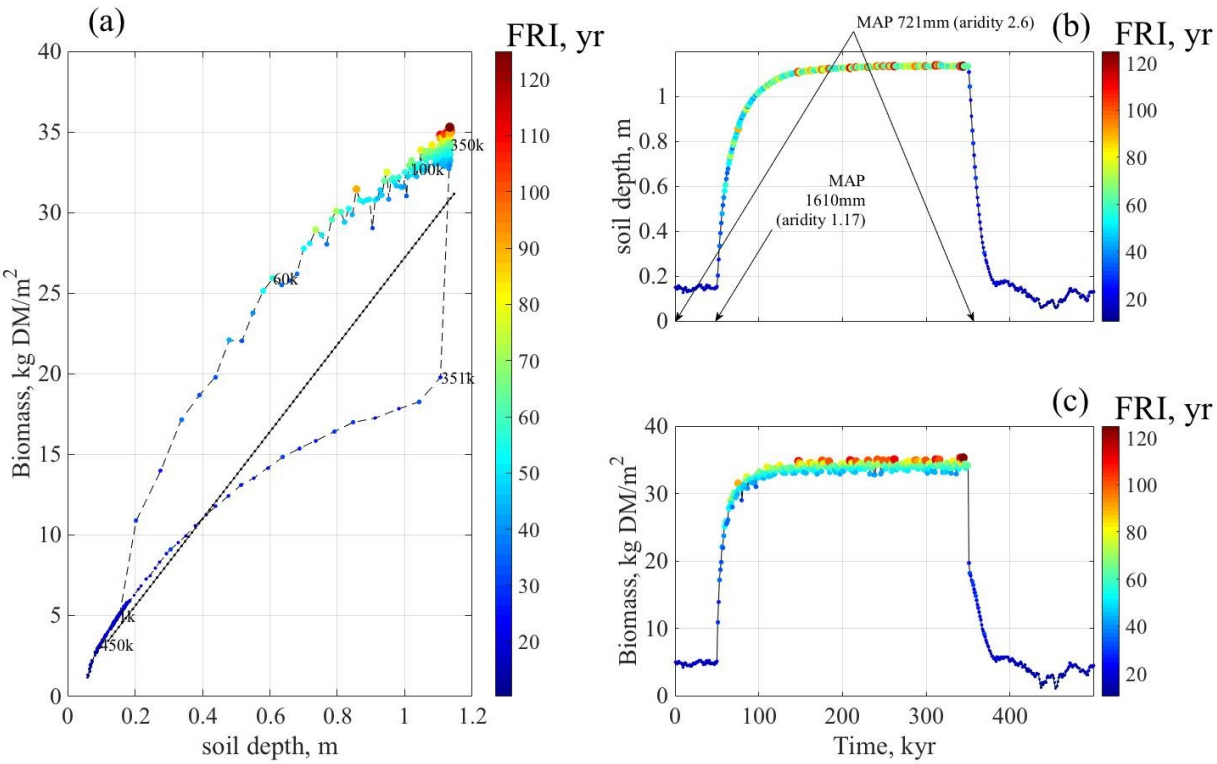

Figure A- V-1– Coevolution patterns of biomass, fire regime and soil depth of a hypothetical system facing north, as they develop as a response to abrupt changes in rainfall (a); and the evolution of soil depth (b) and biomass (b) with time across the 500ky simulation. Simulation started with MAP of 721mm , whereas climate changes were forced on the model at 50kyr and 350kyr, changing MAP to 1610 mm and back to 721mm, respectively. All markers represent a 1kyr mean of soil depth, biomass and fire return interval (FRI or forest age) for the same period. Marker size and color represent the length of the FRI, in which the bigger the marker the longer FRI is. Numbers atop some of the markers in (a) represent year number (in kyr) and were plotted in order to show the progression of the coevolution process; dashed line in (a) is a linear fit to modelled steady state combinations of soil depth and biomass across the aridity gradient.

South facing slope

Despite having treated by the same rainfall regime, the modelled south facing system followed a different pattern (Figure A- V-2). Straight after the start of the simulation, the two state variables increased despite the relatively low rainfall and FRI (721mm/yr; Figure A- V-2b and Figure A- V-2c) toward steady state conditions for this aridity (aridity=1.83) (Figure 4-2). A steeper increase in soil depth combined with higher FRI occurred after the change in MAP to 1610mm after 50kyr, until steady state soil depth and biomass were reached at around 200kyr mark (Figure A- V-2b). The steep increase in both soil depth and biomass are suggested to be related to the high *Ic* values on these aridities, making runoff generation and fluvial erosion depend more on rainfall intensity than on *Ic*. The low fluvial erosion rates throughout the simulation is suggested to be the reason for the deep soils and high biomass density. Here, the hysteresis-like behaviour does not complete a full cycle (Figure A- V-2a), as seen on the north slope (Figure A- V-1a). The large biomass fluctuations after the first change in MAP are attributed to the fact that, in this aridity (which is <1), fire damage and post fire vegetation recovery strategy is typical to 100% *obligate seeders* (Figure 3-3).

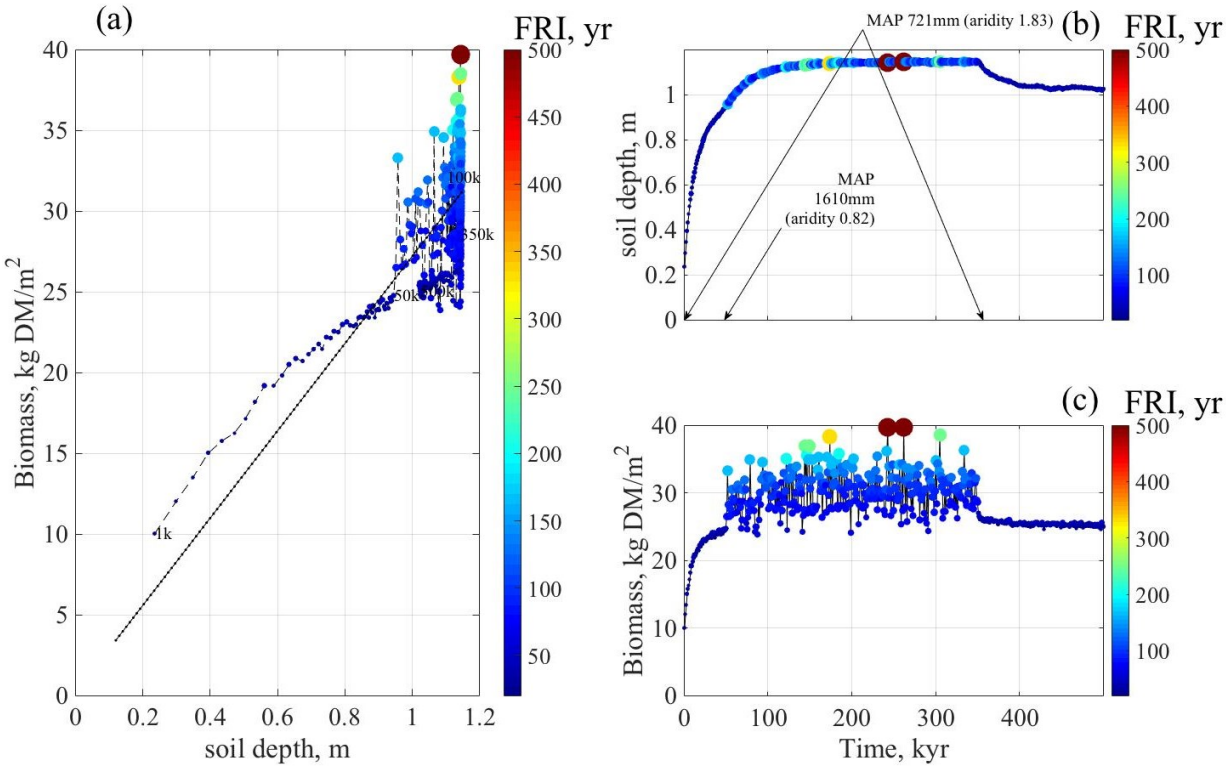

Figure A- V-2– Coevolution patterns of biomass, fire regime and soil depth of a hypothetical system facing south, as they develop as a response to abrupt changes in rainfall (a); and the evolution of soil depth (b) and biomass (b) with time across the 500ky simulation. Simulation started with MAP of 721mm , whereas climate changes were forced on the model at 50kyr and 350kyr, changing MAP to 1610 mm and back to 721mm, respectively. All markers represent a 1kyr mean of soil depth, biomass and fire return interval (FRI or forest age) for the same period. Marker size and color represent the length of the FRI, in which the bigger the marker the longer FRI is. Numbers atop some of the markers in (a) represent year number (in kyr) and were plotted in order to show the progression of the coevolution process; dashed line in (a) is a linear fit to modelled steady state combinations of soil depth and biomass across the aridity gradient.

Conclusion

Results enables the visualization different feedbacks, processes and trajectories of change in coevolution and the rates in which they occurs across the two aspects. The experiment presented on Figure A- V-1 and Figure A- V-2 elaborates the patterns and rates in which systems coevolve from one state to the another due to fluctuation in climate. These changes take place as long as soil, biomass, climate and fire (regime and effects) are not in steady state. These different trajectories are suggested to cause asymmetry in vegetation, soil and possibly landscape.

Appendix VI - Microclimate site configuration Table

		Logger	Incoming Short Wave Radiation	Air Temperature	RH	Rainfall
The Triangle	Open	CX1000 Campbell Scientific x1	CS300L pyronometer, Campbell Scientific x1	CS215 ,Campbell scientific x1	CS215 ,Campbell scientific x1	TB3 tipping-bucket rain gauge, Hydrological Services Pty, Ltd x1
	South	CX1000 Campbell Scientific x2	CS300L pyronometer, Campbell Scientific x3	CS215 ,Campbell scientific x1	CS215 ,Campbell scientific x1	Manual troughs x3
	North	CX1000 Campbell Scientific x2	CS300L pyronometer, Campbell Scientific x3	CS215 ,Campbell scientific x1	CS215 ,Campbell scientific x1	Manual troughs x3
Reefton	Open	CX1000 Campbell Scientific x1	CS300L pyronometer, Campbell Scientific x1	CS215 ,Campbell scientific x1	CS215 ,Campbell scientific x1	TB3 tipping-bucket rain gauge, Hydrological Services Pty, Ltd x1
	South	CX1000 Campbell Scientific x2	CS300L pyronometer, Campbell Scientific x3	CS215 ,Campbell scientific x1	CS215 ,Campbell scientific x1	Manual troughs x2
	North	CX1000 Campbell Scientific x2	CS300L pyronometer, Campbell Scientific x3	CS215 ,Campbell scientific x1	CS215 ,Campbell scientific x1	Manual troughs x2
Christmas Hills	Open	CX1000 Campbell Scientific x1	CS300L pyronometer, Campbell Scientific x1	CS215 ,Campbell scientific x1	CS215 ,Campbell scientific x1	TB3 tipping-bucket rain gauge, Hydrological Services Pty, Ltd x1
	South	CX1000 Campbell Scientific x2	CS300L pyronometer, Campbell Scientific x3	CS215 ,Campbell scientific x1	CS215 ,Campbell scientific x1	Manual troughs x3
	North	CX1000 Campbell Scientific x2	CS300L pyronometer, Campbell Scientific x3	CS215 ,Campbell scientific x1	CS215 ,Campbell scientific x1	Manual troughs x3

Wind Speed	Litter temperature	Soil temperature (surface)	Soil temperature (profile)	Soil moisture (surface)	Soil moisture (profile)
3-cup anemometers 014A-L, Campbell Scientific x1	-	Delta T ML3 Theta probe	-	-	-
-	HMP60 Vaisala x2	Delta T ML3 Theta probe	30cm: Standard thermocouple; 130cm: 107L; temperature probe, Campbell Scientific (replaced by standard thermocouple)	Delta T ML2x Theta probe	Decagon EC-5 Depths: 30cm, 60cm, and 90cm
-	HMP60 Vaisala x2		30cm: Standard thermocouple; 130cm: 107L; temperature probe, Campbell Scientific (replaced by standard thermocouple)	Delta T ML2x Theta probe	Decagon EC-5 Depths: 30cm, 60cm, 90cm and 130cm
3-cup anemometers 014A-L, Campbell Scientific x1	-	-	-	-	-
-	iButton sensor (DS1923, Maxim; Integrated Inc., San Jose, CA) x2	Delta T ML2x Theta probe	Standard thermocouple	Delta T ML2x Theta probe	Decagon EC-5; Depths: 30cm, 60cm, 90cm and 105cm
-	iButton sensor (DS1923, Maxim ; Integrated Inc., San Jose, CA) x2	Delta T ML2x Theta probe	Standard thermocouple	Delta T ML2x Theta probe	Decagon EC-5 Depths: 20cm and 40cm
3-cup anemometers 014A-L, Campbell Scientific x1	-	-	-	-	-
-	HMP60 Vaisala x2	Delta T ML3 Theta probe	Standard thermocouple	ML3 Theta probe	Decagon EC-5; Depths: 25cm and 55cm
-	HMP60 Vaisala x2	Delta T ML3 Theta probe	30cm: Standard thermocouple; 130cm: 107L; temperature probe, Campbell Scientific (replaced by standard thermocouple)	Delta T ML3 Theta probe	Decagon EC-5 Depths: 25cm (Faulty) and 55cm

Appendix VII - Calculating Net radiation, Potential evapotranspiration and Vapour pressure deficit

Calculating net radiation

Net radiation (R_{net}, [MJ/m2/day]) was calculated using the daily measurements of incoming short wave radiation, Air temperature, Relative Humidity and Litter temperature:

$$R_{net} = SW_{net} + LW_{net} \quad \text{(VII.1)}$$

where SW_{net} is net short wave and LW_{net} is net long wave radiation [MJ/m2/day].

Net shortwave radiation fluxes (SW_{net}, [MJ/m2/day]) for the open and below canopy sites were calculated using the daily sum of measured incoming shortwave radiation (SW_{in}, [MJ/m2/day]), assuming diffuse component had been measured by the sensors as they measured the direct component:

$$SW_{net} = SW_{in}(1 - \alpha) \quad \text{(VII.2)}$$

where α is value for albedo.

Net long wave radiation fluxes (LW_{net}, [MJ/m2/day]) were calculated for each site by subtracting the outgoing component (LW_{out}, [MJ/m2/day].) from the incoming component (LW_{in}, [MJ/m2/day].):

$$LW_{net} = LW_{in} - LW_{out} \quad \text{(VII.3)}$$

Outgoing long wave radiation was calculated using:

$$LW_{in} = \varepsilon_{surf}\sigma_{SB}T_{surf}^4 \quad \text{(VII.4)}$$

where ε_{surf} is surface emissivity; σ_{SB} is the Stephan-Boltzman Constant (4.903×10^{-9}, $MJ/K^4/m^2/day$) and T_{surf} is surface temperature [K], measured here as litter temperature under the canopy, which was measured inside two litter packs at each site, situated around a central pole. Please see *Nyman et al*.(Nyman et al., 2015a) for details about litter temperature measurements in litter packs. For calculating LW_{out} in the open site, T_{surf} was modelled using an equation that predicts litter temperature from air temperature, short wave radiation and wind speed (eqn. 4 in Slijepcevic et al., 2013).

Incoming long wave radiation was calculated using a method by *Sicart et al.* (2006), which is done by partitioning incoming long wave radiation reaching from the canopy and from the sky using:

$$LW_{in} = \left(1 - V_f\right) \varepsilon_{canopy} \sigma_{SB} T_{air}^4 + V_f f \varepsilon_{sky} \sigma_{SB} T_{sky}^4 \quad \text{(VII.5)}$$

where ε_{canopy} and ε_{sky} are canopy and sky emissivity, respectively; T_{air} and T_{sky} (K) are temperatures measured under the canopy and the open, respectively; and V_f is sky view fraction, which is calculated using *HemiView* software (Delta T Devices) from hemispherical photos (Nyman et al., 2018). For the open site V_f was set to 1, assuming there is no abstraction from the sky. Sky emissivity is calculated using (Sicart et al., 2006):

$$\varepsilon_{sky} = 1.24 \left(\frac{10 e_a}{T_{sky}}\right)^{\frac{1}{7}} \quad \text{(VII.6)}$$

The f factor adjusts for cloudiness, which is a function of clearness index (τ_{ci}) and relative humidity (RH) (Sicart et al., 2006):

$$f = 1 + 0.44RH + 0.18\, \tau_{ci} \quad \text{(VII.7)}$$

Clearness index is the fraction of daily incoming short wave radiation from the daily extra-terrestrial radiation R_a [MJ/m^2/day]:

$$\tau_{ci} = \frac{SW_{in}}{R_a} \quad \text{(VII.8)}$$

$$R_a = \frac{24(60)}{\pi} G_{sc} d_r [\omega_s \sin(\varphi_L) \sin(\delta) + \cos(\varphi_L) \cos(\delta) \sin(\omega_s)] \quad \text{(VII.9)}$$

$$d_r = 1 + 0.033\, cos\left(\frac{2\pi}{366} DOY\right) \quad \text{(VII.10)}$$

$$\delta = 0.409 * \sin\left(\frac{2\pi}{366} DOY - 1.39\right) \quad \text{(VII.11)}$$

$$\omega_s = \frac{\pi}{2} - arctan\left(-\frac{tan(\varphi_L) tan(\delta)}{\sqrt{X}}\right) \quad \text{(VII.12)}$$

$$X = 1 - \tan^2(\varphi_L) \tan^2(\delta) \quad \text{(VII.13)}$$

where G_{sc} is solar constant (0.082 MJ/m^2/min); d_r id inverse relative distance Earth-Sun; ω_s is sunset hour angle (rad), φ_L id latitude (rad) and δ is solar angle (rad). Note that 2016 was a leap year, so number of days in the year was set to 366.

Calculating Potential Evapotranspiration

Potential evapotranspiration (*Ep*) for below the canopy and in the open were calculated using the Priestley-Taylor equation (Priestley & Taylor, 1972):

$$E_P = \frac{\alpha_E}{\lambda}\frac{\Delta}{\Delta+\gamma}(R_{net} - G) \quad \text{(VII.14)}$$

where α_E is a constant (1.26); λ is latent heat of vaporization; G is soil heat flux (assumed zero); Δ is the gradient of saturated vapour pressure with temperature and γ is the psychrometric constant. Latent heat of vaporisation is:

$$\lambda = 2.501 - 2.361\ 10^{-3} * T_{daily} \quad \text{(VII.15)}$$

where T_{daily} is mean daily air temperature. Psychrometric constant (kPa/^{o}c) is:

$$\gamma = \frac{1.013\ 10^{-3} P}{0.622\ \lambda} \quad \text{(VII.16)}$$

where P is atmospheric pressure that can be calculated using elevation, z (m):

$$\mathrm{p} = \left(101.3\frac{293 - 6.5\ 10^{-3} z}{293}\right)^{5.26} \quad \text{(VII.17)}$$

gradient of saturated vapour pressure is calculated by:

$$\Delta = \frac{408\ e_s}{(237.3 + T_{daily})^2} \quad \text{(VII.18)}$$

where e_s is the saturated vapour pressure (kPa), calculated by averaging the minimum (e_{s-min}) and maximum (e_{s-max}) saturated vapour pressure (kPa):

$$e_s = \frac{e_{s-max} + e_{s-min}}{2} \quad \text{(VII.19)}$$

$$e_{s-l} = 0.6108\ exp^{\frac{17.27\ T_l}{T_l+237.3}} \quad \text{(VII.20)}$$

where e_{s-l} is maximum (minimum) saturation vapour pressure using maximum (minimum) daily temperatures, T_l (^{o}c).

Calculating Vapour pressure deficit (VPD)

VPD is calculated using:

$$\text{VPD} = e_s - e_a \quad \text{(VII.21)}$$

where e_a is actual vapour pressure (kPa), calculated using mean daily relative humidity measurements:

$$e_a = \frac{RH}{100} e_s \quad \text{(VII.22)}$$

Appendix VIII Additional Raw Data for Chapter 5

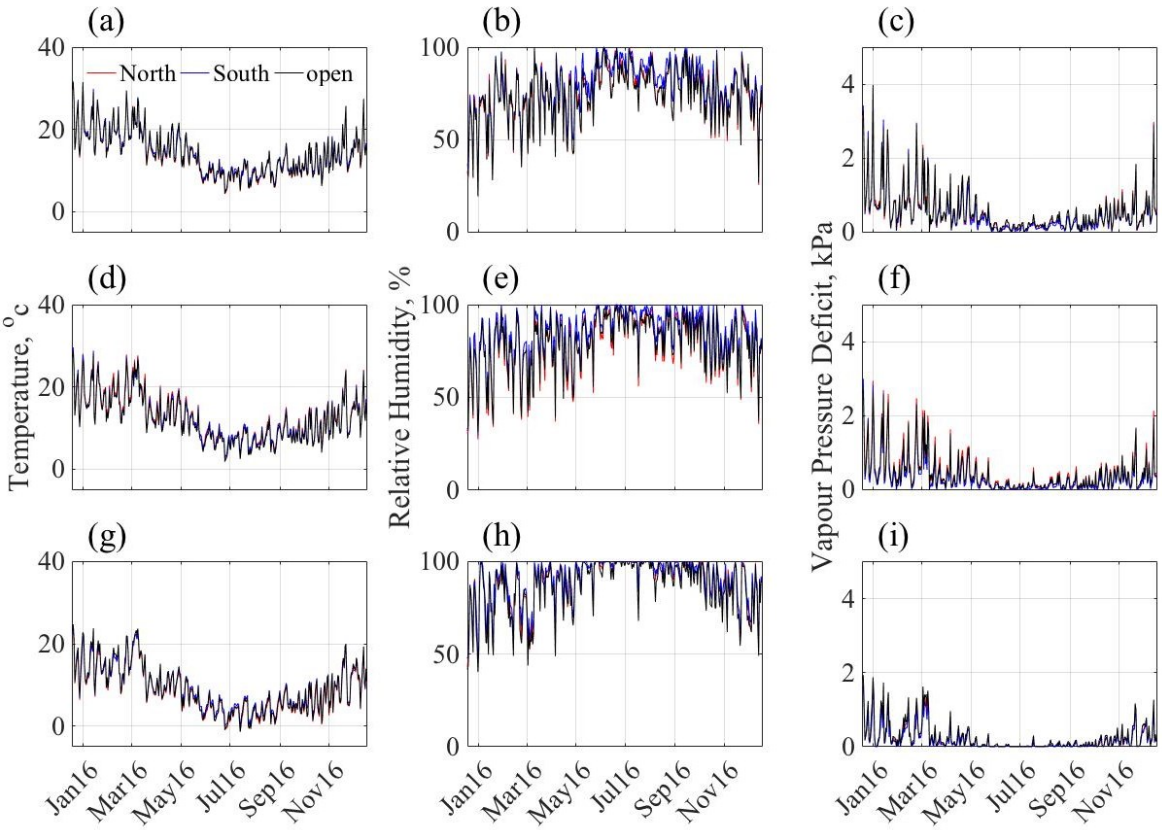

Figure A- VIII-1 - Time series of measured air temperature (left column) and relative humidity (middle column) and calculated Vapour pressure Deficit (Eqn. VII.22, right column) under the canopy and in the open at CH (a-c), RT (d-f) and TT (g-i).

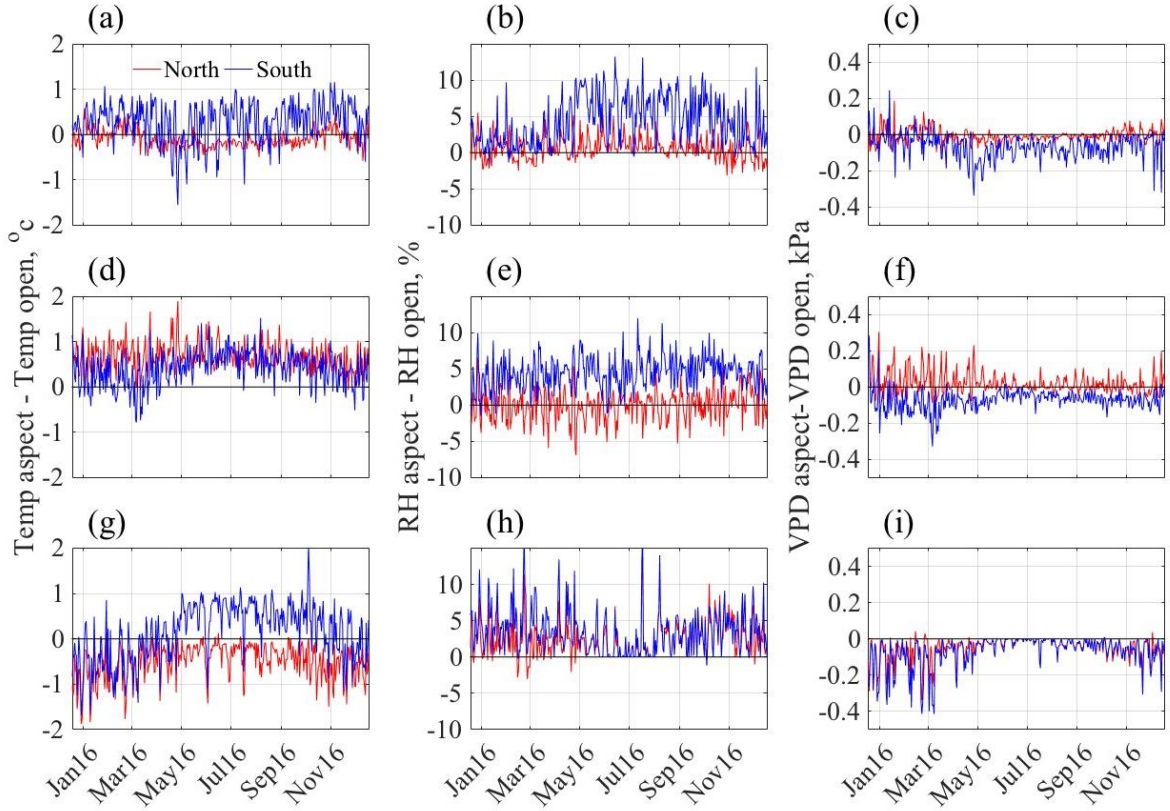

Figure A- VIII-2 -: Time series of the differences between measured air temperature (left column), relative humidity (middle column) and calculated Vapour Pressure Deficit (Eqn. VII.22, right column), under the canopy and in the open; at CH (a-c), RT (d-f) and TT (g-i).

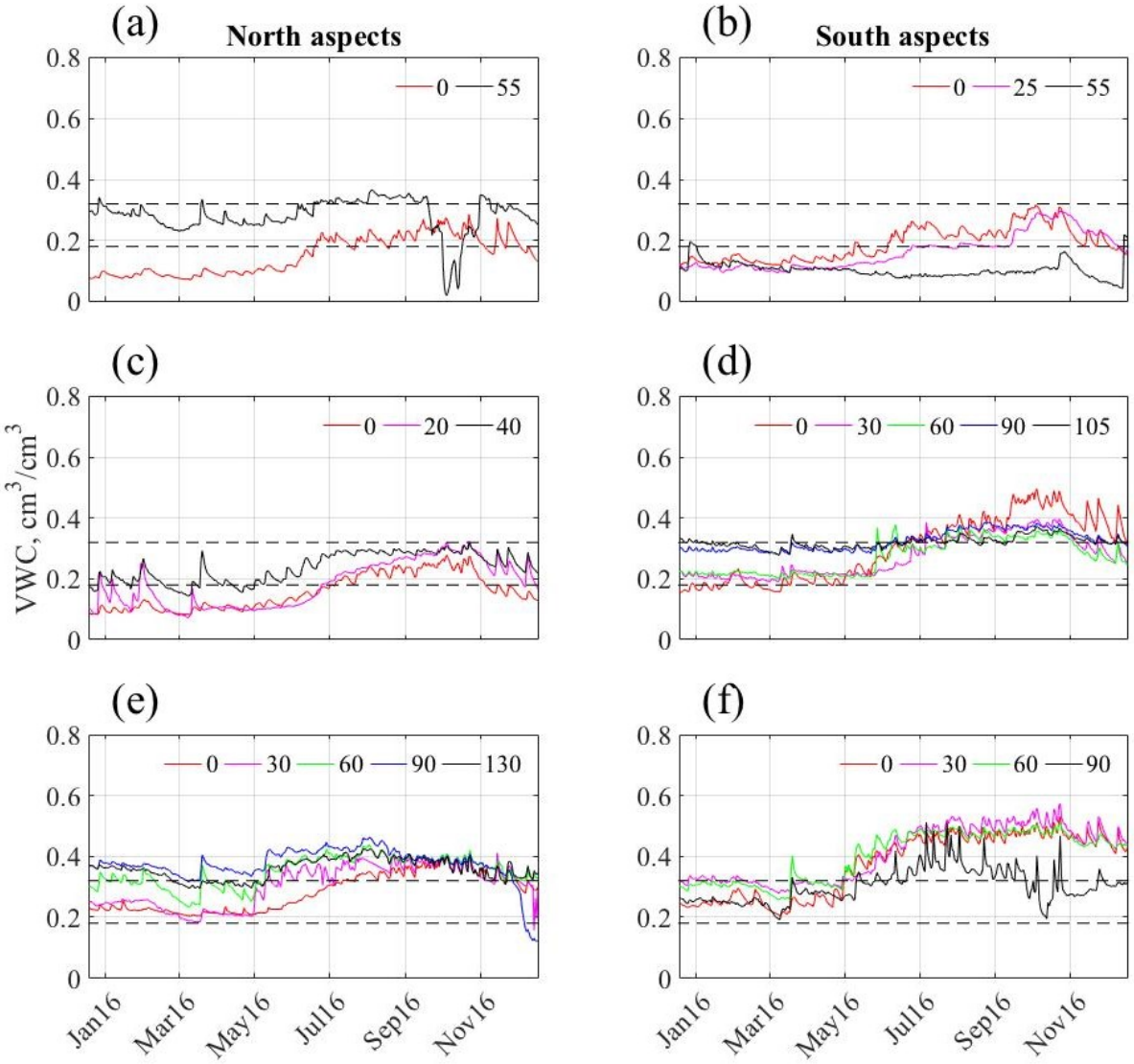

Figure A- VIII-3 - Time series of the volumetric soil moisture content for all the sensors involved in the analysis at CH north and south (a-b), RT north and south (c-d) and TT north and south (5-6). Depths in legend are in cm. Horizontal dashed lines represent theoretical volumetric moisture content at field capacity (top) and wilting point (bottom). Note that the sensor in 25cm at CH North was faulty and was removed from the analysis.